Numerical Methods for the Interaction of Atoms with Intense Low Frequency Laser Pulses

Dean Thomas Pyke

Thesis submitted to the University of London
for the degree of Doctor of Philosophy

2016

Numerical Methods for the Interaction of Atoms with Intense Low Frequency Laser Pulses

Department of Mathematics
Royal Holloway, University of London

Declaration of Authorship

I, Dean Thomas Pyke, hereby declare that this thesis and the work presented in it is entirely my own. Where I have consulted the work of others, this is always clearly stated.

Signed:

(Dean Thomas Pyke)

Date:

Summary

In recent years intense laser fields have become more available over a frequency range extending from the infrared to the ultraviolet in the form of short pulses. In the low frequency regime where the photon energy is much lower than the ionisation potential, the advent of high intensity lasers has allowed detailed investigation into phenomena such as above threshold ionisation (ATI), high order harmonic generation (HHG) and attosecond pulse generation. The numerical integration of the time dependent Schrödinger equation (TDSE) has become the main theoretical approach for the quantitative study of laser-atom interaction and investigation of these short pulses of very high intensity makes this method unavoidable if accurate results are required. In this thesis we begin by examining fundamental features of the dynamics of an atom when interacting with an intense electromagnetic field, looking at the description of the field, the Hamiltonian and mechanisms of ionisation. We then investigate the numerical solution of the TDSE, looking at different methods of representation of the wave function and analyse different time propagation algorithms. We then present the results of our programs using one dimensional model potentials in a wide range of laser parameters. We investigate new methods to calculate observables; such as the time dependent surface flux method combined with exterior complex scaling. We vary the frequency, intensity, pulse length and carrier phase of the laser, studying how these parameters affect observables including the ATI spectrum. Finally we extend our program to the full three dimensional atom, again over a range of laser parameters and discuss the computational difficulties for intense low frequency laser pulses. We use these programs to try to understand the low energy structure (LES) found in recent experiments for intense low frequency pulses.

Acknowledgements

Firstly I would like to thank my supervisors, Francisca Mota-Furtado and Pat O'Mahony, for the time they invested in me and for their support and encouragement throughout my time at Royal Holloway. Their assistance was invaluable and I am indebted to them both for the opportunity they enabled me to undertake. I am also grateful to Bernard Piraux and Aliou Hamido for their collaboration throughout my PhD and to Eric Cormier and Armin Scrinzi for their helpful correspondence.

These 4 years have been a great adventure with thanks in no small part to the wonderful friends I made during this time. In particular I would like to thank Andrew, Caroline, Christian, Dale, Eugenio, George, Guillaume, Joachim, Konstantinos, Matteo and Pavlo as well as Jim, Giorgia and Rumi for all the fun times and fond memories we shared together. To my friends at home I would like to thank Tom and Tommy B for their support and companionship and for the memorable and fascinating travels we embarked on each summer. I am very lucky to have friends as good as them. Also to James, whose company is always a pleasure. I hope our pub trips continue long into the future.

Very special thanks go to my brother and my parents for always being there for me, especially during my PhD. Without them it wouldn't have been possible for me to have made it this far and I will be forever grateful and in their debt. I would also like to thank Vince Miller for his help in me getting to where I am today. He is and always will be greatly missed.

To Graham, Debbie, Matthew, Michelle and Sophie. Thank you for taking me in as one of your own and becoming a second family to me. The great support and friendship you've always shown me means so much. Finally, to Sarah for always being there for me and being the constant source of my happiness. Thank you for putting up with my long absences and for always picking me up whenever I am down. Words cannot describe how much you mean to me.

Contents

Chapter 1

Introduction

The interaction of a laser field with atoms, or more generally matter, is an intensively studied field in physics. The possibility of multiphoton transitions was theoretically predicted by Maria Göppert-Mayer in 1931. Later in 1960, Theodore Maiman constructed the first laser; a high intensity radiation source with monochromatic character which soon led to a wide range of applications and newly discovered effects resulting from the interaction between photons and a variety of matter. In 1979, above threshold ionisation (ATI) was observed for the first time, where a photoelectron absorbs more photons than the minimum required for multiphoton ionisation (MPI).

The first experiments exploring non-linear optical effects due to multiphoton absorption mechanisms were performed in the early 1970s with nanosecond pulses where the pulse form could be described only on a statistical level [51]. However, in recent years the development of sources means that intense laser fields have become more available over a frequency range extending from the infrared (IR) to the ultraviolet (UV) in the form of short pulses with a well-defined, stabilised and controllable carrier envelope phase [51, 9]. In the low frequency regime, where the photon energy is much lower than the ionisation potential, the advent of high-intensity lasers with intensities in the order of or exceeding $I = 3.5 \times 10^{16}$ W $\cdot$ cm^{-2} in conjunction with increased theoretical research into the development of numerous mathematical methods and numerical algorithms to solve the time dependent Schrödinger equation (TDSE) by means of spectral and finite difference grid methods [29, 33, 38, 20] has allowed detailed investigations of nonlinear phenomena such as ATI [40], high order harmonic generation (HHG) [40, 78], multiphoton multiple ionisation [35] and

attosecond pulse generation [4].

However, it is not a simple task to analyse the mechanisms behind the above processes since it is after the laser is turned off that the relevant information is extracted from the numerical solution of the TDSE. In 1965, Keldysh [41] introduced a dimensionless parameter which defines the laser-field environment and shows the regime of ionisation based on the laser field parameters. This was termed the Keldysh parameter and is given by

$$\gamma = \frac{\sqrt{2mI_p}\,\omega}{eE_0} \tag{1.1}$$

where m is the mass of the particle, I_p is the ionisation potential of the atom, ω is the frequency of the laser and E_0 is the strength of the electric field. For $\gamma \gg 1$, ATI and HHG occur via multiphoton transitions whilst for $\gamma \ll 1$ ionisation is dominated by the tunnelling mechanism. In the latter case the electron can escape from its parent atom by tunnelling through a barrier formed by the superposition of the atomic Coulomb potential and the time dependent electric field. Once free, the electron is accelerated in the field and can then, after the field changes direction, return to the parent ion where it can scatter or recombine which leads to HHG [23, 3]. This picture is the basis of the well known classical *Simple Man's Model* and the quantum *Strong Field Approximation* (SFA), also known as the *KFR Model* [2, 26, 60].

In particular, increased interest and rapid progress in HHG, where an intense optical field interacts with the atom producing harmonics of the driving field, has provided a reliable, reasonably compact source of coherent radiation. Due to improved levels of control of the optical process and advances in phase matching, experimentalists are now able to produce ever shorter and more intense pulses going into the X-ray region as conversion efficiency of HHG is improved and harmonics of higher orders are generated [23]. As well as its utility as a bright source of high energy photons, HHG has opened a window of insight into intense optical field-atom interactions.

As such it has become more important than ever for fast, accurate numerical approaches to the solution of the TDSE to be achieved. As computers become more

powerful and with ever expanding memory capabilities it has now become possible for theorists to be able to study these field-atom interactions to higher intensities and lower frequency of laser field than ever before.

In this thesis we explore different efficient and numerically stable time propagators to solve the TDSE including the fourth order Runge-Kutta, the explicit Fatunla method and the explicit Arnoldi method, analysing the advantages and disadvantages of each. We combine these with the spectral methods to represent the wave function in space and we consider basis sets of Sturmians and B-splines. We calculate a series of observables - electromagnetic spectra, angular distributions, currents etc. to try to understand the physical mechanisms present. The application and success of these valuable digital tools of integration allow us to investigate a particularly difficult case: the study of the low frequency hydrogen atom, with frequency $\omega = 0.0228$ a.u. which has been of much interest in recent years.

Interest in the study of ionisation of atomic and molecular systems by low frequency laser fields has peaked with the discovery of an unexpected phenomenon, the manifestation of spike-like structure in the photoelectron energy distribution at low energy. This spike, termed the low energy structure (LES) [79, 46, 75] becomes prominent using mid-infrared laser wavelengths of $\lambda = 800$ - 2000nm with intensities of $I = 10^{13}$ - 10^{15} W $\cdot$ cm^{-2} and came to note when it was published in the prestigious journal Nature [17]. It causes great surprise in the area because it was not predicted by the SFA which was typically used to describe the ionisation process of high intensity and low frequency regime. In numerically solving the TDSE in this regime, firstly in one dimension for a model atom and then for the full three dimensional Hydrogen atom, we look at some results obtained from the wave function Ψ, giving details as to how we obtained the results computationally, and aim to investigate possible causes of the LES and interference effects in general.

1.1 Structure of the Thesis

This thesis is organised as follows.

- In chapter 2 we begin by examining the basic features of the dynamics of an atom when interacting with an intense electromagnetic field. We set up the main equations used and our work will be presented for the case of the Hydrogen atom, which can be used to model multielectronic systems and molecules within the single active electron (SAE) approximation. We introduce and consider a number of necessary components of the TDSE including the electromagnetic field in the dipole approximation, the Hamiltonian operator and the choice of gauge used in calculations, giving advantages and disadvantages of each. We then look at mechanisms of ionisation and associated nonlinear phenomena mentioned above. We talk about classical dynamics of electrons before finishing by discussing the strong field approximation (SFA) and the low energy structure (LES).

- In chapter 3 we discuss the numerical integration of the TDSE which has become the main theoretical approach for the quantitative study of a vast amount of phenomena. We look at different methods of representing the wave functions using a spectral decomposition method and give details on the time propagators mentioned above, giving advantages and disadvantages of each. We introduce other numerical methods that can aid in the fast and efficient solution of the TDSE such as exterior complex scaling (ECS) before looking at a detailed comparison of the time propagation techniques, solving both one dimensional calculations for model potentials and three dimensional calculations for the Hydrogen atom.

- In chapter 4 we present results and findings from calculations carried out in one dimension using the numerical methods discussed. We look at a variety of phenomena including the electron probability density and ATI spectrum for a range of wavelengths, culminating in the investigation of very low frequency

laser-atom interaction. We show results and give details regarding the implementation of the ECS and time dependent Surface Flux Method (tSURFF) for calculating the ATI spectrum.

- Finally, in chapter 5 we extend the methods and results shown for one dimension by investigating the three dimensional Hydrogen atom for a range of frequencies. We again calculate a number of observables including the angular distribution of the ionised electrons. We also investigate the breakdown of the adiabatic limit. We show results for the ECS in 3D before briefly discussing and showing results for investigation into other atoms, including negatively charged Hydrogen and Argon.

Chapter 2

Laser Atom Interaction in an Intense Field

2.1 Introduction

We begin by examining the basic features of the dynamics of an atom when interacting with an intense electromagnetic field. In this chapter we will set up the main equations used in the chapters to follow. Simple modifications of the theory can be used to model multielectronic systems and molecules within the single active electron (SAE) approximation.

In the following we will consider intense laser fields, in particular in the lower frequency regime, with intensities I ranging from 10^{13} to 10^{15} $\mathrm{W \cdot cm^{-2}}$. The low frequency regime is defined for frequencies ω which are low with respect to the Hydrogen ionisation potential $I_p = 13.6\mathrm{eV}$, so that $\hbar\omega \ll I_p$, where $\hbar$ is the reduced Planck constant. The typical frequency values we will be studying are in the infrared region for wavelengths λ extending from 800nm to 2μm. The corresponding periods would be from about 16 to 400 femtoseconds and we will consider laser pulses typically with a few optical cycles.

In general we need to describe a laser-atom system as a complete system, represented by a Hamiltonian which is partitioned into an atomic Hamiltonian and an atom-laser interaction Hamiltonian. Solving such a system would mean to simultaneously solve the coupled equations of motion of quantum electrodynamics (QED) for the laser field and the time dependent Schrödinger equation (TDSE) for the atomic system. The fact that we are working with intense fields allows us to use a simplified approximation where the interaction between the electromagnetic field and the atom is treated semi-classically. The laser light is then treated as a classical electromagnetic

field described by Maxwell's equations while the atoms are described by quantum mechanics with the solution of the TDSE, without a need to quantify the effect of the exchange of photons in the state of such intense laser fields. In short, the laser field affects the atom but the atom does not affect the laser field. For intense fields, the number of photons present in the dominant mode of a quasi-monochromatic laser is extremely high. The number $N(\omega)$ of photons of frequency ω in a volume V is related to the intensity of a field of frequency ω by the relation

$$I(\omega) = \frac{c\hbar\omega N(\omega)}{V}, \tag{2.1}$$

where c is the speed of light in a vacuum. For example, in a pulse generated by a typical Nd:YAG laser with photon energy $\hbar\omega = 1.17$ eV and wavelength $\lambda = 2\pi c/\omega = 1064$ nm, in a relatively low intensity $I = 10^{12}$ W $\cdot$ cm^{-2}, the number of photons in a volume $V = \lambda^3$ is given by $N(\omega) \approx 2 \times 10^8$. Such a large number of photons concentrated on a few modes provides a good justification for using a classical description of the laser field.

We then represent the Hamiltonian for the system in the form

$$\hat{H} = \hat{H}_0 + \hat{H}_{\mathrm{I}}, \tag{2.2}$$

where $\hat{H}_0$ is the atomic Hamiltonian operator and $\hat{H}_{\mathrm{I}}$ is the field-atom interaction Hamiltonian operator. We note that $\hat{H}_{\mathrm{I}}$ is time dependent since the laser field is time dependent and oscillatory. The expectation values of the physical observables that will be monitoring the motion of the electrons during the interaction will also be oscillatory.

2.2 The External Field

The classical electromagnetic field is described by two vector fields, the electric field $\mathbf{E}(\mathbf{r}, t)$ and the magnetic field $\mathbf{B}(\mathbf{r}, t)$, which satisfy the Maxwell equations at position vector $\mathbf{r}$ and time t. In SI units we can write these in source-free form as,

$$\nabla \cdot \mathbf{E} = 0 \tag{2.3}$$

$$\nabla \cdot \mathbf{B} = 0 \tag{2.4}$$

$$\nabla \times \mathbf{E} = -\frac{\partial \mathbf{B}}{\partial t} \tag{2.5}$$

$$\nabla \times \mathbf{B} = \epsilon_0 \mu_0 \frac{\partial \mathbf{E}}{\partial t}, \tag{2.6}$$

where ϵ_0 and μ_0 are the electric permittivity and the magnetic permeability of vacuum respectively and satisfy the relation $\epsilon_0 \mu_0 = 1/c^2$. The electromagnetic field can also be described by the vector potential $\mathbf{A}(\mathbf{r}, t)$ and by the scalar potential $\phi(\mathbf{r}, t)$. Maxwell's equations lead to the following relations between the fields and the potentials,

$$\mathbf{B} = \nabla \times \mathbf{A} \tag{2.7}$$

and

$$\mathbf{E}(\mathbf{r}, t) = -\frac{\partial}{\partial t}\mathbf{A} - \nabla \phi. \tag{2.8}$$

We can see that the electromagnetic field is described by four components and therefore is overdetermined meaning that the vector and scalar potentials are not uniquely determined. For an arbitrary scalar function $\chi(\mathbf{r}, t)$, the same electromagnetic field can be described by the potentials $\mathbf{A}'(\mathbf{r}, t)$ and $\phi'(\mathbf{r}, t)$, given by

$$\mathbf{A}' = \mathbf{A} + \nabla \chi \tag{2.9}$$

and

$$\phi' = \phi - \frac{\partial \chi}{\partial t}. \tag{2.10}$$

For a given dynamical situation the choice of this scalar function $\chi(\mathbf{r}, t)$ can give a convenient mathematical description of the electromagnetic field. This process is referred to as the choice of gauge. One of the most commonly used gauges is the Coulomb gauge, in which case we choose the scalar function χ such that

$$\nabla \cdot \mathbf{A} = 0. \tag{2.11}$$

For an electromagnetic field in a vacuum, assuming the Coulomb gauge, we have $\phi = 0$. The fields are then given by

$$\mathbf{B} = \nabla \times \mathbf{A} \tag{2.12}$$

and

$$\mathbf{E} = -\frac{\partial}{\partial t}\mathbf{A}. \tag{2.13}$$

In addition, from equations (2.6), (2.12) and (2.13) it can be shown that the vector potential $\mathbf{A}$ satisfies the homogeneous wave equation

$$\nabla^2 \mathbf{A} - \frac{1}{c^2}\frac{\partial^2 \mathbf{A}}{\partial t^2} = 0. \tag{2.14}$$

A transverse plane wave solution of the homogeneous wave equation is of the form

$$\mathbf{A}(\mathbf{r}, t) = \boldsymbol{\epsilon} A_0 \sin(\mathbf{k} \cdot \mathbf{r} - \omega t - \varphi) \tag{2.15}$$

where the wavevector $\mathbf{k}$ gives the propagation direction and the wavelength is $\lambda = 2\pi/k$, with $k = |\mathbf{k}|$. The dispersion relation connects the frequency ω with the magnitude k of the wavevector by $\omega = ck$. The vector potential has amplitude A_0 and its polarisation direction is given by the unit vector $\boldsymbol{\epsilon}$. The Coulomb gauge condition (2.11) is satisfied since $\mathbf{k} \cdot \boldsymbol{\epsilon} = 0$ as the wave is transverse and so $\mathbf{k}$ is perpendicular to $\boldsymbol{\epsilon}$. The electric and magnetic fields are then calculated according to (2.12) and (2.13), giving

$$\mathbf{B}(\mathbf{r},t) = \frac{E_0}{c}(\mathbf{k}\times\boldsymbol{\epsilon})\cos(\mathbf{k}\cdot\mathbf{r}-\omega t-\varphi) \tag{2.16}$$

and

$$\mathbf{E}(\mathbf{r},t) = \boldsymbol{\epsilon}E_0\cos(\mathbf{k}\cdot\mathbf{r}-\omega t-\varphi) \tag{2.17}$$

where E_0 and $\boldsymbol{\epsilon}$ are the amplitude and polarisation direction of the electric field respectively. The electric field amplitude is given by $E_0 = \omega A_0$ and a comparison between the amplitudes of the electric and magnetic fields shows that $B_0 = E_0/c$, illustrating the fact that magnetic effects are much weaker than electric effects.
A wave for which the electric field vector points in a fixed direction $\boldsymbol{\epsilon}$ is said to be linearly polarised. Combining two of these waves which are orthogonal and with a non-zero phase difference results in a single wave which rotates with the angular frequency ω and this is then said to be elliptically polarised light. Should the amplitude E_0 of the two linear waves be the same and they have a phase difference of $\pm\pi/2$ then the light is said to be circularly polarised. We can write the vector potential and electric field for arbitrary polarisation as

$$\mathbf{A}(\mathbf{r},t) = \boldsymbol{\epsilon}_a A_{0,a}\cos(\mathbf{k}\cdot\mathbf{r}-\omega t-\varphi_a) + \boldsymbol{\epsilon}_b A_{0,b}\sin(\mathbf{k}\cdot\mathbf{r}-\omega t-\varphi_b) \tag{2.18}$$

and

$$\mathbf{E}(\mathbf{r},t) = \boldsymbol{\epsilon}_a E_{0,a}\sin(\mathbf{k}\cdot\mathbf{r}-\omega t-\varphi_a) + \boldsymbol{\epsilon}_b E_{0,b}\cos(\mathbf{k}\cdot\mathbf{r}-\omega t-\varphi_b) \tag{2.19}$$

where $\boldsymbol{\epsilon}_a$ and $\boldsymbol{\epsilon}_b$ are real unit polarisation vectors perpendicular to $\mathbf{k}$. In this work we will be dealing with linearly polarised fields.

2.3 The Hamiltonian

A particle of charge q moving with momentum p in an electromagnetic field is subject to the Lorentz force and it can be shown [25] that the effect of the Lorentz force

on the motion of the particle can be described by the equations of motion, both classically and in quantum mechanics by the following transformation

$$\mathbf{p} \to \mathbf{p}' = \mathbf{p} - q\mathbf{A}. \tag{2.20}$$

In quantum mechanics the transformation (2.20) gives the momentum operator in the form

$$\hat{\mathbf{p}} = -\mathrm{i}\hbar\nabla \to \hat{\mathbf{p}}' = -\mathrm{i}\hbar\nabla - q\mathbf{A}. \tag{2.21}$$

The Hamiltonian of a particle of mass m moving in a potential $V(\mathbf{r}, t)$ originally written as

$$\hat{H}_0 = \frac{\hat{\mathbf{p}}^2}{2m} + V(\mathbf{r}, t) \tag{2.22}$$

then takes the new form

$$\hat{H} = \frac{(\hat{\mathbf{p}} - q\mathbf{A}(\mathbf{r}, t))^2}{2m} + q\phi + V(\mathbf{r}, t) \tag{2.23}$$

when the particle is considered in an electromagnetic field with the vector potential $A(\mathbf{r}, t)$. In empty space, so that $\phi = 0$, we can then decompose this into an atomic part and an interaction part so that $\hat{H} = \hat{H}_0 + \hat{H}_\mathrm{I}$. These are given by (2.22) and

$$\hat{H}_\mathrm{I} = \hat{H} - \hat{H}_0 = -\frac{q}{2m}(\mathbf{A} \cdot \hat{\mathbf{p}} + \hat{\mathbf{p}} \cdot \mathbf{A}) + \frac{q^2}{2m}\mathbf{A}^2. \tag{2.24}$$

In general the operators $\mathbf{A}$ and $\hat{\mathbf{p}}$ do not commute. However in the Coulomb gauge, where (2.11) holds true, we can use the relation

$$\nabla \cdot (\mathbf{A}f) = \mathbf{A} \cdot (\nabla f) + (\nabla \cdot \mathbf{A})f = \mathbf{A} \cdot (\nabla f) \tag{2.25}$$

where f is an arbitrary function and so we can write

$$\hat{H}_\mathrm{I} = -\frac{q}{m}\mathbf{A} \cdot \hat{\mathbf{p}} + \frac{q^2}{2m}\mathbf{A}^2. \tag{2.26}$$

Furthermore whilst the atomic potential V can depend on time, for example when looking at charged particle accelerators or atom collisions, we restrict our dependence to position only, so that $V(\mathbf{r},t) \rightarrow V(\mathbf{r})$, since the binding energy of the field free atom remains constant throughout the duration of any laser pulse. For Hydrogen the potential $V(\mathbf{r})$ represents the proton-electron interaction as is given by the Coulomb potential

$$V(\mathbf{r}) = -\frac{q^2}{4\pi\epsilon_0 r}. \tag{2.27}$$

To describe the interaction of a laser field with a Hydrogen atom we need to solve the TDSE, which is given, in Dirac notation, as

$$\mathrm{i}\hbar\frac{\partial}{\partial t}|\Psi(\mathbf{r},t)\rangle = [\hat{H}_0(\mathbf{r}) + \hat{H}_\mathrm{I}(\mathbf{r},t)]|\Psi(t)\rangle, \tag{2.28}$$

where $q = -e$ and e is the magnitude of the charge of the electron in the above formulae.

2.3.1 The Dipole Approximation

The solution of the TDSE needs the evaluation of matrix elements of the interaction operator $\hat{H}_\mathrm{I}(\mathbf{r},t)$ and we therefore need to consider the spatial dependence of this operator through its factor $\mathbf{A}\cdot\nabla$.

We can now make an important simplification known as the dipole approximation by assuming the electromagnetic field is uniform over the volume of the atom, which in turn removes the positional dependence from the electric field and vector potential. We can do this since the wavelength of the radiation we use is much larger than the size of the atom. To show this we take the plane wave form of the vector potential and use a Taylor expansion giving

$$\begin{aligned}\mathbf{A}(\mathbf{r},t) &= \frac{1}{2\mathrm{i}}\left\{\boldsymbol{\epsilon}A_0\exp[\mathrm{i}(\mathbf{k}\cdot\mathbf{r}) - \omega t] - \text{c.c.}\right\} \\ &= \frac{1}{2\mathrm{i}}\left\{\boldsymbol{\epsilon}A_0\exp(-\mathrm{i}\omega t)\left(1 + \mathrm{i}\mathbf{k}\cdot\mathbf{r} + \frac{1}{2!}\mathrm{i}(\mathbf{k}\cdot\mathbf{r})^2 + \cdots\right) - \text{c.c.}\right\}\end{aligned} \tag{2.29}$$

We write the matrix elements between the initial and final states $|\varphi_0\rangle$ and $\langle\psi|$ respectively, as

$$\begin{aligned}\langle\psi|\hat{H}_{\mathrm{I}}|\varphi_0\rangle &\propto \langle\psi|\mathbf{A}\cdot\nabla|\varphi_0\rangle \\ &\propto \exp(-\mathrm{i}\omega t)\boldsymbol{\epsilon}\cdot\left(\langle\psi|\nabla|\varphi_0\rangle + \langle\psi|(\mathrm{i}\mathbf{k}\cdot\mathbf{r})\nabla|\varphi_0\rangle + \frac{1}{2!}\langle\psi|(\mathrm{i}\mathbf{k}\cdot\mathbf{r})^2\nabla|\varphi_0\rangle\cdots\right) - \text{c.c.}\end{aligned} \tag{2.30}$$

We are integrating each of the above matrix elements over a region of space of the size of an atom, about 1 Ångström. In the case of low frequencies, taking for an example a typical wavelength of $\lambda = 800$nm so that $|\mathbf{k}| = 2\pi/\lambda$, the element $(\mathbf{k}\cdot\mathbf{r})$ is of the order of 10^{-4} and the power series in $(\mathbf{k}\cdot\mathbf{r})$ converges rapidly. This justifies the use of the electric dipole approximation, which means that we can neglect the spatial variation on the electromagnetic field over the region of interest. We can then assume that the fields and the vector potential depend on the single variable, time, so that $\mathbf{A}(\mathbf{r},t) \to \mathbf{A}(t)$. The electric field then takes on the simpler form

$$\mathbf{E}(t) = \hat{\boldsymbol{\epsilon}}E_0\cos(\omega t + \phi), \tag{2.31}$$

where ϕ here is a phase offset.

There are situations however, where the dipole approximation is not applicable. Firstly when using a laser pulse of a very short wavelength the radiation can then become comparable in size to the target atom and as such it is unreasonable to neglect the spatial inhomogeneity. This limit is shown in figure 2.1 as the upper dipole limit. In addition, recent further studies by Ludwig et al. [47] have shown that the dipole approximation also breaks down in the mid-infrared intensity range, where we shall concentrate our investigations, and the low frequency limit. In this regime electrons can acquire very high energies due to the fact that the maximum velocity of the ionised electron increases with intensity and wavelength and so the ratio v/c increases. Since the dipole approximation neglects spatial variation in the field we can see from equation (2.7) that $\mathbf{B} = 0$ and as such we neglect the magnetic field for all calculations. As v/c increases the magnetic field component of the laser

field begins to play more of a prominent role. As a result neglecting the magnetic field becomes unjustified and therefore the dipole approximation cannot be used to achieve accurate results. As shown in the illustration, the wavelength of 800nm, which is used in upcoming chapters, has an intensity limit of 5×10^{15} W $\cdot$ cm^{-2} before non-dipole effects become important. In addition, marked on the figure are the relativistic limit, the radiation pressure limit, and the limit where the spatially spread electron wave packet essentially misses the ion under the influence of the magnetic field. In this thesis we will only consider the parameter region where the dipole approximation is valid.

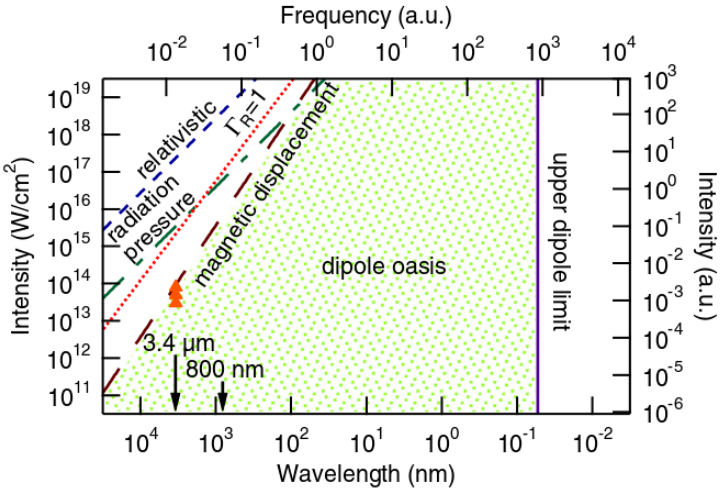

Figure 2.1: Illustration of the wavelength-intensity parameter space in strong-field ionisation, taking the magnetic field component into account. The area where the dipole approximation is considered as valid (dipole oasis) is depicted as the green dotted region. Shown are the short wavelength limit (solid purple line), magnetic displacement limit (brown dashed line), radiation pressure limit (green dashed line), relativistic limit (blue dashed line) and the limit where the spatially spread electron wave packet essentially misses the ion under the influence of the magnetic field (red dotted line). Reprinted figure with permission from [47]. Copyright 2014 by the American Physical Society.

2.4 Gauges

In quantum mechanics the calculations pertaining to the interaction of electromagnetic radiation with matter should be independent of the gauge of the electromag-

netic field employed in the formulation of the problem. There are a number of gauges that we can choose to work in with the two most commonly used being the velocity gauge (VG) and the length gauge (LG). The two gauges are equivalent as long as no other approximations are used however both transformations change the physical meaning of the operators.

To begin we write the full TDSE in the Coulomb gauge and from there we can formulate the TDSE into the gauge we wish to carry out the calculations in. Writing equation (2.28) in a different form and in atomic units ($q = -1, m = 1, \hbar = 1$) we obtain explicitly in the coordinate representation

$$\mathrm{i}\frac{\partial}{\partial t}\Psi(\mathbf{r},t) = \left[-\frac{1}{2}\nabla^2 + V(\mathbf{r}) - \mathrm{i}\mathbf{A}\cdot\nabla + \frac{1}{2}\mathbf{A}^2 - \phi\right]\Psi(\mathbf{r},t). \tag{2.32}$$

The transformations (2.9) and (2.10) leave $\mathbf{E}$ and $\mathbf{B}$ unchanged as well as the form of the TDSE provided that

$$\Psi' = \mathrm{e}^{\mathrm{i}\chi}\Psi \tag{2.33}$$

and as such the TDSE will be written in the same form as (2.32) with transformed vector and scalar potentials and wave function and any observables measured will also be unchanged. In the solution of the TDSE it is always convenient to assume a unitary transformation that suppresses the term proportional to $\mathbf{A}^2$ in equation (2.26). This term only introduces rapid oscillations in the phase of the wave function and perturbs the stability of the numerical approaches used. Taking $\phi = 0$ and taking the scalar function χ to be

$$\chi = -\frac{1}{2}\int_{-\infty}^{t}\mathbf{A}^2(t')\mathrm{d}t' \tag{2.34}$$

we obtain;

$$\mathbf{A}' = \mathbf{A} \tag{2.35}$$

and

$$\phi' = \frac{1}{2}\mathbf{A}^2 \tag{2.36}$$

and the unitary transformation is now

$$\Psi' = \exp\left[\frac{\mathrm{i}}{2}\int_{-\infty}^{t}\mathbf{A}^2(t')\mathrm{d}t'\right]\Psi \equiv \Psi^{\mathrm{V}}, \tag{2.37}$$

which eliminates the $\mathbf{A}^2$ term from the equation. The upper index V indicates that we are now in the VG. As such we can now state the TDSE in the VG

$$\mathrm{i}\frac{\partial}{\partial t}\Psi^{\mathrm{V}}(\mathbf{r},t) = \left[-\frac{1}{2}\nabla^2 + V(\mathbf{r}) - \mathrm{i}\mathbf{A}\cdot\nabla\right]\Psi^{\mathrm{V}}(\mathbf{r},t). \tag{2.38}$$

The form of the TDSE in (2.38) with interaction Hamiltonian

$$\hat{H}_{\mathrm{I}}(t) = -\mathrm{i}\mathbf{A}(t)\cdot\nabla \tag{2.39}$$

is said to be in the velocity gauge since the vector potential is coupled to the velocity operator $-\mathrm{i}\nabla$.

We now obtain another form of the TDSE by introducing the Göpert-Mayer (GM) transformation. For this transformation we take $\chi = \mathbf{r}\cdot\mathbf{A}(t)$, which then gives the new potential terms and unitary transformation;

$$\mathbf{A}' = 0, \tag{2.40}$$

$$\phi' = \frac{\partial}{\partial t}(\mathbf{r}\cdot\mathbf{A}(t)) = -\mathbf{r}\cdot\mathbf{E}(t) \tag{2.41}$$

and

$$\Psi' = \exp\left[\mathrm{i}\mathbf{r}\cdot\mathbf{A}(t)\right]\Psi \equiv \Psi^{\mathrm{L}}, \tag{2.42}$$

where the upper index L now indicates we are working in the LG. This now leads to an alternate form of Hamiltonian with the interaction term given by

$$\hat{H}_{\mathrm{I}}(t) = \mathbf{r}\cdot\mathbf{E}(t) \tag{2.43}$$

giving an equivalent form of the TDSE, in which we have eliminated the vector potential completely, as

$$\mathrm{i}\frac{\partial}{\partial t}\Psi^{\mathrm{L}}(\mathbf{r},t) = \left[-\frac{1}{2}\nabla^2 + V(\mathbf{r}) + \mathbf{r}\cdot\mathbf{E}\right]\Psi^{\mathrm{L}}(\mathbf{r},t). \tag{2.44}$$

A significant difference between the gauges is the representation of the kinetic and canonical momentum. To investigate this we use the Ehrenfest theorem to study the time evolution of the average of the momentum operator $\hat{\mathbf{p}}$ in both the velocity and the length gauge. The Ehrenfest theorem states that given any quantum mechanical observable $\hat{O}$, with expectation value $\langle\hat{O}\rangle$, the evolution of the expectation of the operator is given by

$$\frac{\mathrm{d}}{\mathrm{d}t}\langle\hat{O}\rangle = -\mathrm{i}\langle[\hat{O},\hat{H}]\rangle + \langle\frac{\partial\hat{O}}{\partial t}\rangle. \tag{2.45}$$

If the operator $\hat{O}$ doesn't vary in time, that is $\partial\hat{O}/\partial t = 0$, and the operator commutes with the Hamiltonian then the expectation value of the operator does not vary in time and the observable is said to be a constant of motion. Applying this theorem to $\hat{\mathbf{p}}$ in the velocity gauge gives

$$\frac{\mathrm{d}}{\mathrm{d}t}\langle\hat{\mathbf{p}}\rangle = -\mathrm{i}\langle[\hat{\mathbf{p}},\hat{H}]\rangle. \tag{2.46}$$

In the velocity gauge this can be shown to give the relation

$$\frac{\mathrm{d}}{\mathrm{d}t}\langle\hat{\mathbf{p}}\rangle = -\langle\nabla V\rangle. \tag{2.47}$$

That is that the evolution of the canonical momentum in the velocity gauge depends only on the gradient of the scalar potential. Then the kinetic momentum, which is the quantity measured, given by $\boldsymbol{\pi}(t)$, is related to the canonical momentum by the equation

$$\boldsymbol{\pi}(t) = \mathbf{p}(t) + \mathbf{A}(t). \tag{2.48}$$

The canonical momentum gains physical meaning at the end of the laser interaction when $\mathbf{A} = 0$. If the system is such that $\langle\nabla V\rangle = 0$ then the canonical momentum $\hat{\mathbf{p}}$

becomes a constant of motion. In laser-atom interaction a system satisfying this is a free particle in a laser field.

In the length gauge the evolution of the canonical momentum instead gives

$$\frac{\mathrm{d}}{\mathrm{d}t}\langle\hat{\mathbf{p}}\rangle = -\langle\nabla V\rangle + q\mathbf{E}(t). \tag{2.49}$$

So in the length gauge the kinetic momentum is equal to the canonical momentum. The role of the Coulomb potential is decoupled from the role of the electric field from the perspective of forces. Thus using the LG gives an advantage since the shift in the kinetic momentum in the VG can lead to difficulties or incorrect results if not properly identified.

When solving the TDSE we choose a gauge in which to work in order to best fit the laser parameters. The two formulations of the TDSE impose different demands on the computations in terms memory and time requirements. We will see conclusively from our calculations shown in subsequent chapters that in the majority of cases the VG is the optimal gauge to formulate the TDSE in for the case of short low frequencies laser pulses. In our calculations we use basis functions to represent the wave function in coordinate space. We see that in strong fields that the density of these basis functions is an important parameter. It can be shown that in the LG significantly more functions are needed due to the highly oscillatory nature of the solution which is suppressed in the VG by the shift in the kinetic momentum shown in the Ehrenfest theorem. In the VG, the solution to the TDSE is smoother meaning that a lower density of grid points will be needed. The increase in the necessary number of basis functions in the LG will increase the computational time considerably in the position integration used to create the Hamiltonian matrices. These matrices are needed to solve the TISE and generate the eigenvalues and eigenvectors of the system and then in the time integration used to calculation the evolution of the solution throughout the duration of the pulse.

We can see from the interaction Hamiltonian that the interaction term in the LG grows linearly with the position $\mathbf{r}$. When we investigate lower frequencies and higher

intensities the electron can reach high momentum very quickly causing it to travel far from the origin in a small amount of time. This is largely suppressed in the VG since the subtracted quantity essentially removes the momentum due to the strong field. As such the canonical momentum in the VG can be interpreted as the mean mechanical momentum averaged over one cycle [65] and the study of longer pulses becomes much easier and less computationally challenging in the VG.

2.5 Classical Motion in a Monochromatic Field

The classical dynamics of an electron in a electromagnetic field are governed by the Lorentz equation, which in atomic units, is defined as [39]

$$\frac{\mathrm{d}}{\mathrm{d}t}\boldsymbol{\pi}_{cl} = -[\mathbf{E}(t) + \mathbf{v} \times \mathbf{B}(t)] \tag{2.50}$$

which in the dipole approximation, where $\mathbf{B} = 0$, reduces to

$$\frac{\mathrm{d}}{\mathrm{d}t}\mathbf{v} = -\mathbf{E}(t). \tag{2.51}$$

We can see from this that in this limit the acceleration of the electron is simply provided by the electric field. From this we can calculate the velocity of an electron which has velocity $\mathbf{v}_0$ at time t_0

$$\begin{aligned} \mathbf{v}(t) &= -\int_{t_0}^{t} \mathbf{E}(t')\mathrm{d}t' + \mathbf{v}_0 \\ &= \mathbf{A}(t) - \mathbf{A}(t_0) + \mathbf{v}_0. \end{aligned} \tag{2.52}$$

In the velocity gauge we recall that the canonical momentum is given in terms of the classical velocity as

$$\mathbf{p}(t) = \mathbf{v}(t) - \mathbf{A}(t), \tag{2.53}$$

which in turn allows us to express equation (2.52) as

$$\mathbf{p}(t) = \mathbf{p}(t_0) \tag{2.54}$$

which shows the conservation of the electron canonical momentum. With this we can then divide the classical momentum into two quantities. A quiver motion and a drift motion which have velocities

$$\mathbf{v}_q = \mathbf{A}(t) \tag{2.55}$$

and

$$\mathbf{v}_d = \mathbf{v}_0 - \mathbf{A}(t_0) = \mathbf{p}(t_0). \tag{2.56}$$

The position of an electron at the origin at t_0 at future times can be found by integrating the velocity and is given by

$$\begin{aligned} \mathbf{r}(t) &= \int_{t_0}^{t} \mathbf{A}(t')\mathrm{d}t' + \mathbf{v}_d(t - t_0) \\ &= \boldsymbol{\alpha}(t, t_0) + \mathbf{v}_d(t - t_0), \end{aligned} \tag{2.57}$$

where we have defined the quiver amplitude or radius, the displacement of the electron due to its quiver motion in the field

$$\boldsymbol{\alpha}(t, t_0) = \int_{t_0}^{t} \mathbf{A}(t')\mathrm{d}t'. \tag{2.58}$$

2.5.1 The Ponderomotive Energy

We now introduce an important parameter, the cycle averaged quiver energy of the free electron in the field known as the *ponderomotive energy* U_p. Taking an electron initially at rest in a monochromatic electric field, along the x axis, described by

$$\mathbf{E}(t) = \mathbf{i}E_0 \cos(\omega t), \tag{2.59}$$

the kinetic energy is given by

$$E_k = \frac{E_0^2}{2\omega^2} \sin^2(\omega t) \tag{2.60}$$

and the cycle averaged kinetic energy is then given by

$$\langle E_k \rangle_T \equiv U_p = \frac{E_0^2}{4\omega^2} = \frac{I}{4\omega^2}, \tag{2.61}$$

where here we have defined the ponderomotive potential U_p. The notation $\langle\rangle_T$ indicates averaging over a time period of an optical cycle, $T = 2\pi/\omega$.

If we consider first only electrons that once ionised do not ever return to the parent ion, known as *direct electrons*, then we can immediately conclude from equation (2.60) that the maximal kinetic energy obtainable for an ionised electron that doesn't return to the parent ion is $E_k^{\mathrm{dir,max}} = 2U_p$ [14]. This bound is useful as a benchmark in the analysis of experimental spectra [18] and in particular for high intensity [52].

2.5.2 Volkov Solutions

The quantum equivalent for the dynamics of an electron in an monochromatic electromagnetic field are given by the Volkov solutions. The Schrödinger equation for a free electron in an laser field is given by

$$\mathrm{i}\frac{\partial}{\partial t}\Psi^{vol}(\mathbf{r},t) = \left(-\frac{1}{2}\nabla^2 + \hat{H}_{\mathrm{I}}(t)\right)\Psi^{vol}(\mathbf{r},t) \tag{2.62}$$

where $\hat{H}_{\mathrm{I}}(t) = \mathbf{A}\cdot\mathbf{p}$ is the interaction Hamiltonian operator. The equation is exactly solvable and its solutions are known as *Volkov States*, plane waves with an oscillating phase which is dependent on the vector potential. When the dipole approximation is used then the solutions are [40]

$$\Psi^{vol}(\mathbf{r},t) = \frac{1}{(2\pi)^{3/2}}\exp(\mathrm{i}\mathbf{p}\cdot\mathbf{r})\exp\left(-\mathrm{i}\Phi(\mathbf{p},\mathbf{r},t)\right). \tag{2.63}$$

The phase $\Phi(\mathbf{p},\mathbf{r},t)$ is given by

$$\Phi(\mathbf{p},\mathbf{r},t) = \mathbf{p}\cdot\boldsymbol{\alpha}(t) + E_k t \tag{2.64}$$

where

$$\boldsymbol{\alpha}(t) = \int_{t_i}^{t}\mathbf{A}(t')\mathrm{d}t' \tag{2.65}$$

is the classical quiver amplitude of a free electron in a laser field and t_i is the initial time of interaction. In a linearly polarised field the electron oscillates along the direction of polarisation with an amplitude $\alpha_0 = E_0/\omega^2 = A_0/\omega$. In the strong field regime this quiver amplitude can greatly exceed the size of the bound state orbitals and thus must be considered carefully when numerically solving the TDSE. This is due to the fact that the range of the variables used must contain the quiver amplitude of the electron throughout the calculation or numerical reflections can cause the resulting wave function to be incorrect.

2.6 Mechanisms for Ionisation

As the photon energy and intensity of the field change we find ourselves in different regimes where the dominant processes of ionisation vary. We look now at three different processes that depend on the regime we are in, multiphoton ionisation (MPI), above threshold ionisation (ATI) and tunnelling. The first regime we look at is for intensities $I < 10^{14}$ Wcm^{-2} and is the multiphoton regime. This is where the electron simultaneously absorbs more than one photon and means that the electron can be ionised by photons with energies less than the threshold energy that is required. The second is for intensities 10^{14} Wcm^{-2} $< I < 10^{15}$ Wcm^{-2} and is tunnelling ionisation. This is where electrons can tunnel through a potential barrier formed by the superposition of the atomic Coulomb potential and the electric field and escape from the atom. As the field intensity increases the potential barrier becomes more distorted and the length can be greatly reduced thus reducing the distance the electron must travel to become ionised. At even higher intensities $I > 10^{15}$ Wcm^{-2} the barrier can become distorted and suppressed to such an extent that the energy level of the initial wave packet is higher that the potential barrier. The electron can then easily escape the atom. This is known as over the barrier ionisation. In this section we also introduce a number of important parameters as well as observable results of ionisation.

2.6.1 Multiphoton Ionisation Regime

We look first at the multiphoton regime. In the case that the photon energy is lower than the ionisation potential of the target atom then the electron requires more than one photon to be ionised. In the case of a single electron we then get the *multiphoton ionisation* (MPI) reaction

$$n\hbar\omega + A^q \rightarrow A^{q+1} + e^- \tag{2.66}$$

where q is the charge of the target atomic system A, $\hbar\omega$ is the photon energy and n, a positive integer, is the number of photons absorbed during ionisation. Figure 2.2 shows the possible ionisation processes in the multiphoton ionisation regime. In a) the electron absorbs a photon of frequency $\omega > I_p$ and is ionised into the continuum. In b) the frequency of the laser is $\omega < I_p$ and so it takes $n > 1$ photons for the electron to have enough energy to escape the binding potential and be ionised. In c) once the electron has absorbed the n photons needed to acquire enough energy it continues to absorb another s photons to finally escape with a kinetic energy $E_k = \hbar\omega(n+s) - I_p$ in a process called ATI which will be covered in more detail in section 2.6.2.

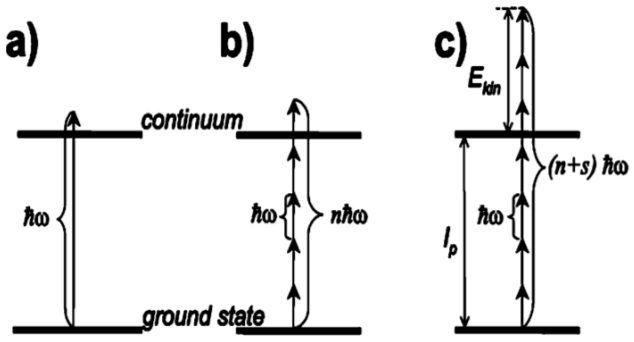

Figure 2.2: Diagram of ionisation processes: a) Single photon ionisation; b) Multiphoton ionisation by n photons; c) Above-threshold ionisation by $(n + s)$ photons. [55].

In the past MPI has been modelled by perturbation theory of the lowest order where the n-photon ionisation rate is given by

$$\Gamma_n = \sigma_n I^n \tag{2.67}$$

where σ_n is the cross section. This equation holds up to a high value of n and for sufficiently low laser intensities $I \ll I_s \simeq 3.5 \times 10^{16}\mathrm{W} \cdot \mathrm{cm}^{-2}$ where I_s is the saturation intensity. When the intensity of the laser reaches this order of magnitude then the atomic states can no longer be considered unperturbed since they are now coupled with the laser field and hence undergo dynamic shifting known as AC Stark shifting. These shifts in energy are non-perturbative and hence a perturbative approach is no longer accurate. Figure 2.3 shows evidence of this saturation intensity calculated through numerical solution of the TDSE for a photon energy of $\omega = 0.7$a.u. and varying intensities. The plot shows that the ionisation probability after 10 optical cycles grows monotonically according to (2.67) from $I = 10^{11}\mathrm{W} \cdot \mathrm{cm}^{-2}$ until a peak at around the saturation intensity of $3.5 \times 10^{16}\mathrm{W} \cdot \mathrm{cm}^{-2}$ after which the ionisation probability begins to fall.

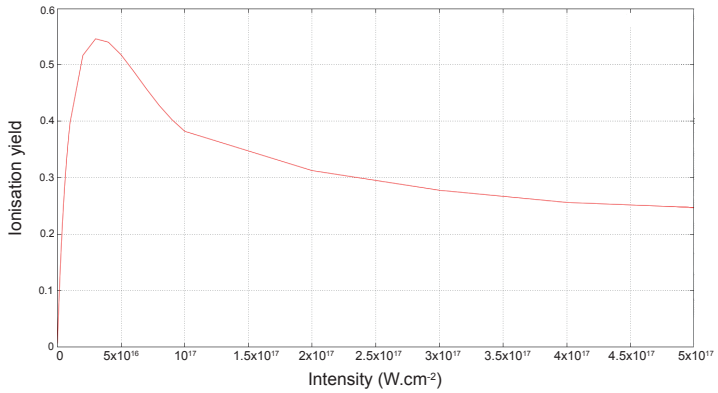

Figure 2.3: Ionisation probability after 10 optical cycles for a laser frequency of $\omega = 0.7$ and a range of intensities from $I = 10^{11}$ to 5×10^{17} $\mathrm{W} \cdot \mathrm{cm}^{-2}$ for a 1D model atom using the soft-Coulomb potential.

2.6.2 Above Threshold Ionisation

Above Threshold Ionisation was the first phenomenon of intense laser-atom interaction to be detected experimentally in the late 1970s and early 1980s with Agostini

et al. [1] claiming that their measurements were the first to detect an additional photon absorption beyond the minimum number necessary for ionisation of an atom. The assumption that once the electron had absorbed enough photons to acquire the minimum energy to be ionised then ionisation would occur only holds under certain conditions. Once the laser intensity is high enough then the absorption of photons will not stop at the minimum amount. The electron will then undergo ATI. In 1980 Gontier and Trahin applied perturbation theory to ATI with the result being a generalisation of equation (2.67)

$$\Gamma_{n+s} \propto I^{n+s} \tag{2.68}$$

where s is the number of photons absorbed after it reaches the minimum number required for ionisation. The ATI photoelectron spectrum can be seen to consist of multiple peaks, separated by the photon energy $\hbar\omega$ and appearing at energies E_s satisfying the equation

$$E_s = \hbar\omega(n+s) - I_p. \tag{2.69}$$

A typical ATI spectrum can be seen in figure 2.4. The spectrum was obtained using our program for the interaction of Hydrogen with a laser of photon energy $\hbar\omega = 2\text{eV}$ at a moderate intensity of $I = 5 \times 10^{12}\ \text{W} \cdot \text{cm}^{-2}$ for 12 optical cycles. It shows the series of peaks predicted by equation (2.69). The peaks drop in intensity as s grows since the rate for a $n+s$ photon process is proportional to I^{n+s}. This typical form of spectrum follows lowest order perturbation theory due to the relatively low intensity. As the intensity increases, perturbation theory breaks down and higher energy peaks appear whose amplitude dependence does not follow that of (2.68). This effect can be seen in figure 2.7.

Figure 2.5 [22] shows another ATI spectrum for Hydrogen in the presence of a laser of frequency $\omega = 2/\hbar$ eV and intensity of $I = 10^{14}\ \text{W} \cdot \text{cm}^{-2}$. Here we get a large series of peaks separated by 2 eV and see a number of features predicted by semi-classical mechanics. Firstly we get a drop in amplitude at $2U_p$ showing the maximal

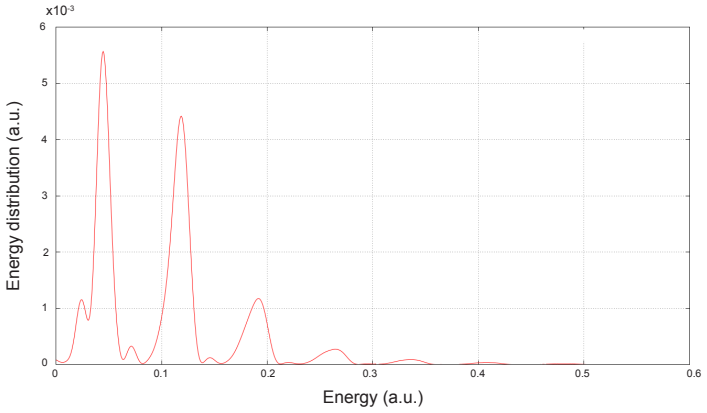

Figure 2.4: Electron energy spectra showing above threshold ionization (ATI) of Hydrogen at a laser angular frequency of $\hbar\omega = 2\text{eV}$ and laser intensity 5×10^{12} W $\cdot$ cm^{-2} for a 12 cycle pulse.

kinetic energy of a direct electron and then the spectrum displays a plateau form where the ATI peaks vary much less rapidly up to another cut off of $10U_p$. This plateau and second cut off occurs due to rescattering of the wave packet on the nucleus after evolution in the laser field.

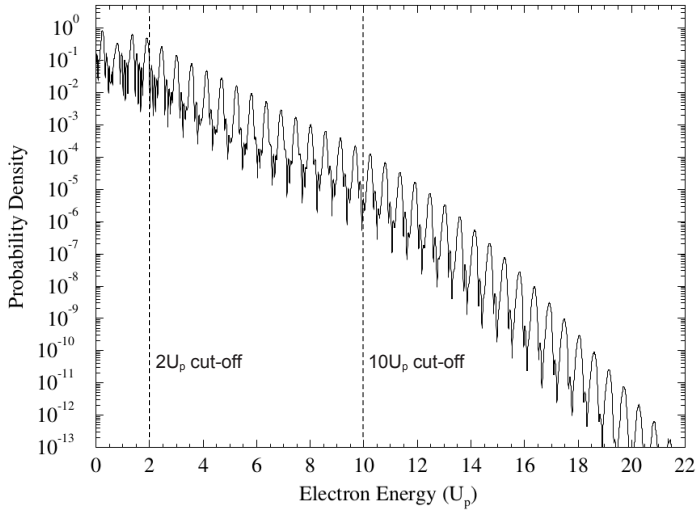

Figure 2.5: Electron energy spectra showing above threshold ionisation (ATI) of Hydrogen at a laser angular frequency $\hbar\omega = 2\text{eV}$ and laser intensity $I = 10^{14}$ W $\cdot$ cm^{-2}. Adapted from [22].

2.6.3 Stark Shifts

We consider now an additional effect the laser field has on the atom, the change in the atomic energy levels when acted on by the electric field. This results in shifting of the atomic energy levels known as *Stark shifting* and is given using perturbation theory to second order, for the energy level i by the equation [59]

$$\Delta E_i = \frac{E_0^2}{4\omega^2}\left[1 - \sum_{i \neq f} \bar{f}_{fi} \frac{\omega_{fi}^2}{\omega_{fi}^2 - \omega^2}\right] \tag{2.70}$$

where ω_{fi} is the difference in energy of the initial and final states and $\bar{f}_{fi}$ is the oscillator strength, which defines the probability of absorption or emission in transitions between energy levels of an atom. We look at the two limits of this equation in the length gauge in order to examine how the states are affected by the shifting. Firstly in states close to the continuum which are weakly bound, for example Rydberg states, $\omega_{fi} \ll \omega$ and the ratio in the summation above vanishes leaving

$$\Delta E_i = \frac{E_0^2}{4\omega^2} \equiv U_p \tag{2.71}$$

which as seen before equals the ponderomotive potential which we refer to here as the *ponderomotive shift*. We can see that as the frequency of the laser falls and the intensity rises then the shift in the energies can grow very high. In contrast if we look at a deeply bound state, for example the ground state, the spacing in energy levels is much larger so that $\omega_{fi} \gg \omega$. This means that in the right hand side of (2.70) the summation term is dominated by the oscillator strength terms and tends to 1 according to the Thomas-Reiche-Kuhn sum rule. This gives

$$\Delta E_i \approx 0. \tag{2.72}$$

This shift in the high lying bound states and continuum states means that we get a shift in the ionisation potential of the atom dependent on the frequency of the laser. This gives a new ionisation potential of $I_p(I) = I_p + U_p$. It leads to large scale

suppression of ionisation and damping of the lowest peaks in the energy spectrum which is illustrated in figure 2.6.

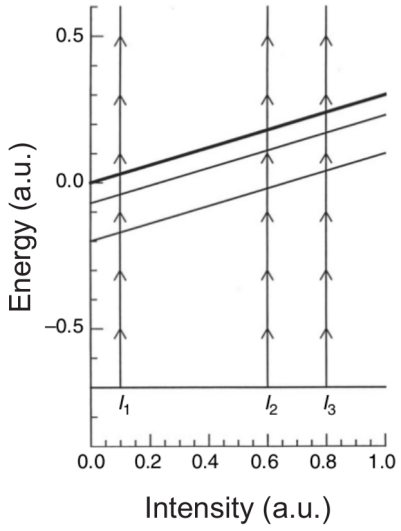

Figure 2.6: Diagram showing the suppression of the low energy peaks in the electron spectrum. The intensity dependent ionisation potential $I_p(I)$ increases linearly with I. The diagram shows that at the intensity I_1 ionisation is possible by the absorption of 4 photons while at the higher intensities I_2 and I_3 this is no longer possible. [40].

Figure 2.6 also shows another phenomenon which can be seen in our results in later chapters. For intensities I_2 and I_3 one of the Rydberg states has been shifted into a four photon resonance with the ground state which can lead to resonantly induced substructures on the peaks of the ATI spectrum.

Finally, we make one remark regarding the length of the pulse. For a relatively long laser pulse the electron is likely to escape the focal point of the laser whilst the pulse is still present. The spatial inhomogeneity of the laser field intensity will then impose a force on the escaping electron and its quiver motion will be converted to kinetic energy. This change in the kinetic energy by U_p directly cancels with the change in the ionisation potential due to the stark shift effect.

For short pulses the laser turns off before the electron can escape and the shift in the ionisation potential remains. The peaks in the ATI spectrum given in (2.69) now shift position to

$$E_s = \hbar\omega(n+s) - (I_p + U_p). \tag{2.73}$$

An ATI spectrum exhibiting this behaviour can be seen in figure 2.7. In a) and b) we see the resultant spectrum for the interaction of Xenon with a $\lambda = 1064$nm laser [40]. In a) the intensity is relatively low and as such the expected behaviour of the peaks predicted by equation (2.69) are clearly visible. However in b) the intensity is sufficiently large enough that perturbation theory can no longer predict the amplitude and position of the ATI peaks. As well as peaks of higher energy that are not predicted we also see the peak suppression mentioned above. Here the first $s = 1$ peak in figure 2.4 can disappear beneath the threshold and the $s = 2$ and $s = 3$ peaks are clearly suppressed below the expected amplitude.

2.6.4 Tunnelling Regime

Under different conditions there are mechanisms for ionisation different to the multiphoton regime. If the intensity of the laser is high enough and the frequency is low enough then the field is able to distort the potential so that a potential barrier is formed which the electron can then tunnel through. This is due to the fact that for the intensities of light mentioned above, the strength of the electric field has reached the order of $10^8 - 10^9$ V $\cdot$ cm^{-1} and is comparable to the atomic Coulomb potential. This strong field then forms a superposition with the Coulomb field which creates a slowly moving oscillating barrier which the electron can tunnel through. This can be seen in figure 2.8 a).

The rate of tunnelling is highly dependent on the field strength and the stronger the field is, the smaller the barrier becomes. Therefore, during tunnelling, most electrons are ionised at the peak of the electric field and no electrons can escape when the field takes zero value. The ADK tunnelling rate [2] is given in atomic units by

$$W = W_0 \exp\left[-\frac{2(2I_p)^{3/2}}{3E_0}\right] \tag{2.74}$$

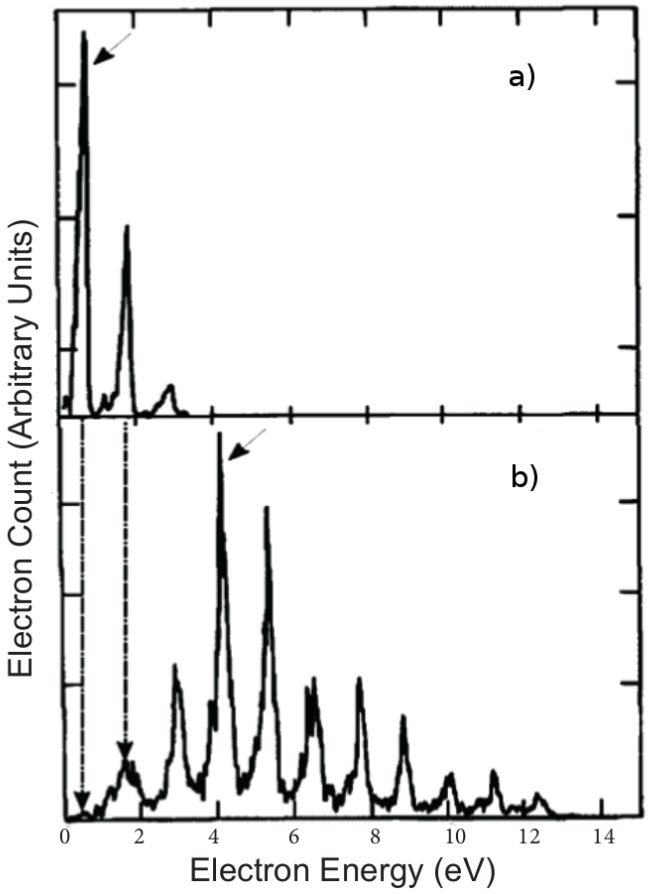

Figure 2.7: Electron energy spectra showing above threshold ionisation (ATI) of xenon at a laser wavelength $\lambda = 1064$nm and laser intensity of a) $I = 2.2 \times 10^{12}$ W $\cdot$ cm^{-2} and b) $I = 1.1 \times 10^{13}$ W $\cdot$ cm^{-2}. [40].

where W_0 is a function of the amplitude of the electric field, E_0, the ionisation potential, I_p and the atomic core charge, Z.

As the intensity grows the interaction terms becomes stronger which in turn makes the potential barrier smaller. For very intense lasers when the barrier gets so small that the ground state is no longer bound then we move into the over the barrier regime where the electron can leave the atom directly without tunnelling. This can be seen in figure 2.8 b).

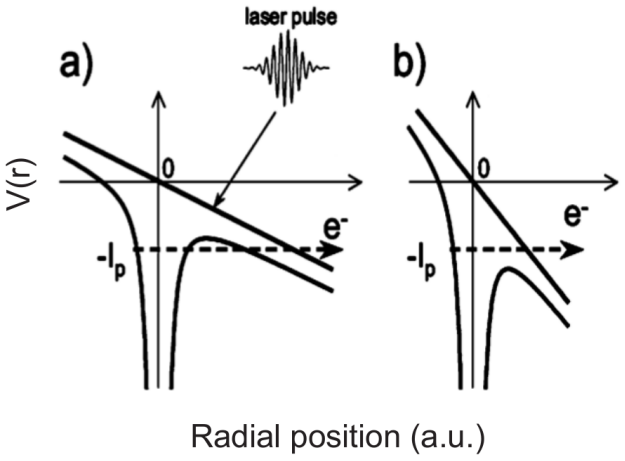

Figure 2.8: Diagram of strong field ionisation processes: a) tunnel ionisation; b) over the barrier ionisation. [55].

2.6.5 The Keldysh Parameter

In this section we have looked at different processes for ionisation and therefore we now look for a method in which we can determine which regime our calculations will fall into. In a paper on the ionisation of atoms in strong laser fields [41] Keldysh introduced a dimensionless parameter which defines the laser-field environment and shows the regime of ionisation based on the laser field parameters. This was termed the *Keldysh parameter* and is given by

$$\gamma = \frac{\omega}{\omega_{\text{tunnel}}} = \frac{\sqrt{2mI_p}\,\omega}{eE_0} = \sqrt{\frac{I_p}{2U_p}}. \tag{2.75}$$

This parameter can be interpreted as the ratio of the laser and tunnelling frequencies, i.e. the ratio of the the wave period of the field against the 'time' it takes for the electron to tunnel through the created potential barrier. Therefore, on the condition that the period of the electric field is varying slowly enough that the electron can successfully tunnel through before the direction of the field changes and the barrier begins to widen again then the ratio will be low and it will indicate that tunnel ionisation should be dominant. The parameter sets a boundary value for which the

two limiting cases of nonlinear photoionisation are defined. As such the limit when $\gamma \gg 1$, when the tunnelling time is much longer than the period of the field, is known as the *multiphoton ionisation regime* whereas the limit $\gamma \ll 1$ is known as the *tunnelling regime* and this is where we focus our calculations to investigate low frequency and the adiabatic limit. Figure 2.9 shows the possible photoionisation regimes for different values of the photon energy and laser intensity for Carbon 60.

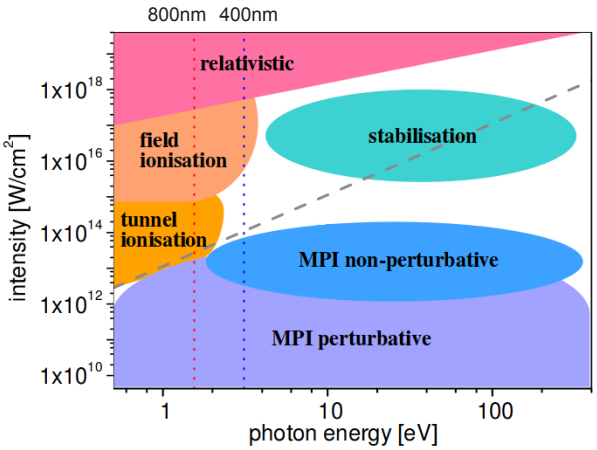

Figure 2.9: Different photoionisation regimes as a function of the laser intensity and photon energy. The vertical dotted red and blue lines indicate photon energies related to the laser wavelength of 800nm and 400nm, respectively. The dashed grey line shows the case of $\gamma = 1$ for C_{60} ionisation which separates the multiphoton regime ($\gamma \gg 1$) from the tunnelling regime ($\gamma \ll 1$). [66].

2.7 Classical Calculations

We consider the classical dynamics of an electron in the presence of a laser field which play an important role in understanding many strong field phenomena.

2.7.1 The 3 Step Model

We look now at an intuitive semi-classical view on ionisation in a strong field known as the *Simple Man Model* or the *Three Step Model* [40, 44]. The model assumes that tunnelling plays a role in the ionisation process, i.e. that $\gamma \leq 1$. The model separates the process of ionisation into three steps which are shown in figure 2.10.

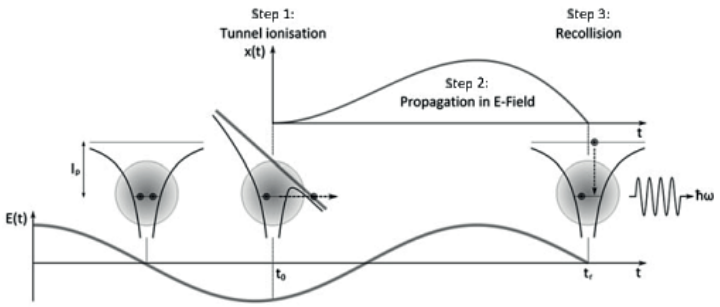

Figure 2.10: The three steps of the Simple Man Model. Firstly the Coulomb potential and electric field superimpose to create a finite potential wall that the electron can tunnel through to become ionised. Next the electron is accelerated in the electric field and is turned around. Finally, the electron recollides with the core. [74].

These steps are:

1. The Coulomb potential and the slowly oscillating laser field combine to create a barrier in the direction of the laser field. The height and width of this barrier is determined by the ionisation potential of the atom as well as the strength of the electric field. When the amplitude of the electric field is high enough then the barrier width is sufficiently small so that the electron can tunnel through thus ionising the atom.

2. The electron is then accelerated by the laser field. When the field switches sign the electron is then accelerated back towards its parent ion.

3. The electron returns to the vicinity of the parent ion and recollides. Here the electron can do a number of things. It could scatter elastically, scatter inelastically (leading to excitation or ionisation of the parent ion) or radiatively recombine into one of the ions empty states. Should this recombination happen, this releases a photon of energy $\omega = E_k + I_p$ where E_k is the kinetic energy gained by the free electron in the field and I_p is the ionisation potential of the atom. This is called high harmonic generation (HHG).

The three step model uses a number of assumptions. Firstly that the electron is born

in the continuum at time t_0 near the core of the parent ion following tunnelling. The electron is then treated as a free electron with initial velocity $\mathbf{v}_0 = 0$. Secondly that the pull of the Coulomb potential is neglected once the electron is born. This is not unreasonable due to the very large distances the electron can travel in the strong field and the dominance of the strength of the field over the atomic potential in that time.

Using initial conditions set by our assumptions we can investigate the trajectories of the ionised electrons and determine the times of recombination. For recombination we require that the electron returns back to the vicinity of the parent ion at time t and as such (2.57) gives

$$\mathbf{r}(t) = \boldsymbol{\alpha}(t, t_0) + \mathbf{v}_d(t - t_0) = 0. \tag{2.76}$$

It is worth mentioning in the above equation that the detachment time t_0 is an implicit function of t and that the moment of return is uniquely determined by the moment of ionisation. We can also calculate the kinetic energy of the electron at the return using equation (2.52)

$$E_k = \frac{1}{2}[\mathbf{A}(t) - \mathbf{A}(t_0)]^2. \tag{2.77}$$

Of particular interest is whether there is a maximum value of kinetic energy the electron can acquire whilst in the field. We can calculate this maximum value, denoted E_k^{max}, by considering that the largest kinetic energy value will correspond to the longest time the electron can remain in the field before recombining. Therefore

$$E_k^{\text{ret,max}} = E_k(t_r^{max}, t_0) \tag{2.78}$$

where t_r is the time of recombination. We can determine this time t_r^{max} then by solving

$$\frac{\partial}{\partial t} E_k(t, t_0)\bigg|_{t=t_r^{max}} = 0. \tag{2.79}$$

To calculate this we assume a laser polarised along the x axis and of the form of (2.31). The velocity of the electron at the time of recombination is then

$$v_x(t) = -\frac{E_0}{\omega}[\sin(\omega t) - \sin(\omega t_0)] \tag{2.80}$$

giving the kinetic energy

$$E_k^{\text{ret}}(t, t_0) = 2U_p[\sin(\omega t) - \sin(\omega t_0)]^2. \tag{2.81}$$

where the detachment time is calculated using equation (2.76) and is given now by solving

$$x(t) = \frac{E_0}{\omega^2}[\cos(\omega t) - \cos(\omega t_0) + \omega(t - t_0)\sin(\omega t_0)] = 0. \tag{2.82}$$

Substituting (2.81) into (2.79) and solving gives us the result of a maximum kinetic energy for a rescattered electron of $3.17U_p$ [19, 42]. This value is for electrons detached at $t_0 = 0.1\pi/\omega$ and returning to the parent ion at $t = 1.94\pi/\omega$. Therefore the maximal energy of an emitted photon at the time of return is given by

$$\omega^{max} = I_p + E_k^{\text{ret,max}} = I_p + 3.17U_p. \tag{2.83}$$

When elastic rescattering occurs and the energy is conserved the drift energy increases. The maximal energy is obtained when the electron backscatters at an angle of 180 °. We then obtain a drift energy upon scattering of [30]

$$E_k^{\text{res}}(t, t_0) = U_p[2\sin(\omega t) - \sin(\omega t_0)]^2. \tag{2.84}$$

Maximising this, again under the condition (2.76), then yields another famous cut-off energy, that of a rescattered electron which is given by $E_k^{\text{res,max}} = 10U_p$.
Possible detachment times and kinetic energies on recombination are given in figure 2.11 (a) and (b) respectively. The size of the dots is proportional of the amplitude of the electric field at the time of detachment. The detachment time for each dot is chosen for times between $t_0 = 0$ and $t_0 = T/4$. Electrons detached after $T/4$

and before the end of the optical cycle do not ever return to the core. We can take a number of things from figure 2.11. Firstly that the shortest trajectories come from detachment when the field is weak and the probability to tunnel ionise is low. Secondly that there exist trajectories that return to the core many times. Thirdly that the $3.17U_p$ cut off is due to electrons detaching close to the electric field maximum and returning around half an optical cycle later. Finally, that trajectories whose durations are equal to $\frac{5T}{4}$, $\frac{7T}{4}$, $\frac{9T}{4}\cdots$ show additional cut offs of lower energy. For each of these recollision energies there are two trajectories that the electron can take on its journey before recollision. These are known as the *short* and *long* trajectories. These electrons provide the dominant contribution to photoelectron spectra.

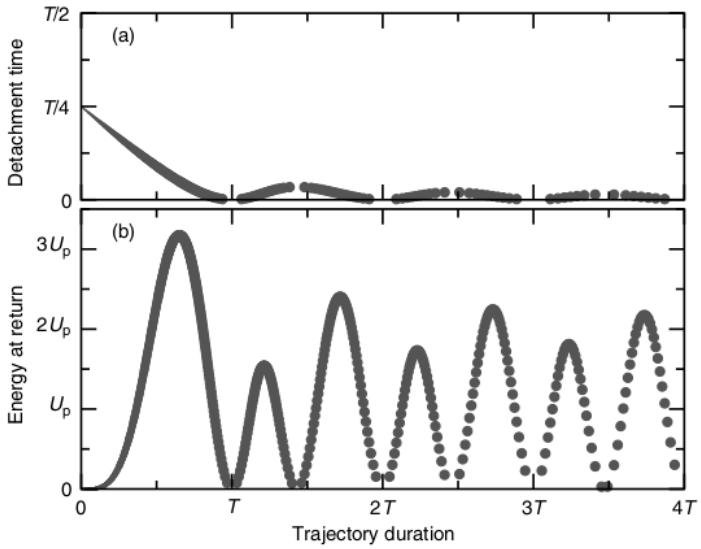

Figure 2.11: (a) Detachment times t_0 as a function of the trajectory duration for trajectories of electrons with $\mathbf{v}_0 = 0$ at $\mathbf{r}_0 = 0$. After time t_0, the electron interacts only with the electric field found in equation (2.31), oscillates in the field and is finally driven back to the parent ion at time t. (b) Kinetic energy of the electron when it returns to the origin. [40].

2.7.2 High Harmonic Generation

One important consequence of the recombination described in section 2.7.1 is the generation of high order harmonics. On recombination the atom responds in a

nonlinear way and emits coherent radiation at frequencies equal to integer multiples of the driving laser frequency. Due to the inversion symmetry of the atom only odd harmonics are emitted. The harmonics are initially at low order and can be predicted by perturbation theory. However, Shore and Knight [68] discovered that by using a laser of sufficient intensity to restructure the continuum, hence altering the amount of time that the electron may interact with the laser, then harmonics of a much higher order can be produced. This creation of higher harmonics is due to high energy electrons generated by above threshold ionisation returning to the ground state on recombination. Since this discovery high-harmonic generation (HHG) has been observed experimentally with a wide range of laser parameters.

An example of a typical HHG spectrum is shown in figure 2.12 for Xenon. The spectrum shows after an initial cut off after the first harmonic there is a plateau of many harmonic orders followed by a another cut-off accurately predicted by classical methods in equation (2.83) in section 2.7.1.

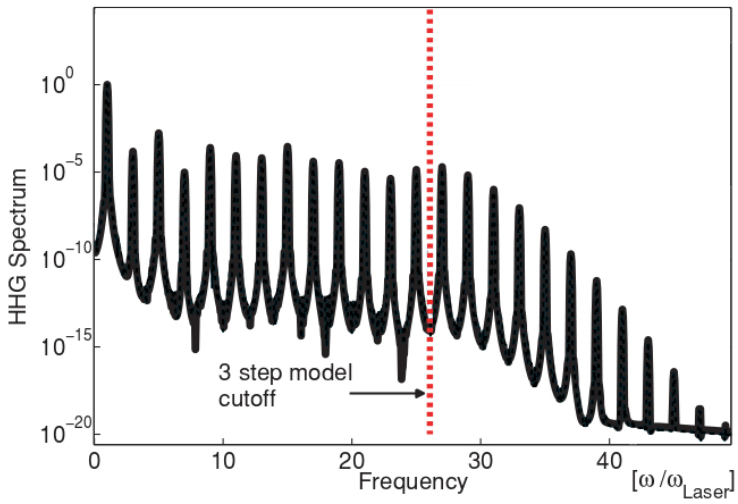

Figure 2.12: An example HHG Spectrum of Xenon. The laser used was 800nm and $1.5 \times 10^{14}\mathrm{W} \cdot \mathrm{cm}^{-2}$ for 20 optical laser cycles. The dotted red line indicates the cut-off frequency predicted by the 3 step model, $E_k^{\mathrm{ret,max}} = I_p + 3.17U_p$. Figure adapted with permission from [78].

One of the most important applications of HHG is the formation of attosecond pulses [69]. The plateau gives a comb of peaks of constant amplitude equally spaced in

frequency and if the harmonics are appropriately phased then in the time domain the emitted signal would consist of a train of pulses separated by $T/2$, of duration in the attosecond range. This can be utilised to probe phenomena with the same periodicity e.g. of electronic motion in various kinds of materials. In addition by combining multiple harmonics the intensity of the outgoing radiation can be increased by a number of orders of magnitude giving the intensity of the pulse trains to be in the order of $I = 10^{15}$ W $\cdot$ cm^{-2} [3]. Furthermore it has also been shown that the generation of zeptosecond pulses may also be possible using the interference of x-ray emissions from multiple scattering events [36]. Whilst we do not calculate the HHG in future chapters it is a very important and useful phenomenon.

2.8 Strong Field Approximations

As an alternative to the intensive and challenging full numerical solution to the TDSE many theorists have made attempts to solve the TDSE using approximations and analytical methods. The most successful of these is called the Strong Field Approximation (SFA). In SFA it is assumed that when the active electron is bound then it interacts only with the Coulomb potential and not with the electric field. Subsequently, once it is ionised it then interacts only with the electric field. In addition, all bound states except for the ground state are neglected so the electron cannot be excited to higher states.

2.8.1 KFR Theory

Keldysh used the above assumptions to propose an ansatz for the ionisation amplitude [2]. A number of other non-perturbative methods have been performed led predominantly by Faisal [26] and Reiss [60] and are known as KFR theory since they are related to the previous work of Keldysh. The KFR approach uses Volkov states to represent the final state of the electron and field free eigenstates to represent the initial bound electron. The ionisation amplitude of an electron in an initial bound state $|\Psi_0(t_i)\rangle$ at an initial time t_i is given by

$$M_{\mathbf{p}}(t_f, t_i) = \langle \Psi_{\mathbf{p}}(t_f) | \hat{U}(t_f, t_i) | \Psi_0(t_i) \rangle \tag{2.85}$$

where $\hat{U}(t_f, t_i)$ is the time-evolution operator associated with the full TDSE. Therefore $|M_{\mathbf{p}}|^2$ gives the probability of finding the electron in a scattering state with asymptotic momentum $\mathbf{p}$ at the time t_f.

The evolution operator is gauge invariant and satisfies the TDSE

$$\mathrm{i}\frac{\partial}{\partial t}\hat{U}(t, t') = [\hat{H}_0 + \hat{H}_{\mathrm{I}}(t)]\hat{U}(t, t'). \tag{2.86}$$

The evolution operator also satisfies integral equations of the Volterra type and therefore the solution of (2.86) is given by [40] as

$$\begin{aligned} \hat{U}(t, t') &= \hat{U}_0(t, t') - \mathrm{i}\int_{t'}^{t} \mathrm{d}t'' \hat{U}(t, t'')\hat{H}_{\mathrm{I}}(t)\hat{U}_0(t'', t') \\ &= \hat{U}_0(t, t') - \mathrm{i}\int_{t'}^{t} \mathrm{d}t'' \hat{U}_0(t, t'')\hat{H}_{\mathrm{I}}(t)\hat{U}(t'', t') \end{aligned} \tag{2.87}$$

where $\hat{U}_0(t, t')$ is the evolution operator satisfying

$$\mathrm{i}\frac{\partial}{\partial t}\hat{U}_0(t, t') = \hat{H}_0\hat{U}_0(t, t'). \tag{2.88}$$

Inserting (2.87) into our original equation for the ionisation amplitude (2.85) then gives

$$M_{\mathbf{p}}(t_f, t_i) = -\mathrm{i}\int_{t_i}^{t_f} \mathrm{d}t' \langle \Psi_{\mathbf{p}}(t_f) | \hat{U}(t_f, t')\hat{H}_{\mathrm{I}}(t') | \Psi_0(t_i) \rangle \tag{2.89}$$

where we have made use of the fact that $\langle \Psi_{\mathbf{p}}(t_f) | \hat{U}_0(t_f, t_i) | \Psi_0(t_i) \rangle = \langle \Psi_{\mathbf{p}}(t_f) | \Psi_0(t_f) \rangle = 0$ since $|\Psi_{\mathbf{p}}(t_f)\rangle$ is a scattering state orthogonal to $|\Psi_0(t_f)\rangle$. The time evolution operator also satisfies the integral equation

$$\begin{aligned} \hat{U}(t, t') &= \hat{U}^{vol}(t, t') - \mathrm{i}\int_{t'}^{t} \mathrm{d}t'' \hat{U}(t, t'')\hat{V}\hat{U}^{vol}(t'', t') \\ &= \hat{U}^{vol}(t, t') - \mathrm{i}\int_{t'}^{t} \mathrm{d}t'' \hat{U}^{vol}(t, t'')\hat{V}\hat{U}(t'', t') \end{aligned} \tag{2.90}$$

where $\hat{U}^{vol}$ corresponds to the TDSE (2.62). Inserting (2.90) into (2.89) gives, after simplification,

$$M_{\mathbf{p}}(t_f,t_i) = -\mathrm{i}\int_{t_i}^{t_f} \mathrm{d}t' \langle \Psi_{\mathbf{p}}(t_f)|\hat{U}^{vol}(t_f,t')\left[\hat{H}_{\mathrm{I}}(t')\Psi_0(t')\rangle - \mathrm{i}\int_{t_i}^{t'} \mathrm{d}t''\hat{V}\hat{U}(t',t'')\hat{H}_{\mathrm{I}}(t'')|\Psi_0(t'')\rangle\right] \tag{2.91}$$

which is still exact and gauge invariant. Replacing the final state $|\Psi_{\mathbf{p}}(t_f)\rangle$ with a Volkov state defined in section 2.5.2 and neglecting the second term in the square brackets we arrive at the SFA amplitude, or the *Keldysh* amplitude

$$M_{\mathbf{p}}^{(SFA)}(t_f,t_i) = -\mathrm{i}\int_{t_i}^{t_f} \mathrm{d}t' \langle \Psi_{\mathbf{p}}^{vol}(t_f)|\hat{H}_{\mathrm{I}}(t')|\Psi_0(t_i)\rangle. \tag{2.92}$$

This ionisation amplitude integrates over all possible ionisation times where the transition from the ground state to the final Volkov state may take place. It can be interpreted as the interaction Hamiltonian ionises the bound electron at the time t' and then it moves freely in the field and is represented by a Volkov state. Since the atom is ionised at the initial time t_i a surprising result that follows is that with simple manipulation we can rewrite the SFA amplitude in the form

$$M_{\mathbf{p}}^{(SFA)}(t_f,t_i) = -\mathrm{i}\int_{t_i}^{t_f} \mathrm{d}t' \langle \Psi_{\mathbf{p}}^{vol}(t_f)|\hat{V}(\mathbf{r})|\Psi_0(t_i)\rangle, \tag{2.93}$$

details of which can be found in [13]. This seems to suggest that the ionisation is mediated by the binding potential of the atom rather than the electric field. This can be explained by the fact that time reversal ionisation turns into recombination and that in the solutions of the TDSE for $\hat{U}$ above we have treated $\hat{H}_{\mathrm{I}}$ and $\hat{V}$ equally. KFR theory and similar approximations have been shown to be an accurate, less expensive means of solving the problem of laser-atom interaction for the cases where the laser parameters dictate that a full quantum mechanical treatment of the problem would be memory intensive and time consuming, such as in the case of low frequency or very high intensity. They have the large advantage over perturbation theory that they do not treat the laser field as a minor perturbation but as of similar level of strength to the Coulomb binding potential. It also factors in that at

times the atomic potential will be dominant whereas at other times the laser field will take over. It is also a very intuitive theory and can be applied to ionisation, non-sequential ionisation by including higher order terms and high harmonic generation. However, the method does have its downfalls. Firstly the laser induced shifts such as the Stark shifts mentioned in 2.6.3 are not included in the calculation of the amplitudes. As well as this the effect of the Coulomb potential after ionisation is neglected whereas in reality, even though the laser field is dominant the electron is still influenced by the atomic potential especially when the laser field accelerates it back in the direction of the ion and the distance between them decreases. A remedy for this is the possibility of using Coulomb-Volkov wave functions as opposed to the Volkov states $|\Psi^{vol}(t)\rangle$ used above. An example taken from the papers of Ivanov and Smirnova [70, 71] is a wave function of the form

$$\Psi^{CV}(t) = \Psi^{vol}(t)B(\mathbf{r},t) \tag{2.94}$$

where $B(\mathbf{r},t)$ is the distortion of the Volkov solution due to the influence of the Coulomb potential. This is given by

$$B(\mathbf{r},t) = [\phi(\mathbf{r}_L(t_f,t,\mathbf{r}))\exp(-\mathrm{i}\mathbf{p}\cdot\mathbf{r}_L(t_f,t,\mathbf{r}))]\,\mathrm{e}^{\mathrm{i}G(\mathbf{r},t)} \tag{2.95}$$

where $\phi(\mathbf{r})$ is the final field-free Coulomb state, $G(\mathbf{r},t)$ is a phase correction given by

$$G(\mathbf{r},t) = \int_t^{t_f} \hat{V}[\mathbf{r}_L(t',t,\mathbf{r})]\mathrm{d}t' \tag{2.96}$$

and $\mathbf{r}_L(t',t,\mathbf{r})$ is the modified trajectory in the laser field given by

$$\mathbf{r}_L(t',t,\mathbf{r}) = \mathbf{r} + \int_t^{t'} \mathbf{p}_L(t'')\mathrm{d}t'' \tag{2.97}$$

with

$$\mathbf{p}_L(t) = \mathbf{p} + \mathbf{A}(t). \tag{2.98}$$

There are further issues with the SFA when the intensity of the laser becomes too high. Here the method does not take into account the saturation limit of the atom and therefore if $I > I_{sat}$ then the approximation will overestimate the ionisation rates especially if the pulse is long. In addition if the intensity is such that $U_p \gg I_p$ then the assumption that the initial state is an unperturbed eigenstate is no longer valid. There has been other work on improving KFR theory including examining the role of the Volkov states on the electromagnetic spectrum [15], consideration of the previously mentioned neglect of the shifts in the ATI peak positions [50] and in addition to the method mentioned above, other considerations into the Coulomb potentials effect after ionisation [11].

2.9 The Low Energy Structure

A recent new discovery of an unexpected phenomenon is the manifestation of a spike-like structure in the photoelectron energy distribution at very low energy. This spike, termed the low energy structure (LES) becomes prominent when using mid-infrared laser wavelengths like the parameters we will explore in chapters 4 and 5 and can be seen in figure 2.13. The figure shows measured results for a number of different atoms and molecules as well as the KFR calculation using Volkov states which shows no LES structure. The dashed line labelled E_H defines the high-energy limit of the LES used in the analysis. Inset in the figure shows how the first-order KFR calculation neglects rescattered electrons and consequently is not expected to reproduce the rescattering plateau. It is this neglecting of the rescattered electrons which causes the KFR theory to not reproduce the LES. Full scale quantum calculations by numerical solution of the TDSE are shown to accurately replicate the LES [17].

As well as not being predicted by strong field approximations the structure was unexpected because dynamics are generally thought to become simpler as one lowers the frequency since the number of photons needed to ionise the atom grows very large and the Keldysh parameter γ drops to very low values. The tunnelling ionisation rate in a static electric field is a smooth, featureless function of the final momenta

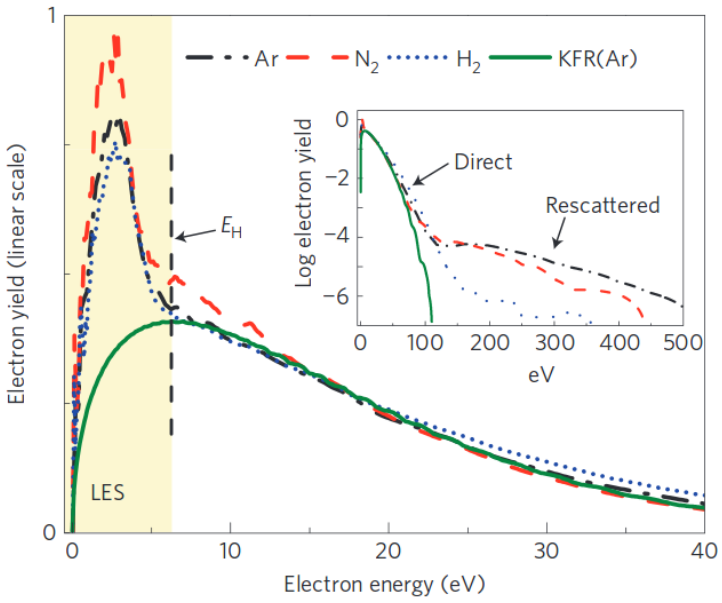

Figure 2.13: The low-energy region of the spectra for argon, molecular nitrogen and molecular hydrogen produced by an $I = 1.5 \times 10^{14}$ W $\cdot$ cm^{-2} laser at a wavelength of $\lambda = 2\mu$m. We clearly see the KFR result shows no LES peak. Inset: The breakup of the spectra into direct and rescattered electrons on a logarithmic scale. Reprinted by permission from Macmillan Publishers Ltd: Nature Phys. [17], copyright 2009.

and little low energy activity is expected. One reason why the LES had escaped observation previously is due to the fact that the LES only becomes visible and broadens in width as the wavelength of the laser increases. In addition whilst the low energy part of spectrum shows this unexpected phenomenon, the rest of the spectrum remains as predicted by other methods, this making it difficult to notice unless low energy dynamics are specifically being investigated. Many physical reasons for the origin of the structure have been put forward such as low-energy forward scattering, leading to caustic structures in semi-classical trajectory calculations [80], the perturbative effect of multiple rescattering of the ionised electron with the peaks in LES arising due to multiple scattering contributions to the transverse momentum [46] and two-dimensional focusing effect of the classical phase-space distribution at high angular momenta and low energy [45].

Furthermore, more recently there have been additional reports of a very low energy structure (VLES) and a zero energy structure (ZES) also being found in the case of

mid-infrared intense laser pulses interacting with atoms and molecules [79]. These can be seen in figure 2.14 which shows the electron momentum distributions for argon, comparing experiment with theory. The physical origins of the VLES and the ZES are still under speculation but Wolter et al. [79] speculate that the V-shaped structure (VLES) in these momentum distributions at very low energies ($E < 0.5$eV) is due to high-order focal points in the combined Coulomb and laser fields. It is also shown by Wolter that the ZES is caused by ionisation of high lying Rydberg states and thus provides information on the recapture of tunnel ionised electrons and corresponds to a map of the Rydberg population onto the momentum plane.

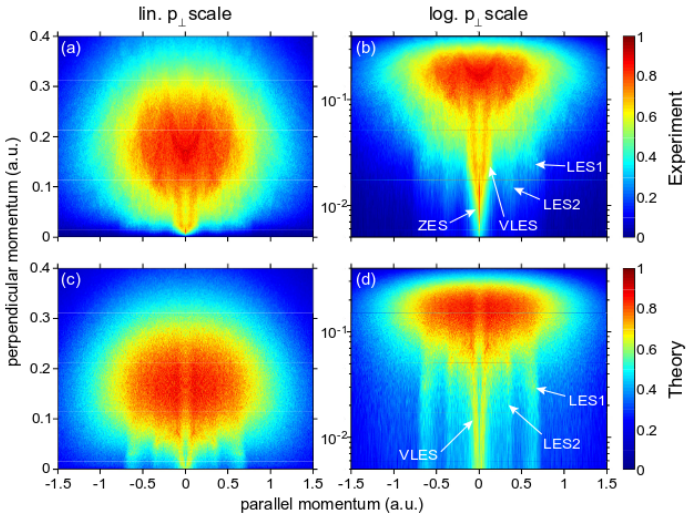

Figure 2.14: Measured (top) and simulated (bottom) electron momentum distributions for argon interacting with a 68 fs pulse with peak intensity of $I_0 = 0.9 \times 10^{14}$ W $\cdot$ cm^{-2} and a central wavelength of $\lambda = 3.1\mu$m. The first- and second-order LESs (LES1, LES2), the VLES, and the ZES structures are marked. Reprinted figure with permission from [79]. Copyright 2014 by the American Physical Society.

In the next chapter we develop numerical methods that will allow us to investigate laser-atom interaction at the frequencies and intensities necessary to investigate the LES, and we study how the adiabatic limit is reached at low frequencies and possible consequences for analysing and interpreting the above structures.

Chapter 3

Numerical Methods for the Time Dependent Schrödinger Equation

3.1 Introduction

For electromagnetic fields with moderate intensities and frequencies the interaction between light and matter can be investigated using analytical techniques such as perturbation theory or semi classical methods whilst for the case of the interaction with a short range potential the strong field approximation is commonly used. However for short, high intensity, low frequency pulses the numerical integration of the time dependent Schrödinger equation (TDSE) has become the main theoretical approach for the quantitative study of a vast amount of phenomena, including strong field processes in atoms and molecules, where the numerical solution of the TDSE is unavoidable if accurate results are required.

This numerical method can be expensive in terms of computational memory requirements, limiting the method to single or few electron atoms. It is also time consuming to run when the laser parameters require a larger basis set to represent Ψ or the total pulse lengths are long. However the ability to obtain an accurate solution to the problem with no analytical approximations makes the numerical integration of the TDSE a popular and important method. In some parameter regimes the results obtained can also then be compared with those obtained using analytical methods to check the validity and accuracy of the approximations.

In cases of many electron atoms we use the single active electron (SAE) approximation which assumes that the laser field strongly interacts with only one active

electron. This is of course valid for examining a single electron atom such as Hydrogen but it is also a good approximation for alkali metal atoms since the valence electron sits outside a closed shell. In addition the SAE approximation is not limited to the alkali metal atoms, indeed any situation where the probability of excitations of more than one electron is small can make use of the approximation. An example is when the photon energy is much smaller than the energy needed to ionise one electron from the system. Here sequential processes dominate the ionisation meaning that one electron is completely ionised before another electrons excitation begins.
There are shortfalls to the use of the SAE however, such that it ignores any simultaneous interactions of more than one electron with the laser field and also that the active electron may interact with other electrons in the system which can lead to non-sequential ionisation. Even so, the great reduction in difficulty and the methods precise results mean that the SAE approximation is a useful tool in strong field physics. For certain atoms the SAE approximation has been shown to be valid and accurate in a large range of laser frequency and intensity [7] and modifications and corrections are available in cases of atoms and molecules where the spectra are more sensitive to structural details and the SAE approximation is less accurate.
In this chapter we investigate the numerical methods for solving numerically the time dependent Schrödinger equation (TDSE) for a system with Hamiltonian operator $\hat{H}$,

$$\mathrm{i}\frac{\partial}{\partial t}\Psi(\mathbf{r},t) = \hat{H}\Psi(\mathbf{r},t), \tag{3.1}$$

where we use atomic units, $\hbar = m = 1$. The solution is given by the wave function $\Psi(\mathbf{r},t)$, defined for all position $\mathbf{r}$ and time t. We note that the equation is of first order in t meaning that given an initial solution $\Psi(\mathbf{r},t_0)$ then the solution at all subsequent times can be determined. The total Hamiltonian which depends explicitly on time is given by

$$\hat{H}(\mathbf{r},t) = \hat{H}_0(\mathbf{r}) + H_{\mathrm{I}}(\mathbf{r},t), \tag{3.2}$$

with $\hat{H}_0$ the unperturbed Hamiltonian describing the atom and H_{I} the time dependent interaction Hamiltonian. The numerical solution is separated into two parts, firstly the representation of $\Psi(\mathbf{r}, t)$ in coordinate space and secondly the integration on time as we propagate the wave function solution of the TDSE. In order to represent the wave function in coordinate space, two main approaches are generally used, grid methods or spectral methods. Amongst the grid methods are the finite difference method and the finite element method, where a finite region of space (a box) is discretised with a finite grid of points. At each time t we find the solution values at each of the grid points or in the domain defined by the grid. For spectral methods the solution is defined by its development on a complete basis set of convenient square-integrable functions. The initial equation is then replaced by a system of coupled differential equations, whose solution determines the coefficients of the solution decomposition in the initial basis set. In this thesis we concentrate on a spectral method and use a variety of basis sets which we describe later in the chapter.

For the time propagation of the solution of the TDSE we can use either an explicit propagation scheme, where only products of matrix-vectors are needed, or an implicit scheme, which entails the solution of a system of equations. The considerations when choosing the best numerical method to use are the accuracy of the results obtained and the resources needed to achieve that accuracy in terms of computational time. As we shall see in the work presented here, one method can be ideal for one particular problem or a particular set of parameters but will not produce accurate results for another set of parameters. Each case needs its own accurate study. One of the difficulties faced by the numerical solution of the TDSE is its stiffness. The coefficients of the TDSE solution oscillate with frequencies that are linked to the eigenvalues of the system Hamiltonian. When propagating the solution in time, the time step needed is of the same order of magnitude as the inverse of the largest of the Hamiltonian eigenvalues. Depending on the system that is studied the matrices can become very large and as a result the propagation will need a very small time step.

When the eigenvalues become too large an implicit scheme is needed to propagate the solution in time. From a numerical point of view this solution is rarely appealing as the accuracy is obtained at the cost of computation time and is not always possible. The challenge is to develop methods that can deal with the stiffness of the system, maintaining numerical stability and required accuracy and achieving acceptable computational time for this accuracy to be obtained.

In the parameter region we are interested in, that of high intensity and low frequency, electrons can be ionised with very high speeds and therefore the wave packet can extend out to large distances. In both grid based and spectral methods this can mean a significant increase in the computational effort required to represent the wave packet in coordinate space. One method to allow calculations to be carried out more quickly and to the same level of accuracy is to introduce a mask function or complex scaling in order to truncate the wave packet and reduce their expansion in coordinate space. As such we investigate and discuss one method of scaling called exterior complex scaling (ECS) which we implement in many of our calculations in the following chapters.

In this chapter we present numerical methods that we have developed and used to achieve the results we present in this work. In section 2 we recall the main results from the spectral approach to be used in the time propagation of the TDSE and in section 3 we we briefly describe different propagation methods including the fourth-order Runge-Kutta integrator, Fatunla's explicit method, Arnoldi's explicit method and a predictor-corrector method. In section 4 we then analyse the advantages and disadvantages of the time propagation methods, giving results for some simple one dimensional models and for the three dimensional Hydrogen atom. Finally in section 5 we describe the ECS method.

3.2 The Spectral Representation

In order to solve numerically equation (3.1), the TDSE, we use a spectral approach. Spectral methods use a complete basis set $\{\varphi_i(\mathbf{r})\}$ of square integrable functions

to write the solution of equation (3.1), the wave function $\Psi(\mathbf{r},t)$, as the following truncated expression

$$\Psi(\mathbf{r},t)=\sum_{i=1}^{N}a_i(t)\varphi_i(\mathbf{r}), \tag{3.3}$$

in a Hilbert space where the coefficients $a_i(t)\in\mathbb{C}$ are time dependent. The value N represents the number of terms in the expansion and is taken sufficiently large as to represent the wave function to the desired accuracy. As a result, the TDSE is transformed into a matrix equation for the vector $\mathbf{a}(t)=\{a_i(t)\}$ given by

$$\mathrm{i}\mathbf{B}\frac{\mathrm{d}}{\mathrm{d}t}\mathbf{a}(t)=\mathbf{H}(t)\mathbf{a}(t), \tag{3.4}$$

where $\mathbf{H}$ is the matrix form of the Hamiltonian and $\mathbf{B}$ is the symmetric, positive definite overlap matrix. The overlap matrix for a non-orthonormal basis and the Hamiltonian have elements defined by

$$[\mathbf{B}]_{ij}=\langle\varphi_i|\varphi_j\rangle \tag{3.5}$$

and

$$[\mathbf{H}]_{ij}=\langle\varphi_i|\hat{H}(\mathbf{r},t)|\varphi_j\rangle \tag{3.6}$$

In most cases we adopt the velocity gauge and the interaction Hamiltonian therefore takes the form

$$H_{\mathrm{I}}(\mathbf{r},t)=-\mathrm{i}\mathbf{A}(t)\cdot\nabla \tag{3.7}$$

where $\mathbf{A}(t)$ is the vector potential of a pulse which will be defined in later chapters. In using this expansion we have reduced the TDSE down to a set of coupled first order differential equations which can be solved to a high degree of accuracy. In the following we examine a number of choices of basis sets and look at the advantages and disadvantages of each. The choice of basis will usually depend on the physics of the problem and on the scale of the laser parameters.

The convergence of the spectral methods depends on the analytical properties of the solution, on the order of the polynomials used and the density of the mesh points and basis functions. For highly oscillating solutions a larger density of basis functions will be needed to represent the wave function whilst smoother solutions can be represented by fewer. If there is a probability of the electron acquiring large momentum and travelling out to large distances then the box will have to be large enough accommodate this, again leading to more basis functions being required. The order of the number of basis functions and size of the box is closely related to the field strength and frequency. In practice, each computation is performed several times, each time modifying one parameter until the quantity of interest remains unchanged and we know we have convergence.

The integration over time of the wave packet is given by the solution of the following N-dimensional system of first order differential equations

$$\frac{\mathrm{d}}{\mathrm{d}t}\mathbf{a}(t) = -\mathrm{i}\mathbf{B}^{-1}\mathbf{H}(t)\mathbf{a}(t), \tag{3.8}$$

The matrix $\mathbf{B}$ is always symmetric and positive definite and as such we do not need to evaluate explicitly its inverse. This allows for a numerically stable and fast Cholesky decomposition. The vector $\mathbf{a}(t)$ is said to be $\mathbf{B}$-orthogonal and its norm is given by

$$\mathbf{a}(t)^{\dagger} \cdot \mathbf{B} \cdot \mathbf{a}(t) = 1. \tag{3.9}$$

In general, the success of the spectral method depends on finding a balance between using a sufficiently large enough set of field-free eigenstates of the atom to make sure the wave function is accurately represented whilst avoiding computational issues associated with obtaining numerical solutions of very large systems of ordinary differential equations. In the following section we look at two basis sets we use during our calculations; the Sturmian functions and the B-spline functions. Both of these sets of functions provide a discrete representation of the continuum states due to the fact they are $\mathcal{L}^2$ integrable. A method of reducing the number of basis

functions needed to accurately propagate the solution, by reducing the stiffness of the set of equations, is also covered in the following section.

3.2.1 The Sturmian Basis

In choosing a basis set we wish to represent the solution of the TDSE in configuration space in such a way that accuracy is achieved without the basis set being too large. If N is too high then the stiffness of the equations will force the time step to be very small and each step will be slow to compute due to the order of the equations calculated in each step. As such we want a basis set to fully represent the solution of the TDSE throughout the time integration to an acceptable accuracy without causing computational issues, though this can be difficult to achieve at low frequency due to the highly oscillatory nature of the wave function. In three dimensions, for the case of atomic Hydrogen, we solve the TDSE, in the velocity gauge, which is given in atomic units by the equation

$$\mathrm{i}\frac{\partial}{\partial t}\Psi(\mathbf{r},t) = \left[-\frac{1}{2}\nabla^2 - \frac{1}{r} - \mathrm{i}\mathbf{A}\cdot\nabla\right]\Psi(\mathbf{r},t). \tag{3.10}$$

We expand the wave function, using spherical harmonics $Y_{l,m}(\theta,\phi)$, where, in spherical harmonics, θ and ϕ are the polar and azimuthal angles respectively, as [33]

$$\Psi(\mathbf{r},t) = \sum_{n,l,m} a_{n,l}(t)\frac{S^{\kappa}_{n,l}(r)}{r}Y_{l,m}(\theta,\phi) \tag{3.11}$$

where r is the radial distance, l is the angular quantum number and m is the magnetic quantum number. As before $a_{n,l}$ are the time dependent coefficients which now depend on the angular momentum and $S^{\kappa}_{n,l}(r)$ are the Coulomb Sturmian functions defined for a given angular momentum l and radial index n as

$$S^{\kappa}_{n,l}(r) = C^{\kappa}_{n,l}r^{l+1}\mathrm{e}^{-\kappa r}L^{2l+1}_{n-l-1}(2\kappa r), \tag{3.12}$$

where κ is a dilation parameter which defines the radial extent of our basis, the radial index n is a positive integer satisfying $n \geq l+1$ and $L^{2l+1}_{n-l-1}(2\kappa r)$ are the Laguerre polynomials and $C^{\kappa}_{n,l}$ is a normalisation factor given by

$$C^{\kappa}_{n,l} = \sqrt{\frac{\kappa}{n}}(2\kappa)^{l+1}\left(\frac{(n-l-1)!}{(n+l)!}\right)^{1/2}, \tag{3.13}$$

derived from the normalisation condition $\int_0^\infty S^{\kappa}_{n,l}(r)S^{\kappa}_{n,l}(r)\mathrm{d}r = 1$. The Coulomb Sturmian functions form a complete and discrete set of $\mathcal{L}^2$ integrable functions and are an exact solution of the radial hydrogenic Sturm-Liouville eigenvalue problem [34]. As a result, these functions are well adapted to describe the energy spectrum of atomic hydrogen throughout the integration on time as it interacts with the external field. The matrices associated with the corresponding Hamiltonian are tridiagonal, allowing for economical storage giving the freedom to use large numbers of Sturmian functions. This is due to the fact that we can store just the three diagonals of non-zero entries as a smaller array reducing the amount of memory required to store the Hamiltonian matrices. A given basis of Coulomb-Sturmian functions is characterised by a fixed value of the dilation parameter κ giving a further advantage of allowing for powerful checks on convergence by altering κ. In addition they are orthogonal over the Coulomb potential.

We now look at the Coulomb Sturmian functions against radial position r in order to see how changing the parameters affects the shape and amplitude of the Sturmian functions. In figure 3.1 we take $n = 4$ and $l = 0$ for all cases and alter κ for values of $\kappa = 0.3$ (black line), $\kappa = 0.5$ (grey line) and $\kappa = 1$ (dashed line). We can see that by decreasing κ the function takes on a greater radial spatial extent and would be more suitable for representing the wave function in a case where the wave packet extends to large distances. If, however, we were only interested in more confined wave packets we would benefit more by taking a larger value of κ.

Figure 3.2 shows the functions against radial position r for fixed $l = 2$ and $\kappa = 0.5$ with $n = 3$ (black line), $n = 5$ (grey line) and $n = 8$ (dashed line). We see that as n increases, the function covers a larger radial extent as well as showing more oscillatory behaviour. In our numerical calculation we observe a steep increase in the number of oscillations in the solution $\Psi(\mathbf{r}, t)$ as we decrease the frequency. As such for lower frequency it will become necessary to use a large number of Sturmian

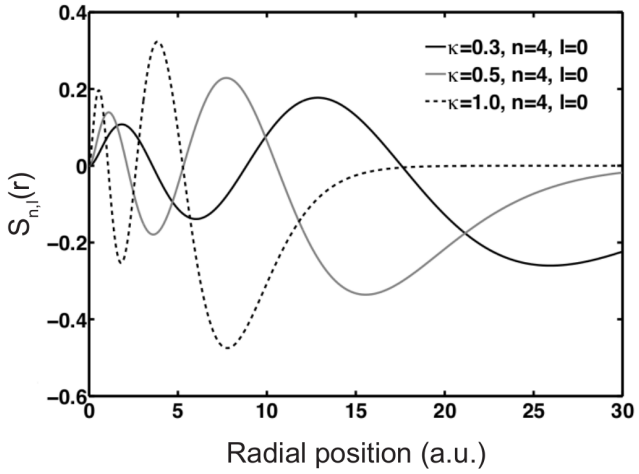

Figure 3.1: The Coulomb Sturmian basis functions for $n = 4$ and $l = 0$ and for $\kappa = 0.3$ (black), $\kappa = 0.5$ (grey) and $\kappa = 1$ (dashed).

functions in order to represent the wave function.

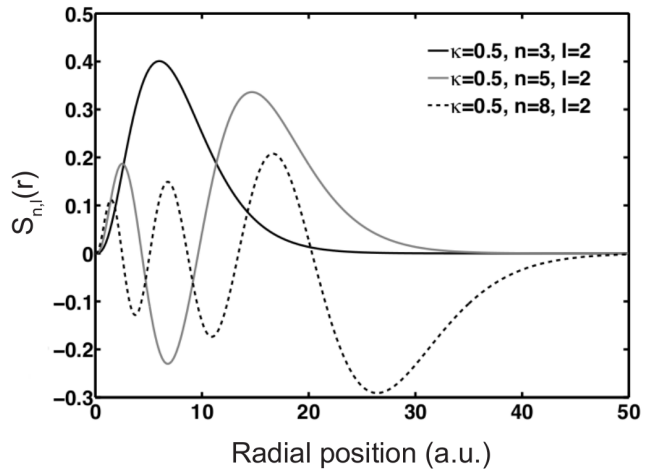

Figure 3.2: The Coulomb Sturmian basis functions for $l = 2$ and $\kappa = 0.5$ and for $n = 3$ (black), $n = 5$ (grey) and $n = 8$ (dashed).

3.2.2 The B-Spline Basis

We now examine another basis set comprising of B-spline functions [8] and initially look at a 1D system. In this case we define the box in which the calculations take

place as opposed to using a dilation parameter. This method can be more intuitive since we can exactly define our workspace size based on the quiver amplitude and laser parameters. This is an important decision since choosing a box too small will result in our ionised electrons reaching the edge of the box and causing artificial reflections which distort our results. Choosing a box too big means a larger basis size is required to accurately represent the wave packet resulting in a longer computation and more data being stored than necessary.

The B-spline functions are defined on an interval $[a, b]$ on a given set of non-decreasing knots $t_0 \leq t_1 \leq \cdots \leq t_m$. The interval is divided into l sub-intervals $I_j = [\xi_j, \xi_{j+1}]$ by a sequence of $l+1$ ascending breakpoints ξ_j. In one dimension our symmetric box is represented by the parameters $a = -x_{max}$ and $b = x_{max}$.

Each B-spline, of order k, is a function made up of different polynomial pieces on adjacent sub-intervals joined at the breakpoints and hence each is defined over an interval $[t_i, t_{i+k}]$ containing $k+1$ consecutive knots. As such exactly one B-splines starts at each knot t_i, $i = 1, \cdots, n$, and ends k knots later, where n is the number of splines in our set.

We can define the multiplicity of the knot sequence μ_i given by $\mu_i = k - \nu_i$ where ν_i relates to the continuity condition $C^{\nu_i - 1}$ at the associated break points. At the end points no continuity is required and as such $\nu_1 = \nu_{l+1} = 0$ giving maximum multiplicity of k. An example of order $k = 3$ can be seen in figure 3.3.

The break points are usually equally spaced. The grid mesh points, between two break points, are not arbitrarily chosen, rather they are the abscissae of the Gaussian quadrature associated with the basis functions. The spectral approaches are appropriate for an accurate description of the bound and resonant states of the quantum system under consideration and in particular the resonant states very close to the ionisation threshold [24]. The fact that the mesh points are chosen to be the abscissae of the Gaussian quadrature is advantageous when it comes to constructing our Hamiltonian matrices since the basis elements and their derivatives will already be computed on the points we integrate using the Gaussian Quadrature. In addition,

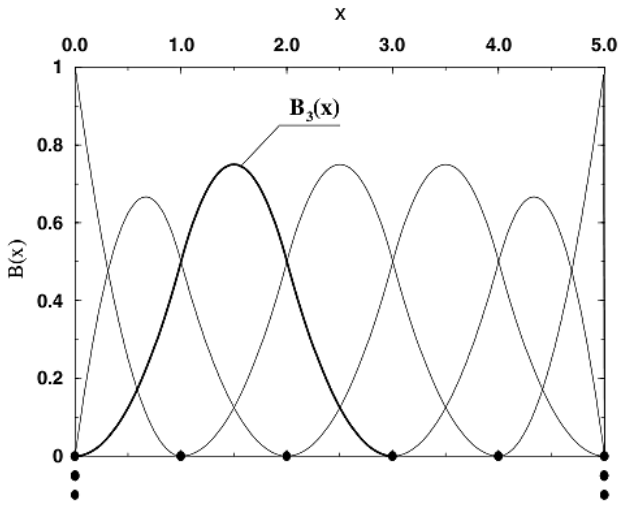

Figure 3.3: The full set of B-splines of order $k = 3$ relative to the knot sequence $0, 0, 0, 1, 2, 3, 4, 5, 5, 5$. Knots are represented by full circles. [8].

further calculations on the wave function during and after the propagation, such as computing the Fourier transform or integrating to find the position of the electron will be much easier and faster to compute. This is especially useful if we need to make calculations during the time propagation since the integrations will often need to be carried out at every time step.

The i^{th} B-spline of order k is defined iteratively for x, in one dimension, as

$$B_i^k(x) = \frac{x - t_i}{t_{i+k-1} - t_i} B_i^{k-1}(x) + \frac{t_{i+k} - x}{t_{i+k} - t_{i+1}} B_{i+1}^{k-1}(x) \tag{3.14}$$

with

$$B_i^1(x) = \begin{cases} 1 & \text{if } \; t_i \leq x \leq t_{i+1} \\ 0 & \text{otherwise.} \end{cases} \tag{3.15}$$

Similarly, we can also define the derivative of a B-spline as a piecewise polynomial function of order $k - 1$

$$\mathrm{D}B_i^k(x) = \frac{k-1}{t_{i+k-1} - t_i} B_i^{k-1}(x) - \frac{k-1}{t_{i+k} - t_{i+1}} B_{i+1}^{k-1}(x) \tag{3.16}$$

where D represents the derivative w.r.t. x of the B-splines.

As such we now expand our wave function $\Psi(x,t)$ as

$$\Psi(x,t) = \sum_{i=1}^{N} a_i(t) B_i^k(x). \tag{3.17}$$

There are many advantages of switching to a B-spline basis over other basis sets. Firstly B-splines are "complete enough" when using a relatively low number of basis functions. While in essence any basis set can be made practically complete if very large, usually linear dependences will limit the size of the basis. With the B-splines, even for a large basis, linear dependences are negligible, due to the local nature of the splines which can be seen from the initial condition in equation (3.15). This makes the B-splines particularly useful in representing the continuum states and as such the use of B-spline methods has grown considerably in recent times. A further advantage is that, due to the local nature of the functions, we can alter positions of the break points as well as the density of the B-splines in different regions of our box. In regions where the wave function is varying quickly we can deal with the rapid oscillations by having a large density, whereas in calmer regions we can use fewer functions which saves on time and memory. For example, as we will see later, the use of exterior scaling allows far fewer basis functions to be used in the scaled region whereas more are needed in the unscaled region. The B-splines allow this to be carried out far more effectively and easily than the Sturmian functions.

Calculation of the matrix elements of the Hamiltonian in the B-spline basis is also simpler than before. These are now, for the unperturbed Hamiltonian,

$$[\mathbf{H}_0]_{ij} = -\frac{1}{2}\int_{-x_{\max}}^{x_{\max}} B_i(x)\frac{\mathrm{d}^2}{\mathrm{d}x^2}B_j(x)\mathrm{d}x + \int_{-x_{\max}}^{x_{\max}} B_i(x)V(x)B_j(x)\mathrm{d}x \tag{3.18}$$

and for the interaction Hamiltonian,

$$[\mathbf{H}_{\mathrm{I}}]_{ij} = \begin{cases} -\mathrm{i}A(t)\int_{-x_{\max}}^{x_{\max}} B_i(x)\frac{\mathrm{d}}{\mathrm{d}x}B_j(x)\mathrm{d}x & \text{(VG)} \\ E(t)\int_{-x_{\max}}^{x_{\max}} B_i(x)xB_j(x)\mathrm{d}x & \text{(LG).} \end{cases} \tag{3.19}$$

One further calculation must be made due to the fact the B-splines do not form an orthogonal basis. To obtain the eigenvalues and eigenvectors, rather than the TISE,

we instead solve a generalised eigenvalue problem

$$\mathbf{H}_0\mathbf{\Psi} = \mathbf{ES}\mathbf{\Psi} \tag{3.20}$$

where $\mathbf{E}$ is a vector of the eigenvalues, Ψ is the wave function and $\mathbf{S}$ is an overlap matrix given by

$$[\mathbf{S}]_{ij} = \int_{-x_{\max}}^{x_{\max}} B_i(x)B_j(x)\mathrm{d}x. \tag{3.21}$$

The form of the B-splines mean that these are best computed using a Gauss-Legendre (GL) quadrature to calculate the matrices numerically over each sub-interval I_j. This works because each sub-interval is split into a number of Gaussian points n_g and hence when we integrate we use the quadrature with the B-splines and their derivatives already evaluated at the quadrature points. A GL quadrature of n_g points will compute exactly the integral of a polynomial of degree $2n_g$ and since a B-spline of order k is a polynomial of degree $k-1$ on each segment then $(k-1)/2$ GL points will compute the overlap integral exactly whilst just a few more are needed to give machine accuracy for the remaining integrals. The matrices generated are sparse and diagonal with bandwidth $2k+1$. In general however, we have found that fewer basis functions are needed with the B-splines in comparison to the Sturmians. There are however downsides to using this basis set. The non-orthogonality of the basis set can lead to increased computations during time propagation due to the fact that the overlap matrix must be included in calculations when the basis set is not orthogonal. In addition as we increase the number of B-spline functions this introduces large eigenvalues to the problem. In order to overcome the stiffness we have to use very small time steps in order to preserve the convergence of the problem during the time integration. We can overcome both problems by switching to an orthogonal basis known as the *atomic basis*. This is covered in the next sections. The integration over time also depends strongly on the time propagator used. We discuss a number of methods in the next section.

The B-spline method can easily be extended to three dimensions. We now solve the reduced Schrödinger equation which is given as

$$\left[-\frac{1}{2}\frac{\mathrm{d}^2}{\mathrm{d}r^2}+\frac{l(l+1)}{2r^2}+V(r)\right]U_{n,l}(r)=EU_{n,l}(r) \tag{3.22}$$

where l is the angular momentum and $U_{n,l}$ are radial functions. This is then solved by expanding the radial solutions in terms of B-splines as

$$U(r)=\sum_{i=1}^{N}a_{n,l}^{i}B_i^k(r). \tag{3.23}$$

The breakpoint sequence is now defined on the box $[a,b]$ with $a=0$ and $b=r_{max}$ and the Hamiltonian matrices are defined as

$$[\mathbf{H}_0]_{ij}^{l}=-\frac{1}{2}\int_0^{r_{\max}}B_i(r)\frac{\mathrm{d}^2}{\mathrm{d}r^2}B_j(r)\mathrm{d}r+\frac{l(l+1)}{2}\int_0^{r_{\max}}\frac{B_i(r)B_j(r)}{r^2}\mathrm{d}r+\int_0^{r_{\max}}B_i(r)V(r)B_j(r)\mathrm{d}r \tag{3.24}$$

and overlap matrix

$$[\mathbf{S}]_{ij}=\int_0^{r_{\max}}B_i(r)B_j(r)\mathrm{d}r. \tag{3.25}$$

The radial function U can then be combined with the spherical harmonics to form the solution to the full TDSE as is seen in chapter 5.

3.2.3 The Atomic Basis

In order to overcome the problems of orthogonality and stiffness, we can make a basis transformation from the B-spline basis to an orthogonal atomic basis. To construct this basis we use the stationary states of the atomic Hamiltonian, found by solving the TISE, and form the invertible matrix $\mathbf{U}$ with the columns as the eigenstates. We now perform the transformations

$$\mathbf{a}^{at}=\mathbf{U}^T\mathbf{a},\ \mathbf{H}_0^{at}(x)=\mathbf{U}^T\hat{H}_0\mathbf{U}\ \text{ and }\ \mathbf{H}_{\mathrm{I}}^{at}(x)=\mathbf{U}^T\mathbf{H}_{\mathrm{I}}\mathbf{U} \tag{3.26}$$

where **a** is the vector of time dependent coefficients in the original B-spline basis and the index *at* represents the atomic basis. This then gives the new TDSE we must solve as

$$\mathrm{i}\frac{\partial}{\partial t}\Psi^{at}(x,t) = \left[\hat{H}_0^{at} + \hat{H}_\mathrm{I}^{at}(x,t)\right]\Psi^{at}(x,t) \tag{3.27}$$

where $\Psi^{at}(x,t)$ is the wave function in the atomic basis and the overlap matrix in the new basis is the identity matrix. The matrix form of the TDSE we need to solve with our time propagator is

$$\mathrm{i}\frac{\mathrm{d}}{\mathrm{d}t}\mathbf{a}^{at}(t) = \mathbf{H}^{at}(\mathbf{r},t)\mathbf{a}^{at}(t). \tag{3.28}$$

Whereas before the atomic Hamiltonian matrix $\mathbf{H}_0$ was banded, $\mathbf{H}_0^{at}$, the atomic Hamiltonian in the atomic basis, is now diagonal. This allows for economical storage in vector form, however we must be aware that the interaction matrix $\mathbf{H}_\mathrm{I}^{at}$ is now full which requires more memory to store. We can now expand our wave function, in 1D, in the following way

$$\Psi^{at}(x,t) = \sum_i a_i(t)\varphi_i^{at}(x) + \sum_j a_{E_j}(t)\varphi_{E_j}^{at}(x) \tag{3.29}$$

where we have split the wave function into its bound and continuous parts and E_j are the positive eigenvalues. This wasn't possible before since each state was represented by a superposition of all coefficients. The high lying states with the largest eigenvalues are highly oscillatory and in most physical situations play very little role in the solution of the TDSE. This oscillatory motion causes the system to become very stiff. In the atomic basis we can remove the corresponding states from (3.29) and reduce the stiffness of the system of equations and much larger time steps can then be used reducing computation time. In addition, we reduce the effective size of the basis used in calculations during propagation and therefore the order of all calculations is reduced and less data is stored. During propagation the population of any states can be monitored with simple calculations or removed from the wave function which can then be used to study the continuum wave function

alone. Using the atomic basis also has the advantage that it is more straightforward to obtain observable quantities from the expansion coefficients $a_i(t)$. For example, the probability of finding the atom in the state $|\Psi_j\rangle$ at the time t is simply $|a_j(t)|^2$. The photoelectron energy spectra can also be readily calculated as we will see in the next chapter. Finally, insight into the photoionisation dynamics can be obtained by monitoring populations in ground and excited states while the atom is interacting with the laser pulse. We will drop the superscript at in all future calculations.

3.3 Time Propagation

We now consider different time propagation schemes used to carry out the integration over time and discuss the advantages and disadvantages of each before directly comparing different methods. In all calculations we assume the atomic basis is used and therefore we look for the solution of equation

$$\mathrm{i}\frac{\mathrm{d}}{\mathrm{d}t}\mathbf{a}(t) = \mathbf{H}(t)\mathbf{a}(t). \tag{3.30}$$

After constructing the full Hamiltonian matrix we can then solve the coupled system of linear equations obtained and propagate the wave packet through time and as such examine the evolution of the packet. For all cases we start the propagation with the electron in the ground state which in the atomic basis means our initial vector of coefficients is taken to be $\mathbf{a}(t_0) = (1, 0, \cdots, 0)$.

In choosing a time propagation method we have a choice between using an implicit or explicit method. Whilst explicit methods use a known solution for a current time to calculate later times, i.e. $\mathbf{a}(t+\delta t) = g(\mathbf{a}(t))$, implicit methods use a combination of current and later times, i.e. $\mathbf{a}(t+\delta t) = g(\mathbf{a}(t), \mathbf{a}(t+\delta t))$. Whilst use of implicit methods require more computational effort and are much harder to implement they are more suited to solving stiff equations and more numerically stable than explicit methods at the intensities and frequencies that we will investigate. However since we have lowered the stiffness of our system by carrying out the transformation to the atomic basis we use two explicit methods since they in general provide good

accuracy for less computational effort and both have proved to be stable for solving the TDSE in the atomic basis.

Using the expansion (3.3) we reduce the TDSE down to the form

$$\dot{\mathbf{a}}(t) = -\mathrm{i}\hat{H}(t)\mathbf{a}(t) = f(t)\mathbf{a}(t). \tag{3.31}$$

3.3.1 The Stability Function

In order to judge the efficiency and accuracy of the different numerical methods we implement in our calculations, we analyse the stability of the one-step numerical time propagation schemes. To do this we consider the following standard test problem, Dahlquist's equation

$$\frac{\mathrm{d}a}{\mathrm{d}t} = \lambda a \tag{3.32}$$

were λ is a complex constant. If we assume that $a(0) = \eta$, the solution of this equation is $a(t) = \eta \mathrm{e}^{\lambda t}$. Usually a system of equations is said to be *stiff* when its Jacobian matrix has some eigenvalues with very large negative real part. In the case of (3.32), assuming that the real part of λ is negative and very large leads to a solution that tends extremely rapidly to zero. We have to look for the conditions that will be imposed on the numerical time propagation scheme so that the numerical solution $a_n = a(n\delta t) \to 0$ as $n \to \infty$, where δt is the time step. By applying the one-step numerical time propagation scheme to (3.32), we obtain

$$a_{n+1} = R(\lambda\delta t)a_n, \tag{3.33}$$

where $R(z)$ is the stability function. In order for $y_n \to 0$ as $n \to \infty$, we must impose $R(\lambda\delta t) < 1$ thereby setting a constraint on the time step we can use. The set $S = \{z = \lambda\delta t \in \mathbb{C}; |R(z)| \leq 1\}$ is called the stability domain of the numerical scheme. A scheme is said to be A-stable if $\mathbb{C}^- = \{z;\ \mathrm{Re}\ z \leq 1\}$ and if it also has the property $\lim_{\mathrm{Re}(\lambda\delta t)\to-\infty} |R(\lambda\delta t)| = 0$ then the scheme is said to be L-stable. L-stable schemes are the most stable ones [43].

3.3.2 Runge-Kutta

Firstly we use an explicit fourth-order Runge-Kutta (RK) method [58]. The idea is that we move from $\mathbf{a}(t)$ to $\mathbf{a}(t+\delta t)$ by multiplying an estimated slope by the time step δt. It is fourth order because we combine four estimated slopes and average in order to get one accurate slope.

We solve (3.31) using the following slope estimations

$$\begin{aligned} k_1 &= f(t, \mathbf{a}) \\ k_2 &= f(t + \frac{1}{2}\delta t, \mathbf{a} + \frac{1}{2}\delta t k_1) \\ k_3 &= f(t + \frac{1}{2}\delta t, \mathbf{a} + \frac{1}{2}\delta t k_2) \\ k_4 &= f(t + \delta t, \mathbf{a} + \delta t k_3) \end{aligned} \tag{3.34}$$

which are then combined as a weighted average as

$$\mathbf{a}(t+\delta t) = \mathbf{a}(t) + \delta t \frac{1}{6}(k_1 + 2k_2 + 2k_3 + k_4) \tag{3.35}$$

which carries a one step error of the order $O(\delta t^5)$ and a global error of the order $O(\delta t^4)$. In general, in order to reduce the error we can either decrease the step size or increase the order of the RK process.

Each of the values k_1 to k_4 can be explained physically. Firstly k_1 is the slope at the beginning of the time step and if we continue this slope half way through the time step then we arrive at k_2, an estimate of the slope at the midpoint. If we were to use the slope k_2 to the midpoint instead then we get another estimate at the midpoint, that of k_3. Finally should we use the slope k_3 to step across the whole time step then we end up at k_4, an estimate of the slope at the midpoint. These slopes can be seen in figure 3.4.

Fourth-order RK was chosen due to its simplicity and the fact that it is very reliable when it comes to convergence, however, it is generally reliant on a small step size which may need trial and error to find and is very time consuming. For greater accuracy with faster implementation an adaptive step size RK method can be used

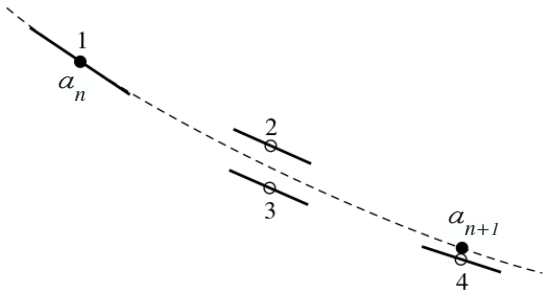

Figure 3.4: Fourth-order Runge-Kutta method. The figure shows the four estimates of the slopes. Once at the start a_n, twice at the midpoint and once at the end of the time step, a_{n+1}. From these derivatives the final function value (black dot) is calculated. Adapted from [58].

where can control the error via a parameter ϵ. The program then effectively takes each step twice, once as a full step and once as two halves. It looks ahead at each calculation to see how big the steps can become whilst keeping within the allowed error. Although this means more calculations are being carried out at each time step the overall number of steps will decrease dramatically since the terrain of our integration will vary greatly during the pulse length. When the topography is rough the algorithm will slow and integrate more carefully whilst during smooth terrain the step size can become very large without fear of losing accuracy. One must be wary however of setting ϵ too small since if we are greedy with the accuracy then the time step can become so small that calculations can take exceedingly and unnecessarily long. When looking at low frequency when large accuracy is needed many adaptive step size calculations fail due to using too many steps of a small size. In these cases it is best to use one of the methods which follow.

3.3.3 Fatunla Time Propagation

We next examine another time propagation scheme, the Fatunla method. The idea behind Fatunla's method is to take into account the intrinsic frequencies of the atom-field system by introducing interpolating oscillatory functions that approximate the solution of the TDSE. This allows one to deal with problems involving eigenvalues

that differ by many orders of magnitude. This is why Fatunla's method has the capability to solve stiff equations, while requiring only matrix vector products. To illustrate this we write equation (3.31) as

$$\frac{\mathrm{d}}{\mathrm{d}t}\Psi(t) = -\mathrm{i}\hat{H}(t)\Psi(t) = \mathbf{f}(t,\Psi). \tag{3.36}$$

The solution $\Psi(t)$ over a subinterval $[t_n, t_n + \delta t = t_{n+1}]$ is approximated by the interpolating oscillatory function

$$\tilde{\mathbf{F}}(t) = (\mathbf{I} - \mathrm{e}^{\mathbf{\Omega}_1 t})\mathbf{c}_1 - (\mathbf{I} - \mathrm{e}^{-\mathbf{\Omega}_2 t})\mathbf{c}_2 + \mathbf{c}_3 \tag{3.37}$$

where $\mathbf{I}$ is the identity matrix, $\mathbf{\Omega}_1$ and $\mathbf{\Omega}_2$ are diagonal matrices and $\mathbf{c}_i (i = 1, 2, 3)$ are constant vectors. We fix (3.37) so that the function coincides with the solution at the endpoints of the interval $[t_n, t_{n+1}]$ and that it satisfies the differential equation at $t = t_n$. We then arrive at the recursion formula

$$\Psi_{n+1}(t) = \Psi_n(t) + \mathbf{R}\mathbf{f}_n + \mathbf{S}\mathbf{f}_n^{(1)}, \tag{3.38}$$

where we have used the notation $\mathbf{f}_n = \mathbf{f}(t_n, \psi_n)$ and $\mathbf{f}_n^{(1)} = \frac{\mathrm{d}}{\mathrm{d}t}\mathbf{f}(t,\Psi)\Big|_{t=t_n}$. $\mathbf{R}$ and $\mathbf{S}$ represent diagonal matrices defined by

$$\mathbf{R} = \mathbf{\Omega_2}\Upsilon - \mathbf{\Omega_1}\Xi \tag{3.39}$$

and

$$\mathbf{S} = \Upsilon + \Xi, \tag{3.40}$$

where Υ and Ξ are diagonal matrices with non zero entries given in [27, 28]. The recursion formula (3.38) depend on the stiffness matrices $\mathbf{\Omega}_{1,2}$ which can be written in terms of the function $\mathbf{f}_n$ and its derivatives up to the third order in t_n. We use a Taylor expansion of $\Psi_{n+1} = \Psi(t_n + \delta t)$ and Maclaurin series of

$$\mathrm{e}^{\Omega_1 \delta t} = \sum_{j=0}^{\infty} \frac{\delta t^j}{j!}\Omega_{1,j} \tag{3.41}$$

and

$$\mathrm{e}^{-\Omega_2 \delta t} = \sum_{j=0}^{\infty} \frac{\delta t^j}{j!}(-1)^j \Omega_{2,j} \tag{3.42}$$

substituted into (3.38). We then acquire a simple system of equations for $\mathbf{\Omega}_{1,2}$ given by

$$\Omega_{1,j} = \frac{1}{2}(-D_j + \sqrt{D_j^2 + 4E_j}), \tag{3.43}$$

and

$$\Omega_{2,j} = \Omega_{1,j} + D_j \tag{3.44}$$

where D_j and $E_j (j = 1, \cdots, N)$ are given in term of the derivatives $\mathbf{f}_n^{(k)}$ where $\mathbf{f}_n^{(k)} = \frac{\mathrm{d}^k}{\mathrm{d}t^k}\mathbf{f}(t, \Psi)\Big|_{t=t_n}$ by [28] as

$$D_j = \frac{f_{n,j}^{(0)} f_{n,j}^{(3)} - f_{n,j}^{(1)} f_{n,j}^{(2)}}{f_{n,j}^{(1)} f_{n,j}^{(1)} - f_{n,j}^{(0)} f_{n,j}^{(2)}} \tag{3.45}$$

and

$$E_j = \frac{f_{n,j}^{(1)} f_{n,j}^{(3)} - f_{n,j}^{(2)} f_{n,j}^{(2)}}{f_{n,j}^{(1)} f_{n,j}^{(1)} - f_{n,j}^{(0)} f_{n,j}^{(2)}}, \tag{3.46}$$

provided the denominators in equations (3.45) and (3.46) are not zero. Fatunla [28] has established that his method is *L-stable*, i.e. unconditionally stable and non-oscillatory and exponentially fitted to any complex value λ. This means that the corresponding stability function $R(\lambda\delta t) = \exp(\lambda\delta t)$ gives the optimum stability properties. The j^{th} component of the truncation error at $t = t_{n+1}$ is given by

$$\begin{aligned} \mathbf{T}_{n+1,j} = \frac{\delta t^5}{5!}[\mathbf{f}_{n,j}^{(4)} + (\Omega_{2,j}^3 - \Omega_{2,j}^2\Omega_{1,j} + \Omega_{2,j}\Omega_{1,j}^2 + \Omega_{2,j}^3)\mathbf{f}_{n,j}^{(1)} \\ - \Omega_{1,j}\Omega_{2,j}(\Omega_{1,j}^2 - \Omega_{1,j}\Omega_{2,j} + \Omega_{2,j}^2)\mathbf{f}_{n,j}] + \mathcal{O}(\delta t^6) \end{aligned} \tag{3.47}$$

The implementation of equation (3.38) to calculate Ψ_{n+1} requires the calculation of the function $\mathbf{f}_n$ and its first derivatives at each value of t_n, and also the stiffness

matrices $\mathbf{\Omega}_1$ and $\mathbf{\Omega}_2$ to obtain the matrices $\mathbf{R}$ and $\mathbf{S}$. We also calculate the truncation error $\mathbf{T}_{n+1}$ to control the size of the integration step imposing a boundary criterion for $|\mathbf{T}_{n+1}|$. Note that to calculate the truncation error, we also need to evaluate $\mathbf{f}_n^{(4)}$. The stiffness parameters carry the intrinsic information on the natural oscillations of the system. Due to this fact, Fatunla's scheme can afford larger values of the time step compared with other explicit methods such as Runge-Kutta.

To test the propagation scheme we solve the one dimensional TDSE with a model short range Gaussian potential of the form

$$V(x) = -V_0 \mathrm{e}^{-\beta x^2}. \tag{3.48}$$

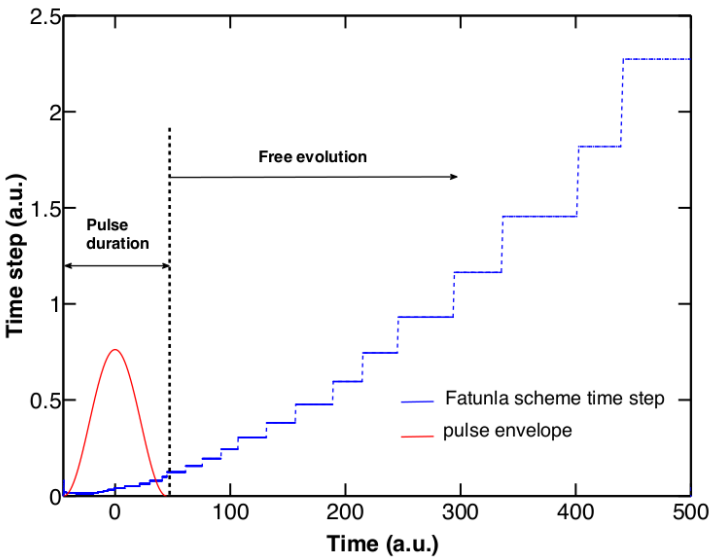

Figure 3.5: Evolution of the time step in Fatunla's method (blue line) for a Gaussian model problem. The cosine square pulse envelope (red line) is also shown on an arbitrary scale. The Gaussian potential parameters are $V_0 = 1$ a.u. and $\beta = 1$ a.u. and we use a laser pulse of frequency $\omega = 0.7$ a.u. and intensity $I = 10^{14}$ W $\cdot$ cm^{-2} for 10 optical cycles. [29].

The atom interacts with a $\cos^2$ pulse of intensity $I = 10^{14}$ W $\cdot$ cm^{-2} and frequency $\omega = 0.7$ a.u. with a duration of 10 optical cycles corresponding to 90 a.u. of time. We take the vector potential to be

$$A(t) = A_0 \cos^2\left(\frac{\pi t}{\tau}\right) \sin(\omega t)\ ,\ -\tau/2 \leq t \leq \tau/2. \tag{3.49}$$

Figure 3.5 shows the evolution of the time step [29]. The pulse envelope is also plotted in arbitrary units to illustrate the duration of the pulse. We see that the time step becomes increasingly large after the end of the pulse, reaching values of $\delta t > 2$ at the end of the total propagation (500 a.u. of time). It is clear that the most demanding part of the propagation, and therefore the most time consuming, is during the interaction of the pulse with the system. This observation is important since it is often necessary to propagate the wave function up to large distances after the end of the pulse, such as with the tSURFF method to calculate the photoelectron spectrum which we look at in the next chapter.

In figure 3.5, the time step is adapted according to the condition $10^{-14} < |\mathbf{T}_{n+1}| < 10^{-9}$, that is, if the truncation error is lower than the lower bound 10^{-14} then we increase the time step, and if it is higher than the upper bound 10^{-9} it is decreased. With this choice, the overall conservation of the norm is about 10^{-5}. For many physical problems, this level of accuracy in the norm is sufficient but, if a higher accuracy is needed, then we might expect that it is sufficient to shift the bounds of the truncation error. However, as shown in figure 3.6, such a conclusion is not correct. Here we consider three different constraints on the truncated error and calculate on a logarithmic scale, the absolute error on the norm denoted by Δ as a function of time. This error is defined as the absolute value of the difference between 1 and the norm at time t. In these three cases, the time propagation is started with the same time step, namely 10^{-3} a.u. This time step always increases and decreases as expected. In all three cases, we observe a significant loss of accuracy in Δ at the very beginning of the time propagation [29]. As described by Madroñero and Piraux [48], this is due to initially very small values of the denominators in equations (3.45) and (3.46) which leads to inaccurate values of the stiffness matrix elements and of the truncated error. This problem is therefore intrinsically related to Fatunla's method and leads to difficulties in correctly controlling the time step. In fact, if we

keep the time step constant from the beginning, we have a much better control of Δ. We have also checked that this is true even in the field free case. On the other hand, we see from the inset in figure 3.6 that we maintain a higher accuracy when the constraint on the truncated error is more severe. In addition, we also observe several small jumps in Δ, the magnitude of which are much smaller than the jump in Δ at the beginning of the time propagation. We attribute these jumps to an accumulation of roundoff errors. Indeed, we expect more roundoff errors in the case that the constraint on the truncated error is the strongest since a smaller time step leads to a larger amount of calculations. Note that the jump observed in the red continuous line corresponds to a change of only one digit in the accuracy of the norm. The overall relative accuracy we obtain even for the most severe constraint we use on the truncation error is of the order of 10^{-5}. To achieve a greater accuracy, it is necessary to use a fixed and very small time step. These results show clearly that the achievable accuracy for the adaptive time step approach in Fatunla's method has a lower bound for a given initial time step. As a result, the use of Fatunla's method rests on a compromise between the computer time required and the accuracy needed. In conclusion, Fatunla's method allows one to treat stiff problems while fully exploiting the advantages of explicit schemes, namely that it only involves matrix vector multiplications.

3.3.4 Arnoldi Time Propagation

As we progress to more complex problems involving lower frequencies and higher intensities the spatial extent travelled by the electron becomes ever more large and the wave function begins to oscillate more drastically. To deal with this we must increase the size of our box considerably and therefore the size of the basis needed to represent the wave function in order to achieve convergence with respect to position. In doing this our RK method becomes less economical to use as the time step shrinks and accuracy in the integration over time becomes harder to achieve. To reduce the computer time needed we have to increase the time step used and hence we look

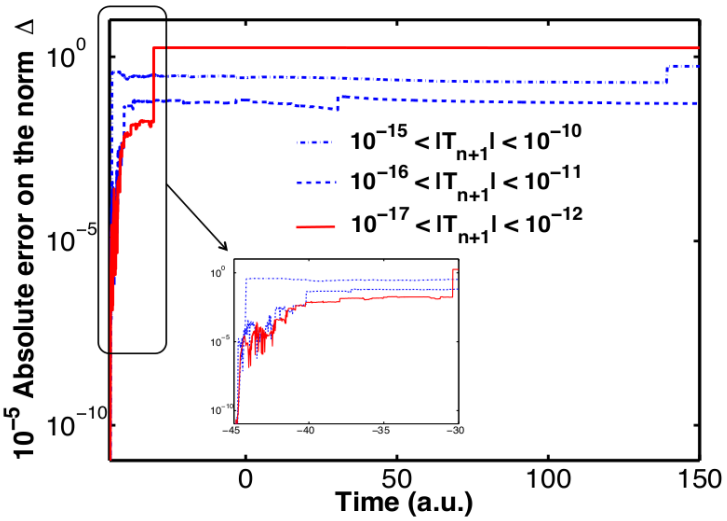

Figure 3.6: Absolute error in the norm $\Delta = |(|\Psi(\mathbf{r},t)| - |\Psi(\mathbf{r},t_0)|)|$ on a logarithmic scale for different lower and upper bounds of the truncation error. The parameters of the Gaussian model problem are the same as in figure 3.5. The inset is a blow-up of the region at the beginning of the time propagation. [29].

now at a final time propagator scheme, an iterative Arnoldi method [72, 62].

This method uses projection on a Krylov subspace to solve the series of differential equations in $\mathbf{a}$ for a fixed time step δt. It will originally proposed by Arnoldi [6] in the calculation of the eigenstates of a matrix and we use it here as a time propagator to solve equation (3.28). An assumption made is that the interval $[t, t+\delta t]$ is sufficiently small that the full Hamiltonian $\mathbf{H}$ can be assumed constant for this short amount of time. This assumption allows us to take the solution of (3.28) to be

$$\mathbf{a}(t+\delta t) = \exp(-\mathrm{i}\mathbf{H}(t)\delta t)\mathbf{a}(t). \tag{3.50}$$

where $\mathbf{H}$ is the Hamiltonian in the atomic basis. If $\mathbf{H}$ is diagonalisable we can then represent it in the form $\mathbf{H} = \mathbf{U}\boldsymbol{\Lambda}\mathbf{U}^{-1}$, where $\boldsymbol{\Lambda}$ is a diagonal matrix formed of the eigenvalues λ_i of $\mathbf{H}$ and $\mathbf{U}$ is a matrix with the corresponding eigenvectors of $\mathbf{H}$ as its columns. We can then write (3.50) as

$$\mathbf{a}(t+\delta t) = \mathbf{U}\exp(-\mathrm{i}\Lambda(t)\delta t)\mathbf{U}^{-1}\mathbf{a}(t). \tag{3.51}$$

However, for very large N this may be unnecessary and computationally very de-

manding. Instead, we can define the exponential in equation (3.50) using a Taylor expansion of the form

$$\mathbf{a}(t+\delta t) = \left(\mathbf{I} - \mathrm{i}\delta t\mathbf{H}(t) + \cdots + \frac{(-\mathrm{i}\delta t)^k}{k!}\mathbf{H}^k(t) + \cdots\right)\mathbf{a}(t) \tag{3.52}$$

To apply the method we construct a Krylov subspace basis spanned by $(m+1)$ linearly independent vectors generated by the repeated action of the Hamiltonian on our vector of coefficients

$$\mathrm{K}_{m+1} = span\{\mathbf{a}, \mathbf{H}\mathbf{a}, \mathbf{H}^2\mathbf{a}, \ldots, \mathbf{H}^m\mathbf{a}\}. \tag{3.53}$$

To construct the orthonormal Krylov subspace, we first use Gram-Schmidt orthogonalisation on the initial vectors $\{\mathbf{a}, \mathbf{H}\mathbf{a}, \mathbf{H}^2\mathbf{a}, \ldots, \mathbf{H}^m\mathbf{a}\}$ to form $m+1$ orthonormal vectors, $\{\mathbf{q}_0, \mathbf{q}_1, \cdots, \mathbf{q}_m\}$, collected as columns of the matrix $\mathbf{Q}$. The procedure starts with $\mathbf{q}_0 = \mathbf{a}/|\mathbf{a}|$, where the norm is defined as $|\mathbf{a}| = \sqrt{\mathbf{a}^\dagger \cdot \mathbf{a}}$. The $\mathbf{q}_n$ are formed by calculating $\mathbf{H}\mathbf{q}_{n-1}$ and then orthonormalising each vector with respect to $\mathbf{q}_0, \mathbf{q}_1, \cdots, \mathbf{q}_{n-1}$. We can then use this matrix to form an upper Hessenberg matrix $\mathbf{h}$ using the equation

$$\mathbf{H}\mathbf{Q} = \mathbf{Q}\mathbf{h}, \tag{3.54}$$

to give

$$\mathbf{h} = \mathbf{Q}^T\mathbf{H}\mathbf{Q} \tag{3.55}$$

where $\mathbf{h}$ is of size $(m+1)\times(m+1)$, considerably smaller and easier to diagonalise than the full Hamiltonian $\mathbf{H}$ whilst the obtained eigenvalues and eigenvectors are good approximations to the original Hamiltonian. We see here that $\mathbf{h}$ is the Krylov subspace representation of the full Hamiltonian, and that in this procedure, we obtain simultaneously the Krylov vectors $\mathbf{q}_0, \mathbf{q}_1, \cdots, \mathbf{q}_m$. Arnoldi's algorithm is general and applies also to non-Hermitian matrices. It reduces a dense matrix to an upper Hessenberg form matrix, and in the particular case of hermitian matrices, to a symmetric tridiagonal form.

Since $\mathbf{H}^n \simeq (\mathbf{Q}\mathbf{h}\mathbf{Q}^T)^n = \mathbf{Q}\mathbf{h}^n\mathbf{Q}^T$ we can see that our Arnoldi propagator can then be defined as

$$\mathbf{a}(t+\delta t) = \mathbf{Q}\exp(-\mathrm{i}\mathbf{h}\delta t)\mathbf{Q}^T\mathbf{a}(t) \tag{3.56}$$

where since m is kept relatively small, $\exp(-\mathrm{i}\mathbf{h}\delta t)$ can be easily exponentiated by diagonalising $\mathbf{h}$.

The choice of m is important here and whilst for higher frequencies where the oscillation of the solution is less rapid we can take the Krylov basis size as low as $m = 5$, as the frequency drops and the intensity rises m will have to be taken higher in order to achieve convergence in both space and time due to the rise in the number of basis functions needed. To carry out calculations in the mid-infrared regime needed to investigate the low energy structure we have to take m as high as 160. Similarly using the LG also requires a higher value of m than identical calculations in the VG. In comparison to the RK method the Arnoldi method is correct to the order of $O(\delta t^{m+1})$ and as such much higher accuracy can be achieved through increasing m or reducing the size of the time step. In practice the choice of m relies on the interplay of several parameters including the frequency and intensity of the laser, the basis size and box size and the time step chosen.

We have found from our calculations, as by [56], that enlarging the size of the Krylov space allows for larger time steps to be considered. In figure 3.7 we give the number of Krylov vectors necessary to obtain convergence of our results as a function of the time step used in the calculations for the case of the one dimensional Gaussian model potential with the same parameters as in figure 3.5. In our calculations, the time step δt is kept constant during the propagation. The choice of the optimal value of the time step and of the corresponding dimension of the Krylov space is therefore the result of a compromise while trying to reduce the computer time.

In numerical calculations, the Arnoldi algorithm requires some modifications. After a first calculation of a new Krylov vector q_{n+1}, we ensure that the norm is equal to one, by re-checking the orthogonality against the previously calculated vectors,

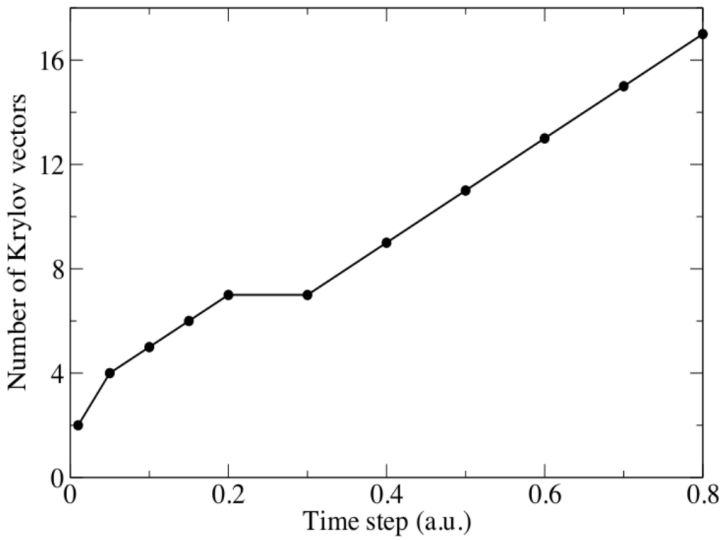

Figure 3.7: Number of Krylov vectors required to obtain convergence of the final vector propagated for different values of the (fixed) time step. The parameters of the Gaussian model problem are the same as in figure 3.5. [29].

and perform again the Gram-Schmidt procedure if necessary. The norm here is the control factor and in principle the orthogonality condition determines the maximum size of the Krylov subspace and the algorithm can be used with $m-1$ vectors. Also, if we start generating the Krylov vectors from the ground state of the system, then $\mathbf{a}(t_0)$ is an eigenstate of the Hamiltonian, making it impossible to build a linearly independent set of Krylov vectors. To solve this problem, instead of using the vector $\mathbf{a}(t_0)$ as a starting point, we use a modified vector $\mathbf{a}(t_0)+\epsilon$, with a vector ϵ of random entries no larger than 10^{-10}.

From equation (3.50) the stability function associated to the numerical time propagator based on Arnoldi's algorithm is given by $R(\lambda\delta t) = \exp(\lambda\delta t)$ and gives the optimum stability properties, the same properties as the Fatunla method. However, it is worth remembering that equation (3.50) is only valid if the Hamiltonian is time independent. It is therefore a good approximation only for small values of δt. In the present case, there are two types of errors. The first one is directly related to Arnoldi's algorithm for the calculation of the exponential of a matrix as in equation (3.52). This type of error from the expansion has been discussed in detail by Saad [61] and later on by Hochbruck and Lubich [37]. We have checked that this type of

error is always negligible and does not depend on the time step. The second type of error is due to assuming that the Hamiltonian does not depend explicitly on time over the time step δt. We estimated this type of error by calculating $||\mathrm{d}\mathbf{a}/\mathrm{d}t + \mathrm{i}\mathbf{H}\mathbf{a}||$ and checked that, as expected, it is of the order δt^2.

The method offers more efficiency than RK and faster performance since the relatively low value of m compared to the size of the basis means far fewer calculations are computed and in addition fewer time steps can often be used. Arnoldi can also be considered a unitary operator to order m in δt and as such the method conserves the norm of the wave packet to up to 10 digits throughout propagation. In terms of further improvements, again an adaptive step size could be considered, as well as an adaptive size of the Krylov subspace. Arnoldi allows for very convenient error tolerance control since for a given m the difference of the propagated wave function $\Psi^{(m)}(t+\delta t)$ to the lower order function $\Psi^{(m-1)}(t+\delta t)$ can be calculated with little extra effort and as such $||\Psi^{(m)}(t+\delta t) - \Psi^{(m-1)}(t+\delta t)||^2$ can be used as an error tolerance parameter.

The innovative use of the Arnoldi method as an explicit approach offers then the convenience that we only require matrix-vector and scalar products, which then transforms the method in a time-efficient approach as is the case for Fatunla's method. Furthermore, this particular scheme is norm-conserving with the advantage of providing a check for the method, even though it also means that it is not easy to quantify the error in the calculation of the norm.

3.4 Comparison of Time Propagation Methods

In this section we use a predictor-corrector (P-C) scheme to compare the explicit Arnoldi and Fatunla time propagation methods described above. The predictor is either Fatunla's or Arnoldi's algorithm whilst the corrector is a fully implicit method of Runge-Kutta type of order s. The numerical solution for a given time using an implicit RK method is given by

$$\mathbf{a}_{n+1} = \mathbf{a}_n + \delta t \sum_{i=1}^{s} c_i f(t_i, \mathbf{Y}_i), \tag{3.57}$$

where f is defined as in equation (3.31) as $f(t_i, \mathbf{Y}_i) = -\mathrm{i}\hat{H}(t_i)\mathbf{Y}_i$ with $t_i = t_n + c_i'\delta t$, where c_i and c_i' are coefficients defining the Runge-Kutta method . The quantities $\mathbf{Y}_i$ estimate the solution at intermediate time t_i and are obtained by solving the following $(sN \times sN)$ system of equations

$$\mathbf{Y}_i = \mathbf{a}_n + \delta t \sum_{k=1}^{s} c_{ik}'' \tag{3.58}$$

where again c_{ik}'' are coefficients defined by the method.

3.4.1 The Above Threshold Ionisation Spectrum

In order to compare different time propagation methods we look at the computational efficiency of calculating the ATI spectrum using each method. In order to plot the spectrum we calculate the probability of ionisation with energy E by projecting the wave function at the end of the pulse $t = \tau$ onto the field free continuum states of energy E, giving

$$P(E) = |\langle\ \varphi_E(x)|\Psi(x,\tau)\ \rangle|^2. \tag{3.59}$$

We use the discrete states in the box to mimic the continuum and carry out the projection. Hence in the atomic basis, taking into account even and odd states in x, we have

$$P(E_i) = P\left(\frac{E_{i-1} + E_i + E_{i+1} + E_{i+2}}{4}\right) = \frac{|\langle\varphi_i(x)|\Psi(x,\tau)\rangle|^2}{E_{i+1} - E_{i-1}} + \frac{|\langle\varphi_{i+1}(x)|\Psi(x,\tau)\rangle|^2}{E_{i+2} - E_i}, \tag{3.60}$$

which simplifies to

$$P\left(\frac{E_{i-1} + E_i + E_{i+1} + E_{i+2}}{4}\right) = \frac{|a_i(\tau)|^2}{E_{i+1} - E_{i-1}} + \frac{|a_{i+1}(\tau)|^2}{E_{i+2} - E_i}, \tag{3.61}$$

where $a_i(\tau)$ represents the i^{th} atomic state with positive eigenvalue at the end of the pulse. In later chapters we show other methods to calculate the ATI spectrum such as direct projection onto Coulomb wave functions.

3.4.2 One Dimensional Gaussian Potential

We now look at results for the case of the one-dimensional Gaussian potential given by

$$V(x) = -V_0 \mathrm{e}^{-\beta x^2} \tag{3.62}$$

where the potential parameters V_0 and β can be altered to choose the ionisation potential and number of bound states. We see a selection of parameters and bound state energies in table 3.1 for cases used below. We can see that V_0 is related to the strength of the potential and increasing this will increase the ionisation potential, whilst β is related to the width of the potential and lowering this increases the number of bound states for fixed V_0.

V_0	β	Energy (a.u.)
1.0	1.0	−0.4773899773828144
1.0	0.1	−0.79526702487439793
		−0.42806021756209423
		−0.15419507232419039
		−0.00606807395921935
4.0	1.0	−2.7744947605788566
		−0.7839196725805436
4.0	0.1	−3.5716132995713665
		−2.7544712303409185
		−2.0193560537353119
		−1.3727672048768107
		−0.8238657568118924
		−0.3869373621565752
		−0.0889289021969690

Table 3.1: Potential parameter choices for V_0 and β in the potential (3.62) as well as the corresponding bound state energies. [32].

The electron wave packet is developed in a basis of 200 B-splines and the time scaled coordinate (TSC) method is used during the propagation [33]. The codes are run on an INTEL XEON 2.33 GHz Processor 51.40 (32 GB Ram).

In figure 3.8 we take an intensity of $I = 10^{14}$ W $\cdot$ cm^{-2}, a frequency of $\omega = 0.7$ a.u. and carry out the calculations for 10 optical cycles corresponding to a propagation time of $\tau = 90$ fs using a vector potential defined in equation (3.49).

At these parameters we have an amplitude of $A_0 = 5.3378 \times 10^{-9}\sqrt{I}/\omega = 0.076$ a.u. which corresponds to an electric field amplitude of $E_0 = A_0\omega = 0.05$. This gives a Keldysh parameter of $\gamma = 12.9$ putting us firmly in the multiphoton regime. The energy distribution is calculated by propagating the scaled wave packet to a stationary state until a time of 1500 a.u. when convergence of the spectrum in comparison to the unscaled spectrum is achieved. The results shown are obtained using the two explicit propagators above, Fatunla and Arnoldi. Both methods converge to the same result but Fatunla's propagator uses 2.3s of computer time with an adaptive time step while Arnoldi's propagator using five Krylov vectors and a fixed time step $\delta t = 0.3$ a.u. takes 6.2s. For these laser parameters both methods give easily the correct result. However Arnoldi's method performs poorly from a computational point of view. This can be understood by referring to figure 3.5 where we show that Fatunla's propagator allows the use of ever larger time steps, particularly during the time integration after the pulse has ended, while Arnoldi's propagator keeps the same time-step throughout the propagation.

To check how these methods behave in a more challenging case, we consider the same model potential with a pulse of frequency 0.1 a.u. with the same number of optical cycles and peak intensity. In this case, the total pulse duration is equal to 630 a.u. We see in figure 3.9 that again both methods give the same converged results. These results are obtained after propagating the wave packet up to a time of 2500 a.u. The running time with Fatunla's propagator is equal to 958.27s while in this case, Arnoldi's propagator performs better taking 553.69s for a subspace of 20 Krylov vectors and a fixed time step $\delta t = 0.1$ a.u. It can be seen that in

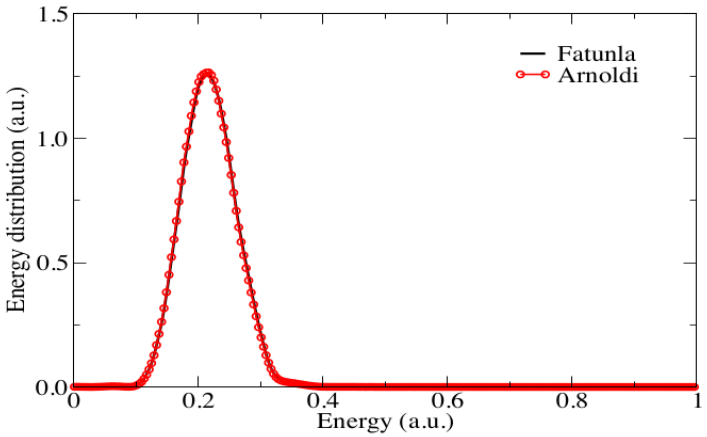

Figure 3.8: Photoelectron energy spectrum for the Gaussian model potential. The time propagation uses Fatunla's propagator with adaptive time step and Arnoldi's propagator with five Krylov vectors and a fixed time step $\delta t = 0.3$ a.u. The parameters of the model problem are $V_0 = 1$ and $\beta = 1$ for a laser pulse of frequency $\omega = 0.7$ a.u. and intensity $I = 10^{14}$ W $\cdot$ cm^{-2} for a duration of 10 optical cycles. The relative difference between both curves is of the order of 10^{-3}. [29].

general, Arnoldi's propagator performs better than Fatunla's propagator for smaller frequencies.

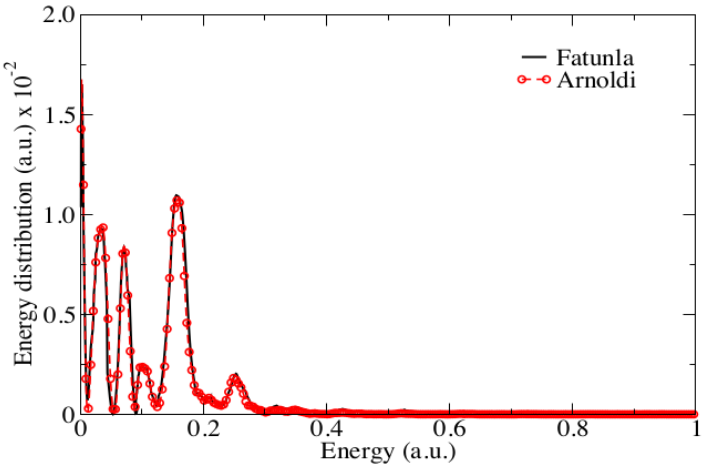

Figure 3.9: Photoelectron energy spectrum for the Gaussian model potential. The time propagation uses Fatunla's propagator with adaptive time step and Arnoldi's propagator with 20 Krylov vectors and a fixed time step $\delta t = 0.1$ a.u. The parameters of the model problem are $V_0 = 1$ and $\beta = 1$ for a laser pulse of frequency $\omega = 0.1$ a.u. and intensity $I = 10^{14}$ W $\cdot$ cm^{-2} for a duration of 10 optical cycles. The relative difference between both curves is of the order of 10^{-3}. [29].

To further investigate the algorithms we increase the number of bound states supported by our potential by choosing $V_0 = 4$ and $\beta = 0.1$. This results in 8 bound states as opposed to the single bound state in the previous example. The pulse has a frequency $\omega = 0.5$ a.u. with a duration of 100.53 a.u. that corresponds to 8 optical cycles. The peak intensity used here is $I = 10^{16}$ W $\cdot$ cm^{-2}. In this case, we use 1700 B-splines to propagate the wave packet up to a time of 5000 a.u. Figure 3.10 shows the energy distribution obtained using Fatunla's propagator (straight line) and the predictor-corrector scheme (squares), which is used to test the accuracy of Fatunla's method. Comparison of these two methods shows that Fatunla keeps the accuracy in the results down to a value of 10^{-5} a.u.for the energy distribution. Fatunla's propagator takes 379.36 s while the P-C method with adaptive time step takes 1801.49s. It is clear that Fatunla uses remarkably less computer time and works as long as the accuracy required is up to six digits.

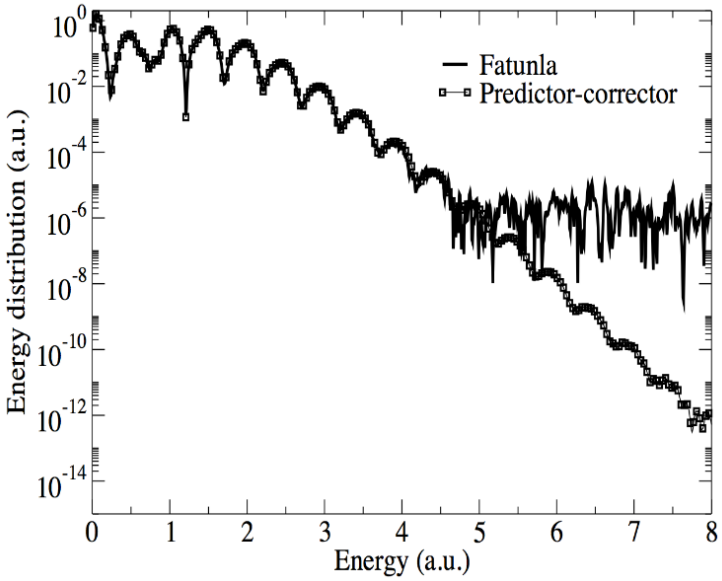

Figure 3.10: Photoelectron energy spectrum for the Gaussian model potential. The time propagation uses Fatunla's propagator with adaptive time step and the predictor-corrector method. The parameters of the model problem are $V_0 = 4$ and $\beta = 0.1$ with a pulse of frequency $\omega = 0.5$ a.u. and intensity $I = 10^{16}$ W $\cdot$ cm^{-2} for a duration of 8 optical cycles. [29].

Figure 3.11 shows the same energy distribution obtained with Arnoldi's propagator.

We show the results obtained with Arnoldi's approach and two different fixed time steps and compare these results with those obtained with the P-C scheme. The Krylov subspace contains 20 vectors and the wave packet is again propagated up to 5000 a.u. The white circles show the results for a time step $\delta t = 0.03$ a.u. and the black circles for $\delta t = 0.3$ a.u. We note that increasing the time step leads to less accurate results by comparison with the P-C method. Arnoldi scheme takes 5957.19s for a time step of 0.03 a.u. and 598.11s for a time step of 0.3 a.u.

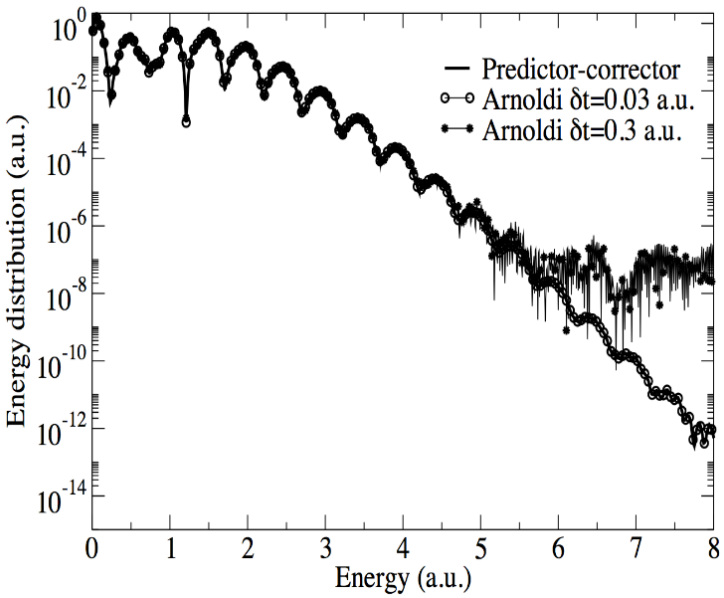

Figure 3.11: Photoelectron energy spectrum for the Gaussian model potential. The time propagation uses Arnoldi's propagator with fixed time step and the P-C method with adaptive time step. The parameters of the Gaussian model problem are as in figure 3.10. [29].

3.4.3 Hydrogen Atom

We now apply these methods to the more complex case of the interaction of the hydrogen atom with a cosine square laser pulse. We use a spectral method based on the expansion of the wave function in a basis of Coulomb Sturmian functions, without implementing the TSC method. Unless otherwise stated, we performed all calculations on a laptop (with an INTEL core 2 duo processor of 2.4 GHz). The first pulse we use has a frequency of 0.7 a.u., a duration of 10 optical cycles and

an intensity $I = 10^{14}$ W $\cdot$ cm^{-2}, as in the case of figure 3.8. In these rather simple conditions, we use 10 angular momenta partial waves. The non-linear parameter κ of the Coulomb Sturmian functions is taken equal to 0.3 a.u. Fatunla's and Arnoldi's algorithms produce the converged energy distribution as shown in figure 3.12 The calculations carried out with Fatunla's propagator and an adaptive time step take 10.50s of computer time. The integration performed with Arnoldi's method takes 13.72s. For a time step of $\delta t = 0.05$ a.u. and 100 Coulomb Sturmian functions per angular momentum, it needs only 5 Krylov vectors. In this case Arnoldi's method is slower than Fatunla's method, due to the number of basis functions we need to use. As this number increases, higher eigenvalues are generated in the Hamiltonian spectrum thereby increasing the stiff character of the system of equations to solve. In that case, more Krylov vectors have to be included to maintain the accuracy of the results.

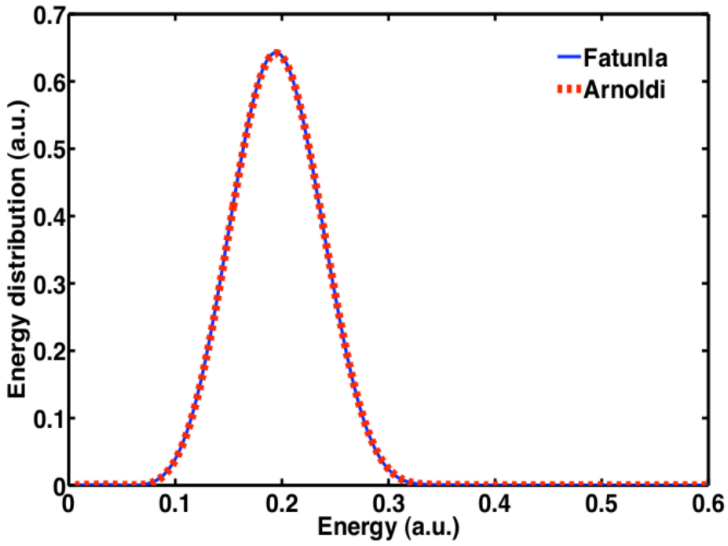

Figure 3.12: Photoelectron energy spectrum resulting from the interaction of the hydrogen atom with a cosine square pulse. Fatunla's and Arnoldi's propagators are used. The pulse has a frequency of $\omega = 0.7$ a.u. and intensity of $I = 10^{14}$ W $\cdot$ cm^{-2} for a duration of 10 optical cycles. The basis-set of functions used is a set of 100 Coulomb Sturmian functions per angular momentum function. Ten angular momenta are included and the non-linear parameter κ of the Coulomb Sturmian functions is equal to 0.3. The Arnoldi propagator uses 5 Krylov vectors and a time step of $\delta t = 0.05$ a.u.The relative difference between both curves is of the order of 10^{-3}. [29].

In figure 3.13 we illustrate the effect of reducing the number of Krylov vectors m from 5 to 4. It is surprising to see that the propagator gives a completely flat spectrum when the dimension of the Krylov space is insufficient. 3.13 shows that for a basis set of 100 Coulomb Sturmian functions per angular momentum, accurate results for the energy distribution require a minimum of 5 Krylov vectors.

These calculations performed in a Coulomb Sturmian basis can be further tested by varying their non-linear parameter κ. If instead of using $\kappa = 0.3$, we use $\kappa = 0.4$, all the other parameters remaining the same, we again obtain a completely flat energy distribution. By increasing the value of the non-linear parameter κ, the value of the eigenenergies increases thereby increasing the stiff character of the problem. To successfully reproduce an accurate energy distribution we now would need to increase the number of Krylov vectors. If on the other hand, we keep the value of κ equal to 0.3 and increase the number of basis functions, converged results are only obtained when 8 Krylov vectors are used. The increase in the number of Coulomb Sturmians generates higher eigenenergies thereby increasing again the stiffness of the system. The eigenvalues of the matrix $\mathbf{h}$ range from the eigenvalue of the initial state (by construction) to approximately the highest one of matrix $\mathbf{H}$. In summary, any change which results in a higher maximum eigenvalue for $\mathbf{H}$ necessitates an increase in the number of Krylov subspace vectors required for convergence.

In figure 3.14 we compare the performance of Arnoldi's and Fatunla's methods for a more difficult case. We consider a pulse of frequency $\omega = 0.114$ a.u. and a duration of 20 optical cycles. The pulse intensity is the same as before, $I = 10^{14}$ W $\cdot$ cm^{-2}. We use a basis set of 600 Coulomb Sturmian functions per angular momentum. 10 angular momenta are included in the calculations and the non-linear parameter $\kappa = 0.3$. Both energy distributions agree but Fatunla's scheme, which needs a very small time step, takes 66004s of computer time while Arnoldi's method takes 1419s with 25 Krylov vectors and a time step of 0.05 a.u. This case illustrates clearly that Arnoldi's algorithm copes in an efficient way with the stiffness of the problem by increasing the size of the Krylov subspace.

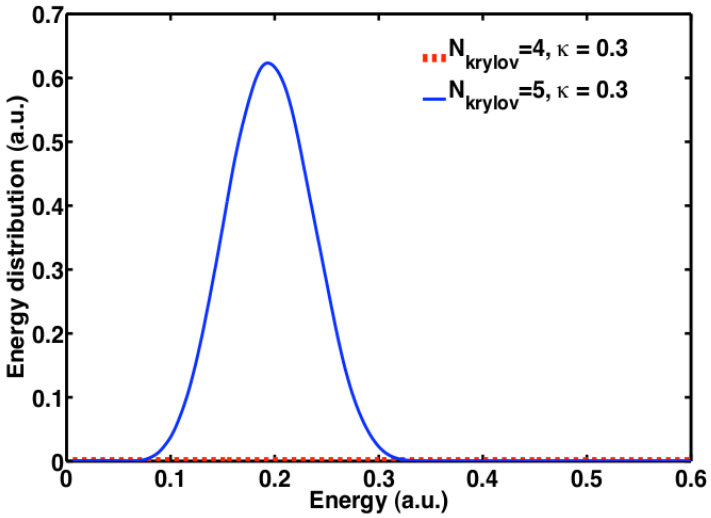

Figure 3.13: Photoelectron energy spectrum resulting from the interaction of the hydrogen atom with a cosine square pulse. Arnoldi's propagator is used. The pulse parameters are as in figure 3.12, using 100 Coulomb Sturmian functions per angular momentum. Ten angular momenta are included and the non-linear parameter κ of the Coulomb Sturmian functions is equal to 0.3. For a time step of $\delta t = 0.05$ a.u., we compare results when 5 and 4 Krylov vectors are used. [29].

In figure 3.15 we show results obtained for the challenging case of a pulse of very low frequency $\omega = 0.0228$ a.u. and a duration of 4 optical cycles for the same intensity as before. To reproduce the energy distribution we need to use 1200 Coulomb Sturmian functions per angular momentum. 80 angular momenta are included in the calculations and the non-linear parameter of the Coulomb Sturmian functions is equal to 0.3. For this rather stiff problem Arnoldi's algorithm has to include a minimum of 70 Krylov vectors for a time step $\delta t = 0.05$ a.u. The calculation takes around 24 hours on an 8 processor cluster using OpenMP parallelisation. The use of parallelisation in the coding means that the computation time needed to complete the time propagation is reduced significantly since each processor of the machine being used carries out calculations at the same time. Thus certain parts of the code can be completed 8 times quicker than standard coding. Fatunla's algorithm also reproduces the same energy distribution but the computer time used is more than four times larger. In fact, we observe that for larger scale problems where the degree of stiffness is important, Fatunla's method requires time steps that become

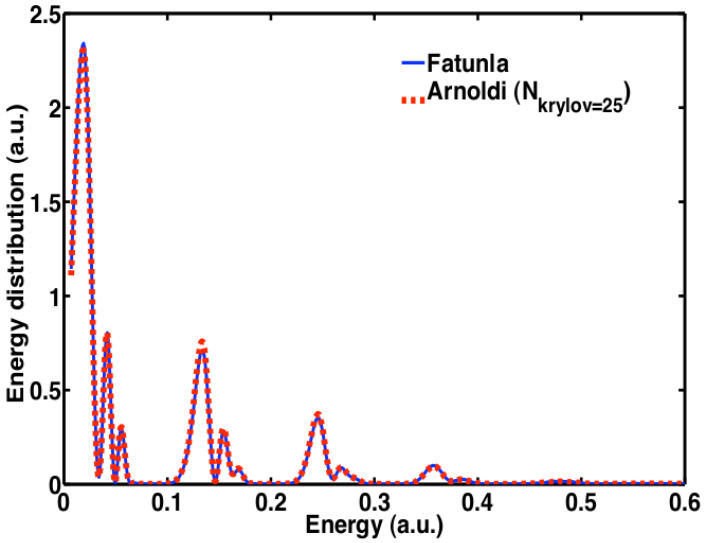

Figure 3.14: Photoelectron energy spectrum resulting from the interaction of the hydrogen atom with a cosine square pulse. Arnoldi's propagator is used. The pulse has a frequency of $\omega = 0.114$ a.u. and intensity of $I = 10^{14}$ W $\cdot$ cm^{-2} for a duration of 20 optical cycles. We use a set of 600 Coulomb Sturmian functions per angular momentum. Ten angular momenta are taken into account and the non-linear parameter of the Coulomb Sturmian functions $\kappa = 0.3$. The Arnoldi propagator uses 25 Krylov vectors and a time step of $\delta t = 0.05$ a.u. The relative difference between both curves is of the order of 10^{-3}. [29].

prohibitively small thereby increasing the computational time.

We can conclude that given the size of the system, in order to investigate low energies and frequencies, that the time propagator must be explicit. This means that it involves only matrix-vector products instead of solving large system of algebraic equations at each time step as is the case for implicit methods such as the RK. In addition, this propagator must have optimum stability and accuracy properties to cope with the stiffness of the system. Whilst both the Fatunla and Arnoldi methods share the same optimum stability properties we can see that their accuracy properties differ significantly in most of the problems we have looked at in this section. The accuracy of the method depends essentially on the stiffness of the system to solve which determines the appropriate choice of the propagator.

We have seen that the relative accuracy of Fatunla's method is always limited to about 10^{-6}. In some cases, this might be sufficient but we should not forget that

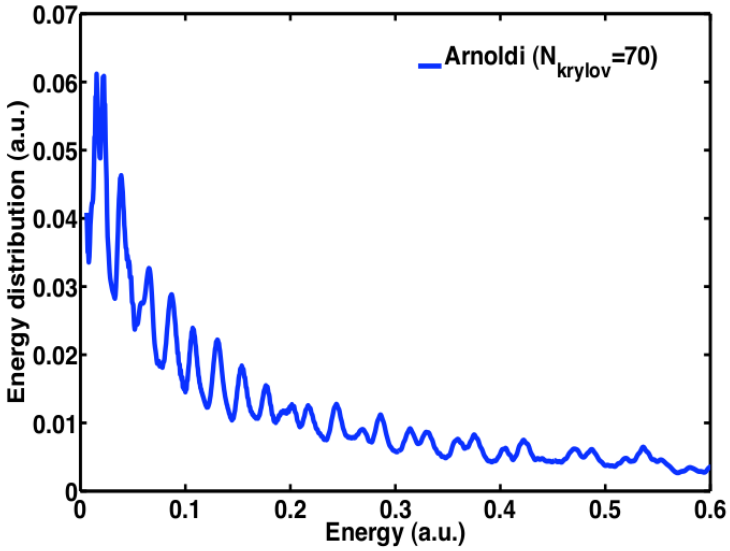

Figure 3.15: Photoelectron energy spectrum resulting from the interaction of the hydrogen atom with a cosine square pulse. Arnoldi's propagator is used. The pulse has a frequency of $\omega = 0.0228$ a.u. and intensity of $I = 10^{14}$ W $\cdot$ cm^{-2} for a duration of 4 optical cycles. The basis-set of functions used is a set of 1200 Coulomb Sturmian functions per angular momentum. 80 angular momenta are taken into account and the non-linear parameter κ of the Coulomb Sturmian functions is equal to 0.3. The Arnoldi propagator uses 70 Krylov vectors and a time step of $\delta t = 0.05$ a.u. [29].

when the degree of stiffness increases, the adaptive time step becomes excessively small making the method inapplicable. By contrast, highly accurate results are obtained with Arnoldi's algorithm in all cases we have looked at. However, for a given time step, there is a minimal number of Krylov vectors to take into account. If the actual number used is smaller than this minimal number, generally there is an abrupt transition and the results are wrong giving a flat or incorrect spectrum. On the other hand, when the degree of stiffness is high, this minimal number may become very large thereby imposing strong limitations on the applicability of the method. This is the case when the spacing in x between grid points becomes very small or, for spectral methods, when the size of the basis set is very large. In applying Arnoldi's scheme, it is therefore important to try to reduce the stiffness as much as possible. We have mentioned above that transformation to the atomic basis in which the Hamiltonian is diagonal and to eliminate the highest energy eigenvalues which, in principle do not play any physical role, can solve this problem. In that

case however, the AC Stark shift of the levels will not be evaluated accurately. In the coming chapters we use Arnoldi time propagation due to the nature of the laser parameters we will look at.

3.5 Exterior Complex Scaling

As previously mentioned, at high laser intensities and low frequencies, the ionised electrons can acquire high kinetic energies, and their quiver motion can become large. This implies that the electron will travel large radial distances and a dense set of basis functions will be needed to achieve accurate results. For this reason, absorbing potentials or mask functions can be incorporated near the end of a smaller grid in order to remove the probability flux that reaches the boundaries. In this way spurious reflections of the wave function on the box edge can be avoided. We look at exterior complex scaling (ECS) and in this method the wave packet is absorbed into the complex plane by rotation after a set distance from the origin.

There are many cases where we would like the interior of our calculations around the atom to remain unscaled. This allows us to calculate the correct eigenvalues and for them to remain real whilst still receiving the benefits of the scaling such as the dramatic reduction of computational space and time needed. This in turn allows much faster and larger calculations. Outside that region one must, by some means, truncate the solution without compromising the inner region. The ECS transformation achieves this by scaling the coordinates only outside a fixed radius x_0 in a way that leaves the inner region exact. The transformation in one dimension is defined as

$$x \to \begin{cases} -x_0 + (x + x_0)\mathrm{e}^{\mathrm{i}\theta}, & \text{for} \quad x < -x_0 \\ x, & \text{for} \quad |x| \leq x_0 \\ x_0 + (x - x_0)\mathrm{e}^{\mathrm{i}\theta}, & \text{for} \quad x > x_0. \end{cases} \tag{3.63}$$

This transformation alters the plane waves at values $x > x_0$ as

$$e^{\pm ipx} \rightarrow e^{\pm ipx_0} e^{\pm ip\ \cos(\theta)(x-x_0)} e^{\mp ip\ \sin(\theta)(x-x_0)}. \tag{3.64}$$

For positive momentum p, representing waves travelling to $+\infty$, the functions become exponentially damped with increasing distance whilst for negative momentum they grow exponentially. The corresponding situation with reversed signs arises for $x < -x_0$ and therefore we can distinguish incoming from outgoing waves simply by their normalisibility or remove the incoming wave completely [64].

This has the effect of creating two scaling regions which can be seen in figure 3.16. Once we achieve converged results our solution should not depend on θ in any way inside the radius $|x| < x_0$. This is because ECS provides the exact solution within the unscaled area whilst outside the scaled area the wave function will decay at a rate proportional to θ. The main idea of the ECS method is that for $\theta \neq 0$ we set boundary conditions that on the ECS contour the wave function will vanish as $x \rightarrow \infty$ effectively imposing outgoing scattering boundary conditions on the solution of the TDSE. For this reason the ECS method is useful in our situation of electron matter interaction in an intense laser field. The ECS method is a perfect absorber [64] due to the fact that the error, caused by parts of the wave packet travelling to the scaled region and then returning to the unscaled region, is negligible. It has a major advantage over other masking functions or boundary absorbers due to the fact that the wave packet is not lost when it reaches the boundary x_0 and ideally, it keeps a record of the dynamics in the outer region, which, in principle, could be recovered [64]. When the wave packet passes through the boundary and gets damped, if the laser field changes direction and part of the wave packet reenters the unscaled region it will still be completely accurate as long as the value of the edge of the complex grid x_{max} is large enough. This value is significantly smaller than what would be needed for a full unscaled calculation.

The ECS can be used in conjunction with the spectral representation of the wave function [49] and in all calculations with the ECS transformation we use the B-spline basis.

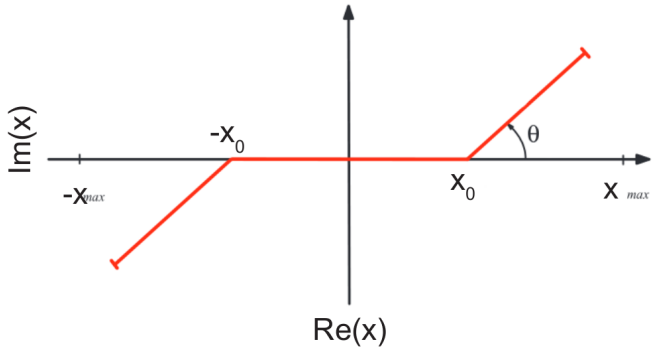

Figure 3.16: The complex contour x after the application of exterior complex scaling in one dimension with scaling radius x_0 and scaling angle θ.

One problem with introducing the ECS is the creation of a discontinuity of the B-splines at the point where the scaling starts. Therefore an important aspect of the method is to focus on this discontinuity at $x = x_0$. Here we need our wave packet to travel smoothly from the real interior of the contour to the complex exterior. The scaled wave function $\Psi(X(x))$ is always continuous but its derivative is discontinuous since

$$\frac{\mathrm{d}}{\mathrm{d}x}\Psi(X(x)) = \frac{\mathrm{d}X}{\mathrm{d}x}\Psi'(X(x)) = q(x)\Psi'(X(x)) \tag{3.65}$$

where $q(x)$ represents the complex contour $X(x)$ as

$$X(x) = \int_0^x q(x')\mathrm{d}x' \tag{3.66}$$

so that $\mathrm{d}X = q\mathrm{d}x$ and q satisfies

$$q(x) = \begin{cases} 1, & \text{for} \quad x \leq x_0 \\ \mathrm{e}^{\mathrm{i}\theta}, & \text{for} \quad x > x_0. \end{cases} \tag{3.67}$$

This Jacobian factor $q(x)$ is automatically included in the matrix calculations because the limits of the integrals are explicitly complex on the exterior part of the contour and is discontinuous at this boundary.

The B-splines of order k have continuous derivatives up to order $k-2$ and so in order to represent this new function with discontinuous derivatives we must define the B-splines as $B_i^k(X(x))$, that is put the breakpoints ξ and the knots t_j along the contour line and, most importantly, to place one of the breakpoints and corresponding knot on the discontinuity at $t_j = x_0$. Then $B_i^k(X(x))$ has a discontinuous first derivative with respect to x at $x = x_0$ because the derivative of $X(x)$ is discontinuous at that point. The i^{th} complex B-splines are now defined iteratively as

$$B_i^k(X(x)) = \frac{X(x) - t_i}{t_{i+k-1} - t_i} B_i^{k-1}(X(x)) + \frac{t_{i+k} - X(x)}{t_{i+k} - t_{i+1}} B_{i+1}^{k-1}(X(x)) \tag{3.68}$$

with

$$B_i^1(X(x)) = \begin{cases} 1 & \text{if } \; t_i \leq X(x) \leq t_{i+1} \\ 0 & \text{otherwise} \end{cases} \tag{3.69}$$

where t_i are now the complex knots that follow the exterior complex scaling contour. Figure 3.17 shows the B-splines of order $k = 8$ for; a) the real B-splines defined in section 3.2.2 and b) the complex B-splines defined in equation (3.68) for parameters $x_0 = 20$ and $\theta = 0.5$ rad. We see in b) that either the real or imaginary part of the B-splines show a discontinuous slope and so the derivatives are discontinuous. Furthermore we note with interest that it is only the B-splines that straddle the discontinuity point R_0 that have non zero imaginary part. Due to the definition of the B-splines, any splines that do not touch R_0 are real even if they lie entirely on the complex part of the contour.

The matrix elements of the operators that need to be calculated to construct the matrix TDSE are now defined as the sums of the corresponding integrals between complex breakpoints, giving

$$[\mathbf{H}_0]_{ij} = \sum_l -\frac{1}{2} \int_{\xi_l}^{\xi_{l+1}} B_i(x) \frac{d^2}{dx^2} B_j(x) \mathrm{d}x + \int_{\xi_l}^{\xi_{l+1}} B_i(x) V(x) B_j(x) \mathrm{d}x, \tag{3.70}$$

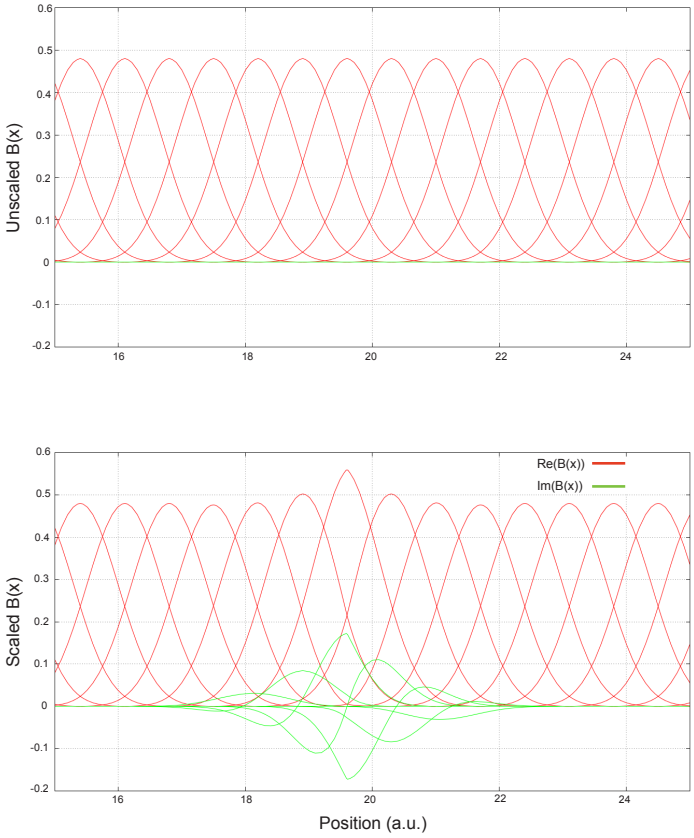

Figure 3.17: B-splines of order $k = 8$. Top: On the conventional real line. Bottom: On the complex exterior scaling contour with $x_0 = 20$, $\theta = 0.5$ rad. The red lines are the real parts of the complex B-splines and the green lines are the imaginary parts.

$$[\mathbf{H}_\mathrm{I}]_{ij} = \begin{cases} \sum_l -\mathrm{i}A(t) \int_{\xi_l}^{\xi_{l+1}} B_i(x) \frac{d}{dx} B_j(x) \mathrm{d}x & \text{(VG)} \\ \sum_l E(t) \int_{\xi_l}^{\xi_{l+1}} B_i(x) x B_j(x) \mathrm{d}x & \text{(LG)}, \end{cases} \tag{3.71}$$

and

$$[\mathbf{S}]_{ij} = \sum_l \int_{\xi_l}^{\xi_{l+1}} B_i(x) B_j(x) \mathrm{d}x, \tag{3.72}$$

where $\xi_1 = X(-x_{max})$ and $\xi_N = X(x_{max})$ are the boundaries of the exterior complex scaling contour. We again perform these integrals using the Gauss-Legendre quadrature previously used to calculate the Hamiltonian matrices. Each integral calculated is on a straight line for which either end may be real or complex.

The rotation of the Hamiltonian significantly affects the eigenvalues obtained when solving the TISE. With a non rotated Hamiltonian we get a set of real eigenvalues E_i representing bound $E_i < 0$ and continuum $E_i > 0$ states. With a rotated Hamiltonian, with the value of x_0 picked so its sits outside the size of the bound states, the continuous spectrum is rotated into the complex plane at an angle of -2θ. We can see this in figure 3.18 for a model 1D potential and scaling parameters of $\theta = 0.5$ rad and $x_0 = 20$ a.u.

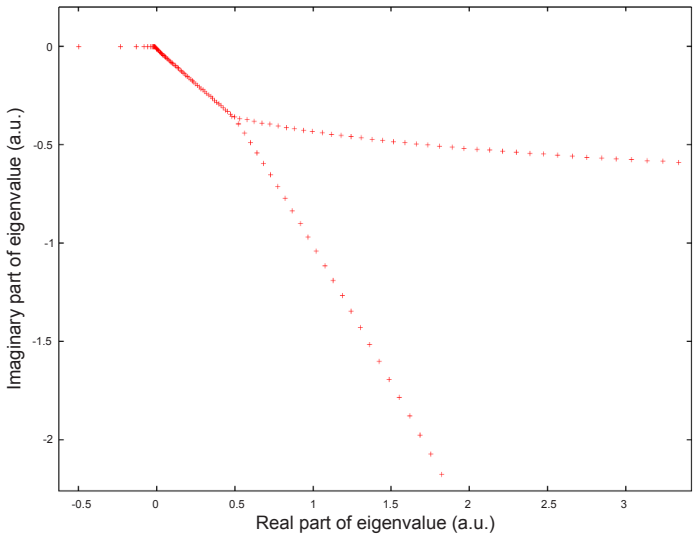

Figure 3.18: Real and imaginary parts of the eigenvalues for the soft Coulomb potential for a value $\theta = 0.5$ rad and $x_0 = 20$ a.u. The analytic continuation of the spectrum into the complex plane is shown.

We also see a bifurcation of the spectrum and the single, discretised, continuum divides into two branches and increasing the number of B-splines causes the angle of the bifurcation to reduce. This can be seen in figure 3.19 for scaling parameters $\theta = 0.3$ rad and $x_0 = 20$ a.u. In each case we achieved identical results after time propagation regardless of the numbers of B-splines.

In our calculations, in order to optimise time and storage constraints we implement a method which splits our box defined in section 3.2.2 into three sections. This takes advantage of the fact that in the complex scaled region where the wave function is damped requires fewer B-splines to represent the wave function. By lowering the

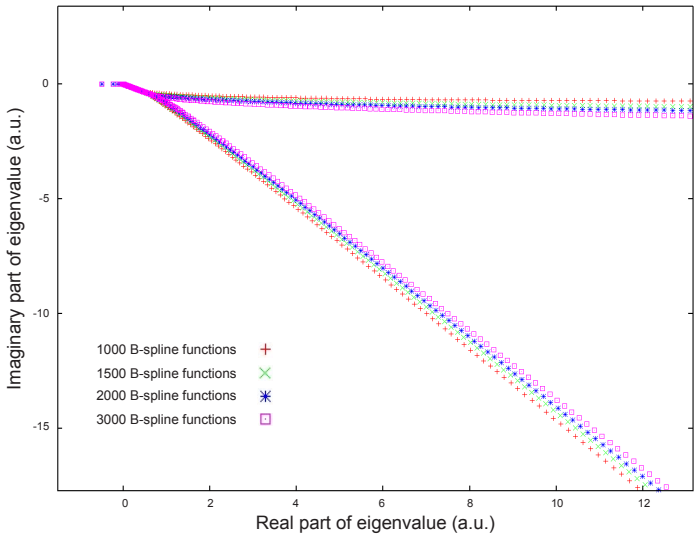

Figure 3.19: Real and imaginary parts of the eigenvalues for the soft Coulomb potential for a value $\theta = 0.3$ rad and $x_0 = 20$ a.u. The bifurcation is shown to slowly close as more B-spline functions are added. The number of B-splines used are 1000 (red), 1500 (blue), 2000 (green) and 3000 (pink).

total number of B-splines in the complex region we can get converged solutions without using an unnecessary number of functions. To do this we define a point on the contour x_1 such that $x_1 > x_0$ and $-x_1 < -x_0$ where the new B-spline mesh begins. This can be seen clearly in figure 3.20 where we have the box parameters $x_0 = 20$ a.u., $x_1 = 35$ a.u. and $x_{max} = 200$ a.u. In the region $|x| < x_1$ we use a density of around 1.4 B-Splines per a.u. of distance whereas outside x_1 we use a density of 0.15 B-Splines. As such we reduce the stiffness of the system of equations by lowering the value of the highest eigenvalue. This in turn then allows us to use a smaller basis set which then reduces the computational time needed.

One interesting result of the implementation of the ECS is that the norm of the system will rise above unity at times corresponding to the bursts of ionisation around the times of the peaks of the electric field. At the end of the pulse, if convergence is achieved, then the norm will drop below unity and then subtracting the norm from unity at the end of the pulse will result in the ionisation probability. The behaviour of the norm can be seen in figure 3.21 for a 2 cycle pulse for uniform complex scaling ($x_0 = 0$) and ECS with $x_0 = 40$ and $\theta = 0.5$. At the end of the calculation both

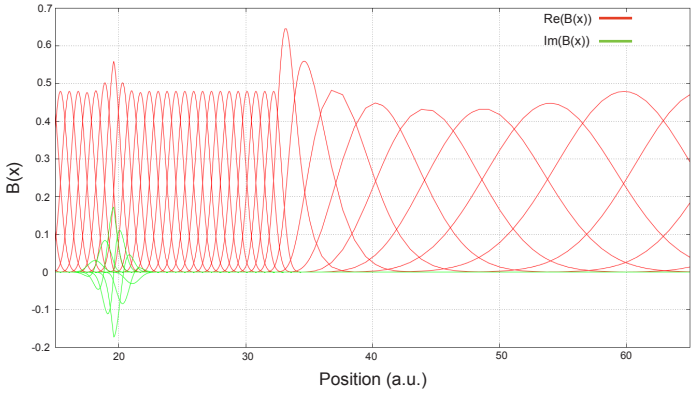

Figure 3.20: B-splines of order $k = 8$ for box parameters of $x_0 = 20$ a.u., $x_1 = 35$ a.u., $x_{max} = 200$ a.u. and $\theta = 0.5$ rad. For $|x| < x_1$ 100 B-splines are used whereas in the much larger distances $x_1 < x < x_{max}$ and $-x_{max} < x < -x_1$ just 25 B-splines are used in each.

gave the correct ionisation probability.

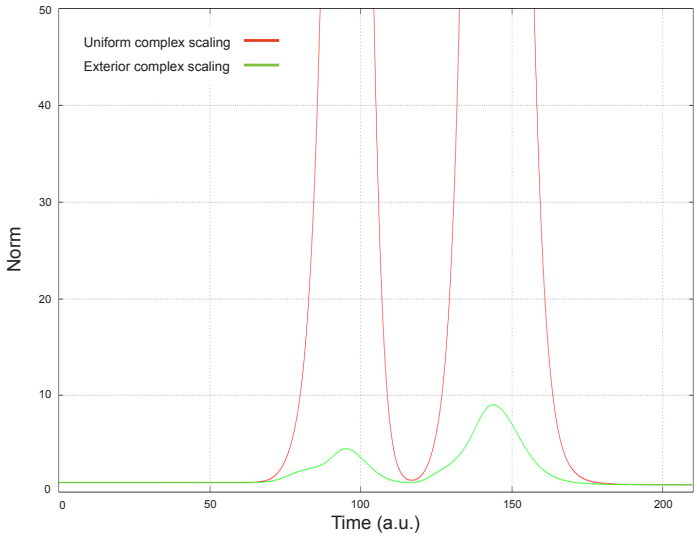

Figure 3.21: The norm of the system for a laser pulse of wavelength $\lambda = 800$nm and intensity $I = 10^{14}$ W $\cdot$ cm^{-2} for 2 optical cycles for uniform complex scaling (red) and ECS with $x_0 = 40$ and $\theta = 0.5$ rad. (green).

In order to implement the ECS method we must make alterations to our time propagation system. For ECS we use the Arnoldi algorithm and the rotation of our Hamiltonian means that the matrices we use to solve the system of equations given by (3.28) now become complex. Since our Arnoldi algorithm was set up for Her-

mitian matrices we must modify it to accommodate our new complex symmetric matrices.

In three dimensions we must use larger basis sets and in general calculations take much longer making the ECS an even more powerful tool. We can extend the ECS method to three dimensions by carrying out the transformation

$$r \to \begin{cases} r, & \text{for} \quad r \leq R_0 \\ R_0 + (r - R_0)\mathrm{e}^{\mathrm{i}\theta}, & \text{for} \quad r > R_0 \end{cases} \tag{3.73}$$

where r is the radial distance from the origin and R_0 and θ are the scaling radius and angle respectively. The method can be adapted from the one dimensional case above and in calculations we now use a grid split into two sections instead of three since there is now just one scaling area. The computational benefits of implementation of the ECS in both one and three dimensions will be seen in later chapters.

Chapter 4

One Dimensional Results

4.1 Introduction

In this chapter we show the results obtained from calculations carried out in one dimension using the numerical methods discussed in chapter 3. In order to probe the dynamics of the electrons we will explore a number of observables in various parameter spaces in one dimension. In one dimension the calculations are less intensive and computationally challenging than in 3D and as such we can look at a wider variety of parameters than we can in three dimensions. In addition we can perform both length and velocity gauge calculations to check convergence at low frequencies. We are interested in obtaining reliable methods to solve the TDSE and to interpret the results. We first look at the case of wavelength $\lambda = 800$nm, corresponding to a frequency of $\omega = 0.0569$ a.u. which models a typical Ti:Sapphire laser used frequently in strong field experimental physics. We then move on to look at the more challenging case of wavelength $\lambda = 2\mu$m corresponding to a frequency of $\omega = 0.0228$ a.u. At this very low frequency, even for short pulses the electron can travel great distances. For example, for a single cycle pulse of a moderate intensity of $I = 10^{14}$ W $\cdot$ cm^{-2} the electron can travel as far as $x = (\tau/2)\sqrt{2E_{\max}} = (\pi/\omega)\sqrt{2 \times 10U_p} \simeq 510.5$ a.u. where τ is the pulse length. This is calculated using the assumption that the electron will be released just before the middle of the pulse and will reach the maximal kinetic energy. This in turn will also give us a converged spectrum up to $E = 10U_p$. In order to represent the wave functions $\Psi(x,t)$ in a box of this size, many basis functions must be used, computational calculations can take a long time and storage requirements are large. Such numerical calculations need to be performed on com-

puters with large amounts of RAM for the storage requirement and a large number of high speed processors for the time requirement.

We calculate a number of physical observables in both the length and velocity gauge using the methods described in chapter 3. For all calculations, unless otherwise stated, we use an atomic basis by expanding initially in a B-spline basis to represent the wave function and use Arnoldi time propagation on a laptop (with an INTEL core 2 duo processor of 2.4 GHz) for the higher frequencies and formulate the TDSE in the velocity gauge.

In one dimension, along the x direction, we solve the time dependent Schrödinger equation (TDSE) in the dipole approximation, in the length gauge (LG), for an atom in a laser pulse with electric field $E(t)$, as

$$\mathrm{i}\frac{\partial}{\partial t}\Psi^L(x,t) = \left[-\frac{1}{2}\frac{\partial}{\partial x} + V(x) + xE(t)\right]\Psi^L(x,t), \tag{4.1}$$

where $V(x)$ is the atomic potential and $\Psi^L(x,t)$ is the wave function solution of the LG equation. In the velocity gauge (VG) the TDSE assumes the form

$$\mathrm{i}\frac{\partial}{\partial t}\Psi^V(x,t) = \left[-\frac{1}{2}\frac{\partial}{\partial x} + V(x) - \mathrm{i}A(t)\frac{\partial}{\partial x}\right]\Psi^V(x,t), \tag{4.2}$$

where $A(t)$ is the vector potential associated with the electric field $E(t)$ and $\Psi^V(x,t)$ is the wave function solution of the VG equation.

In all calculations, unless otherwise stated, we use an electric field represented by a vector potential of the form

$$A(t) = \begin{cases} A_0 f(t)\sin(\omega t + \varphi) & \text{if } \ 0 \le t \le \tau \\ 0 & \text{otherwise,} \end{cases} \tag{4.3}$$

where $f(t)$ here is the pulse envelope given by

$$f(t) = \sin^2\left(\frac{\pi t}{\tau}\right). \tag{4.4}$$

The $\sin^2$ pulse here is equivalent to the $\cos^2$ pulse used in the chapter 3 with the origin of time shifted by $\tau/2$. Here $\tau = 2\pi n_c/\omega$ is the total pulse length of n_c optical

cycles and φ is the carrier envelope phase which we take as zero unless otherwise stated. The peak amplitude A_0 in atomic units is related to the intensity in watts per centimetre squared by the equation $A_0 = 5.3378 \times 10^{-9}\sqrt{I}/\omega$. In all cases we choose the ground state as the initial target state.

Figure 4.1 shows the vector potential $A(t)$ (red line) and the corresponding electric field $E(t) = -\partial_t A(t)$ (green line) plotted over time for the intensity $I = 10^{14}$ W $\cdot$ cm^{-2} for $n_c = 2$ optical cycles. The electric field has been multiplied by a factor of 15 so it can easily been shown on the same scale.

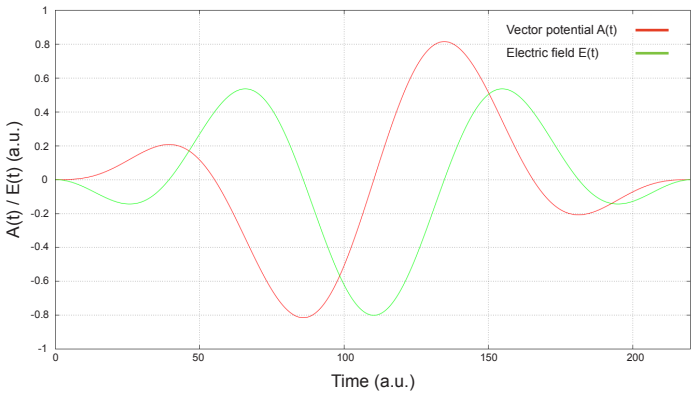

Figure 4.1: The vector potential given by equation (4.3) and the corresponding electric field $E(t)$, multiplied by a factor of 15, for a frequency of $\omega = 0.0569$ a.u. an intensity of $I = 10^{14}$ W $\cdot$ cm^{-2} and a phase $\varphi = 0$ for a duration 2 optical cycles.

4.2 The Potential Function

In order to model a single electron atom in one dimension we choose a suitable potential function $V(x)$ such that it mimics the behaviour of the atom, in particular at medium to large distances from the nucleus. We mainly use the soft Coulomb potential of the form [33]

$$V(x) = -\frac{Z}{\sqrt{x^2 + \alpha}}, \tag{4.5}$$

where Z is the nuclear charge and α is a smoothing parameter. These can be adjusted in order to accurately mimic different atomic species by obtaining the correct energy

eigenvalues for the ground state. The soft Coulomb potential is shown in figure 4.2 for $\alpha = 1$ (red line), $\alpha = 2$ (blue line) and $\alpha = 5$ (green line).

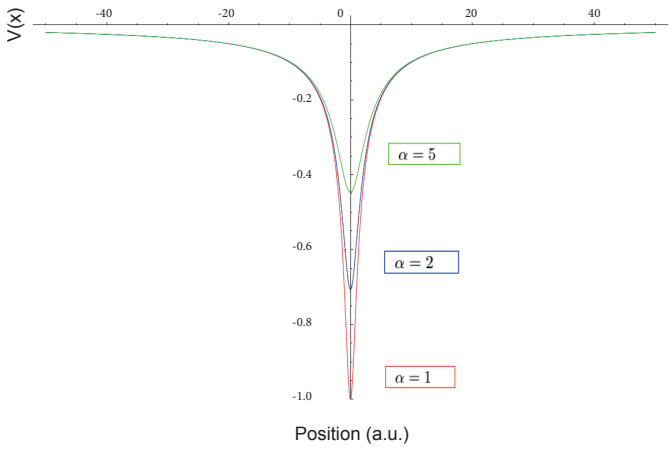

Figure 4.2: The soft Coulomb potential for $\alpha = 1$ (red), 2 (blue) and 5 (green).

Asymptotically this potential mimics the Coulomb potential ($\alpha = 0$) behaviour whilst avoiding the singularity at the origin which would lead to numerical difficulties. By using this softened potential, the motion becomes continuous across $x = 0$ and we still keep one important feature of the Coulomb potential, the Rydberg series of the bound states.

We take the smoothing parameter in all calculations here to be $\alpha = 2$ which gives a ground state energy eigenvalue of $E = -0.5$ a.u. equal to that found in Hydrogen. Increasing α would decrease the depth of the potential well and increases the ionisation potential of the model atom.

4.3 Ionisation by an 800nm Wavelength Laser

At the end of our calculation, once the laser pulse has been switched off, or even throughout the time propagation, we can extract information from the wave function of the system. If convergence is achieved, i.e. we use a box size which is big enough to contain the wave packet, that we use enough basis functions to represent

the wave packet at all time in the calculations and that our time propagator is suited so that an acceptable level accuracy is obtained throughout the calculation, then our wave function will be exact to computational accuracy. We can then use this wave function in order to look at a number of different aspects of the electron behaviour in the system. We look now at a number of these observables for a laser of wavelength $\lambda = 800$nm including probability densities in position and momentum space, ionisation probability and the energy spectrum of the model atom. On investigating these we hope to understand the excitation and ionisation of the model atom, seeing how the various parameters of the intense laser field affect the evolution of the ionised electron, and finally to evolve the numerical methods used here to probe the Hydrogen atom in a full three dimensional calculation at low frequencies.

4.3.1 Electron Density

The first property we look at is the electron probability density distribution. This is a representation of the probability of finding the electron at a certain position in the box we have defined. During the propagation the wave function, which is originally confined to the centre of the box, slowly spreads outwards as the electron gains enough energy to be ionised. Around the origin the ionised electron will be influenced by both the 'atomic' potential and electric field but as it moves away the electric field of the laser then dominates. The probability density can be easily calculated at the end of the pulse, $t = \tau$, and is given by

$$P_\Psi(x) = |\Psi(x, \tau)|^2. \tag{4.6}$$

The electron probability density as a function of position x is shown in figure 4.3 for varying levels of intensity for the three intensities $I = 10^{14}$ (red line), 3×10^{14} (green line) and 5×10^{14} W $\cdot$ cm^{-2} (blue line). We can see that as the intensity increases the probability of finding the electron in the ground state ($x \approx 0$) at the end of the pulse decreases and the spread of the wave packet can be seen to increase. For the

lowest intensity the electron travels around 200 a.u. in the positive x direction and 120 in the negative x direction. For the largest intensity the electron is carried as far as 360 a.u. and 200 a.u. in the positive and negative directions respectively since a higher laser intensity means that the electron absorbs more photons and acquires a higher kinetic energy. Once ionised, the electron then has a higher velocity and can travel further in the time τ. An interesting feature is the appearance of many small oscillations on the far left of the picture which become more prominent with intensity. This is due to interference between wave packets which have been ionised at different times. This effect occurs due to bursts of ionsation during different half cycles of the laser pulse interfering with each other and will be investigated in more detail further on in this chapter as well as the next.

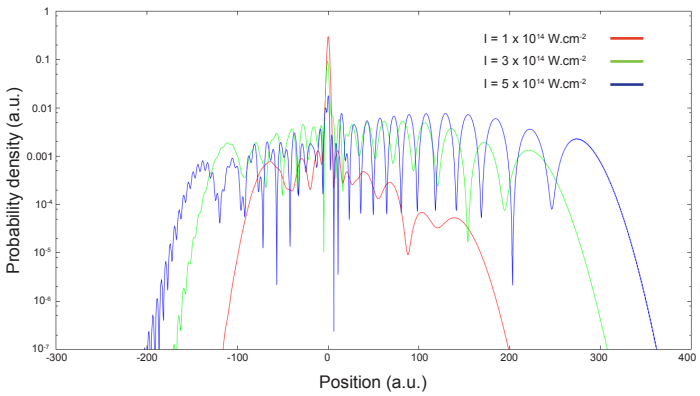

Figure 4.3: The electron probability density on a logarithmic scale at the end of the 2 cycle pulse of frequency $\omega = 0.0569$ a.u. and intensity $I = 10^{14}$ (red), 3×10^{14} (green) and 5×10^{14} W $\cdot$ cm^{-2} (blue) for a vector potential of the form (4.3).

Here we use a time step of $\delta t = 0.2$ a.u. for all calculations. For $I = 10^{14}$ W $\cdot$ cm^{-2} we use a box of $[-400, 400]$ a.u. and 700 'atomic' states with 5 Krylov vectors. Here we cut the atomic states corresponding to the highest eigenvalues from the calculation. Originally 800 B-spline functions were used but after cutting all atomic states with an eigenvalue greater than a cut-off value of $E = 10$ a.u. we reduced the basis size by 100 functions. The cut-off was picked according to the maximum energy of electron we wanted to plot in the ATI spectrum. For the rest of the

thesis when we refer to the number of basis functions used we will give the number used in the time propagation after the cut. For $I = 3 \times 10^{14}$ W $\cdot$ cm^{-2} we extend the box to $[-450, 450]$ a.u. with 800 states and 10 Krylov vectors, whilst for the highest intensity, $I = 5 \times 10^{14}$ W $\cdot$ cm^{-2}, we must use a box of $[-600, 600]$ a.u. with 1400 functions with 20 Krylov vectors. The calculations took 42s, 90s and 310s respectively. The larger box is due to the increase in U_p and therefore the maximum obtainable energy for the electron whilst more B-spline functions are needed to represent the wave function in the bigger area. The increase in the number of Krylov vectors is due to the increase in the number of B-splines which raises the stiffness of the system. To compare computation times for different sizes of Krylov space for $I = 10^{14}$ W $\cdot$ cm^{-2}, we lowered the size of the subspace until the results were no longer converged. 20 Krylov vectors took 100s using 2 processors, 10 Krylov vectors took 61s, 6 Krylov took 45s to run. Using 4 Krylov vectors took 38s to run although slight changes appeared where the probability was very low whilst 3 Krylov vectors caused the density to change significantly. These probability density plots against position x can be seen in figure 4.4.

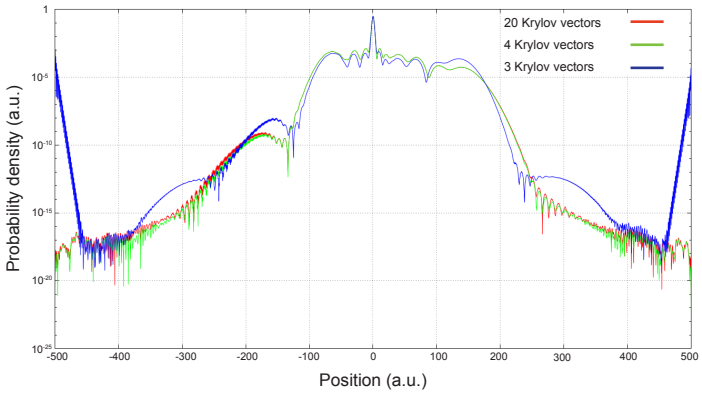

Figure 4.4: The electron probability density at the end of the 2 cycle pulse of frequency $\omega = 0.0569$ a.u. and intensity $I = 10^{14}$ W $\cdot$ cm^{-2} for a vector potential given by equation (4.3). In the Arnoldi time propagation routine the number of Krylov vectors used were 20 (red), 4 (green) or 3 (blue).

The ponderomotive potential and Keldysh parameter for each of these cases, given by equations (2.61) and (2.75) respectively, are: for $I = 10^{14}$ W $\cdot$ cm^{-2}, $U_p = 5.98$

eV = 0.22 a.u. and $\gamma = 1.067$; for $I = 3 \times 10^{14}$ W $\cdot$ cm^{-2}, $U_p = 17.93$ eV = 0.66 a.u. and $\gamma = 0.616$ and finally for $I = 5 \times 10^{14}$ W $\cdot$ cm^{-2}, $U_p = 29.88$ eV =1.10 a.u. and $\gamma = 0.477$. Another important parameter here is the quiver radius which is $\alpha = 16.49$, 28.55 and 36.87 a.u. respectively for each intensity. We can see then for these parameters, for all intensities, the Keldysh parameter does not fall into either category defined in section 2.6.5 and hence we have a mixture of multiphoton and tunnel ionisation.

Since most of the probability of finding the electron remains in the bound states for low frequencies due to the low photon energy it can often distort our plot of the electron probability density. In order to show results more clearly, instead of summing over all states like in equation (4.6), we can sum over just the continuum states when reconstructing the wave packet, thus removing the majority of the density which resides in the bound states. We then have

$$P^c_\Psi(x) = |\Psi^c(x,\tau)|^2 = |\sum_{i=n_b+1}^{N} a_i(t)\psi_i(x)|^2 \tag{4.7}$$

where ψ_i are basis functions and n_b is the number of bound states which can be found in solution of the TISE by counting the number of eigenvalues with energy $E_i < 0$. Figure 4.5 shows the electron probability density for $I = 3 \times 10^{14}$ W $\cdot$ cm^{-2} along with its continuum probability density counterpart against position x. The peak of the bound states rises over hundred times the size of this plot and hence by looking at just the continuum picture we can look more closely at its behaviour without resorting to logarithmic scales. We can see that as we approach the area surrounding the origin, the continuum density drops off to zero.

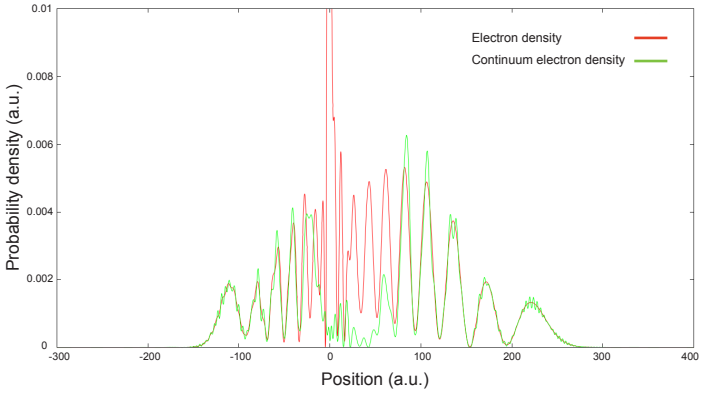

Figure 4.5: The electron probability density (red) and continuum electron probability density (green) on a linear scale at the end of the 2 cycle pulse of frequency $\omega = 0.0569$ a.u. and intensity $I = 3 \times 10^{14}$ for a vector potential given by equation (4.3).

4.3.2 State Populations

We now investigate a different form of laser pulse, in order to match the form chosen by Gräfe et al. [31] and allow for comparison of results. These calculations are carried out in the length gauge since the populations are not gauge invariant. We now use a cosine electric field with Gaussian envelope, given by

$$E(t) = \begin{cases} E_0 \ \exp(\frac{-t^2}{2\sigma^2}) \cos(\omega t) & \text{if} \quad t \leq |\frac{\tau}{2}| \\ 0 \quad \text{otherwise} \end{cases} \tag{4.8}$$

where the parameter $\sigma = 102.3$ here is linked to the full width at half maximum (FWHM) of the pulse envelope and the amplitude of the electric field is given by $E_0 = 0.06$ a.u. corresponding to a laser intensity of $I = 1.6 \times 10^{14} \mathrm{W} \cdot \mathrm{cm}^{-2}$. This gives a Keldysh parameter value of $\gamma = 0.95$ meaning we again sit in the transition between ionisation regime. The field strength and number of cycles are chosen such that population transfer and ionisation occur without fully depleting the atom. The electric field plotted against time t can be seen in figure 4.8 and the pulse runs from -10 femtoseconds (fs) to $+10$fs giving $\tau = 20\text{fs} \approx 826.8$ a.u. Here due to the increase in pulse length we use a box of $[-1200, 1200]$ a.u. and 1800 B-splines which is large

due to the fact we are using the length gauge. For the time propagation we took a time step of $\delta t = 0.2$ a.u. and 10 Krylov vectors. Calculations here took around 25 minutes.

Another issue of interest that we will now look at is the evolution of the populations of the bound states as well as the probability of ionisation. Rather than waiting until the end of the pulse to analyse the wave function we now calculate these at each time step during the propagation. As such we can see clearly how they evolve as the electric field changes in strength and direction. They are calculated by projecting the wave function onto the necessary states at each time step. For example, the ground state probability would be given in the atomic basis by

$$P_1(t) = |\langle \varphi_1(t), \Psi(t) \rangle|^2 = |a_1(t)|^2. \tag{4.9}$$

The ionisation probability can then be calculated as

$$P^{ion}(t) = 1 - \sum_{i=1}^{n_b} |\langle \varphi_i(t), \Psi(t) \rangle|^2 = 1 - \sum_{i=1}^{n_b} |a_i(t)|^2. \tag{4.10}$$

In figure 4.6 we show the populations of the ground (red line) and first excited state (green line) as well as the the ionisation probability (blue line) against time t throughout the pulse. Also shown is the electric field on an arbitrary scale. We can see that the electron begins in the ground state at $t = -\tau/2$ and over time fluctuates with the amplitude of the electric field until eventually reaching a plateau around 0.8 when the electric field reaches a zero value. We can also see probability of the electron being in the first excited state similarly oscillates with the field whilst the ionisation probability continues to rise throughout the pulse. The times of sharp rises in the ionisation probability directly correspond to maxima and minima of the electric field where most ionisation is expected to take place. The largest rise in ionisation probability occurs at $t \simeq 0$ when the electric field reaches its peak value of $E_0 = 0.06$. At the same time we also see a sharp decrease in the ground state population and a slight rise in the population of the first excited state. This is what we would expect since there will be an exchange of electrons between bound states

and also the bound states and the continuum whilst the field accelerates ionised atoms back towards the parent atom. Clearly, altering the field strength would have a large effect on the states. Increasing the strength would cause the bound states to diminish faster and further and as such the ionisation probability would rise quicker, whilst making it lower would result in very little population transfer or ionisation. A high frequency is more likely to directly ionise the electron whereas a low frequency gives rises to more bound state population exchange.

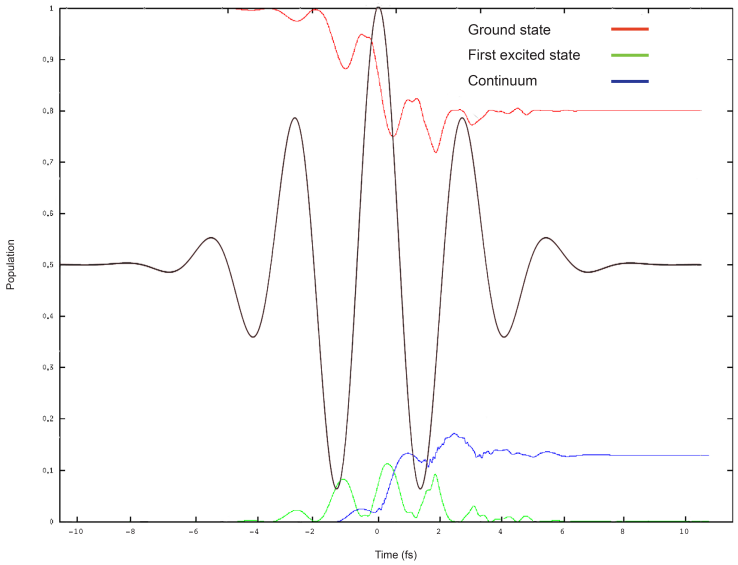

Figure 4.6: The ground state (red), first excited state (green) and continuum populations (blue) throughout a pulse of duration 20fs given by equation (4.8) of frequency $\omega = 0.0569$ a.u. and intensity $I = 1.6 \times 10^{14}\text{W} \cdot \text{cm}^{-2}$. Also plotted is the electric field $E(t)$ on an arbitrary scale.

We note that when observables are calculated during the pulse, they can be dependent on the gauge use. Whilst the phase attached to the wave function during the transformation is cancelled out in calculations of the electron density since we take the absolute value of the wave function, the populations of the different states will only equate in different gauges at times t when $A(t) = 0$. Figure 4.7 shows the ground state population against time t in both the length gauge (red line) and the velocity gauge (green line). We can see that the differences between the gauges are quite considerable throughout the pulse and we note that the difference between the gauges is largest when the electric field is approximately zero. This corresponds to a

shifted peak or trough of the vector potential. When the vector potential $A(t) = 0$ the gauges coincide and take equal value.

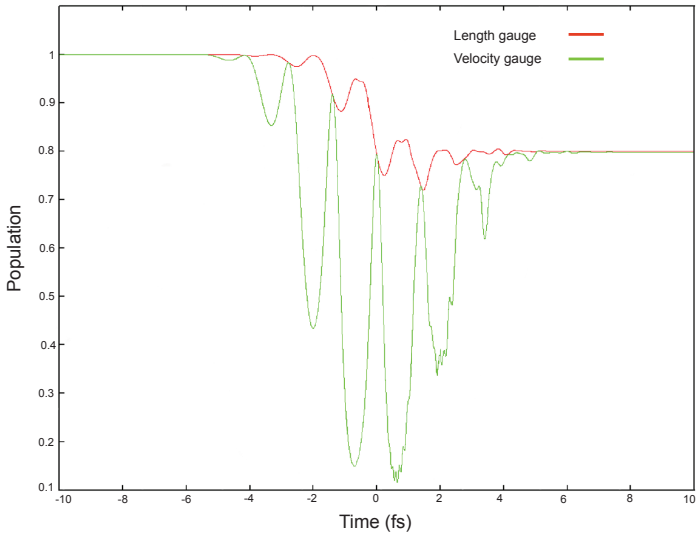

Figure 4.7: The ground state population in both the length gauge (red) and velocity gauge (green) throughout a pulse of duration 20fs given by equation (4.8) of frequency $\omega = 0.0569$ a.u. and intensity $I = 1.6 \times 10^{14}\text{W} \cdot \text{cm}^{-2}$.

4.3.3 Snapshots and Momentum Density

To investigate in more detail how the electric field affects the motion and dynamics of the electron during the time the laser field is on we calculate the electron probability density at different times as the electric field changes accordingly. We examine both the full and continuum wave packets in coordinate space $|\Psi(x,t)|^2$ and then compare its behaviour with the electron density in momentum space $|\Psi(p,t)|^2$ [31] for a pulse given by equation (4.8). The red circles in figure 4.8, which shows the electric field against time t mark the times of the snapshots we plot the electron densities. The calculation now runs from -5 femtoseconds (fs) to $+5$fs giving $\tau = 10\text{fs} \approx 413.4$ a.u. As such, the box size used was $[-600, 600]$ a.u. with 1200 B-splines in the LG and 800 in the VG. In both calculations we took $\delta t = 0.2$ and used 20 Krylov vectors and the run time was 12 min for the LG and 6 min in the VG.

We can see here clearly how the electric field directly affects the electron density

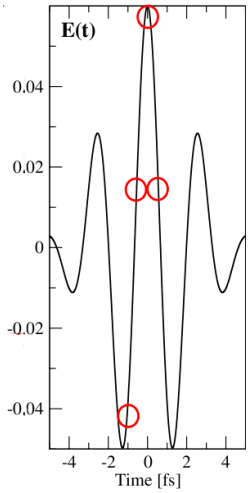

Figure 4.8: The electric field $E(t)$ of duration 20fs given by equation (4.8) of frequency $\omega = 0.0569$ a.u. and intensity $I = 1.6 \times 10^{14}\mathrm{W} \cdot \mathrm{cm}^{-2}$. The red circles mark the times of the snapshots. [31].

during the pulse cycle. The continuum portion of the wave packet makes up around 18% of the full density at the end of the cycle as seen in figure 4.6, which shows the probability density $|\Psi(x,t)|^2$ and continuum probability density $|\Psi^c(x,t)|^2$ against position x at times shown in figure 4.8. The continuum wave packet is generated mostly by three ionisation bursts near the extremes of the field at -1.2 fs, 0 fs and +1.4 fs and some portions of the continuum wave packet created at point of maximum field strength (0 fs) can be seen to be moving to very high values of x. The first ionisation burst at -1.2 fs is followed by a half cycle with maximum field strength and this leads to almost the entire ionised wave packet returning to the vicinity of the atom, whilst although the second burst at 0 fs is stronger, the subsequent half cycle following the burst is weaker and as such the high momentum components leave the vicinity of the atom and only the slower components return to the atom.

In order to analyse the momentum picture we use a Fourier transform to convert the wave function to momentum space, which takes the form

$$\Phi(p,t) = \frac{1}{\sqrt{2\pi}} \int_{-\infty}^{+\infty} \Psi(x,t) \mathrm{e}^{-\mathrm{i}px} \mathrm{d}x. \tag{4.11}$$

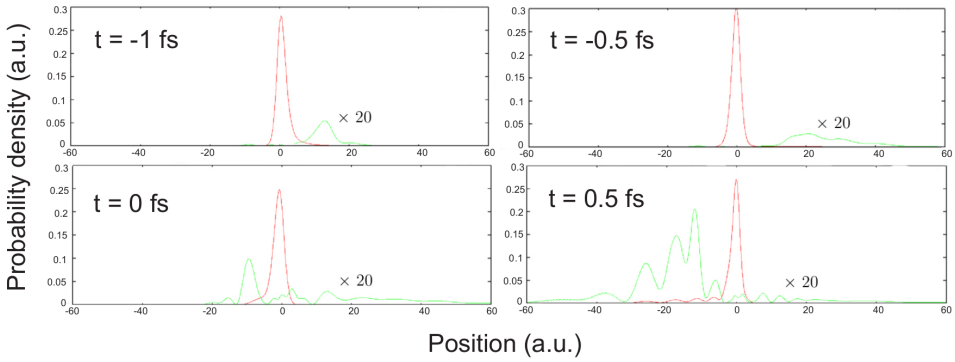

Figure 4.9: The electron probability density $|\Psi(x,t)|^2$ (red) and continuum electron probability density $|\Psi^c(x,t)|^2$ (green) for the electric field with parameters given in figure 4.8 and at times marked by the red circles.

In order to evaluate this integral we use the calculated wave function $\Psi(x,t)$ for each time t in coordinate space expressed in terms of B-splines and use a Gaussian quadrature method. In figure 4.10 we show the electron probability density $|\Psi(p,t)|^2$ and the continuum electron probability density $|\Psi^c(p,t)|^2$ in momentum space at times marked on figure 4.8. We can see from the figure that the electron is accelerated towards $p = 1$ a.u. as the electric field increases in intensity and can reach a momentum of $p = 2.5$ a.u. by 1 fs as the field reaches a maximum value. We see that as the electric field changes direction the momentum changes in sign and the momentum wave packet is pushed in the opposite direction. In addition the density begins to exhibit substructures and oscillations as t increases due to interference between wave packets ionised at different times during the pulse. While both figures 4.9 and 4.10 show strong time dependent oscillations due to the strength and direction of the field, the oscillations in momentum space are much faster than those in coordinate space since the momentum changes more rapidly with the field.

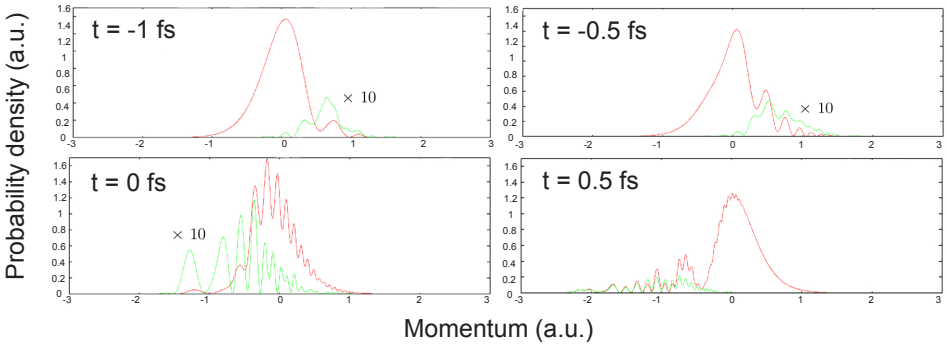

Figure 4.10: The electron momentum density $|\Psi(p,t)|^2$ (red) and continuum electron momentum density $|\Psi^c(p,t)|^2$ (green) in the length gauge for the electric field with parameters given in figure 4.8 and at times marked by the red circles.

4.3.4 Ionisation Yield

The ionisation probability or yield can be readily measured as a function of the intensity of the laser and we are particularly interested in this in the low frequency regime. Even if we should expect a monotonic rise in the yield up to the saturation intensity, figure 4.12 shows that this is not always observed. Figure 4.11 shows this ionisation yield against intensity I for a 2 cycle pulse with a vector potential of the form (4.3). We see that the yield here does rise steadily without ever dropping in value, rising from negligible amounts for $I < 5 \times 10^{13}\mathrm{W} \cdot \mathrm{cm}^{-2}$ before reaching as high as $P^{ion}(\tau) = 0.6$ for $I = 3 \times 10^{14}\mathrm{W} \cdot \mathrm{cm}^{-2}$. We expect this here as the increase in intensity increases the number of photons the electron can absorb and therefore increases the chance of the electron gaining the required energy for ionisation.

We originally calculated the ionisation yields using the full TDSE unscaled calculation before then using the exterior complex scaling method (ECS) which gave identical results in all cases. In order to calculate the ionisation probability using the ECS we choose a scaling point equal to the extent of the bound states meaning that any probability lost due to the scaling is due to ionised electrons. We can then subtract the norm from unity at the end of the pulse in order to be left

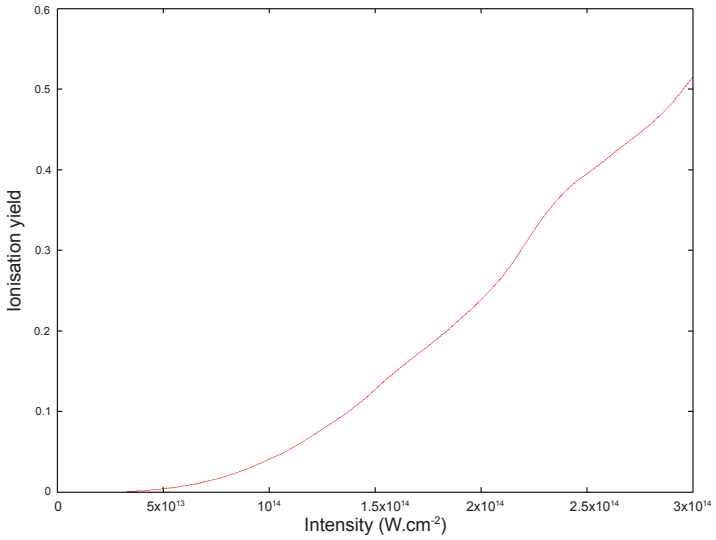

Figure 4.11: The ionisation yield as a function of intensity I, at the end of a 2 cycle pulse of frequency $\omega = 0.0569$ a.u. given by equation (4.3).

with the ionisation probability. We carried out the calculation for intensities every $0.5 \times 10^{13}\mathrm{W} \cdot \mathrm{cm}^{-2}$ from 10^{11} to $3 \times 10^{14}\mathrm{W} \cdot \mathrm{cm}^{-2}$. For the largest intensities the box size and number of B-spline functions becomes very large and hence by using the ECS method we managed to reduce the time of our calculations by over a factor of 100.

Figure 4.12 shows the same picture but this time for a 4 cycle pulse. By increasing the pulse length we allow more time for rescattering of ionised electrons as well as population transfer from bound state to bound state and bound state to continuum. Here, rather than rising monotonically we can see now that the ionisation yield dips periodically at certain intensities with the first dip at around $I = 1.2{\times}10^{14}$ W $\cdot$ cm^{-2}. We see more dips as the intensity rises with the dips becoming of greater amplitude at higher intensities with the largest being at $I = 2.45 \times 10^{14}$ W $\cdot$ cm^{-2} when the probability drops from 0.572 to 0.539. We speculate that these unexpected drops in ionisation yield may be due to the electron becoming trapped in high lying Rydberg states and therefore not becoming ionised. We also note that as expected the increase in the number of cycles causes the probability of ionisation to rise. For example for highest intensity of 3×10^{14} W $\cdot$ cm^{-2} we see that increasing the number of cycles

from 2 to 4 increases the ionisation yield from 0.516 to 0.700. We look at this phenomenon again in this chapter for lower frequency and in three dimensions in the next chapter.

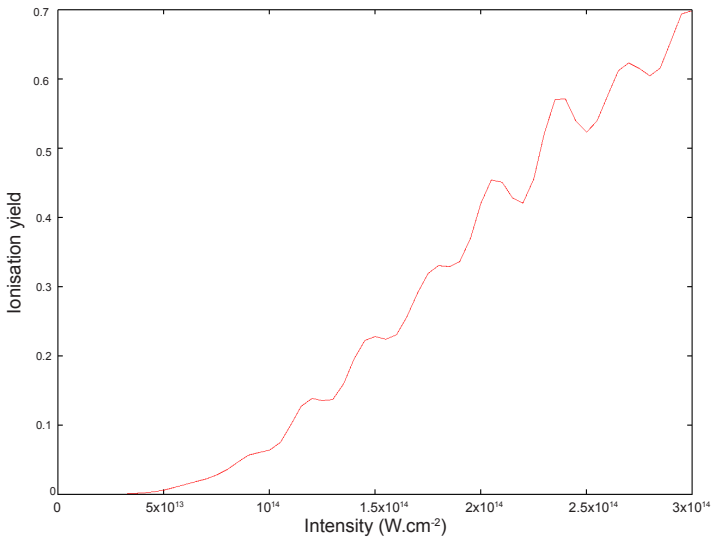

Figure 4.12: The ionisation yield as a function of intensity I, at the end of a 4 cycle pulse of frequency $\omega = 0.0569$ a.u. given by equation (4.3).

4.3.5 The Ionisation Spectrum

The theory behind above threshold ionisation was discussed in section 2.6.2. The mechanism in which this occurs is due to free-free absorption where an electron absorbs photons in a strong field surrounding the atom. We now present results obtained by our calculations and investigate how the spectrum is affected by the intensity of the laser. As the intensity rises and the value of the Keldysh parameter γ falls we expect to see how the change in regime between the multiphoton and tunnel ionisation is shown in the spectrum.

As mentioned in chapter 3, in the atomic basis the ATI spectrum is calculated using the equation

$$P(E_i) = P\left(\frac{E_{i-1} + E_i + E_{i+1} + E_{i+2}}{4}\right) = \frac{|a_i(\tau)|^2}{E_{i+1} - E_{i-1}} + \frac{|a_{i+1}(\tau)|^2}{E_{i+2} - E_i}. \qquad (4.12)$$

In order to calculate this we obtain the value at the points E_i and interpolate to get the values in between. The more positive eigenvalues we have in our discrete basis the better the approximations will be. The correct balance must be achieved here since the larger the basis size the longer the calculations take. In figure 4.13 we show the above threshold ionisation spectrum against energy E for the three intensities $I = 10^{14}$ (red line), 3×10^{14} (green line) and 5×10^{14} W $\cdot$ cm^{-2} (blue line). We can see how the probability of ionisation increases considerably as we move to higher intensity. At the lowest intensity we can see that clearly defined peaks have not yet appeared as the bandwidth of laser causes many peaks at low amplitude to blend together. At the two higher intensities the peaks are now clearly visible and roughly separated by the photon energy $E = 0.0569$ a.u. whilst we can see the effect of the AC stark shift as the highest intensity as the peaks shift to the left at a faster rate than the middle intensity. The lowest energy peak is also clearly shown to have diminished in amplitude. Finally we can see the extent of the highest energy ionised electrons increases considerably as the intensity increases from $E_{max} = 0.7$ a.u. for 10^{14} W $\cdot$ cm^{-2}, to $E_{max} = 1.8$ a.u. for 3×10^{14} W $\cdot$ cm^{-2} to $E_{max} = 2.5$ a.u. for 5×10^{14} W $\cdot$ cm^{-2}.

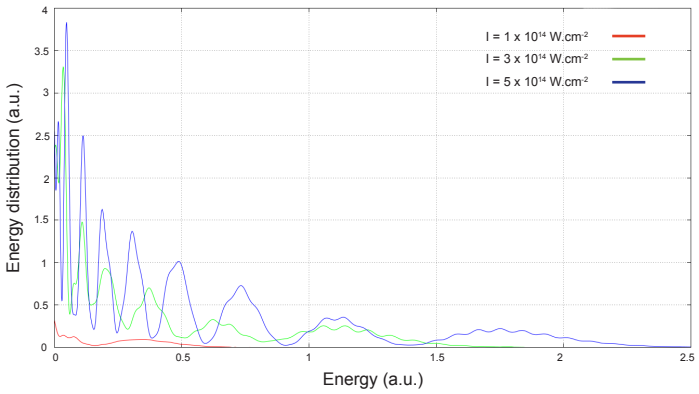

Figure 4.13: The photoelectron energy spectrum as a function of electron energy at the end of the 2 cycle pulse of frequency $\omega = 0.0569$ a.u. and intensities $I = 10^{14}$ (red), 3×10^{14} (green) and 5×10^{14} W $\cdot$ cm^{-2} (blue) for a vector potential given by equation (4.3).

4.3.6 Density Plots

The time evolution of the wave packet during its propagation, can be visualised in plots showing the electron density over time in coordinate and momentum space. We also extend our study to include the effect of a larger number of cycles in the laser pulse. We investigate the behaviour of the wave packet subject to a laser pulse with 4 optical cycles and investigate how the ionisation rate evolves by looking at the electron trajectories throughout the pulse. We take the intensity to be $I = 5 \times 10^{14} \mathrm{W} \cdot \mathrm{cm}^{-2}$ and follow firstly the development of the wave packet in coordinate space.

Figure 4.14 shows the evolution of the electron density against position x. A plot of the scale is found in the figure with a dark plot giving a zero probability and an increasing probability as the colour becomes lighter. The electron remains close to the ground state at the beginning of the pulse before propagating far from the nucleus as t increases. Signs of ionisation occur after just one optical cycle as we see movement of density away from the origin. The probabilities of finding the electron in the bound states has almost completely diminished at the end of the four cycles. Here we used a box of $[-1200, 1200]$ a.u. and 1800 B-splines with a time step of $\delta t = 0.2$ a.u. and 20 Krylov vectors. The calculations on the laptop took around 18 minutes. The population of the ground state (green line) with the vector potential $A(t)$ (red line) against time for the same parameters are shown in figure 4.15. The probability of finding the electron in the ground state at the end of the pulse has again fallen to 0.02 for this intensity with there being times t during the pulse where the ground state has become completely depleted.

We now study the evolution in time of the probability density $|\Psi(p,t)|^2$ in the p direction in momentum space. In figure 4.16 we show the plot of the probability density in momentum space against p and time t for the same intensity, $I = 5 \times 10^{14} \mathrm{W} \cdot \mathrm{cm}^{-2}$. These calculations are carried out in the velocity gauge and hence the probability density is a function of the canonical momentum.

In figure 4.16 we see the shape of the momentum closely resembles the vector poten-

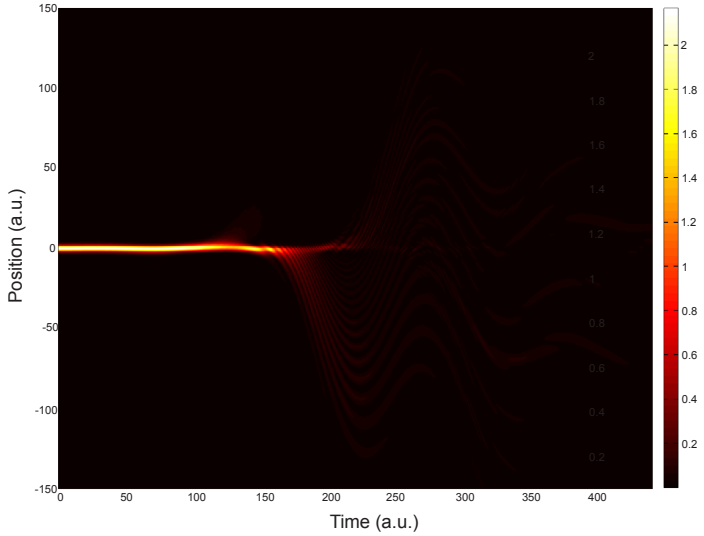

Figure 4.14: The evolution of the probability density $|\Psi(x,t)|^2$ in the x direction throughout a pulse of 4 optical cycles of frequency $\omega = 0.0569$ a.u. and intensity $I = 5 \times 10^{14}\mathrm{W} \cdot \mathrm{cm}^{-2}$ described by the vector potential (4.3).

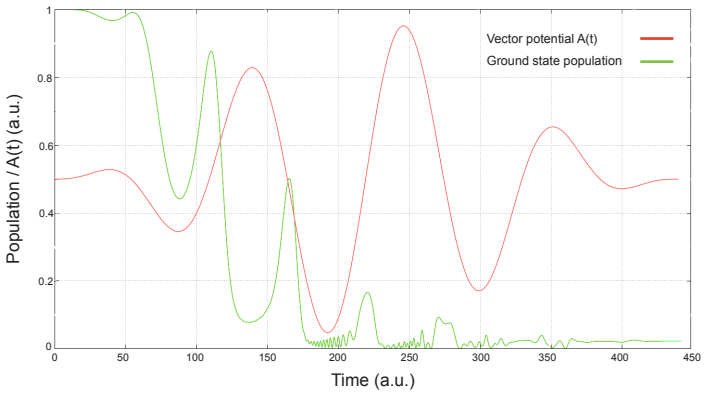

Figure 4.15: The population of the ground state (green) throughout a pulse of 4 optical cycles of frequency $\omega = 0.0569$ a.u. and intensity $I = 5 \times 10^{14}\mathrm{W} \cdot \mathrm{cm}^{-2}$ described by the vector potential (4.3) which is shown on an arbitrary scale (red).

tial due to the shift of the canonical momentum by **A** in the VG. We can see in the final 2 cycles of the pulse that the form distorts with horizontal lines appearing at all values of $|p|$. This represents electrons which have been ionised and are travelling in the field at constant momentum. The time the lines appear represent the time of ionisation. The shape traced out by the vector potential begins to distort as the **p** term on the right hand side of (2.48) becomes much more dominant than the **A** term.

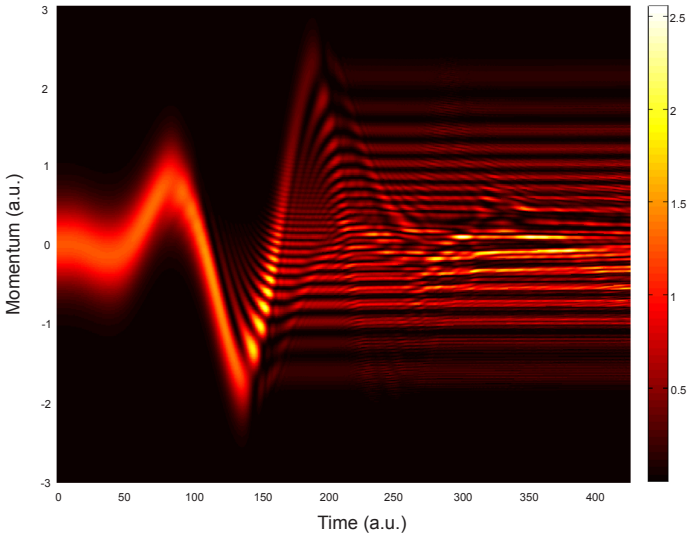

Figure 4.16: The evolution of the probability density $|\Psi(p,t)|^2$ in the p direction in momentum space in the velocity gauge throughout a pulse of 4 optical cycles of frequency $\omega = 0.0569$ a.u. and intensity $I = 5 \times 10^{14}\mathrm{W} \cdot \mathrm{cm}^{-2}$ described by the vector potential (4.3).

We now perform a similar calculation carried out in the length gauge, this time for intensity $I = 10^{14}\mathrm{W} \cdot \mathrm{cm}^{-2}$. Figure (4.17) shows the evolution of the probability density $|\Psi(p,t)|^2$ in the p direction in momentum space in the LG. We carry this out in order to see how the shift of the vector potential $A(t)$ due to the gauge transformation affects our results. In the LG the kinetic momentum is equal to the canonical momentum and as such we see very little change in the form until ionisation begins to occur. Then we can see how the electron is accelerated away from the nucleus and changes direction with the field. It begins to travel at a constant velocity as it escapes the force of the atomic potential.

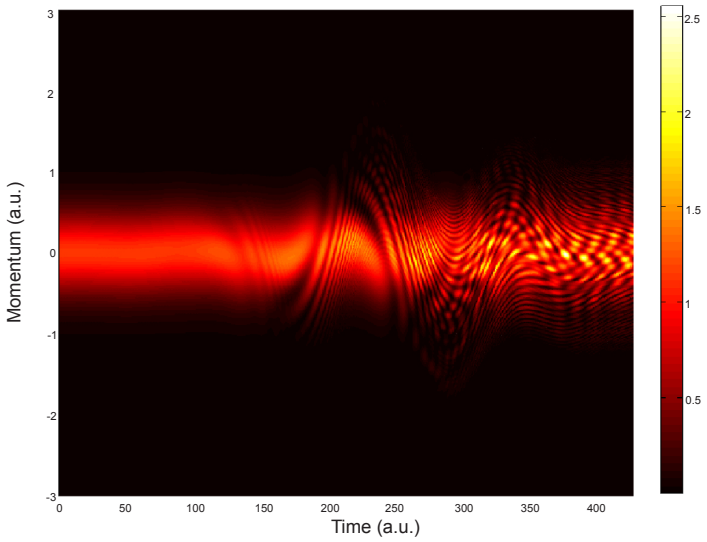

Figure 4.17: The evolution of the probability density $|\Psi(p,t)|^2$ in the p direction in momentum space in the length gauge throughout a pulse of 4 optical cycles of frequency $\omega = 0.0569$ a.u. and intensity $I = 10^{14}\mathrm{W}\cdot\mathrm{cm}^{-2}$ described by the vector potential (4.3).

4.3.7 The Window Operator

An alternative method of extracting energy resolved information from the wave packet which can allow us to calculate the ionisation spectrum [82, 63, 12] uses a window operator defined as

$$\hat{W}_\gamma(E_k) = \frac{\gamma^{2^n}}{(\hat{H}_0 - E_k)^{2^n} + \gamma^{2^n}} \tag{4.13}$$

where n is the order of the energy window, centred at E_k with width 2γ. With increasing order the energy window becomes more rectangular as seen in figure 4.18, whilst γ can be lowered in order to improve the energy resolution.

The method projects the wave function at the end of the pulse onto the energy space

$$|\Phi_\gamma(E_k)\rangle = \hat{W}_\gamma(E_k)|\Psi(x,\tau)\rangle, \tag{4.14}$$

so $\Phi_\gamma(E_k)$ represents the part of the wave packet that contributes to energies in this energy window and as such the probability to find the electron in a state within the energy window $\hat{W}_\gamma(E_k)^2$ is given by

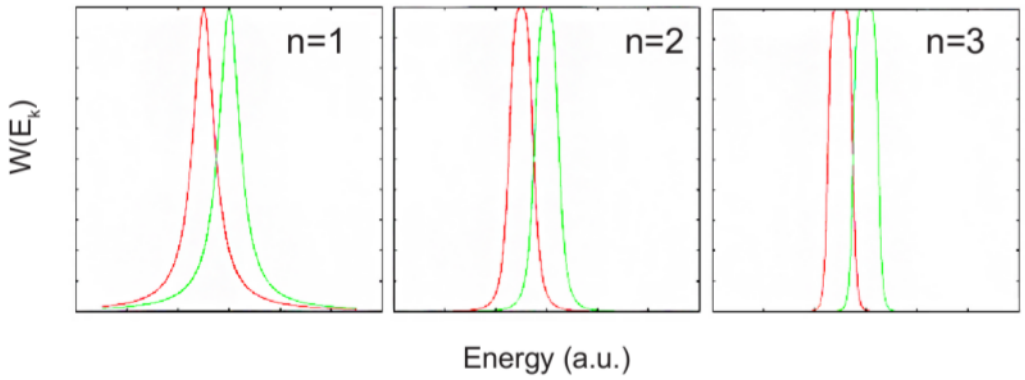

Figure 4.18: Changing shape of the window function for $n = 1, 2, 3$ for $\gamma = 0.001$.

$$P_\gamma(E_k) = \langle \Phi_\gamma(E_k) | \Phi_\gamma(E_k) \rangle = \sum_{|m\rangle} |a_m|^2 \left(\frac{\gamma^{2^n}}{(E_m - E_k)^{2^n} + \gamma^{2^n}} \right)^2, \tag{4.15}$$

where $|m\rangle$ and E_m are the eigenstates and eigenvalues of the atomic Hamiltonian respectively and a_m are the coefficients of the spectral expansion in the atomic basis corresponding to the state m. We can see that as $\gamma \to 0$ then $P_\gamma(E_k) \to |a_m|^2$ as we would expect.

The ATI spectrum can be calculated by taking multiple values of E_k separated by the window width and normalising. Figure 4.19 shows a comparison between ATI spectra using the previously used projection onto continuum states method (red line) and with the window function with $\gamma = 0.004$ and $n = 2$ (green line) for $I = 5 \times 10^{14} \mathrm{W} \cdot \mathrm{cm}^{-2}$. We can see that the two methods agree very well with the peaks in the correct positions. The window operator method has the advantage of continuing the energy spectrum through the threshold and showing the bound states of the atom in direct comparison with the continuum states. Hence we can see in a clear and intuitive way the probability that the electron has of remaining in one of the discrete bound states at the end of the pulse.

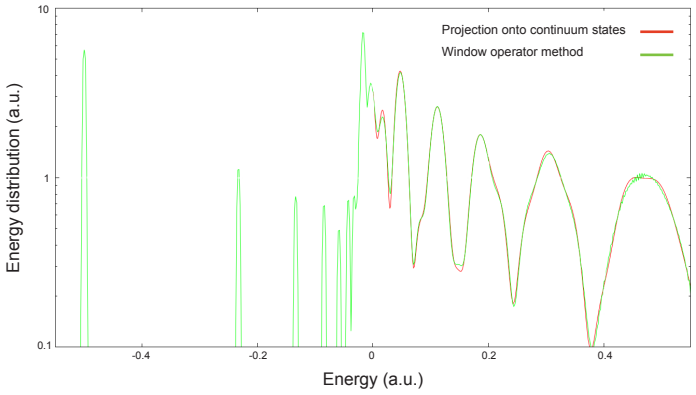

Figure 4.19: The photoelectron energy spectrum for a laser of frequency $\omega = 0.0569$ a.u. and intensity $I = 5 \times 10^{14}\mathrm{W} \cdot \mathrm{cm}^{-2}$ for the pulse described by the vector potential (4.3). It is calculated using two different methods, the window operator method (red) and the projection onto continuum states method (green). The window operator method also shows the probability density of the bound states.

4.3.8 Probability Current

To get an idea of the flow of probability rather than the static densities we examine we can look at the probability current or probability flux. This describes the flow of probability through unit area per unit time. We can think of the current as a liquid travelling through a position at a certain time and we can measure the 'amount' of current travelling through. We can then link this to the density of the wave packet at each time step. If the current is positive then we can interpret this as the probability flowing in the positive x direction whilst if the current is negative then this means the probability is flowing in the negative x direction.

The current at a point x_0 and a time t is defined, in the velocity gauge for an electron without the external electromagnetic field, as

$$\mathcal{J}(x_0, t) = \frac{1}{2m}\Big(\Psi^*(x,t)\hat{p}\Psi(x,t) - \Psi(x,t)\hat{p}\Psi^*(x,t)\Big)\Big|_{x=x_0}. \tag{4.16}$$

We allow for the influence of the electric field by including an extra term involving the vector potential. The current is now defined, in atomic units, as

$$\mathcal{J}^{(VG)}(x_0,t) = \mathrm{Im}\left(\Psi(x,t)^*\frac{\partial}{\partial x}\Psi(x,t)\right)\Big|_{x=x_0} + A(t)|\Psi(x_0,t)|^2. \tag{4.17}$$

In the length gauge we must allow for the difference in measured momentum. The current is then defined as

$$\mathcal{J}^{(LG)}(x_0,t) = \mathrm{Im}\left(\Psi(x,t)^*\frac{\partial}{\partial x}\Psi(x,t)\right)\Big|_{x=x_0}. \tag{4.18}$$

We again look at the three intensities of $I = 10^{14}$, 3×10^{14} and 5×10^{16} W $\cdot$ cm^{-2} at the positions $x_0 = 40$ a.u. and $x_0 = -40$ a.u. In figure 4.20 we show the probability current against time for the position $x_0 = 40$ a.u. for the intensities $I = 10^{14}$ (red line), 3×10^{14} (green line) and 5×10^{14} W $\cdot$ cm^{-2} (blue line). In all cases the current remains very small until we see a large positive series of peaks appear at around the end of the first cycle due to tunnel ionisation caused by the large negative peak in the first optical cycle. Entering the second cycle, the field changes direction and the current reduces in amplitude and finally changes sign as the electron momentum begins to change to a negative value. As the intensity increases the current becomes larger and the change of sign occurs later due to the higher energy and momentum the electron acquires from the field. We can see that as the intensity increases these oscillations become more prominent as higher levels of flux travel through x_0.

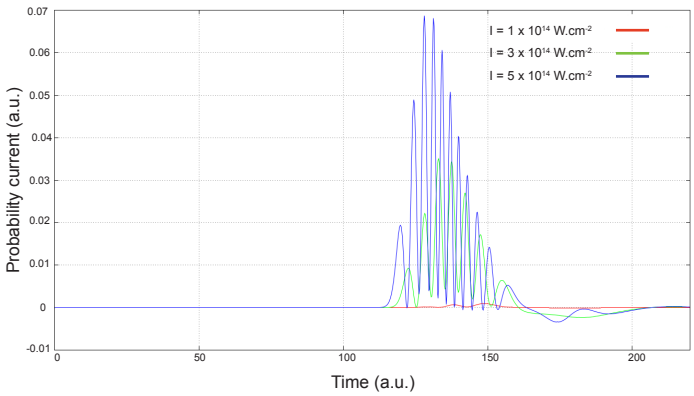

Figure 4.20: The probability current at position $x_0 = 40$ a.u. throughout a 2 cycle pulse of frequency $\omega = 0.0569$ a.u. and intensity $I = 10^{14}$ (red), 3×10^{14} (green) and 5×10^{14} W $\cdot$ cm^{-2} (blue) described by the vector potential (4.3).

Figure 4.21 shows the same current against time for the position $x_0 = -40$ a.u. Here we see that the current is of a much lower amplitude, due to the fact that the tunnelling occurring in the first cycle causes the majority of the density to travel first into the positive x direction. We see the appearance of current at an earlier time here than in figure 4.20 due to the smaller peak of positive amplitude around $t \simeq 45$ a.u. causing tunnel ionisation in the negative x direction.

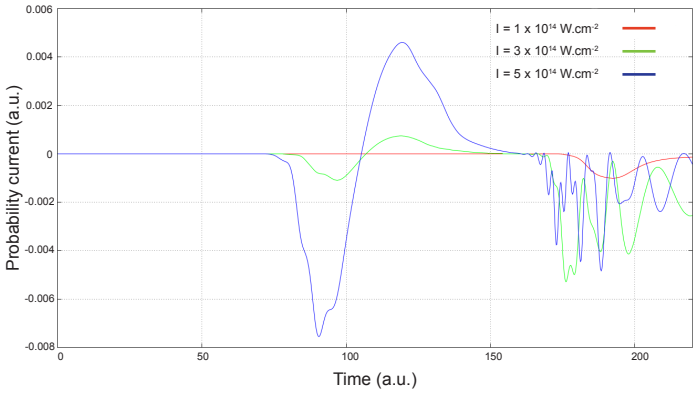

Figure 4.21: The probability current at position $x_0 = -40$ a.u. throughout a 2 cycle pulse of frequency $\omega = 0.0569$ a.u. and intensity $I = 10^{14}$ (red), 3×10^{14} (green) and 5×10^{14} W $\cdot$ cm^{-2} (blue) described by the vector potential (4.3).

4.3.9 Tracking the Wave Packet

One element of interest is in how the wave packet evolves with the laser pulse. This allows us to see the mechanisms of ionisation for different sets of laser parameters. We therefore look at locating the position of the wave packet at each time step during the propagation to allow us to see how electrons in different regions of space react to the change in amplitude and direction of the field. We can track the wave packet throughout the pulse by looking at the population of probability on a surface of radius r at each time step and see how this population changes with the electric field. By doing this we can see exactly the times when the wave packet leaves the radius and also when it returns with a change of direction of the electric field. In order to calculate the probability we pick a radius that coincides with one of the

B-spline break points and then we project the wave function at time t onto the states and sum over all states. We carry out the integral for the projection between $-r$ and r using a Gaussian quadrature using the mesh points as the quadrature points x_i meaning the method is quick and memory efficient. This is important since the calculation can be made thousands of times during an optical cycle. This method is gauge invariant since the calculation of the probabilities involve taking the absolute value and we sum over all states.

In figure 4.22 we look at the probability of finding the electron within a surface of radius r against time for a 4 cycle pulse, at an intensity of $2.5 \times 10^{14}\mathrm{W} \cdot \mathrm{cm}^{-2}$ for radii of $r = 5.45$ a.u. (red line), 20.45 a.u. (green line) and 50.45 a.u. (blue line). Also shown is the electric field on an arbitrary scale which indicates the points of high electric field amplitude when ionisation is most likely to occur. By showing the probability for a variety of radii on the same graph we can pinpoint the position of the electron more accurately. From the figure we can see that whenever the electric field reaches a maximum or minimum there is a noticeable drop in the probability of the electron being within the radius. The probability of finding the electron within the surface of radius $r = 5.45$ a.u. has the steepest drop with each burst of ionisation. The biggest drop occurs at the midpoint of the pulse when the electric field is at its strongest point. As t increases, interference of wave packets released at different optical cycles of the field cause the probability to oscillate. As other parts of the wave packet ionised at previous times return into the radius they interfere with more recently ionised wave packets.

Since the bound states of the model atom are found within a few atomic units of the origin we can extend this to look at the continuum probability on the given surface. Here the probability starts at zero as all probability begins in the bound states. We see peaks of probability from $t > 100$ a.u. onwards as the ionised electron passes through the chosen radius. The width and height of the peak increase with increasing radius. Figure 4.23 shows this continuum probability for the same three radii as figure 4.22 and now carry out the calculation in the length gauge. We

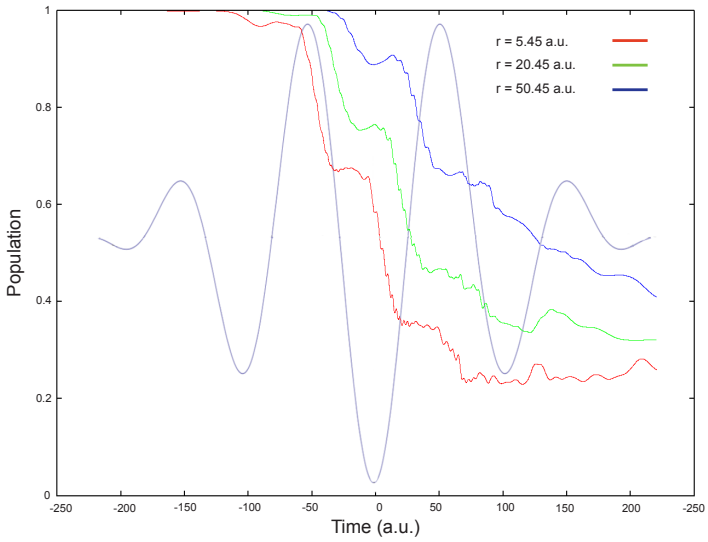

Figure 4.22: The probability of finding the wave packet within a radius of $r = 5.45$ a.u. (red), 20.45 a.u. (green) and 50.45 a.u. (blue) throughout a 4 cycle pulse of frequency $\omega = 0.0569$ a.u. and intensity $I = 2.5 \times 10^{14}$ W $\cdot$ cm^{-2} defined by the vector potential (4.3). Also shown is the electric field on an arbitrary scale.

can see the peaks as expected when the radius is large enough, however, when r is chosen to be small the structure is less defined and we get more of a plateau due to the constant outgoing and incoming electrons oscillating around the origin. For all calculations here we used a box of $[-900, 900]$ a.u. a time step of 0.2 a.u. and 15 Krylov vectors. In the VG we used 1100 B-spline functions which gave a total run time of 8 minutes whilst in the LG we used 1800 functions giving a total run time of 17 minutes.

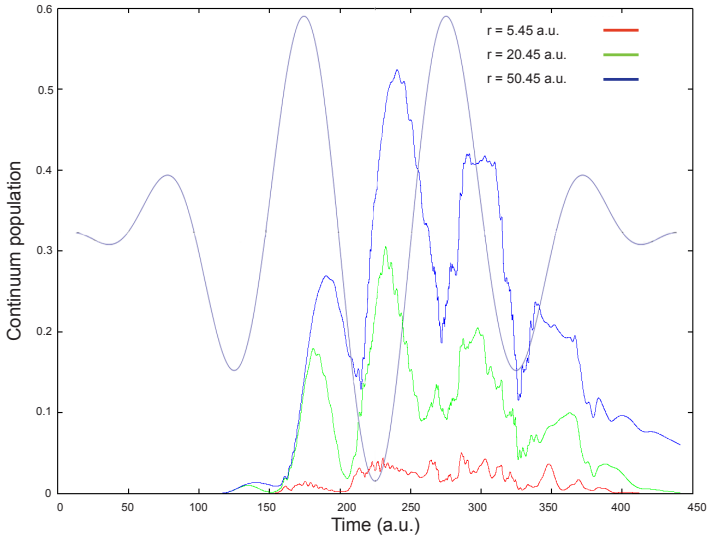

Figure 4.23: The probability of finding the continuum wave packet within a radius of $r = 5.45$ a.u. (red), 20.45 a.u. (green) and 50.45 a.u. (blue) throughout a 4 cycle pulse of frequency $\omega = 0.0569$ a.u. and intensity $I = 2.5 \times 10^{14}$ W $\cdot$ cm^{-2} defined by the vector potential (4.3). Also shown is the electric field on an arbitrary scale. Calculations were carried out in the length gauge.

4.4 Ionisation by a 492nm Wavelength Laser

We now look at another wavelength, that of $\lambda = 492$nm corresponding to a photon frequency of $\omega = 0.1017$ a.u. Although this is a shorter wavelength than $\lambda = 800$nm which was previously used, here we investigate a more computational challenging case due to the fact that we now look at a pulse of many more optical cycles. One feature of the ATI spectrum not examined until now is the appearance of substructures on the low energy ATI peaks, which occur because of interference caused due to the length of the pulse. We look at a different atomic potential, in addition to the soft Coulomb potential, to see how the atomic potential affects the ATI spectrum.

We use a laser pulse of intensity of 4.3×10^{13} W $\cdot$ cm^{-2} and use a large number of optical cycles, taking $n_c = 50$. For the calculations here using both potentials we used a box of $[-1500, 1500]$ and a basis size of 2000 functions. For the propagation we took $\delta t = 0.2$ a.u. and used 40 Krylov vectors. The total run time for the

calculation was 108 minutes. We start with the ATI spectrum using the standard soft Coulomb potential and this can be seen in figure 4.24. In the spectrum we can clearly see a build up of substructures on the right hand side of the ATI peaks at low energy with the effect becoming less prevalent as the energy rises. Bardsley et al. [10] predicted the positions of these sub-peaks to be equal to the translational energy of the ionised electrons, i.e. the total energy minus the quiver energy given by

$$E(t) = E_0 + n\omega - \frac{E_0^2}{4\omega^2}\left(1 - \frac{\omega^2 t^2}{4n_c^2}\right), \tag{4.19}$$

where n is the number of photons absorbed larger than the minimum number needed to ionise the electron. The positions are represented by the peaks of figure 4.24, with the largest sub-peak occurring at energy

$$E = E_{min} = E_0 + n\omega - \frac{E_0^2}{4\omega^2}. \tag{4.20}$$

These structures are due to rescattering interference between multiple outgoing waves and resonances between Floquet states. Calculation of the energies and widths of the Floquet states can give more insight into the strong field dynamics of short pulses.

We now look at a short range Gaussian potential given by the equation

$$V(x) = -V_0 \exp(-x^2/x_0^2), \tag{4.21}$$

and we take $V_0 = 0.63$ a.u. and $x_0 = 2.65$ a.u. which gives 2 bound states with energy levels $E_0 = -0.4451$ a.u. and $E_1 = -0.1400$ a.u. There is also a third very weakly bound state of energy $E_2 = -1.39 \times 10^{-4}$ a.u. We look at a Gaussian potential for two reasons, firstly because for these parameters the potential mimics the two lowest states of Xenon allowing for potential comparison in the future with a three dimensional Xenon approximation and secondly to investigate the effect of the long range Coulomb tail on the ATI spectra. The ATI spectrum for this potential can be seen in figure 4.25 with the laser parameters the same as figure 4.24 where we

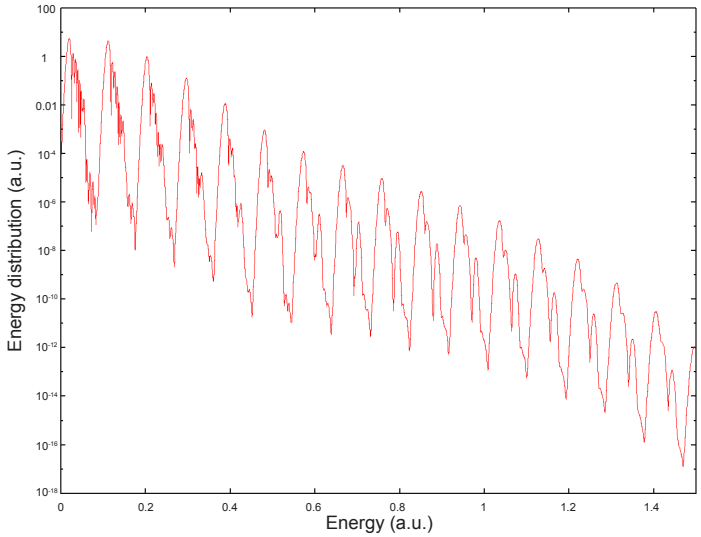

Figure 4.24: The ATI spectrum on a logarithmic scale as a function of electron energy at the end of the 50 cycle pulse of frequency $\omega = 0.1017$ and intensity $I = 4.3 \times 10^{13}\mathrm{W} \cdot \mathrm{cm}^{-2}$ defined by the vector potential (4.3) using the soft Coulomb potential.

plot the ATI spectrum for the soft Coulomb potential (red line) and the Gaussian potential (green line) against energy E.

We note that, although the ATI peaks are separated by the photon energy, the peaks are shifted as predicted in chapter 3 and the three photon peak is pushed below the ionisation threshold and the four photon peak moves down from $E = 0.110$ to 0.074 a.u. The Keldysh parameter for the model potentials are very close due to the similar ionisation potentials. It takes a value of $\gamma = 2.645$ for the soft Coulomb potential and $\gamma = 2.481$ for the Gaussian potential meaning that multiphoton ionisation dominates in both cases and explains the similar structure of the spectrum. We note that despite the soft Coulomb having a lowest energy ground state and thus requiring more photons to ionise an electron, the peaks are still of greater amplitude than that of the Gaussian potential due to the long range Coulomb tail causing more rescattering of electrons which then return to the parent ion. The positions of the peaks are shifted due to the change in ionisation potential although the structures in the peaks are almost identical and therefore do not rely on the rescattering caused by the long range Coulomb tail.

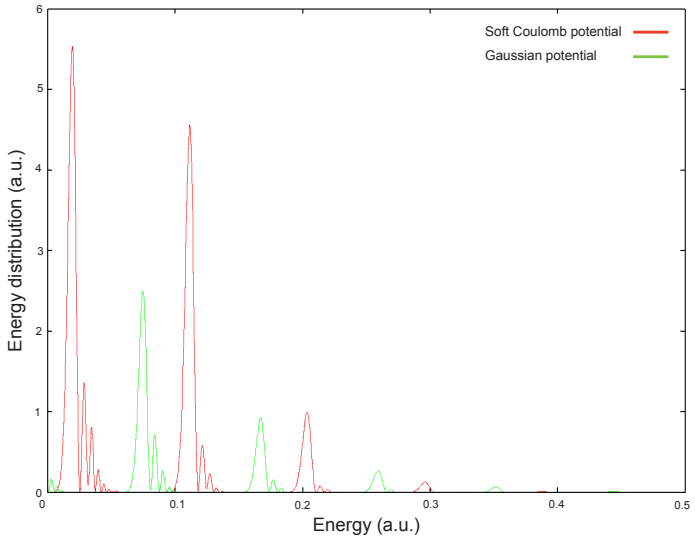

Figure 4.25: The ATI spectrum on a linear scale as a function of electron energy at the end of the 50 cycle pulse of frequency $\omega = 0.1017$ and intensity $I = 4.3 \times 10^{13}\mathrm{W} \cdot \mathrm{cm}^{-2}$ defined by the vector potential (4.3) using the soft Coulomb potential (red) and the Gaussian potential (green).

4.5 Classical Calculations

In section 2.7 we looked at the classical dynamics of an electron in an electric field. We now further our investigation into this by carrying out calculations in one dimension for a wavelength of $\lambda = 800$nm. To remind ourselves of the simple man's theory (SMT), [12] it can be explained in three steps beginning with the ionisation of the atom at a time t_0. The coulomb potential is strongly distorted by the intense field and the superposition of the atomic potential and the electric field forms a barrier that can be tunnelled through by the electron. Whilst tunnelling is a purely quantum phenomenon the resulting electron propagation is described classically. The second step is the acceleration of the electron due to the electric field and when the field changes direction the electron can be accelerated back to the atom at which point it could rescatter. In the third step the electron either rescatters or recombines with atom emitting a photon roughly equal to its kinetic energy.

In one dimension the equations for the velocity, position and energy of the direct electrons, which we have denoted with an upper index (0) become

$$v^{(0)}(t) = -\int_{t_0}^{t} E(t')\mathrm{d}t' = A(t) - A(t_0), \tag{4.22}$$

$$x^{(0)}(t) = \tilde{x}(t) - \tilde{x}(t_0) - A(t_0)(t - t_0), \tag{4.23}$$

where $\tilde{x}(t) = \int_0^t A(t')\mathrm{d}t'$ and

$$E^{(0)}(t) = \frac{1}{2}[A(t) - A(t_0)]^2 \leq 2U_p. \tag{4.24}$$

For the case of rescattered electrons, given by the upper index (1), we consider all electrons which are driven back towards the parent atom and come close enough to rescatter. Hence, we look at all electrons whose position at t_r is small therefore fulfilling the condition $|z^{(0)}(t_r)| \leq d_r$ where t_r is the time of rescattering. We take d_r, the scattering distance, to be 1 a.u. The bigger d_r is allowed to be the more scattering solutions exist. For this one dimensional case we look at 180 degree reflection of the atom after rescattering and the position and energy can then be given by

$$x^{(1)}(t) = \tilde{x}(t) - \tilde{x}(t_0) - A(t_0)(t_r - t_0) + [A(t_r)(\cos\pi - 1) - A(t_0)\cos\pi](t - t_r) \tag{4.25}$$

and

$$E^{(1)}(t) = \frac{1}{2}[A(t) + A(t_0) - 2A(t_r)]^2 \leq 10U_p. \tag{4.26}$$

We plot now the final positions of the electrons for varying ionisation times t_0 as well as the energy in terms of position. For these calculations the electric field is of the form

$$E(t) = E_0 \sin^2\left(\frac{\pi t}{\tau}\right)\cos(\omega t)\ ,\ 0 \leq t \leq \tau \tag{4.27}$$

so that the vector potential follows a similar shape to that given in equation (4.3), with intensity $I = 2.4 \times 10^{14}\mathrm{W}\cdot\mathrm{cm}^{-2}$ and τ is the pulse length of 4 optical cycles.

We consider only emission times t_0 where $|E(t_0)| \geq 0.00834$ to allow the electric field to be of significant strength to ionise the electron.

Figure 4.27 shows the final photoelectron positions at the end of the pulse for the direct electrons (green line) and rescattered electrons (red + signs). We can see that the direct electrons, once ionised, oscillate with the trajectory of the pattern traced out by the vector potential as shown by equation (4.23) whilst the rescattered electrons take a much more complex trajectory set, according to equation (4.25), depending on their original ionisation time as well as the time they rescatter. The electric field over the course of the pulse can be seen in figure 4.26 for reference.

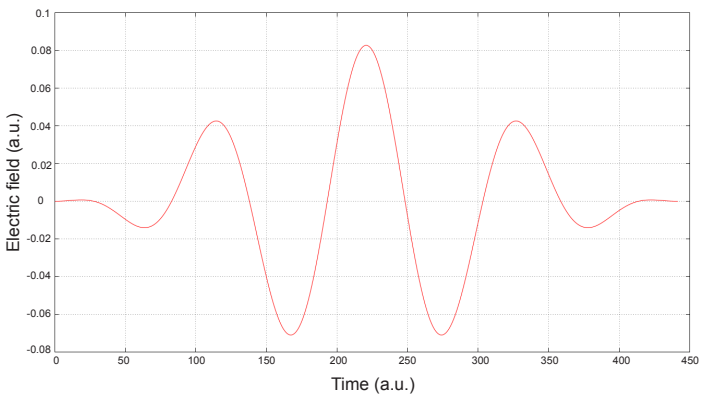

Figure 4.26: The electric field $E(t)$ of 4 optical cycles given by equation (4.27) of frequency $\omega = 0.0569$ a.u. and intensity $I = 2.4 \times 10^{14}\text{W} \cdot \text{cm}^{-2}$.

Figures 4.28 and 4.29 show the classical trajectories for electrons that are directly ionised (green lines) and rescattered (red lines) respectively by showing the energy E against position x at the end of the pulse. It is these emergence of wave packets previously mentioned that can be replicated quantum mechanically with use of the window operator as shown by Bauer [12]. In addition to this we can consider trajectories of these electrons over time for a given ionisation time. We do this by beginning at t_0 and calculating the electron position at small time steps. In the case of rescattering, for each time t we determine whether the rescattering condition above is fulfilled and if so we then follow the trajectory of this rescattering and repeat for each occasion. We can see that electrons of higher energy are more likely

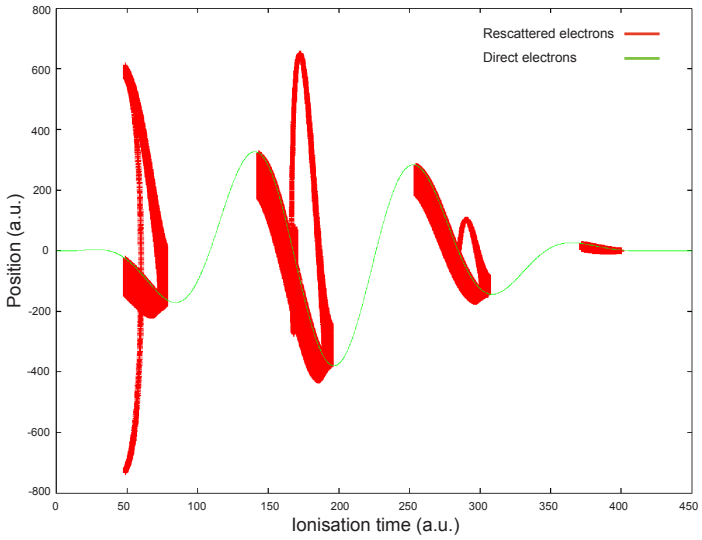

Figure 4.27: Final photoelectron positions $z(\tau)$ for direct electrons (green) and rescattered electrons (red) at the end of the 4 cycle pulse of frequency $\omega = 0.0569$ a.u. and intensity $I = 2.4 \times 10^{14}\mathrm{W} \cdot \mathrm{cm}^{-2}$ described by equation (4.27).

to finish with positive x value.

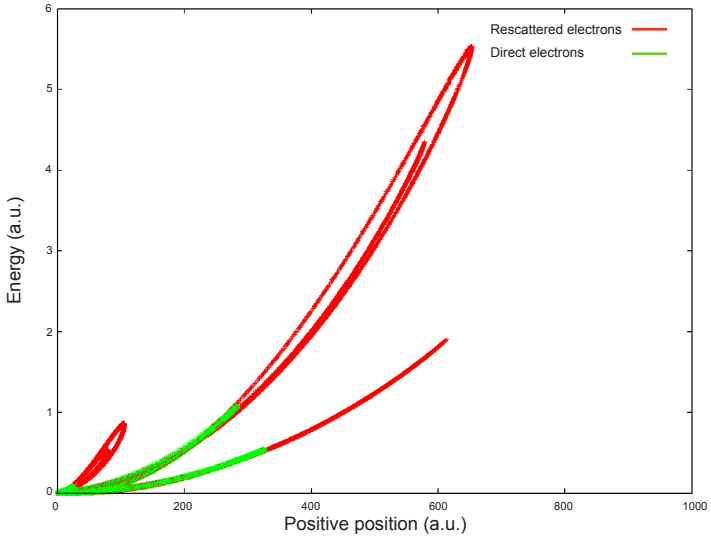

Figure 4.28: Photoelectron energies for positive x for direct electrons and rescattered electrons at the end of the 4 cycle pulse of frequency $\omega = 0.0569$ a.u. and intensity $I = 2.4 \times 10^{14}\mathrm{W} \cdot \mathrm{cm}^{-2}$ described by equation (4.27).

Figure 4.30 shows the trajectories, x, of ionised electrons throughout the pulse. We can see that before ionisation the electrons oscillate as the electric field distorts the

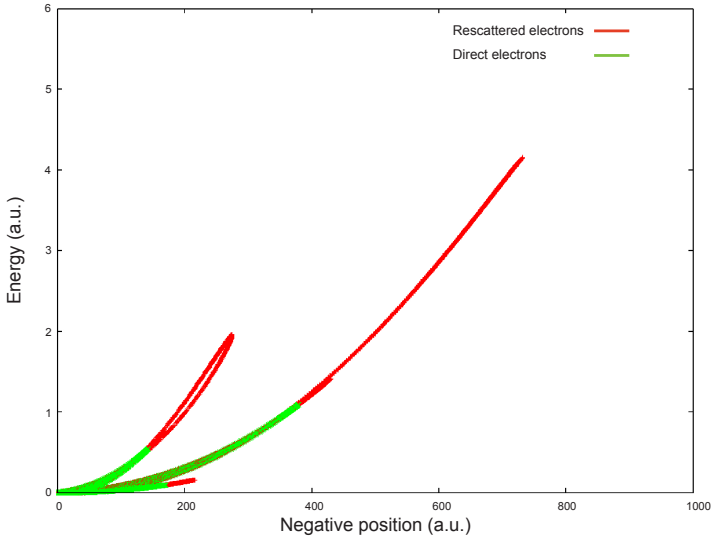

Figure 4.29: Photoelectron energies for negative x for direct electrons and rescattered electrons at the end of the 4 cycle pulse of frequency $\omega = 0.0569$ a.u. and intensity $I = 2.4 \times 10^{14}\text{W} \cdot \text{cm}^{-2}$ described by equation (4.27).

atomic potential before they become ionised and move away from the atom. We also see that the electrons change direction as the electric field switches signs. At $t = 100$ a.u. just after a small negative peak in the electric field the ionisation occurs in the positive x direction. This is due to the fact that the negative electric field distorts the Coulombic potential and creates the tunnel barrier in the positive x direction which allows the electrons to tunnel through and ionise. At $t = 150$ a.u. we can see in figure 4.26 that the electric field has now completely changed direction and a positive peak allows a large release in the negative x direction. Since the field peak here is strong, the atomic potential is more suppressed and the smaller tunnel distance allows for more ionisation. After ionisation the electrons gain high levels of momentum due to the strength of the electric field.

In figure 4.31 we show the rescattered trajectories as a function of time t. We now show just one ionisation time, $t_0 = 50$, in order to highlight the multiple opportunities for rescattering as the electron is pushed back into the vicinity of the atom. In figure 4.32 we show the evolution of the rescattered trajectories as the rescattering occurs later in the pulse between $t_0 = 100$ and 170 a.u. We can

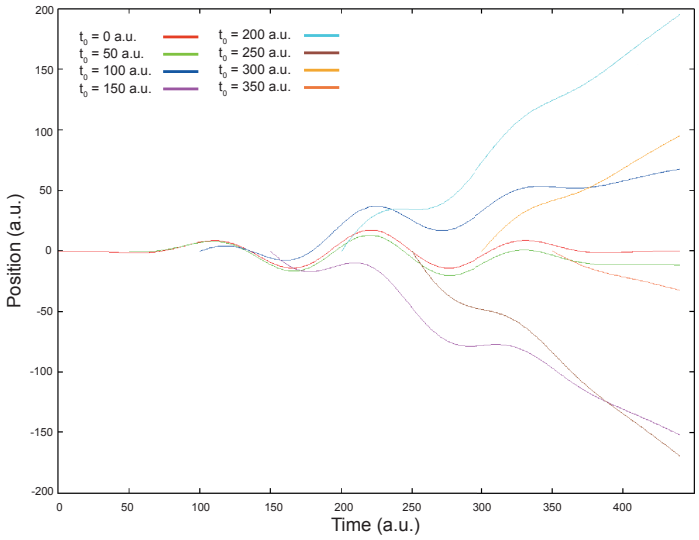

Figure 4.30: Trajectories of direct electrons ionised between times $t_0 = 0$ a.u. and $t_0 = 350$ a.u. during the four cycle pulse of frequency $\omega = 0.0569$ a.u. and intensity $I = 2.4 \times 10^{14}\text{W} \cdot \text{cm}^{-2}$ described by equation (4.27).

see that at $t = 120$ a.u. (green x signs) as the electric field approaches a peak in the positive x direction then the rescattered electrons travel in the negative x direction. At time $t = 150$ a.u. (blue stars), shortly after a peak in the electric field, we see the results of the burst of ionisation in the negative direction with the electrons travelling further distances in x in a shorter time than the previous time. At $t = 170$ a.u. (pink squares) we see that the change in direction of the electric field between now and the previous ionisation time has caused the rescattered electrons to be scattered back in the positive x direction. As the field has only just changed sign and has a lower amplitude these electrons are slower than those of the previous times.

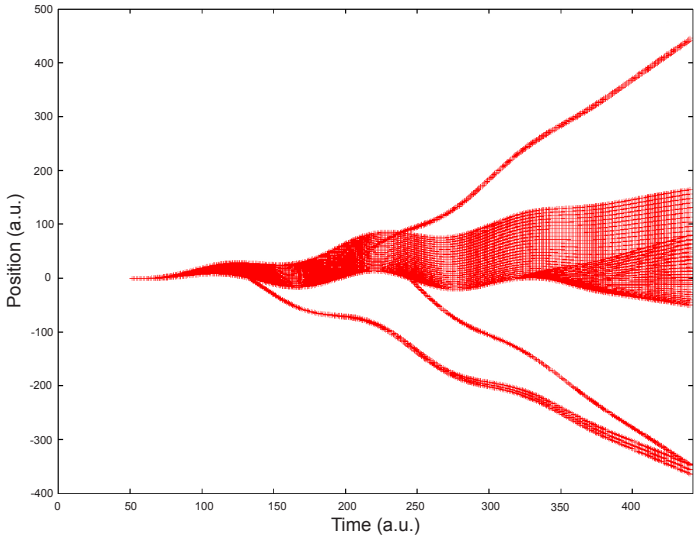

Figure 4.31: Trajectories of rescattered electrons ionised at $t_0 = 50$ a.u. during the four cycle pulse of frequency $\omega = 0.0569$ a.u. and intensity $I = 2.4 \times 10^{14}\mathrm{W} \cdot \mathrm{cm}^{-2}$ described by equation (4.27).

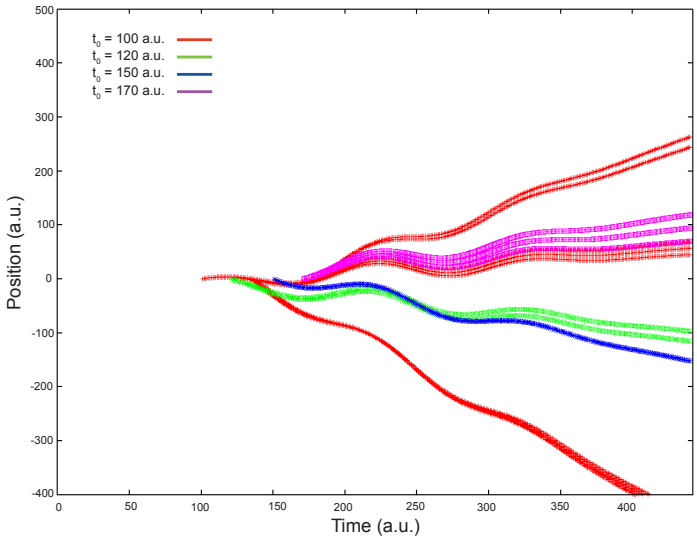

Figure 4.32: Trajectories of rescattered electrons ionised between times $t_0 = 100$ a.u. and $t_0 = 170$ a.u. during the four cycle pulse of frequency $\omega = 0.0569$ a.u. and intensity $I = 2.4 \times 10^{14}\mathrm{W} \cdot \mathrm{cm}^{-2}$ described by equation (4.27).

4.6 Ionisation by a 2000nm Wavelength Laser

We now look at the low frequency of $\omega = 0.0228$ a.u. corresponding to a wavelength of 2000nm. Calculations in this mid infrared part of the spectrum can be used to shed light on recent phenomena such as the physical origin of the low energy structure (LES) which is seen in the photoionisation spectrum of atoms and molecules in intense fields. If we use a laser of sufficient strength, such as $I > 10^{14}\mathrm{W}\cdot\mathrm{cm}^{-2}$, then we are put firmly in the tunnelling regime since the Keldysh parameter gives a value of $\gamma < 0.427$, with the atomic potential reduced to a weak perturbation and the motion of the electron is dominated by its interaction with the laser field. This is important since it has been speculated that rescattering, or more specifically the revisiting of the electron to the atom, plays a key role in the formation of the LES [45]. In all cases here we use a machine of 3.7 GHz processing speed and 4 processors

4.6.1 Electron Density and Ionisation Spectrum

We first look at some of the previously investigated quantities, such as the probability density and the spectra. At this frequency achieving convergence in each gauge becomes particularly difficult since the quiver amplitude alone can become very large. For example for an intensity of $I = 10^{14}\mathrm{W}\cdot\mathrm{cm}^{-2}$ the quiver amplitude is $\alpha = E_0/\omega^2 \simeq 102$ a.u. In addition, assuming ionisation occurs at the beginning of the pulse, the size of the ponderomotive potential, $U_p = 37.35\mathrm{eV}$, means that the electron can travel as far as 1444 a.u. for a typical two cycle pulse. As such a large box is needed and hence a large basis of B-spline functions. Due to this, the stiffness becomes very high and a smaller time step must be used than that of previous frequencies. The use of the length gauge at this frequency requires an exceedingly large basis and calculations can take very long. In order to propagate to more than 2 cycles or to increase the intensity higher than $10^{14}\mathrm{W}\cdot\mathrm{cm}^{-2}$ we must use the VG.

In figure 4.33 we show the probability density against position x at the end of a 2 cycle pulse. We can see here that the wave packet spreads quicker and further than

before and many small oscillations build especially in the direction of the positive x axis. At these parameters we use a box of $[-1000, 1000]$ a.u. and it takes up to 2200 B-splines in the VG (red line) and 3000 in the LG (green line) to achieve convergence giving computation times of 1 hour in the VG and 2.5 hours in the LG. In addition the length gauge requires a much larger number of Krylov vectors due to the increase in stiffness of the system. In the velocity gauge we use 50 Krylov vectors whereas in the length gauge we need at least 80 considerably slowing down calculations. In addition we require a much higher density of B-splines per a.u. of box since the highly oscillating continuum solution requires a precise phase in order to be accurately represented in coordinate space. For a guide we see that the density of the B-splines can be taken to be [8]

$$\rho = \frac{1}{3}\frac{2\pi}{\sqrt{2 \times 10U_p}}. \tag{4.28}$$

For these laser parameters this gives a density of $\rho = 0.4$ B-splines per a.u. of box which for our box gives 2500 B-splines. In practice we found we could take the basis size and box size slightly smaller by lowering the values until the calculation was no longer converged.

The ionisation spectrum plotted against energy E can be seen in figure 4.34 for the 2 cycle pulse. It can be seen to be formed of more complex structures than spectra at higher frequencies and no discernible peaks predicted by equation (2.73) are visible. The reason for this is that tunnelling now controls the ionisation as indicated by the small value of γ. We can see that at very low energy there is a sharp rise in probability of ionisation which may be indicative of a beginning of an LES.

Raising the intensity to $I = 3 \times 10^{14}\mathrm{W} \cdot \mathrm{cm}^{-2}$ we note the electron travels much further in the two cycles. The asymmetry of the density is even more apparent here and the oscillations more rapid. Now we require a box of $[-1500, 1500]$ a.u. and 6500 B-splines to represent the wave function in the VG (red line) which takes a total computation time of around 9 hours to achieve convergence. In the LG it is now almost infeasible to carry out the calculations with the resources available. The

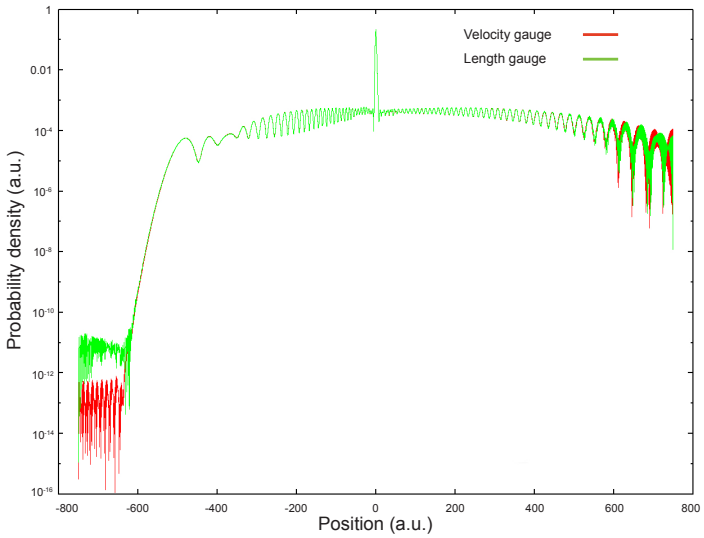

Figure 4.33: The electron probability density on a logarithmic scale at the end of the 2 cycle pulse of frequency $\omega = 0.0228$ a.u. and intensity $I = 10^{14}$ W $\cdot$ cm^{-2} described by equation (4.3). The density is shown for the velocity gauge (red) and the length gauge (green).

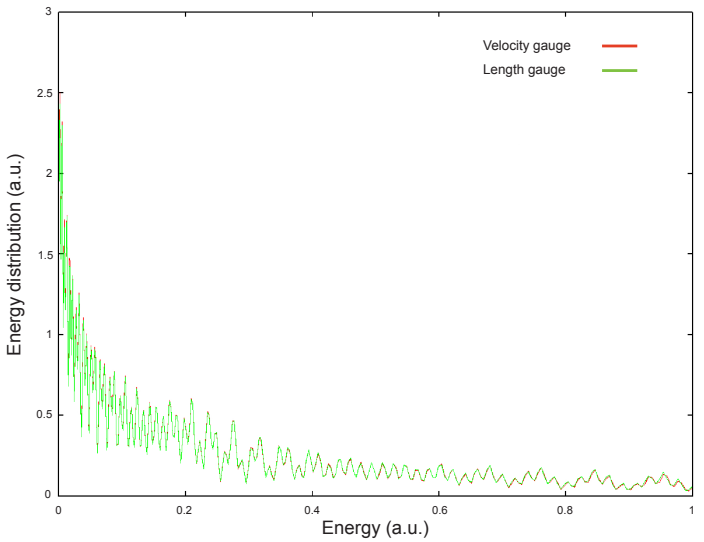

Figure 4.34: The photoelectron energy spectrum at the end of the 2 cycle pulse of frequency $\omega = 0.0228$ a.u. and intensity $I = 10^{14}$ W $\cdot$ cm^{-2} described by equation (4.3). The spectrum is shown for the velocity gauge (red) and the length gauge (green).

closest convergence obtainable on the computers we are currently using, calculated with 10000 B-splines, is shown for comparison (green line). We can see that the agreement is good near the centre however when the electron has propagated to large distances then the difference between the two gauges begins to show.

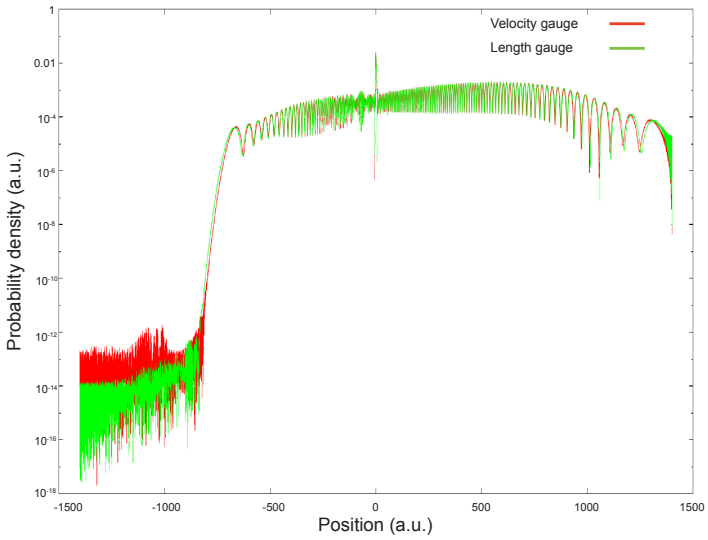

Figure 4.35: The electron probability density on a logarithmic scale at the end of the 2 cycle pulse of frequency $\omega = 0.0228$ a.u. and intensity $I = 3 \times 10^{14}$ W $\cdot$ cm^{-2} described by equation (4.3). The density is shown for the velocity gauge (red) and the length gauge (green).

We now look at a relatively high intensity and increase the number of cycles used meaning we can expect more rescattering and to see a larger low energy peak form on the ATI spectrum. In figure 4.36 we show the electron density against position x for a 4 cycle pulse of intensity 2.5×10^{14} W $\cdot$ cm^{-2}. At these parameters we now need a very large box of size $[-3000, 3000]$ a.u. and 7500 B-spline functions in the VG. The calculation took around 22 hours to complete.

In figure 4.37 we show the ATI spectrum against energy E for the parameters of figure 4.36. We see now that in comparison to figure 4.34 that the spectrum has greater amplitude for higher energies up to $E = 2.5$ a.u. since the ejected electrons have more time to absorb photons from the more intense pulse. For this case the ponderomotive potential is $U_p = 93.37$ eV $= 3.43$ a.u. and the Keldysh parameter is $\gamma = 0.27$ meaning we are in the tunnelling regime. As expected the spectrum

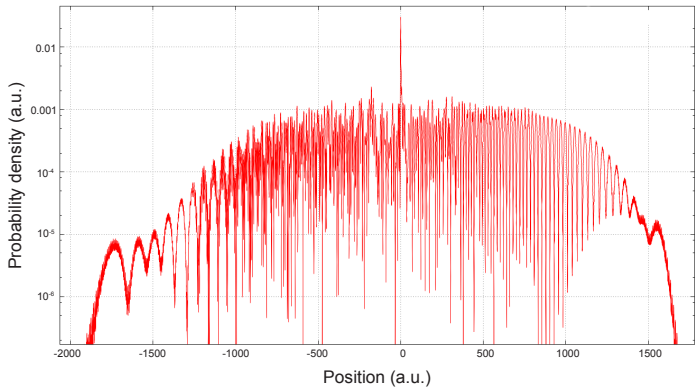

Figure 4.36: The electron probability density on a logarithmic scale at the end of the 4 cycle pulse of frequency $\omega = 0.0228$ a.u. and intensity $I = 2.5 \times 10^{14}$ W $\cdot$ cm^{-2} described by equation (4.3).

lacks the definite peak structure of the multiphoton regime and we now see a very large peak near the ionisation threshold. The peak is much more pronounced and of higher amplitude than of that seen using a 2 cycle pulse and is consistent with a LES.

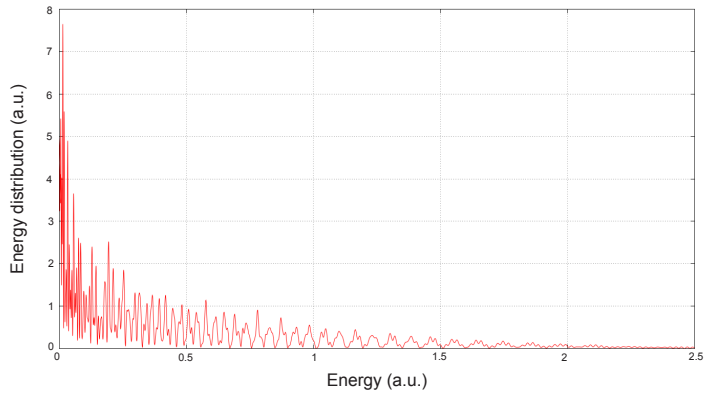

Figure 4.37: The photoelectron energy spectrum at the end of the 4 cycle pulse of frequency $\omega = 0.0228$ a.u. and intensity $I = 2.5 \times 10^{14}$ W $\cdot$ cm^{-2} described by equation (4.3).

Finally, we look at the continuum electron density at this frequency. We have yet to address one problem with calculation of the continuum density, that of gauge invariance. In figures 4.39 and 4.40 we look at the continuum density of the electron

throughout the first and second cycles respectively of a 2 cycle pulse in both the velocity gauge (VG) and the length gauge (LG). The times in which we show the density are marked by the black dots in figure 4.38. Plot a) shows the density at $t = 0.2$ optical cycles and we see that whilst the VG has clear density around the origin, the LG does not show any density on this scale. In b) we see the picture after 0.4 cycles and the VG calculation now shows a larger density at the origin whilst the LG is still negligible. At 0.5 cycles in c) we now see that the VG density has rapidly reduced in magnitude and appears with very small density in agreement with the LG at the origin. This agreement is due to the fact that this is the first time in the pulse that the vector potential $A(t)$ is zero and hence the shift in the continuum density is removed. At 0.6 cycles, in d), the density of the VG reverts back to its larger value and continues to rise now that $A(t)$ is non zero again. At 0.8 cycles in e) oscillations start to form in the negative x direction in both gauges although they are more prominent in the VG. At the end of the first cycle, in f), the gauges agree again and the LG density rises rapidly due to the burst in ionisation corresponding with the maximum in the electric field at that time. From g) (1.2 cycles) to the end of the pulse we see repetition of this behaviour with the VG having high density when $A(t) \neq 0$ and agreement in i) at 1.5 cycles and in l) at the end of the pulse. After 2 cycles we can see that the VG has convergence to the converged correct result and is in complete agreement with the LG.

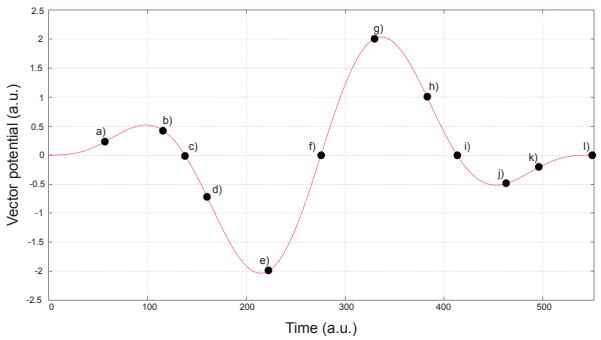

Figure 4.38: The vector potential for a 2 cycle pulse of frequency $\omega = 0.0228$ a.u. and intensity $I = 10^{14}$ W $\cdot$ cm^{-2} described by equation (4.3). The black dots show the positions of the continuum electron density calculations in figures 4.39 and 4.40.

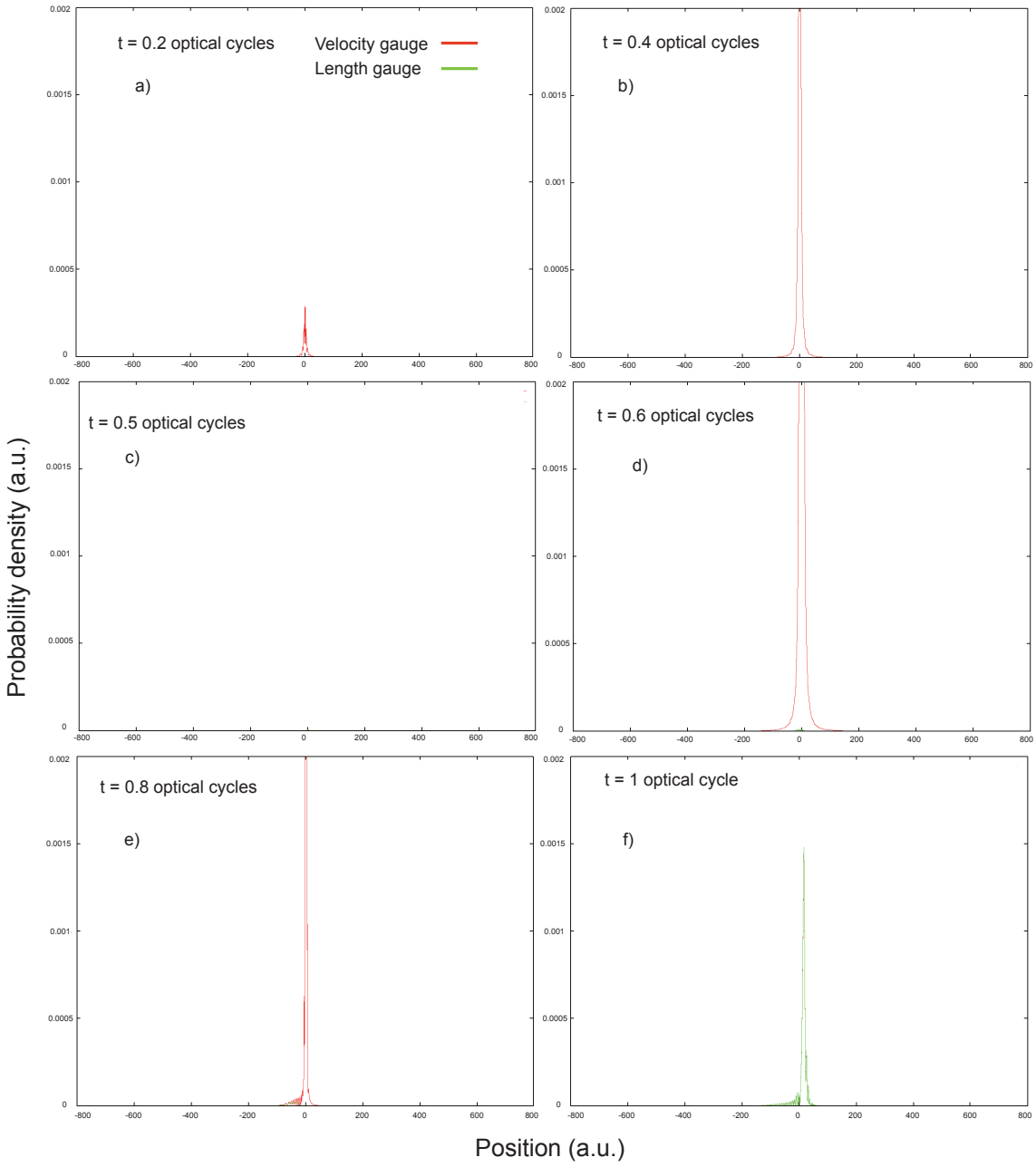

Figure 4.39: The continuum electron probability density throughout the first cycle of a 2 cycle pulse of frequency $\omega = 0.0228$ a.u. and intensity $I = 10^{14}$ W $\cdot$ cm^{-2} described by equation (4.3). The density is shown for the velocity gauge (red) and the length gauge (green) for times shown by the black dots in figure 4.38.

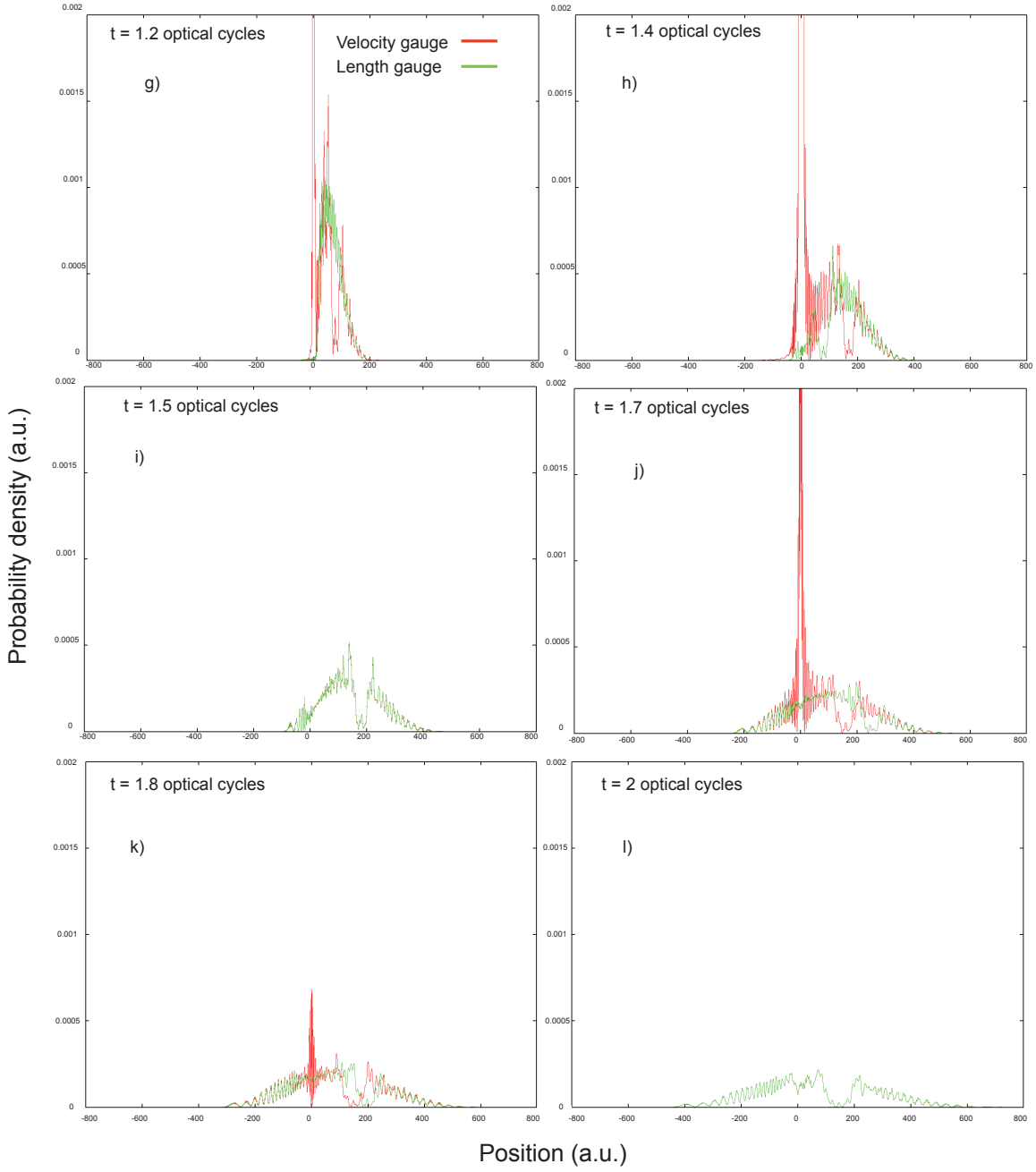

Figure 4.40: The continuum electron probability density throughout the second cycle of a 2 cycle pulse of frequency $\omega = 0.0228$ a.u. and intensity $I = 10^{14}$ W $\cdot$ cm^{-2} described by equation (4.3). The density is shown for the velocity gauge (red) and the length gauge (green) for times shown by the black dots in figure 4.38.

4.6.2 Intensity Averaged Cross Section

In the experiments on the LES the data obtained is averaged over the intensity profile of the laser. We now also take this into account. In an experimental laser, the radiation does not all carry the same intensity but rather has a peak intensity which then falls as we move away from the focal centre of the laser. In order to represent this we average over an intensity profile using the following equation [53]

$$W(E, I_0) = \int_0^{I_0} P(E, I) \left[\frac{\pi w_0^2 z_0}{3} \frac{1}{I} \left(\frac{I_0}{I} + 2 \right) \sqrt{\frac{I_0}{I} - 1} \right] \mathrm{d}I, \tag{4.29}$$

where $P(E, I)$ is the probability of finding the electron with a certain energy E for an intensity I, w_0 is the radius of the focal spot and I_0 is the peak intensity. We use the trapezium rule to evaluate the integral by calculating the spectrum over certain intervals and averaging for each value of E and below look at intervals of $0.05 \times 10^{14} \mathrm{W} \cdot \mathrm{cm}^2$ between $I = 0.5 \times 10^{14}$ W $\cdot$ cm^2 and $I = 1.5 \times 10^{14}$ W/cm^2. A basis set of 3000 B-splines was used with 6 Krylov vectors to calculate the original spectra.

Figure 4.41 shows this averaged spectrum. We can see that the peaks in the previous spectrum at this frequency shown in figure 4.34 are smoothed out by the averaging and we get a smoother spectrum. This is due to the mixture of intensities across the laser diameter resulting in a large number of different values for the ponderomotive potential U_p. This causes a broader range of electron kinetic energies on ionisation. We also see a large peak at $E \approx 0$ which may be indicative of a LES.

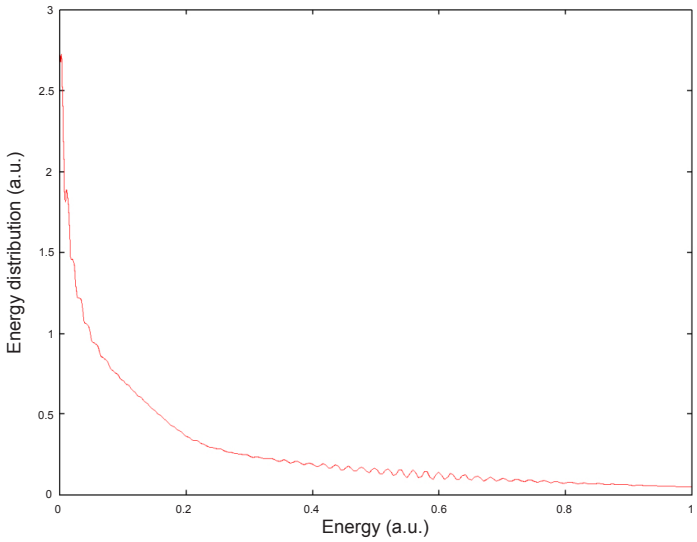

Figure 4.41: The intensity averaged cross section for a 2 cycle pulse of frequency $\omega = 0.0228$ a.u. and peak intensity $I_0 = 10^{14}$ W $\cdot$ cm^{-2} described by the vector potential (4.3).

4.6.3 Density Plots

We look again now at the evolution of electron momentum density. In figure 4.42 we look at the probability density over momentum p and time t for a 2 cycle pulse in the velocity gauge for an intensity of $I = 10^{14}\text{W} \cdot \text{cm}^{-2}$. In comparison to the wavelength of $\lambda = 800$nm we can see the amplitude of the momentum is much higher in this case and the larger quiver motion gives rise to a similar $A(t)$ 'form' but with higher amplitude. We see that during the first cycle the level of ionisation is low. This is due to the fact that at a frequency of $\omega = 0.0228$ a.u. it now takes 22 photons for the electron to have enough energy to escape the binding potential. As such there is very little ionisation after just a single cycle. Towards the end of the second cycle we can now see the formation of horizontal lines representing ionisation and interference begins to appear in the shape.

Figure 4.43 shows the same picture but for the higher intensity of $I = 3{\times}10^{14}\text{W} \cdot \text{cm}^{-2}$. At this higher intensity we can see a significant amount of ionisation occurs due to the strength of the field. We can see that around half way through the pulse, shortly after a peak in the amplitude of the electric field, many horizontal lines appear.

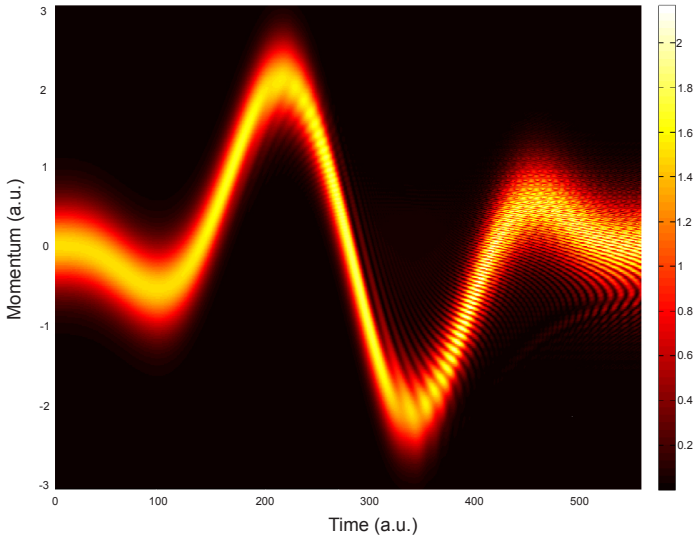

Figure 4.42: The evolution of the probability density $|\Psi(p,t)|^2$ in the p direction in momentum space in the velocity gauge throughout a pulse of 2 optical cycles of frequency $\omega = 0.0228$ a.u. and intensity $I = 10^{14}\mathrm{W}\cdot\mathrm{cm}^{-2}$ described by the vector potential (4.3).

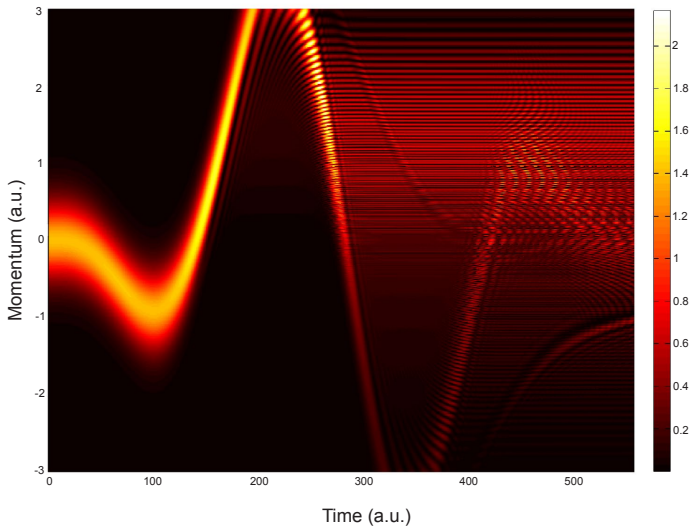

Figure 4.43: The evolution of the probability density $|\Psi(p,t)|^2$ in the p direction in momentum space in the velocity gauge throughout a pulse of 2 optical cycles of frequency $\omega = 0.0228$ a.u. and intensity $I = 3\times10^{14}\mathrm{W}\cdot\mathrm{cm}^{-2}$ described by the vector potential (4.3).

We now extend the time propagation to 4 optical cycles to see the resulting effect more rescattering. The necessary parameters are now very big and a box of over 1000 a.u. in each direction and 4000 B-splines are used. The calculation in the velocity gauge took around 52 hours. It must be noted that the computation time for these cases of calculating the momentum density over time is considerably higher than other calculations due to the fact that the Fourier transform of a large basis set must be computed at every time step. This means that the increase in basis size and the doubling of the number of time steps to investigate 4 optical cycles are particularly time consuming and considering higher intensities with 4 optical cycles was not feasible at this time. The momentum density evolution can be seen in figure 4.44 for this case. We can see by comparing figure 4.44 with figure 4.42 that the ionisation rate grows considerably in the second two optical cycles with horizontal lines appearing across a much larger range of momenta and at a higher density. We can also see the ionisation which was observed at the end of the two cycles in 4.42 continues as the pulse moves into the third cycle.

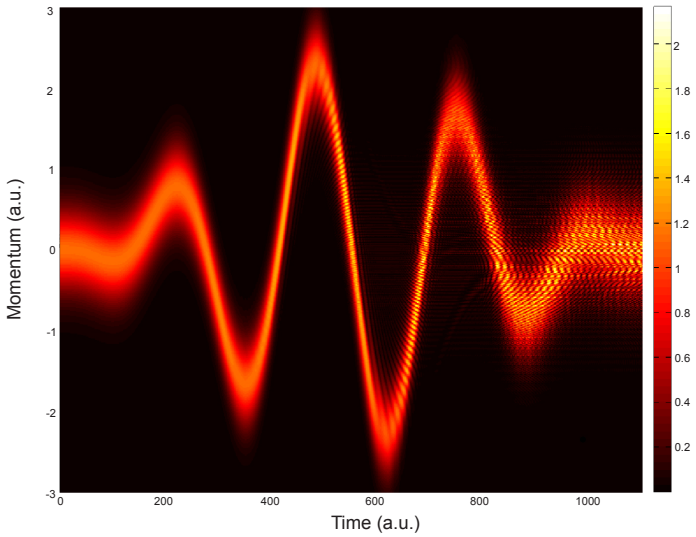

Figure 4.44: The evolution of the probability density $|\Psi(p,t)|^2$ in the p direction in momentum space in the velocity gauge throughout a pulse of 4 optical cycles of frequency $\omega = 0.0228$ a.u. and intensity $I = 10^{14}\mathrm{W}\cdot\mathrm{cm}^{-2}$ described by the vector potential (4.3).

Finally we look at the electron position density for an intensity of $I = 10^{14}\mathrm{W}\cdot\mathrm{cm}^{-2}$

over the 4 cycle period. In contrast to the same calculation over 2 cycles for $\lambda =$ 800nm we can see now that the movement in position is much more difficult to see due to the lower frequency causing less ionisation at higher energies. The number of photons needed to ionise means that over the 4 cycles movement is very limited and it is not until the final cycle that the movement can be clearly seen in the form of vertical lines emerging from the fixed path the bound electrons follow.

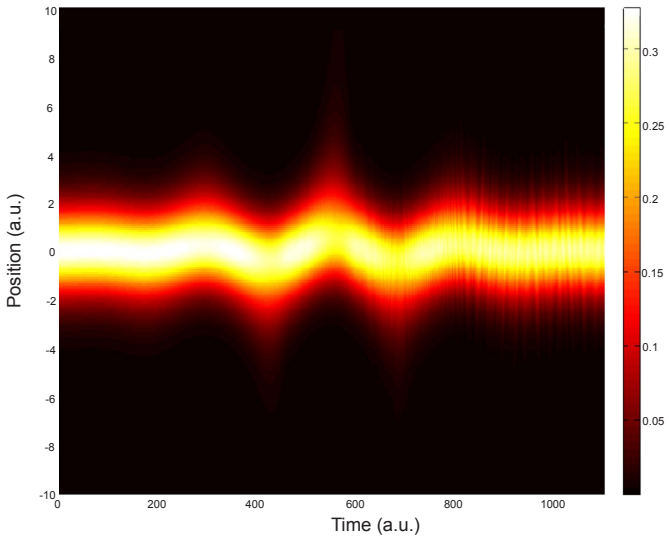

Figure 4.45: The evolution of the probability density $|\Psi(x,t)|^2$ in the x direction throughout a pulse of 2 optical cycles of frequency $\omega = 0.0228$ a.u. and intensity $I = 10^{14}\text{W} \cdot \text{cm}^{-2}$ described by the vector potential (4.3).

4.6.4 Ionisation Yield

We again look now at the ionisation yield and see how the lower frequency affects the ionisation probability. We again calculate the ionisation probability using the exterior complex scaling method (ECS) for intensities from 10^{11} to $3{\times}10^{14}$ W $\cdot$ cm^{-2}. Figure 4.46 shows this yield at the lower frequency for a 2 cycle pulse. We see again the yield rises steadily without ever dropping.

By directly comparing the cases for $\lambda = 800$nm and this lower frequency we can see how the frequency as well as the intensity affects the ionisation yield. Figure 4.47 shows this comparison with $\lambda = 800$nm in red and $\lambda = 2\mu$m in green. We can see

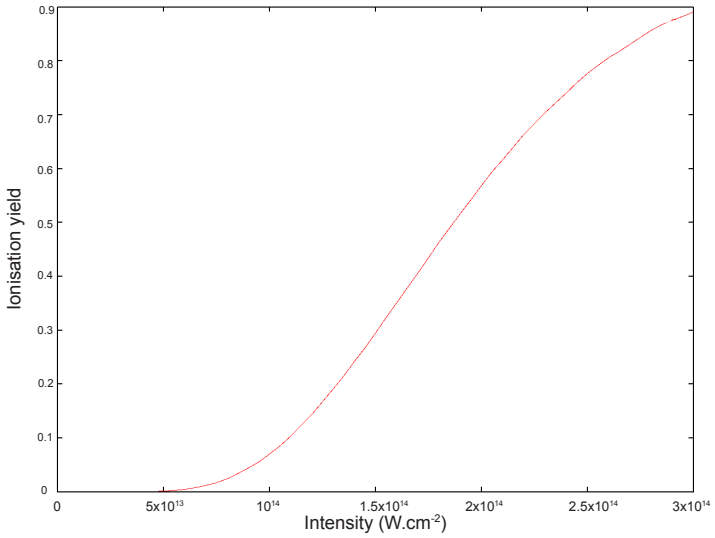

Figure 4.46: The ionisation yield as a function of intensity I, at the end of a 2 cycle pulse of frequency $\omega = 0.0228$ a.u. given by equation (4.3).

that at low intensity the low frequency laser struggles to ionise the atom and more ionisation occurs at the higher frequency. However at around $I = 7.5\times10^{13}$ W $\cdot$ cm^{-2} the ionisation yield rises quickly for the low frequency and overtakes and from that intensity upwards we see more ionisation for the $\lambda = 2\mu$m case.

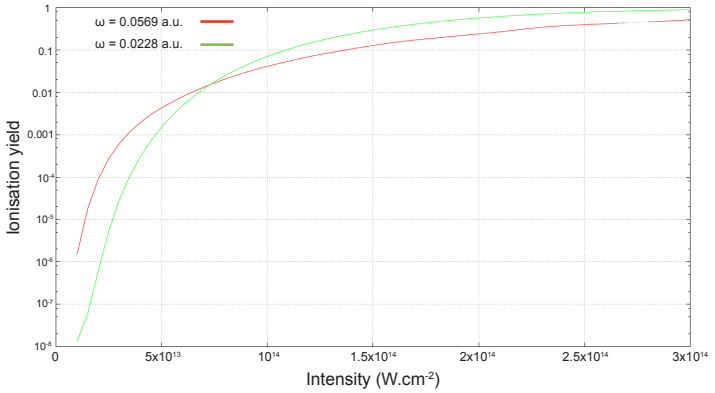

Figure 4.47: The ionisation yield as a function of intensity I, on a logarithmic scale, at the end of a 2 cycle pulse of frequency $\omega = 0.0569$ a.u. (red) and 0.0228 a.u. (green) given by equation (4.3).

Figure 4.48 shows the low frequency picture for a 4 cycle pulse. Again, as in figure 4.12 for 800nm, we can see now that the ionisation yield dips periodically at certain

intensities with the first dip this time around the higher intensity of $I = 2.2 \times 10^{14}$ W $\cdot$ cm^{-2} however this time the dips are not as pronounced and occur less often. This shows that the unexpected behaviour that occurred at $\omega = 0.0569$ a.u. is not frequency dependent. In addition we have seen that this effect occurs for Keldysh parameters values of $\gamma = 1.067$ for 800nm and for $\gamma = 0.427$ for 2000nm meaning it is not exclusive to any ionisation regime.

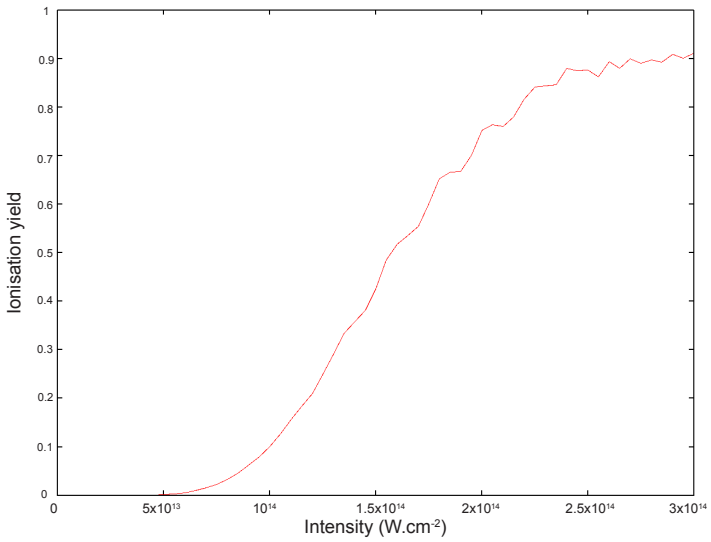

Figure 4.48: The ionisation yield as a function of intensity at the end of a 4 cycle pulse for the electric field given by equation (4.3).

4.6.5 Probability Current

We now see how the increase in wavelength affects the evolution of the probability flux. In figures 4.50 and 4.51 we show the probability current against time for an intensity of $I = 10^{14}$ W $\cdot$ cm^{-2} for 2 cycles and at positions $x_0 = 40$ a.u. (red line) and $x_0 = -40$ a.u. (green line) for $\varphi = 0$ and $\varphi = \pi/2$ respectively. By looking at the two phases we can investigate how the shape of the pulse changes the probability current in addition to the wavelength. Figure 4.49 shows the electric field against time for the phase $\varphi = 0$ (red line) and $\varphi = \pi/2$ (green line). We can see the main difference is that $\varphi = 0$ has a single maximum peak at $t = \tau/2$ whereas $\varphi = \pi/2$ has a maximum and a minimum of equal amplitude as $t \simeq 220$ and 330 a.u.

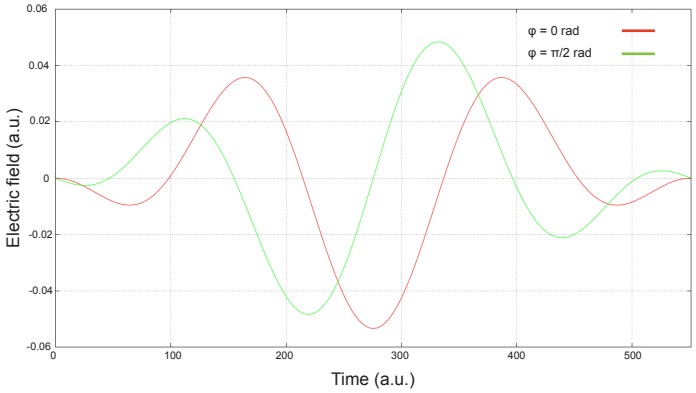

Figure 4.49: The vector potential $A(t)$ as described by equation (4.3) with $\varphi = 0$ (red) and $\pi/2$ (green).

For the phase of $\varphi = 0$ we can see that the number of oscillations has increased considerably in comparison to the calculations at 800nm although the current keeps the same form of having almost zero amplitude up until the second cycle before a large increase in positive current and then a switch to negative current. This is due to the shape of the pulse remaining the same as in the previous calculations and tunnelling remaining the dominant ionisation mechanism. In the negative x direction we see again a similar pattern with the direction of the field being in the negative direction by the time the flux reaches $x_0 = -40$ a.u.

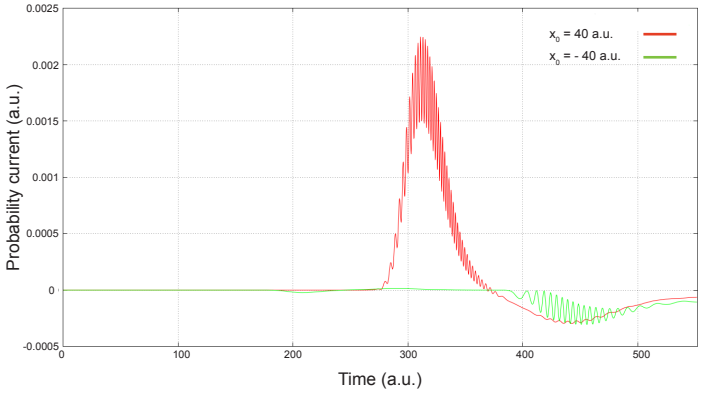

Figure 4.50: The probability current at positions $x_0 = 40$ a.u. (red) and $x_0 = -40$ a.u. throughout a 2 cycle pulse of frequency $\omega = 0.0228$ a.u. and intensity $I = 10^{14}$ W $\cdot$ cm^{-2} described by (4.3) with $\varphi = 0$.

For the phase $\varphi = \pi/2$ we can see that the direction of the probability current is largely unchanged by adding the phase. We can see the large peaks of positive and negative flux are shifted to earlier times as the phase moves the corresponding peak to earlier times in the electric field. We see that the amplitude of the negative current has risen considerably and this is attributed to the appearance of the peak of positive amplitude in the electric field at $t \simeq 110$ a.u. This means that tunnel ionisation occurs in the negative x direction first before the field changes sign. The appearance of two large peaks of equal amplitude instead of just one gives rise to more oscillation in the probability current due to an increase of interference between wave packets ejected at each peak. This effect, termed the double slit ionisation, has been investigated thoroughly by Arbo et al. [5].

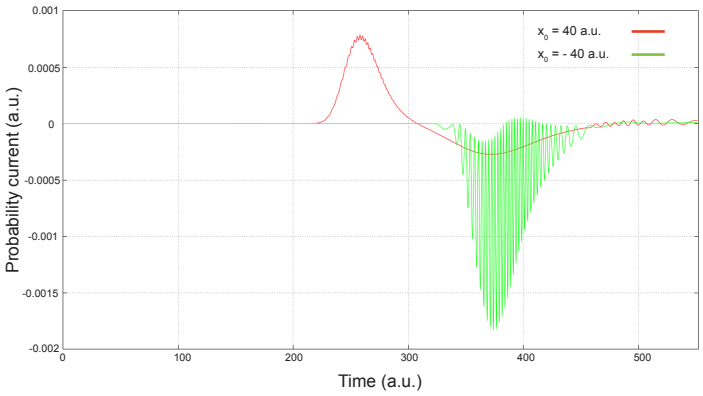

Figure 4.51: The probability current at positions $x_0 = 40$ a.u. (red) and $x_0 = -40$ a.u. throughout a 2 cycle pulse of frequency $\omega = 0.0228$ a.u. and intensity $I = 10^{14}$ W $\cdot$ cm^{-2} described by (4.3) with $\varphi = \pi/2$.

4.6.6 Tracking the Wave Packet

We look again at tracking the wave packet by considering the probability of finding the electron on a surface of radius r throughout the duration of the laser pulse. We take the case of a two cycle pulse of intensity 2.5×10^{14}W $\cdot$ cm^{-2}. In figure 4.52 we show the probability density of finding the wave packet within a radius of $r = 5.33$ a.u. (red line), 10.13 a.u. (green line), 15.47 a.u. (blue line) and 20.27

a.u. (pink line) against time. The main feature observed here is the very steep drop in probability at the minimum amplitude of the electric field at $t \simeq 300$. Only the smallest radius of $r = 5.33$ a.u. shows other major oscillations at the two maximums of the field around $t \simeq 300 \pm 115$ a.u. as well as many small oscillations towards the end of the pulse due to interference between wave packets ejected at different times. In addition, only this radius shows a sharp increase in probability after the drop at the end of the first optical cycle. This is due to very slow electrons which are ionised at the minimum of the field but only travel to just outside this radius and return immediately when the field changes direction. The populations of the radii $r > 5.33$ a.u. remain constant during this turning point in the field.

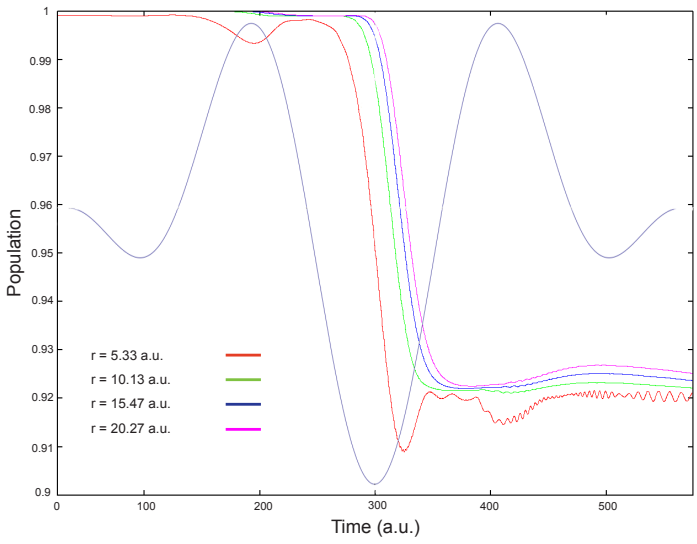

Figure 4.52: The probability of finding the wave packet within a radius of $r = 5.33$ a.u. (red), 10.13 a.u. (green), 15.47 a.u. (blue) and 20.27 a.u. (pink) throughout a 2 cycle pulse of frequency $\omega = 0.0228$ a.u. and intensity $I = 2.5 \times 10^{14}$ W $\cdot$ cm^{-2} defined by the vector potential (4.3). Also shown is the electric field on an arbitrary scale.

We now extend the calculation to 4 optical cycles. In figure 4.53 we show the probability of finding the wave packet on a surface of radius r against time t throughout the pulse. We now take r to be the values 5.33 a.u. (red line), 20.13 a.u. (green line) and 50.47 a.u. (blue line). With these widely varying radii we will be able to accurately locate the position of the wave packets throughout the pulse but choosing

different radii and comparing probabilities within these radii. We see again that we get a staircase structure meaning the electrons do not return to within the radius during the pulse. The only exception to this is at the midpoint of the calculation when there is a large negative amplitude of the field shortly after a positive peak. We see slight rises in the probability here due to the strength of the field at this time. Furthermore, the ionisation occurs at the points of maximum electric field, suggesting tunnelling is the dominant mechanism for ionisation

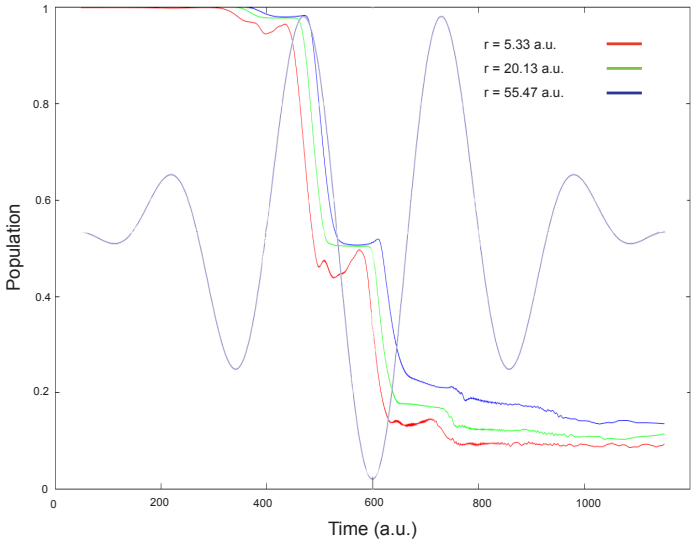

Figure 4.53: The probability of finding the wave packet within a radius of $r = 5.33$ a.u. (red), 20.13 a.u. (green) and 50.47 a.u. (blue) throughout a 4 cycle pulse of frequency $\omega = 0.0228$ a.u. and intensity $I = 2.5 \times 10^{14}$ W $\cdot$ cm^{-2} defined by the vector potential (4.3). Also shown is the electric field on an arbitrary scale.

4.7 Time Dependent Surface Flux Method

Recently a new method of computing strong field photoionisation spectra by solving the TDSE on minimal simulation volumes was devised by Tao and Scrinzi [73], the time dependent surface flux method (tSURFF). It is particularly suited to be used in conjunction with exterior complex scaling. We have implemented it for the first time using B-splines. The method takes advantage of the fact that even very short pulses, when at high intensity and low frequency, cause the electron to travel long

distances. For an example, a laser of wavelength 800nm of one optical cycle, lasting just 100 a.u. of time can cause an electron in the ground state to travel out to a distance of greater than 110 a.u. meaning the box size must be made large even for a short pulse. Rather than letting the system evolve and analysing it at the end of the evolution, this method works by recording the particle flux leaving a finite volume throughout a specified time integration of duration T. Such a procedure does not require the complete wave function, but only that at a certain radius and as such our box can be made much smaller.

We choose a surface radius x_c large enough so that the particle motion can be considered free and that all occupied bound states of the system are inside the radius. We also pick a sufficiently large time T such that all particles with energy $E = k^2/2$ that will ever reach our detector are outside the finite volume $|x| < x_c$. The wave function can then be separated into bound and continuum parts

$$\Psi(x,t) = \Psi_b(x,T) + \Psi_c(x,T) \tag{4.30}$$

where

$$\Psi_b(x,T) \approx 0 \quad \text{for} \quad |x| > x_c \tag{4.31}$$

and

$$\Psi_c(x,T) = \int \mathrm{d}k \; b(k)\psi_k(x) \approx 0 \quad \text{for} \quad |x| \leq x_c \tag{4.32}$$

where $b(k)$ are the spectral amplitudes given by

$$b(k) = \langle \psi_k | \Psi(T) \rangle \mathrm{e}^{-\mathrm{i}Tk^2/2} \tag{4.33}$$

and ψ_k are the scattering solutions with the asymptotic behaviour of plane waves. We use approximate signs instead of equals due to the fact that very slow electrons with $k \approx 0$ may have not reached x_c by the time T. We can obtain the photoelectron spectra amplitudes using equation (4.33) and define them as

$$e^{iTk^2/2}b(k) = \langle\psi_k|\Psi(T)\rangle \approx \langle\psi_k|\Theta(x_c)|\Psi(T)\rangle \approx \langle\chi_k|\Theta(x_c)|\Psi(T)\rangle \tag{4.34}$$

where χ_k are plane waves and $\Theta(x_c)$ is a step function defined by

$$\langle\psi_k|\Theta(x_c)|\Psi(T)\rangle = \int_{|x|>x_c} dx\ \psi_k^*(x)\Psi_c(x,T). \tag{4.35}$$

We convert the above matrix element to a time-integral over surface values and for that we define a *channel Hamiltonian,* $\hat{H}_{\text{chan}}$, such that

$$\hat{H}_{\text{chan}} = H(t) \quad \text{for} \quad |x| > x_c. \tag{4.36}$$

For the case of a short range potential $V(x) = 0$ for $|x| > x_c$, this is exactly the Volkov Hamiltonian defined in section 2.5.2 since the lack of long range potential means that we just have a free electron in a laser field. For the case of a general potential we can write [73]

$$\begin{aligned}
\langle\chi_k|\Theta(x_c)|\Psi(T)\rangle &= \int_0^T dt\ \frac{d}{dt}\langle\chi_k|\Theta(x_c)|\Psi(T)\rangle \\
&= i\int_0^T \langle\chi_k|\hat{H}_{\text{chan}}(t)\Theta(x_c) - \Theta(x_c)\hat{H}(t)|\Psi_c(x,t)\rangle \\
&= i\int_0^T \langle\chi_k|\left[-\frac{1}{2}\frac{d^2}{dx^2} - iA(t)\frac{d}{dx}, \Theta(x_c)\right]|\Psi_c(x,t).
\end{aligned} \tag{4.37}$$

The commutator vanishes everywhere except on the surface x_c and thus becomes

$$\left[-\frac{1}{2}\frac{d^2}{dx^2} - iA(t)\frac{d}{dx}, \Theta(x_c)\right] = -\delta(x-x_c)\frac{d}{dx} - \frac{1}{2}\delta'(x-x_c) - iA(t)\delta(x-x_c) \tag{4.38}$$

The integral then becomes

$$\langle\chi_k|\Theta(x_c)|\Psi(T)\rangle = i\int_0^T \int_{-x_{max}}^{x_{max}} \chi_k(t)^*\left[-\delta(x-x_c)\Psi' - \frac{1}{2}\delta'(x-x_c)\Psi - iA(t)\delta(x-x_c)\Psi\right]dxdt \tag{4.39}$$

where we have dropped the subscript for Ψ. The one dimensional Volkov solution is given by

$$\chi_k^*(t) = \frac{1}{\sqrt{2\pi}} \mathrm{e}^{-\mathrm{i}kx} \mathrm{e}^{\mathrm{i}(k\alpha(t)+k^2/2t)}. \tag{4.40}$$

Using the properties of the δ-function we can eliminate the integral over position. Putting in the definition for χ we are left with just an integral over time of the form

$$\langle \chi_k | \Theta(x_c) | \Psi(T) \rangle = \frac{\mathrm{i}}{\sqrt{2\pi}} \int_0^T \mathrm{e}^{\mathrm{i}(k\alpha(t)+k^2/2t)} \mathrm{e}^{-\mathrm{i}kx_c} \left[-\frac{1}{2}\Psi'(x_c,t) - \frac{\mathrm{i}k}{2}\Psi(x_c,t) - \mathrm{i}A(t)\Psi(x_c,t) \right] \mathrm{d}t. \tag{4.41}$$

Hence the photoelectron spectrum can be calculated as

$$|b(k)|^2 = |\frac{1}{\sqrt{2\pi k}} \int_0^T \mathrm{e}^{\mathrm{i}(k\alpha(t)+k^2/2t)} \mathrm{e}^{-\mathrm{i}kx_c} \left[\frac{k}{2}\Psi(x_c,t) + A(t)\Psi(x_c,t) - \frac{\mathrm{i}}{2}\Psi'(x_c,t) \right] \mathrm{d}t|^2 \tag{4.42}$$

at the points $\pm x_c$ in order to measure the flux in the positive and negative x directions. We also include an extra factor of $1/\sqrt{k}$ in the constant before the integrand for energy normalisation. The method can be extended to a full three dimensional system with a laser linearly polarised in the z direction by replacing the commutator in (4.37) with [73]

$$\left[-\frac{1}{2}\Delta - \mathrm{i}A(t)\frac{\partial}{\partial z}, \Theta(R_c) \right] = -\frac{1}{2}\frac{1}{r^2}\frac{\partial}{\partial r} r^2 \delta(r-R_c) - \frac{1}{2}\delta(r-R_c)\frac{\partial}{\partial z} - \mathrm{i}A(t)\cos(\theta)\delta(r-R_c) \tag{4.43}$$

and replacing the Volkov solution with the 3D Volkov solution defined in section 2.5.2.

In section 4.8 we show that the tSURFF method allows us to obtain results which are very accurate within the unscaled area whilst allowing us to reduce the size of the box we need to carry out our computations by more than a factor of 2. This large reduction of box size and therefore the basis size is particularly important for the very low frequency systems we will investigate.

4.8 Exterior Complex Scaling and tSURFF Results

We now show results of our implementation of the Exterior Complex Scaling (ECS), from section 3.5, which we show can be used to considerably reduce the size of the computations needed as well as those of the tSURFF method described in section 4.7. We show that the ECS rotation and exponential dampening of the wave function can occur without loss of accuracy within the inner unscaled region even for very low frequencies where there are many small oscillations and the low energy of the photons means that the ionisation probability remains low during the pulse.

Using the methods previously mentioned, projection onto continuum states and the window operator method, we would have to calculate the full wave function up to large distances. By using tSURFF we allow the spectrum to be calculated at a certain point in space and therefore we do not need to know the values of the wave function beyond this point. As such it is very beneficial to use the ECS and tSURFF in tandem to dramatically speed up calculations to calculate the ATI spectrum whilst still being able to compute the electron density within the unscaled region.

Since the tSURFF method in this form works for short range potentials we revert back to the Gaussian potential of the form

$$V(x) = -V_0 \mathrm{e}^{-\beta x^2} \tag{4.44}$$

which can be easily modified using the potential parameters V_0 and β in order to alter the ionisation potential and number of bound states as seen in table 3.1.

In order to show the correlation between the tSURFF method and the length of the time integration T, we begin with a simple case of a high laser frequency of $\omega = 0.7$ a.u. for the potential parameters $V_0 = 1$ and $\beta = 1$ which gives a single bound state of energy $E = -0.47$ a.u. For this case we get a solitary peak in the ATI spectrum centred at an energy $E = \omega - I_p = 0.23$ a.u. which can be seen in figure 4.54 in pink. Here since we are looking at a relatively large frequency we calculate the full unscaled set of results. We can see how if the time integration in equation (4.42) is stopped at the end of the pulse, so $T = \tau$ then the spectrum returned is

flat and incorrect (red line). This is due to the fact that a lot of the electrons that need to be measured will reach the detector at a time $t > \tau$ and by stopping the integration at the end of the pulse we are not counting all electrons. By increasing T so that $T = 2\tau$ (green line) nearly all of the electrons have now been counted and the spectrum looks very similar to the exact spectrum. Increasing T again to $T = 4\tau$ gives a tSURFF spectrum identical to the exact spectrum computed using projection methods described earlier.

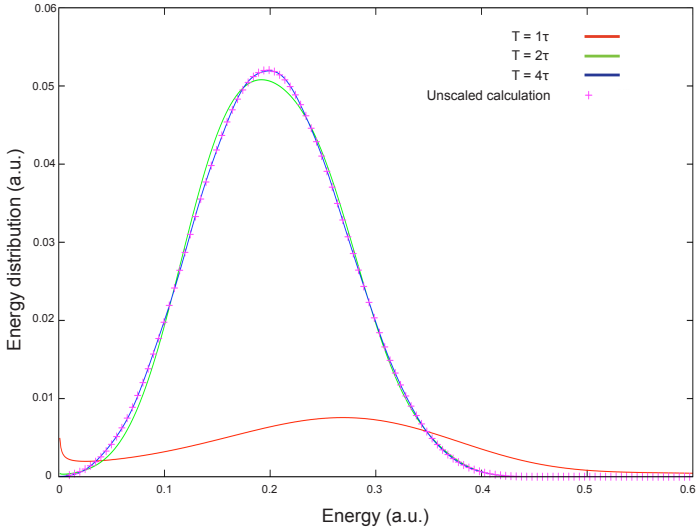

Figure 4.54: The ATI spectrum for the Gaussian potential given by (4.44) with $V_0 = 1$ and $\beta = 1$ for a pulse of frequency $\omega = 0.7$ and intensity $I = 10^{14}$ W $\cdot$ cm^{-2} described by equation (4.3) with total integration time $T = 2\tau$, 3τ and 4τ, compared with the exact result calculated using projection onto continuum states.

We now decrease the frequency to $\omega = 0.5$ a.u. which corresponds to a wavelength of $\lambda = 91$nm and take Gaussian potential parameters of $V_0 = 4$ and $\beta = 0.1$ which gives 7 bound states with a ground state energy of $E = -3.57$ a.u. Due to this large ionisation potential we use a high intensity of $I = 10^{16}$ W $\cdot$ cm^{-2} to allow for a reasonable amount of ionisation without saturating the atom. In order to ensure our ECS calculations are accurate we first run the full unscaled calculation with a box size of $[-350, 350]$ a.u. and 1400 B-splines. The electron density can be seen in figure 4.55 against position x with the unscaled density in red and the scaled densities with scaling points $x_0 = 5$ a.u. (green line), 15 a.u. (blue line) and

20 a.u. (pink line) for a scaling angle of $\theta = 0.2$ radians. The scaling angle can be altered without changing the inner unscaled area. We can see that, whilst the unscaled density carries on until around 300 a.u. the scaled densities are damped immediately at the scaling point and drop quickly to negligible amplitude causing no reflections and ensuring the inside scaled area is exact. In each case we used a box size of $[-70, 70]$ a.u. and 280 B-splines, although for the smallest scaling radius we can lower these parameters further. The calculation took 148s for the unscaled case and just 11s for the ECS calculations. Both calculations were carried out using a single processor on the laptop.

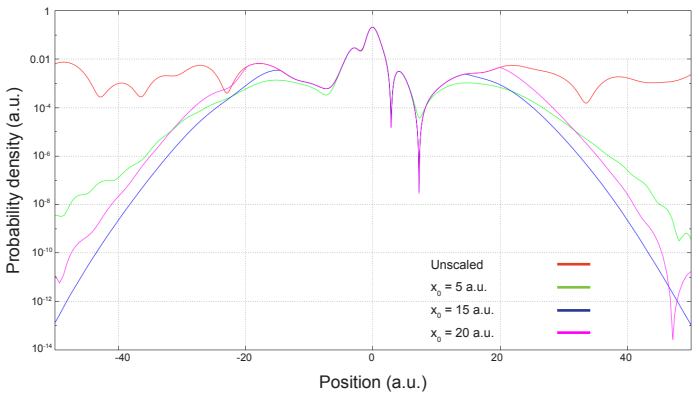

Figure 4.55: The electron probability density at the end of an 8 cycle pulse of frequency $\omega = 0.5$ a.u. and intensity $I = 10^{16}$ W $\cdot$ cm^{-2} given by (4.3). Shown is the full unscaled density (red) and the scaled density carried out using ECS with scaling points $x_0 = 5$ a.u. (green), 15 a.u. (blue) and 20 a.u. (pink) for a scaling angle of $\theta = 0.2$ rad.

The scaling position is arbitrary and can be picked for any value without affecting the unscaled inner area. The smaller we take x_0 to be the smaller we can take x_{max} and the lower the number of basis functions needed. The only restriction we have is that the scaling position must be taken to be larger than the size of the largest bound state of the atom. For an example, figure 4.56 shows the result if we take the scaling position to be within the size of the bound states. We use $x_0 = 2$ a.u. and clearly the density is incorrect and no convergence can be obtained.

We next look at the tSURFF calculation of the ionisation spectrum for these pa-

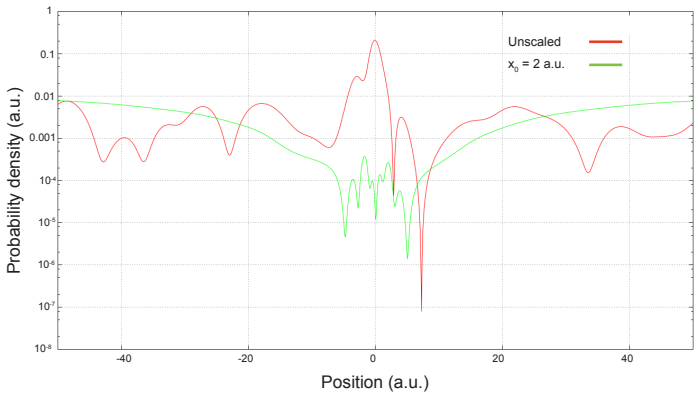

Figure 4.56: The electron density at the end of an 8 cycle pulse of frequency $\omega = 0.5$ a.u. and intensity $I = 10^{16}$ W $\cdot$ cm^{-2} given by (4.3). Shown is the full unscaled density (red) and the scaled density carried out using ECS with scaling point $x_0 = 2$ a.u. (green) for a scaling angle of $\theta = 0.2$ rad.

rameters. The ponderomotive potential for this case is $U_p = 7.73$ eV which gives a value for the Keldysh parameter of $\gamma = 2.5$ putting us firmly in the multiphoton regime. As such we see well defined peaks in the ATI spectrum separated by the photon energy. For the tSURFF calculation the only restrictions we have are that the surface radius must be placed outside the quiver amplitude of the electron, which for this case $\alpha = E_0/\omega^2 = 2.135$ a.u. and also that it is not placed on the scaled region of the mesh. We therefore place the detector at the first mesh point inside the scaling radius $x_0 = 30$ a.u. and use $T = 4\tau$ for the length of the time integration. In figure 4.57 we show the calculation of the ATI spectrum using two methods, firstly by calculating the spectrum by projection onto continuum states (red line) and secondly by using the tSURFF method using the above parameters with the ECS method. On comparison we can see that the agreement is very good throughout the spectrum.

To show the accuracy of the ECS method we plot the electron density as a function of position and time to best show its evolution. By comparing the unscaled and scaled versions of these plots we show very clearly the effectiveness of the ECS and how the inner unscaled part of the density is unchanged. To further show this we also remove the bound states from the calculations in figure 4.58 where we show the

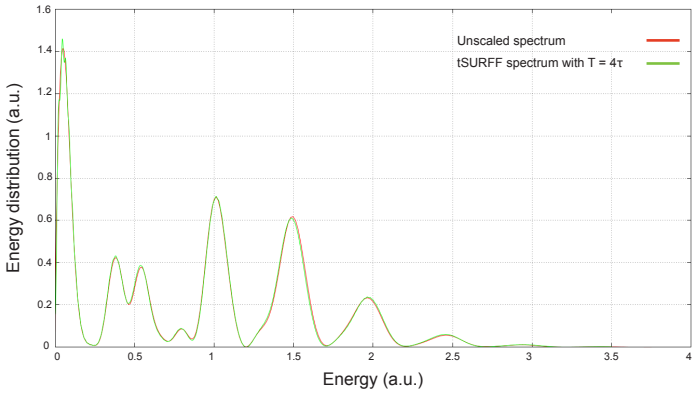

Figure 4.57: The ATI spectra at the end of an 8 cycle pulse of frequency $\omega = 0.5$ a.u. and intensity $I = 10^{16}$ W $\cdot$ cm^{-2} given by (4.3). Shown is the spectrum calculated using projection onto continuum states (red) and using tSURFF with ECS with scaling point $x_0 = 30$ a.u. (green) for a scaling angle of $\theta = 0.2$ rad and length of time integration $T = 4\tau$.

unscaled continuum density for this case. For the density plots at other frequencies we had a very bright thick curve oscillating around the origin making it more difficult to see signs of ionisation. We now have zero amplitude until around 35 a.u. of time where the first ionisation occurs. We can then see the electron trajectories as they move away from the ionised atom as well as the times of highest ionisation when the plot is brightest.

Figure 4.59 shows the same plot, but now we implement the ECS method with $x_0 = 30$ a.u. and $\theta = 0.2$ rad. Upon inspection we can see that the region $|x| \leq 30$ a.u. are identical whilst for $x > 30$ a.u. and $x < -30$ a.u. the graph is black, indicating zero density.

We now examine the probability density as a function of momentum p and time t to see how the ECS method affects the momentum distribution. Figure 4.60 shows the canonical momentum density calculated in the unscaled case. We again see the horizontal lines corresponding to ionsation which occur at times in agreement with the electron continuum density plot in figure 4.58.

Figure 4.61 shows the same calculation using the ECS. We see it is identical in places to the unscaled plot apart from the horizontal lines at momenta $p > 1$ a.u.

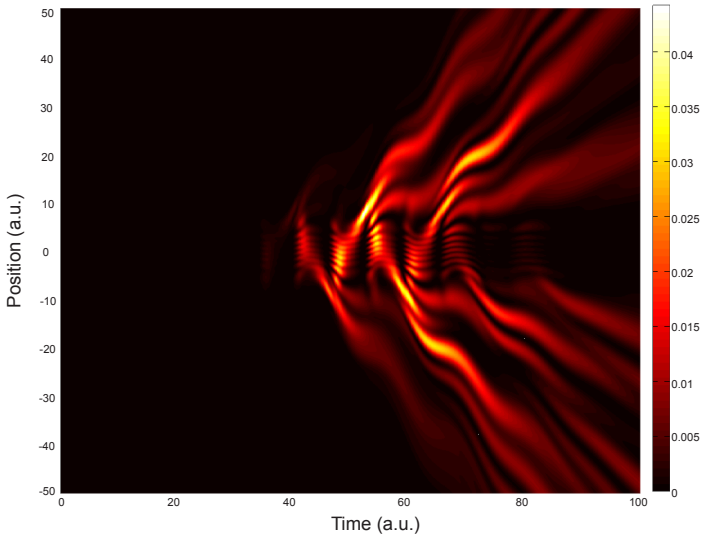

Figure 4.58: The evolution of the continuum probability density $|\Psi^c(x,t)|^2$ in the x direction throughout a pulse of 8 optical cycles of frequency $\omega = 0.5$ a.u. and intensity $I = 10^{16}$ W $\cdot$ cm^{-2} described by (4.3).

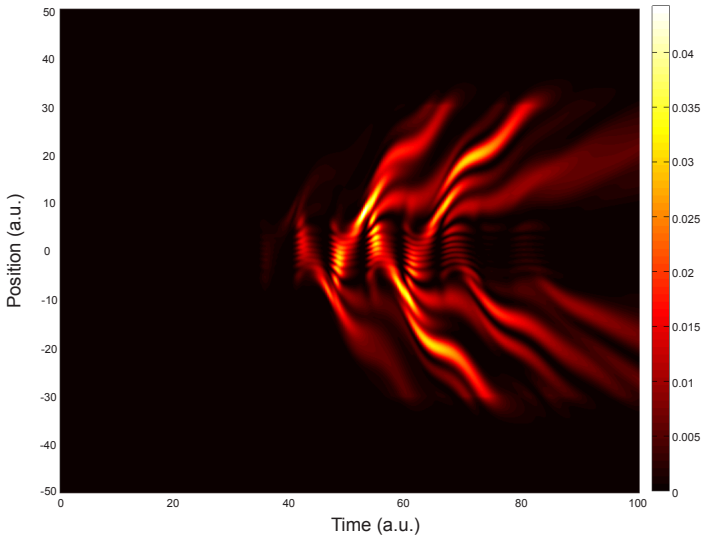

Figure 4.59: The evolution of the continuum probability density $|\Psi^c(x,t)|^2$ in the x direction throughout a pulse of 8 optical cycles of frequency $\omega = 0.5$ a.u. and intensity $I = 10^{16}$ W $\cdot$ cm^{-2} described by (4.3) using ECS with $x_0 = 30$ a.u. and $\theta = 0.2$ rad.

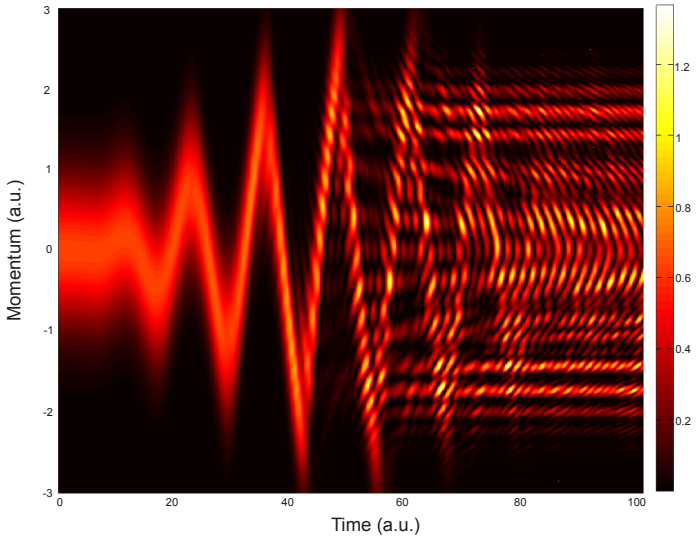

Figure 4.60: The evolution of the probability density $|\Psi(p,t)|^2$ in the p direction in momentum space in the velocity gauge throughout a pulse of 8 optical cycles of frequency $\omega = 0.5$ a.u. and intensity $I = 10^{16}$ W $\cdot$ cm^{-2} described by (4.3).

and $p < -1$ a.u. are now missing in the scaled picture. This is because once ionised these fast electrons travel beyond the unscaled area and are absorbed into the complex plane.

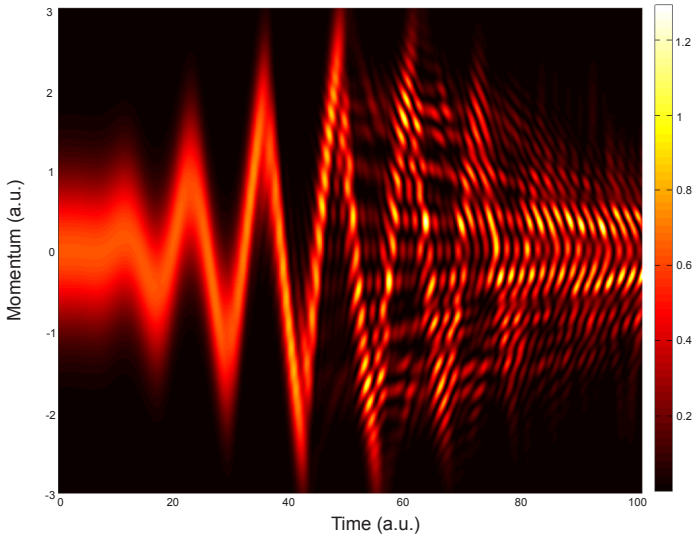

Figure 4.61: The evolution of the probability density $|\Psi(p,t)|^2$ in the p direction in momentum space in the velocity gauge throughout a pulse of 8 optical cycles of frequency $\omega = 0.5$ a.u. and intensity $I = 10^{16}$ W $\cdot$ cm^{-2} described by (4.3) using ECS with $x_0 = 30$ a.u. and $\theta = 0.2$ rad.

We now look at the more challenging case of $\lambda = 800$nm. Up until now we have been using a short range Gaussian potential and here we show that the ECS is fully compatible with the long range soft Coulomb potential as well. Figure 4.62 shows the comparison between unscaled and exterior complex scaled electron density for intensity $I = 3 \times 10^{14}$ W $\cdot$ cm^{-2} and for scaling points $x_0 = 20$ a.u. and $x_0 = 50$ a.u. An interesting feature when using a long range potential is that the density will immediately rise for x slightly larger than x_0 before tending to zero. This is seen in figure 4.62 when x_0 is chosen to be within the quiver amplitude of the electron, which in this case is $\alpha = 28.556$ a.u. When x_0 increases to a greater value than α then the probability damps as usual without first rising.

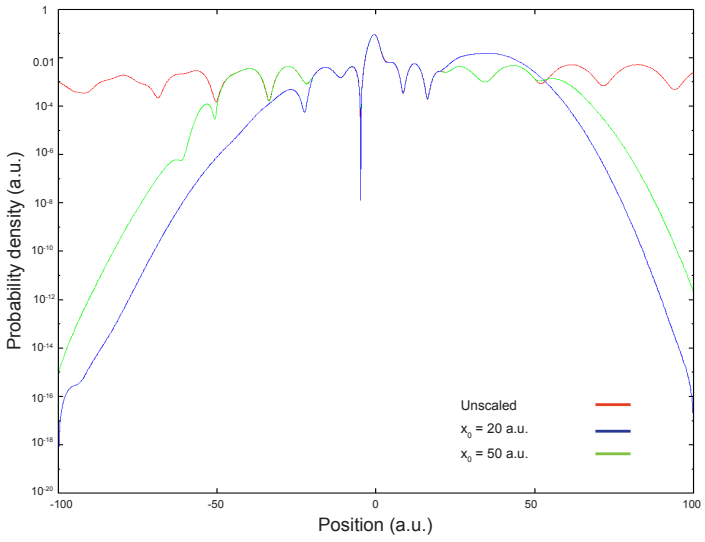

Figure 4.62: The electron probability density at the end of a 2 cycle pulse of frequency $\omega = 0.0569$ a.u. and intensity $I = 3 \times 10^{14}$ W $\cdot$ cm^{-2} described by (4.3). Shown is the full unscaled density (red) and the scaled density carried out using ECS with scaling points $x_0 = 20$ a.u. (blue) and 50 a.u. (green) for a scaling angle of $\theta = 0.5$ rad.

The scaling angle θ should have no effect on any calculations made within the unscaled area such as the ATI spectrum using the tSURFF method. Figure 4.63 shows how changing the scaling angle affects the damping of the wave function and in turn the value $x_{\max}$ and the size of the basis needed. In general we wish to choose θ as large as possible, whilst still achieving convergence and accuracy, in order to damp

the wave function as quickly as possible. By doing this we can choose a smaller value of $x_{\max}$ and hence a smaller basis size, speeding up calculations. In the figure we see three different values of the scaling angle, $\theta = 0.5$ rad (green line), $\theta = 0.3$ rad (blue line) and $\theta = 0.1$ rad (pink line). All give identical results in the unscaled area and we see that the higher θ is the quicker the probability drops to zero. As such a larger box of $[-150, 150]$ a.u. was needed to achieve convergence for $\theta = 0.1$ rad whilst for $\theta = 0.5$ rad a box of $[-75, 75]$ a.u. sufficed. For the unscaled calculation we used a box of $[-400, 400]$ a.u. and 2000 B-splines whilst for the scaled calculations we used 900 and 600 B-splines for $\theta = 0.1$ rad and $\theta = 0.5$ rad respectively. In conclusion we can see that θ can be taken to be large without compromising on the accuracy of the calculation. It is possible to take $\theta > 0.5$ rad however this requires the time step to be made smaller in order to ensure convergence. As such, the advantage in computational time gained by reducing the box size is more than lost by the increase in the number of time steps during the propagation.

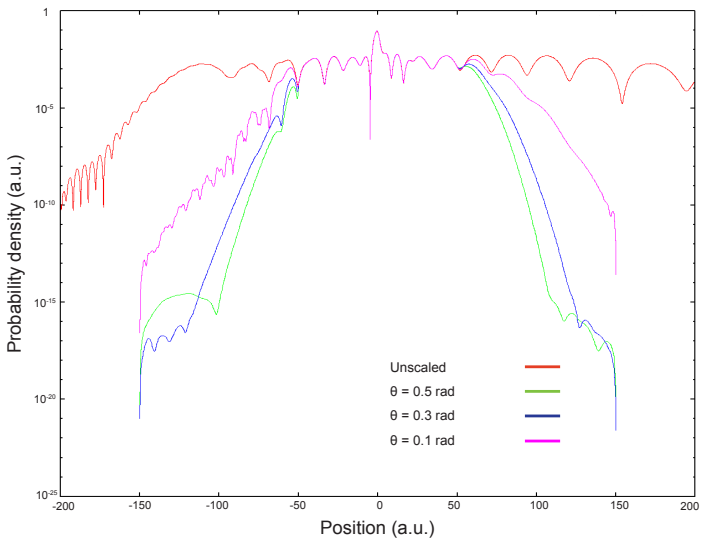

Figure 4.63: The electron probability density at the end of a 2 cycle pulse of frequency $\omega = 0.0569$ a.u. and intensity $I = 3 \times 10^{14}$ W $\cdot$ cm^{-2} described by (4.3). Shown is the full unscaled density (red) and the scaled density carried out using ECS with scaling point $x_0 = 50$ a.u. for a scaling angle of $\theta = 0.5$ rad (green), $\theta = 0.3$ rad (blue) and $\theta = 0.1$ rad (pink).

Another benefit the tSURFF method has over other methods is that we can individ-

ually analyse each contribution, $-x_0$ and $+x_0$, and examine the angular distribution of the electrons by counting the flux that travels in each direction. Figure 4.64 shows this for the case of wavelength 800nm and intensity $I = 10^{14}$ W $\cdot$ cm^{-2} for the soft Coulomb potential. We can see that the vast majority of the electrons were captured in the positive x direction and in particular for energy $E > 0.1$ a.u. where they count for almost all of the spectrum. This is due to the fact that for the second half of the pulse when the majority of the ionisation occurs then the electric field has large negative amplitude. Since we are working in a one dimensional model once the electrons are ionised in this direction it is very unlikely that they travel to the other side of the atom and hence the distribution is heavily skewed in this direction.

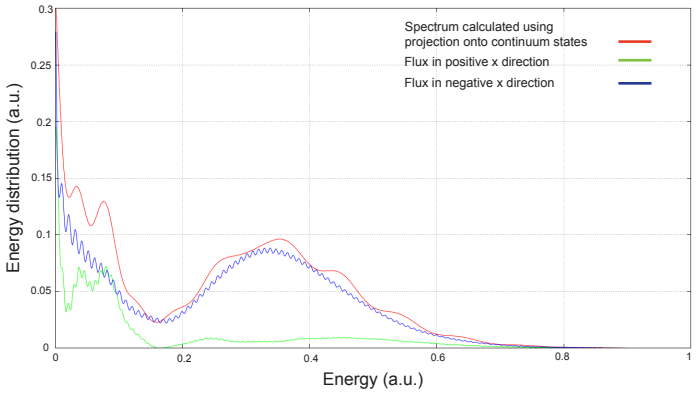

Figure 4.64: The ATI spectrum at the end of a 2 cycle pulse of frequency $\omega = 0.0569$ a.u. and intensity $I = 10^{14}$ W $\cdot$ cm^{-2} described by (4.3). Shown is the spectrum calculated using projection onto continuum states (red) and the angular distribution for positive x (green) and negative x (blue) calculated using the tSURFF method and carried out using ECS with scaling point $x_0 = 40$ a.u. for a scaling angle of $\theta = 0.5$ rad with the time integration length $T = 4\tau$.

4.8.1 Low Frequency

We now tackle the difficult problem of implementing the ECS and tSURFF for the case of $\omega = 0.0228$ a.u. At this frequency many small oscillations and low photon energy means we must use more B-splines for the ECS to retain the accurate results within the unscaled region. Calculating the spectrum using the tSURFF method

is also difficult due to the very low energy of the electrons which escape the atom. These slow electrons, in conjunction with the long pulses force the time integration parameter T to be very large in order to capture all the electrons. However, despite this, calculations at this frequency are considerably quicker than carrying out the full unscaled calculations as we shall see in this section.

Again we use the Gaussian potential of equation (4.44), this time with $V_0 = 0.5$ and $\beta = 1$ giving a single bound state with ground state energy $E = -0.17$ a.u. We start with an intensity of 10^{14} W $\cdot$ cm^{-2} and for the unscaled calculation we use a box size of $[-1200, 1200]$ a.u. with 3200 B-splines. In order to achieve convergence for low frequency we must use a scaling angle of $\theta \leq 0.2$ rad otherwise the norm will rapidly grow and accuracy will be lost. We can choose x_0 as any value outside the bound state radius although convergence is easier to obtain with a larger value of x_0. Figure 4.65 shows the unscaled electron density (red line) as well as the electron density obtained using ECS for $x_0 = 50$ a.u. (blue line) and 120 a.u. (green line) for a scaling angle of $\theta = 0.2$ rad. We can see that the agreement in the unscaled area is very good for both sets of parameters. We use a box size of $[-250, 250]$ a.u. and a basis size of 420 functions, thus cutting the length of the calculation down from 9 hours on an 8 processor computer to 90 minutes on the laptop using 2 processors.

Since we are looking at very low frequency it is even more beneficial to subtract the bound states from the wave function at the end of the calculation. Figure 4.66 shows this electron continuum density plot for the same parameters as above. For the ECS we used a scaling point of $x_0 = 120$ a.u. and the same scaling angle. We can see that the agreement in the continuum is achieved.

For the tSURFF calculations we must now use a large value for x_0 in order to make sure we lie outside the quiver radius, which for this case is $\alpha = 102$ a.u. and therefore we use $x_0 = 120$ a.u. with the detector placed at the mesh point just inside the unscaled area at x_1. In order to capture even the slow electrons we integrate out to a time $T = 10\tau$. We can see in figure 4.67 that we get very good agreement across the entire spectrum. Despite getting excellent agreement there are still very

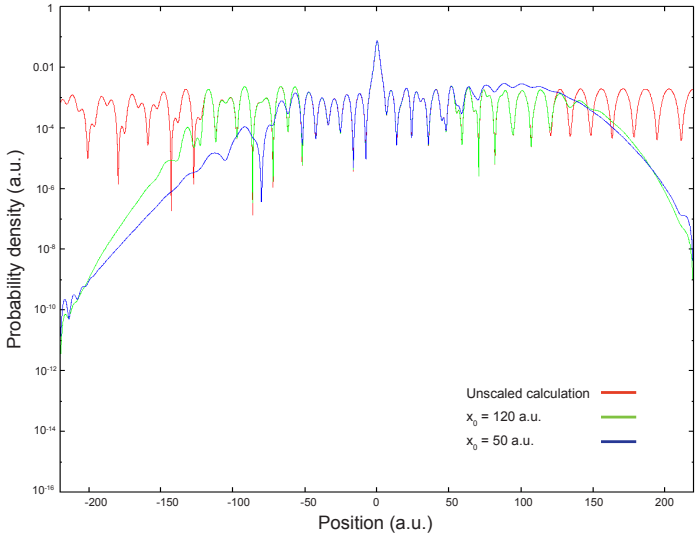

Figure 4.65: The electron probability density at the end of a 2 cycle pulse of frequency $\omega = 0.0228$ a.u. and intensity $I = 10^{14}$ W $\cdot$ cm^{-2} described by (4.3) for a Gaussian potential with $I_p = 0.17$ a.u. Shown is the full unscaled density (red) and the scaled density carried out using ECS with scaling points $x_0 = 50$ a.u. (blue) and 120 a.u. (green) for a scaling angle of $\theta = 0.2$ rad.

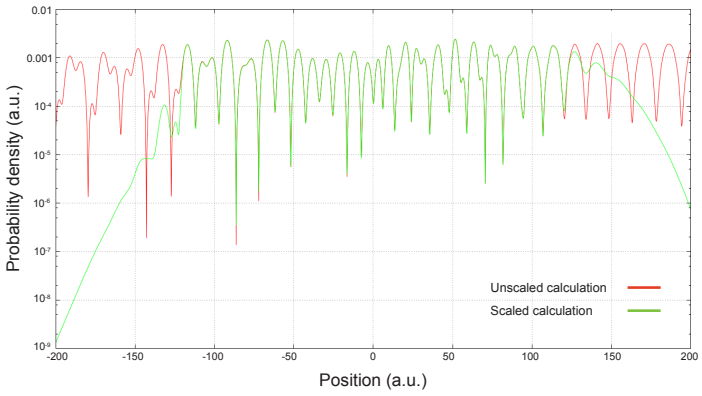

Figure 4.66: The electron continuum probability density at the end of a 2 cycle pulse of frequency $\omega = 0.0228$ a.u. and intensity $I = 10^{14}$ W $\cdot$ cm^{-2} described by (4.3) for a Gaussian potential with $I_p = 0.17$ a.u. Shown is the full unscaled density (red) and the scaled density carried out using ECS with scaling points $x_0 = 120$ a.u. (green) for a scaling angle of $\theta = 0.2$ rad.

low energy electrons which remain inside the radius x_0 at the end of the integration time. By investigating what is left inside this radius we should be able to pick up these very slow electrons. In order to approximate this we project the final wave packet representing the unscaled part of the mesh onto plane waves of momentum k. This gives

$$\langle \chi_k | \Psi(x,t) \rangle = \frac{1}{2\pi k} \int_{-x_1}^{x_1} \mathrm{e}^{-\mathrm{i}kx + \mathrm{i}\omega t} \Psi(x,t) \mathrm{d}x. \tag{4.45}$$

We calculate this using a Gaussian quadrature by splitting the integral up into its real and imaginary parts, before summing over the real break points. The density remaining inside the scaled area at the end of the time integration is then given by $|\langle \chi_k | \Psi(x,t) \rangle|^2$.

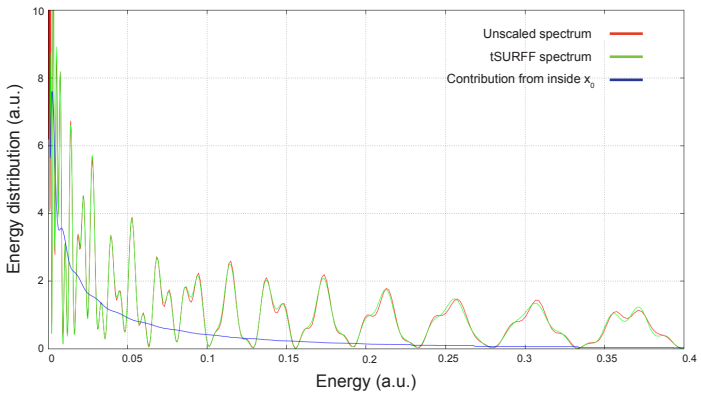

Figure 4.67: The ATI spectra at the end of a 2 cycle pulse of frequency $\omega = 0.0228$ a.u. and intensity $I = 10^{14}$ W $\cdot$ cm^{-2} described by (4.3) for a Gaussian potential with $I_p = 0.17$ a.u. Shown is the spectrum calculated using projection onto continuum states (red) and using tSURFF with ECS with scaling point $x_0 = 120$ a.u. (green) for a scaling angle of $\theta = 0.2$ rad and length of time integration $T = 10\tau$. Also shown is the flux remaining within the radius $[-120, 120]$ a.u. at time T (blue).

We now change the parameters of the Gaussian potential in order to increase the ionisation potential to $I_p = 0.49$ a.u. $= 13.3$eV. This change of the potential is good preparation for the possibility of considering other atoms which have higher ionisation potentials in the future. The electron continuum density against position x is seen for these parameters in figure 4.68. The higher ionisation potential means

the probability of finding the electron in the continuum has decreased and now the density is around the order of 10^{-6}. Despite this, we still get very good agreement between the unscaled (red line) and scaled calculations (green line) using parameters of $x_0 = 120$ a.u. and $\theta = 0.2$ rad.

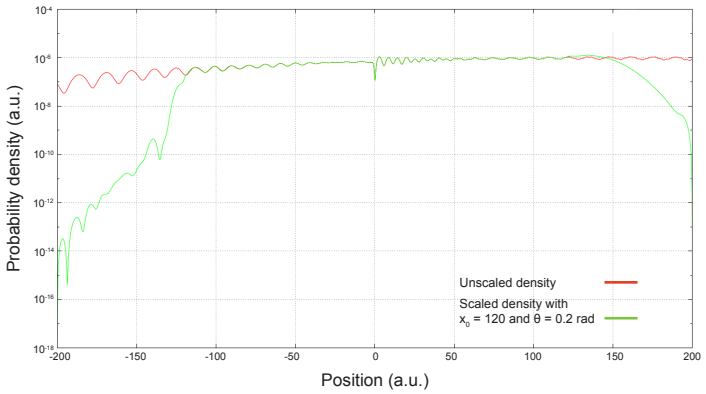

Figure 4.68: The electron probability density at the end of a 2 cycle pulse of frequency $\omega = 0.0228$ a.u. and intensity $I = 10^{14}$ W $\cdot$ cm^{-2} described by (4.3) for a Gaussian potential with $I_p = 0.49$ a.u. Shown is the full unscaled density (red) and the scaled density carried out using ECS with scaling point $x_0 = 120$ a.u. (green) for a scaling angle of $\theta = 0.2$ rad.

The tSURFF calculation for these parameters is seen in figure 4.69. We can see that despite the lower ionisation probability we still get good agreement throughout the spectrum. We show in this figure the convergence obtained and the difference between the results obtained for the integration times $T = 4\tau$ (green line) and $T = 8\tau$ (blue line). We can see that for higher energy the two cases agree, for low energy the integration time $T = 4\tau$ fails to capture slow electrons with energy $E < 0.01$ a.u. whilst $T = 8\tau$ does. By using different values of T we can accurately pinpoint the position of very slow electrons at any time of our choosing. We note that even with $T = 8\tau$ the very slow electrons $E \approx 0$ still haven't reached the detector and the tSURFF spectrum differs slightly from the exact spectrum.

We now examine the ECS for the case of the soft Coulomb potential with ionisation potential $I_p = 0.5$ a.u. This case is more challenging since the long range Coulomb tail makes convergence more difficult. The presence of the tail means that in order

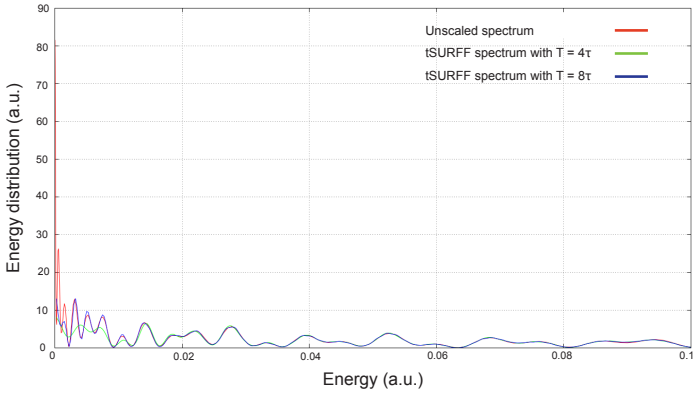

Figure 4.69: The ATI spectra at the end of a 2 cycle pulse of frequency $\omega = 0.0228$ a.u. and intensity $I = 10^{14}$ W $\cdot$ cm^{-2} described by (4.3) for a Gaussian potential with $I_p = 0.49$ a.u. Shown is the spectrum calculated using projection onto continuum states (red) and using tSURFF with ECS with scaling point $x_0 = 120$ a.u. (green) for a scaling angle of $\theta = 0.2$ rad and length of time integration $T = 4\tau$ (green) and $T = 8\tau$ (blue).

to achieve a similar level of accuracy we will have to take the scaling radius to be bigger to minimise the impact of the long range tail. In figure 4.70 we show the comparison of the electron probability density against position x for a 2 cycle pulse of intensity $I = 10^{14}$ W $\cdot$ cm^{-2} for the unscaled case (red line) and for the ECS case with $x_0 = 30$ a.u. (green line) and $x_0 = 50$ a.u. (blue line) for a scaling angle of $\theta = 0.2$ rad. The unscaled calculation required a box size of $[-750, 750]$ with 2200 B-spline functions giving a run time of 7 hours. For the ECS calculations we use a box size of $[-250, 250]$ with 650 basis functions reducing the run time to 2.5 hours. In figure 4.71 we show the same probability density but this time with a larger scaling radius of $x_0 = 220$ a.u. for scaling angle $\theta = 0.1$ rad (green line) and $\theta = 0.2$ (blue line) in comparison to the unscaled calculation (red line) showing that if necessary the scaling point can be extended out to larger distances and the scaling angle θ can be easily changed without compromising on the accuracy of the unscaled region.

We now examine the case of an intensity of $I = 3 \times 10^{14}$ W $\cdot$ cm^{-2} with the ECS method in order to show the accuracy of the method with a particularly challenging

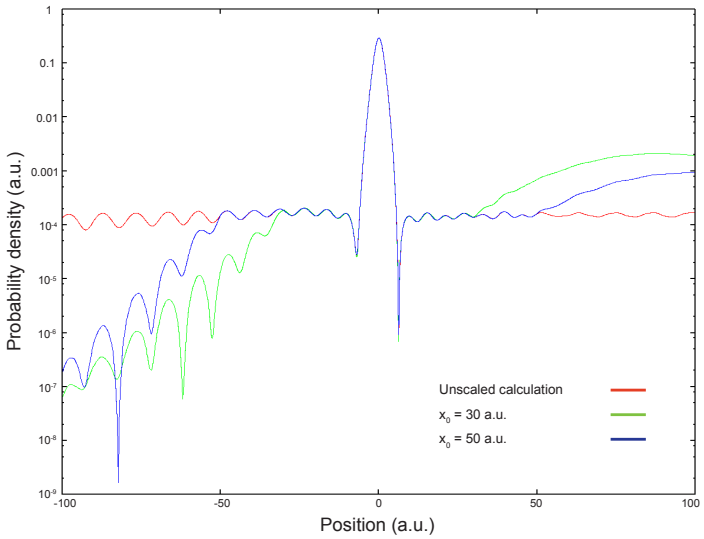

Figure 4.70: The electron probability density at the end of a 2 cycle pulse of frequency $\omega = 0.0228$ a.u. and intensity $I = 10^{14}$ W $\cdot$ cm^{-2} described by (4.3) for the soft Coulomb potential. Shown is the full unscaled density (red) and the scaled density carried out using ECS with scaling points $x_0 = 30$ a.u. (green) and $x_0 = 50$ a.u. (green) for a scaling angle of $\theta = 0.2$ rad.

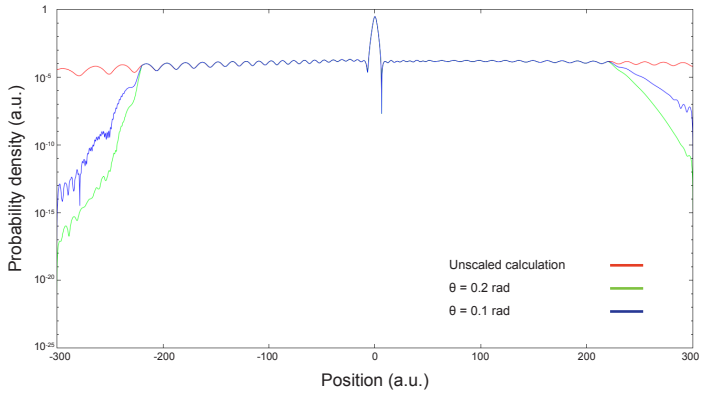

Figure 4.71: The electron probability density at the end of a 2 cycle pulse of frequency $\omega = 0.0228$ a.u. and intensity $I = 10^{14}$ W $\cdot$ cm^{-2} described by (4.3) for the soft Coulomb potential. Shown is the full unscaled density (red) and the scaled density carried out using ECS with scaling point $x_0 = 220$ a.u. and for a scaling angle of $\theta = 0.2$ rad (green) and $\theta = 0.1$ rad (blue).

set of parameters. As previously mentioned the calculations for the unscaled case took around 26 hours to compute. In figure 4.72 we show the accuracy of the method for the above laser parameters with scaling parameters of $x_0 = 450$ a.u. and $\theta = 0.1$ rad. Despite having to make x_0 and hence the basis size, bigger than in previous cases in order to achieve convergence, we still manage to speed up the calculation up significantly. We use a box of $[-500, 500]$ a.u. and 1400 B-splines with for a time step of $\delta t = 0.1$ a.u. and 60 Krylov vectors. The calculation took 6 hours, just 23% of the time taken for the unscaled calculation.

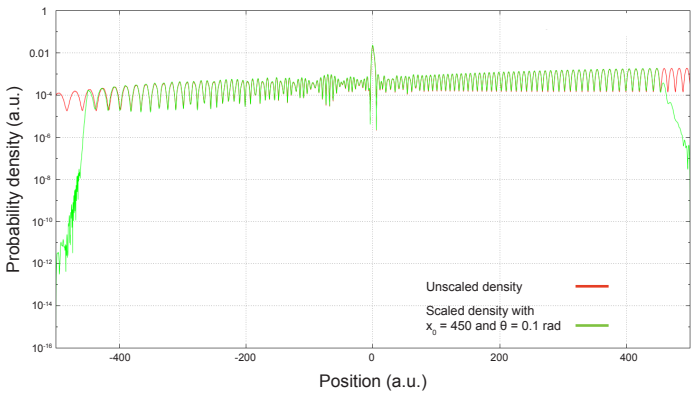

Figure 4.72: The electron probability density at the end of a 2 cycle pulse of frequency $\omega = 0.0228$ a.u. and intensity $I = 3 \times 10^{14}$ W $\cdot$ cm^{-2} described by (4.3) for the soft Coulomb potential. Shown is the full unscaled density (red) and the scaled density carried out using ECS with scaling points $x_0 = 450$ a.u. for a scaling angle of $\theta = 0.1$ rad (green).

To further show the accuracy of the calculations, figure 4.73 shows the continuum electron density for this case on a logarithmic scale.

Finally we look again at the momentum density plots against momentum p and time t. Before, the scaling of the calculation resulted in the horizontal lines at higher momentum disappearing. Again we see the appearance and disappearance of these lines as electrons are ionised and move towards the scaling radius. This is a result of using a bigger scaling radius. It allows us to pinpoint the times the electrons were ionised and leave the unscaled area. Again we can experiment with different values of x_0 to get complete information as to where electrons with momentum k

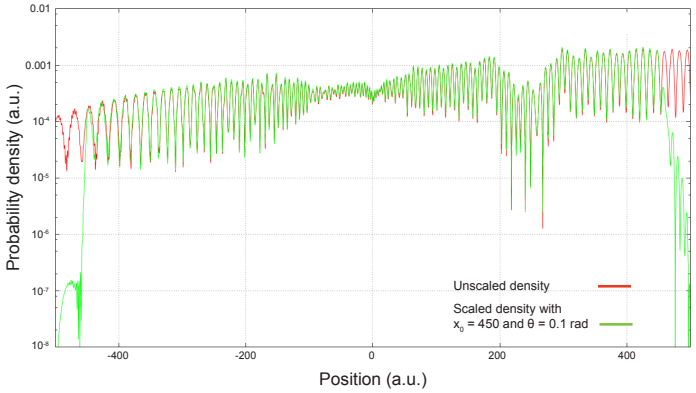

Figure 4.73: The continuum electron probability density on a logarithmic scale at the end of a 2 cycle pulse of frequency $\omega = 0.0228$ a.u. and intensity $I = 3 \times 10^{14}$ W $\cdot$ cm^{-2} described by (4.3) for the soft Coulomb potential. Shown is the full unscaled density (red) and the scaled density carried out using ECS with scaling points $x_0 = 450$ a.u. for a scaling angle of $\theta = 0.1$ rad (green).

are at any point in the pulse. The unscaled calculation can be seen in figure 4.74 and the scaled in figure 4.75 with $x_0 = 450$ a.u. for a scaling angle of $\theta = 0.1$ rad. We have developed reliable methods to solve the TDSE that work at low frequency and we have explored various observables which help explain the dynamics in one dimension. In the next chapter we will take these and apply them to the three dimensional Hydrogen atom where possible.

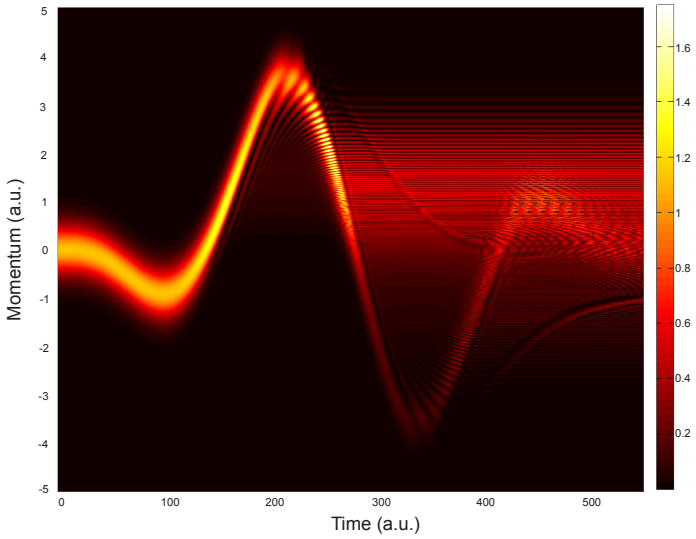

Figure 4.74: The unscaled evolution of the probability density $|\Psi(p,t)|^2$ in the p direction in momentum space in the velocity gauge throughout a 2 cycle pulse of frequency $\omega = 0.0228$ a.u. and intensity $I = 3 \times 10^{14}$ W $\cdot$ cm^{-2} described by (4.3) for the soft Coulomb potential.

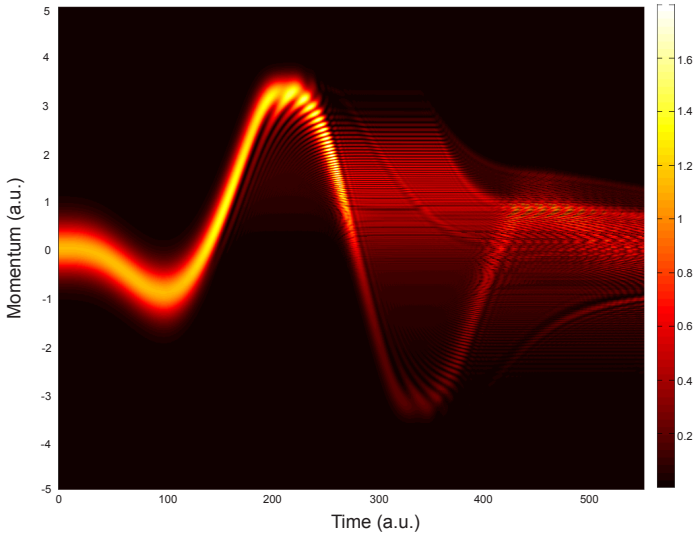

Figure 4.75: The scaled evolution of the probability density $|\Psi(p,t)|^2$ in the p direction in momentum space in the velocity gauge throughout a 2 cycle pulse of frequency $\omega = 0.0228$ a.u. and intensity $I = 3 \times 10^{14}$ W $\cdot$ cm^{-2} described by (4.3) for the soft Coulomb potential with scaling parameters $x_0 = 450$ a.u. and $\theta = 0.1$ rad.

Chapter 5

Three Dimensional Results for Hydrogen and Other Atoms at Low Frequencies

5.1 Introduction

In chapter 4 we developed an accurate one dimensional program which allowed us to investigate various observables and build a platform for a full three dimensional calculation. In this chapter we now extend this program to calculate the interaction of Hydrogen and other atoms in the single active electron approximation with laser fields of various parameters. Here we look again at a variety of frequencies, working towards the low frequency regime where we can investigate the low energy structures first mentioned in section 2.9.

The three dimensional time dependent Schrödinger equation that we solve for the case of the Hydrogen atom, where $V(\mathbf{r}) = -1/r$, in the velocity gauge is

$$\mathrm{i}\frac{\partial}{\partial t}\Psi^V(\mathbf{r},t) = \left[-\frac{1}{2}\nabla^2 + V(\mathbf{r}) - \mathrm{i}\mathbf{A}\cdot\nabla\right]\Psi^V(\mathbf{r},t) \tag{5.1}$$

and in the length gauge is given by

$$\mathrm{i}\frac{\partial}{\partial t}\Psi^L(\mathbf{r},t) = \left[-\frac{1}{2}\nabla^2 + V(\mathbf{r}) + \mathbf{r}\cdot\mathbf{E}\right]\Psi^L(\mathbf{r},t). \tag{5.2}$$

Since the Coulomb potential is spherically symmetric we use spherical polar coordinates (r,θ,ϕ). We follow the same steps as our one dimensional approach and

represent our wave function in r as a finite sum over the B-spline or Sturmian [33] basis functions. However, the addition of extra dimensions means there are more parameters we must now take into account. Our wave function expansion is now

$$\Psi(r,\theta,\phi,t) = \sum_{l=0}^{N_l-1}\sum_{i=1}^{N} a_i^l(t)\frac{B_i^k(r)}{r}Y_{l0}(\theta,\phi) \tag{5.3}$$

where B_i^k are B-splines of order k and Y_{lm} are the spherical harmonics.

In our expansion of the wave function we must truncate the range of angular momentum partial waves to a maximum size N_l and we then represent the wave function using N radial basis functions per angular momentum value l. We consider the case of an atom in its ground state in a linearly polarised field, along the z axis meaning we can set $m = 0$ when $m_{\text{initial}} = 0$ as there is no dependence on the angle ϕ. In our calculations the choice of N_l will heavily impact the efficiency of our calculations, due to the fact that the total size of our basis will grow significantly with increasing N_l. Therefore at low frequency, when the size of our basis is very large due to the large spatial extension of the wave function and stiffness of the system of equations, increasing N_l by just a small number will have a large effect on the memory and time constraints of our calculations. However, N_l must be taken large enough to represent the total range of angular momenta that influence the electron dynamics, given the laser parameters.

We split equation (5.3) into a radial and angular part, so

$$\Psi(r,\theta,\phi,t) = \sum_{l=0}^{N_l-1} R_l(r,t)Y_{l0}(\theta,\phi) \tag{5.4}$$

To obtain our atomic and interaction Hamiltonian matrices we solve the TISE in three dimensions. We do this by considering the reduced radial Schrödinger equation using the fact that in spherical coordinates, the Laplacian can be written as

$$\bigtriangledown^2 = \frac{1}{r^2}\frac{\partial}{\partial r}\left(r^2\frac{\partial}{\partial r}\right) - \frac{\mathbf{L}^2}{2r^2}. \tag{5.5}$$

Substituting (5.4) into (2.38) we obtain

$$\mathrm{i}\sum_{l'=0}^{N_l-1} Y_{l'0}\frac{\partial R_{l'}}{\partial t} = \sum_{l'=0}^{N_l-1}\left[-\frac{Y_{l'0}}{2r^2}\frac{\partial}{\partial r}\left(r^2\frac{\partial R_{l'}}{\partial r}\right) - \frac{l(l+1)}{2r^2}R_{l'}Y_{l'0} - \frac{1}{r}R_{l'}Y_{l'0} + \mathbf{A}.\mathbf{p}R_{l'}Y_{l'0}\right] \tag{5.6}$$

We project onto $(Y_{lm})^*$ and integrate over the angles, using the fact that the spherical harmonics are orthogonal, to obtain

$$\mathrm{i}\frac{\partial R_l}{\partial t} = -\frac{1}{2r^2}\frac{\partial}{\partial r}\left(r^2\frac{\partial R_l}{\partial r}\right) - \frac{l(l+1)}{2r^2}R_l - \frac{1}{r}R_l + \sum_{l'=0}^{N_l-1}\langle Y_{l0}|\mathbf{A}.\mathbf{p}|R_{l'}Y_{l'0}\rangle. \tag{5.7}$$

We note that

$$\frac{1}{r}\frac{\partial}{\partial r}r^2\frac{\partial R_l}{\partial r} = \frac{\partial^2}{\partial r^2}(rR_l) \tag{5.8}$$

and multiply through by r to get

$$\mathrm{i}\frac{\partial (rR_l)}{\partial t} = -\frac{1}{2}\frac{\partial^2 (rR_l)}{\partial r^2} - \frac{l(l+1)}{2r^2}(rR_l) - \frac{1}{r}(rR_l) + A(t)r\sum_{l'=0}^{N_l-1}\langle Y_{l0}|\mathbf{p}_z|R_{l'}Y_{l'0}\rangle, \tag{5.9}$$

where the $\mathbf{p}_z$ term appears since we take a laser linearly polarised in the z direction. Letting $P_l = rR_l$ so $P_l = \sum_{i=1}^{N} a_i^l(t)B_i(r)$ and look at the atomic part of equation (5.9) without the interaction term, which is

$$-\frac{1}{2}\frac{\partial^2 P_l}{\partial r^2} - \frac{l(l+1)}{2r^2}P_l - \frac{1}{r}P_l. \tag{5.10}$$

We can solve this by projecting onto $R_{l'} = P_{l'}/r$ and integrating over the radial coordinate r. The volume element cancels with the $1/r$ in the final term and we can then solve the TISE which in matrix form is

$$\mathbf{H}_i^l \cdot \mathbf{c}_i^l = E_i^l \mathbf{S} \cdot \mathbf{c}_i^l \tag{5.11}$$

where the unperturbed Hamiltonian $\mathbf{H}_i^l$ and overlap matrices $\mathbf{S}$ are constructed in the B-spline basis as given by equations (3.24) and (3.25) and $\mathbf{c}_i^l$ is a vector of the time independent coefficients.

The solution of (5.11) gives the eigenvalues and eigenvectors of this system and we can then convert the unperturbed Hamiltonian to the atomic basis as described in 3.2.3 and obtain a diagonal matrix with the elements comprised of the computed eigenvalues of the Hydrogen atom. Our interaction matrix is harder to obtain as we must deal with the angular parameters in addition to the radial parameters. The momentum component in our interaction term is given by

$$\mathbf{p}_z = -\mathrm{i}\frac{\partial}{\partial z} \tag{5.12}$$

and so converting to spherical coordinates our interaction term is

$$H_{\mathrm{I}}(\mathbf{r},t) = -\mathrm{i}A(t)\left(\cos\theta\frac{\partial}{\partial r} - \frac{\sin\theta}{r}\frac{\partial}{\partial\theta}\right). \tag{5.13}$$

We substitute this into the interaction term of (5.9) to obtain

$$-\mathrm{i}A(t)r\langle\ Y_{l0}(\theta)\ |\left(\cos\theta\frac{\partial}{\partial r} - \frac{\sin\theta}{r}\frac{\partial}{\partial\theta}\right)|\ R_{l'}Y_{l0}(\theta)\ \rangle. \tag{5.14}$$

In spherical coordinates the partial derivative of the spherical harmonics can be calculated using [16] and are given by

$$\frac{\partial}{\partial z}[R(r)Y_{lm}] = c_l\left(\frac{\partial R}{\partial r} - \frac{lR}{r}\right)Y_{l+1,m} + c_{l-1}\left(\frac{\partial R}{\partial r} + \frac{(l+1)R}{r}\right)Y_{l-1,m} \tag{5.15}$$

where

$$c_l \equiv \frac{l+1}{\sqrt{(2l+1)(2l+3)}} \tag{5.16}$$

which comes from the integration of the harmonics over the angles of the first term in the spherical interaction which is only non zero when $l = l' \pm 1$

$$\langle\ Y_{l0}(\theta)\ |\cos\theta|\ Y_{l\pm10}\ \rangle = 2\pi\int_0^\pi Y_{l0}\cos\theta\sin\theta Y_{l\pm10}\mathrm{d}\theta = \frac{2\pi(l+1)}{\sqrt{(2l+1)(2l+3)}} \equiv 2\pi c_l, \tag{5.17}$$

whereas the c_{l-1} terms comes from the second term of the interaction

$$\langle\, Y_{l0}(\theta)\, |\sin\theta\frac{\partial}{\partial\theta}|\, Y_{l-10}\,\rangle = 2\pi\int_0^{\pi} Y_{l0}\sin^2\theta\frac{\partial}{\partial\theta}Y_{l-10}\mathrm{d}\theta = \frac{-2\pi l(l-1)}{\sqrt{(2l-1)(2l+1)}} \equiv -2\pi(l-1)c_{l-1}. \tag{5.18}$$

Our interaction part then becomes

$$-\mathrm{i}A(t)rc_l\left(\frac{\partial R}{\partial r}-\frac{l'R}{r}\right)\delta_{ll'+1}+c_{l-1}\left(\frac{\partial R}{\partial r}+\frac{(l'+1)R}{r}\right)\delta_{ll'-1}. \tag{5.19}$$

Using the fact that

$$\frac{\partial R_l}{\partial r}=\frac{\partial}{\partial r}\left(\frac{rR_l}{r}\right)-\frac{1}{r^2}(rR_l), \tag{5.20}$$

we now convert the equation into a differential equation in P_l similar to the atomic term

$$-\mathrm{i}A(t)c_{l-1}\left(\frac{\partial P}{\partial r}-\frac{lP}{r}\right)\delta_{ll'+1}+c_l\left(\frac{\partial P}{\partial r}+\frac{(l+1)P}{r}\right)\delta_{ll'-1}. \tag{5.21}$$

Projecting onto R_l, as previously shown, then converts the problem from a two dimensional partial differential equation to an infinite set of coupled one dimensional partial differential equations involving just r and time although in practice we solve up to a value N_l. We then obtain the following integrals which can be solved using only the Gaussian quadrature, firstly when $l'=l+1$

$$-\mathrm{i}A(t)\int_0^{r_{max}} B_j(r)c_l\left(\frac{\partial}{\partial r}+\frac{l+1}{r}\right)B_i(r)\mathrm{d}r \tag{5.22}$$

and when $l'=l-1$

$$-\mathrm{i}A(t)\int_0^{r_{max}} B_j(r)c_{l-1}\left(\frac{\partial}{\partial r}-\frac{l}{r}\right)B_i(r)\mathrm{d}r \tag{5.23}$$

We can then convert to the atomic basis and then propagate through time as we did in the one dimensional case.

In the length gauge the interaction Hamiltonian is given by

$$H_I(\mathbf{r},t)=E(t)r\cos\theta \tag{5.24}$$

and following the method above, our radial integrals then become, for $l' = l + 1$

$$E(t) \int_0^{r_{max}} B_j(r) c_l r B_i(r) \mathrm{d}r \tag{5.25}$$

and for $l' = l - 1$

$$E(t) \int_0^{r_{max}} B_j(r) c_{l-1} r B_i(r) \mathrm{d}r. \tag{5.26}$$

The eigenvalues obtained for the Coulomb potential for each partial wave $l = 0$, 1 and 2 is given in table 5.1 which was obtained in the Sturmian basis and checked in the B-spline basis.

$l = 0$	$l = 1$	$l = 2$
-0.4999999999999	-0.1249999999999	-0.0555555555555
-0.1249999999999	-0.0555555555555	-0.0312500000000
-0.0555555555555	-0.0312500000000	-0.0199999999999
-0.0312500000000	-0.020000000000	-0.013888888888
-0.0199999999999	-0.013888888888	-0.0102040816326
-0.0138888888888	-0.0102040816326	-0.0078125000000
-0.0102040816326	-0.0078125000000	-0.0061728395061
-0.0078124999999	-0.0061728395061	-0.0049999999999
0.0061728395061	-0.0049999999999	-0.0041322314049
-0.0049999999999	-0.0041322314049	-0.0034722222222

Table 5.1: The eigenvalues for atomic Hydrogen obtained using the Sturmian basis for partial waves $l = 0$, $l = 1$ and $l = 2$.

The Hydrogen bound state energy levels in atomic units are given by

$$E_n = -\frac{1}{2n^2} \tag{5.27}$$

whilst the Hydrogen ground state, which we use as the initial state for all calculations, is given by the wave function

$$\Psi_{1s} = \frac{1}{\sqrt{\pi}} \mathrm{e}^{-r} \tag{5.28}$$

Figure 5.1 shows this ground state (red line) as well as the first (green line) and second (blue line) excited states against radial position r, represented on the B-

spline mesh. We calculate these states by solving the TISE using matrices created using the B-spline basis.

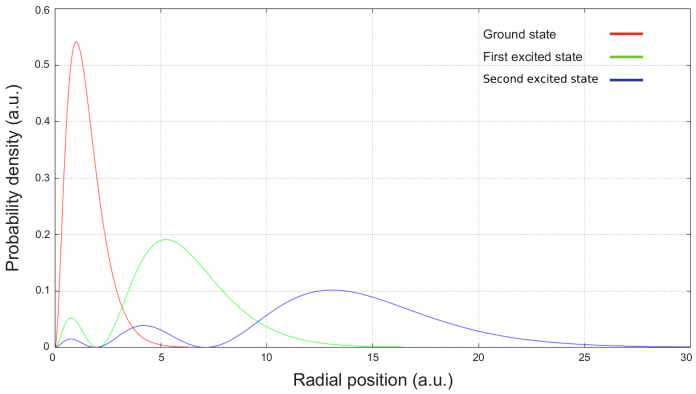

Figure 5.1: The ground state (red), first excited state (green) and second excited state (blue) of Hydrogen against radial position r created using the B-spline basis.

As in one dimension for all calculations, unless otherwise specified we use the following vector potential in the velocity gauge (VG)

$$A(t) = \begin{cases} A_0 f(t) \sin(\omega t + \varphi) & \text{if } \ 0 \leq t \leq \tau \\ 0 \ \ \text{otherwise,} \end{cases} \tag{5.29}$$

with pulse envelope

$$f(t) = \sin^2\left(\frac{\pi t}{\tau}\right), \tag{5.30}$$

which can be seen in figure 5.2. The figure shows a laser linearly polarised in the z direction and with $\varphi = 0$ and $\varphi = \pi/2$. In calculations, unless otherwise stated, we take $\varphi = 0$ and use the B-spline basis transformed into the atomic basis with Arnoldi time propagation and consider an electron initially in the $1s$ ground state for all calculations.

In this chapter we calculate the ATI spectrum and angular distributions. The angle integrated spectrum in the full 3D calculations is given by [21]

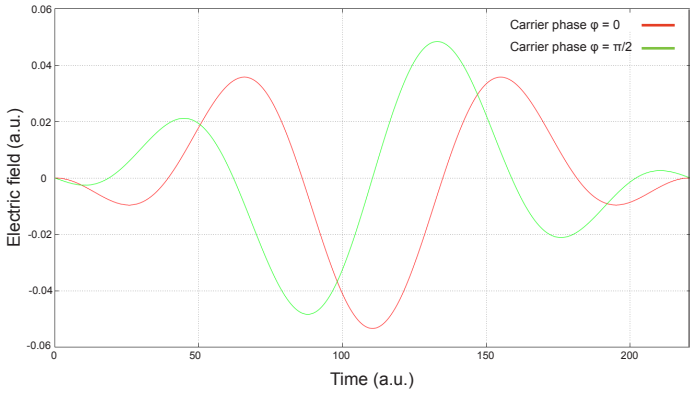

Figure 5.2: The electric field for a laser of frequency $\omega = 0.0569$ a.u. and intensity $I = 10^{14}$ W $\cdot$ cm^{-2} for a duration of 2 optical cycles represented by the vector potential (5.29) with $\varphi = 0$ rad (red) and $\varphi = \pi/2$ rad (green).

$$\frac{\partial P}{\partial E}(E) = \sum_{l=0}^{N_l-1} \frac{\partial P_l}{\partial E}(E) = \sum_{l=0}^{N_l-1} |\langle \phi_E^l(\mathbf{r}) | \Psi(\mathbf{r}, \tau) \rangle|^2 \tag{5.31}$$

where $\partial P_l / \partial E$ denotes the probability density of finding the electron in the l^{th} partial wave at the end of the pulse a energy E. As in the one dimensional case the discretised continuum state $\phi_E^l(\mathbf{r})$ is obtained from the solution of the TISE in the B-spline basis set. Calculating the ATI spectrum for the Hydrogen atom using the projection onto continuum states method poses a problem since our discretisation of the continuum means that for each l we obtain a different set of eigenvalues in the continuum. In order to calculate the spectrum we must then interpolate between the sets of continuum eigenvalues for each l to then calculate the full angle integrated spectrum. However, severe oscillations in the distribution mean that using this interpolation method was not efficient enough to achieve accurate results and in some cases convergence was lost completely. We instead calculated the spectra by projecting the wave function Ψ at the end of the pulse onto a Coulomb wave function which we calculate separately [57]. We then calculate the angular distribution for a particular direction as follows

$$\frac{\partial P}{\partial E \partial \Omega_k}(E, \theta_k, \phi_k) = |\langle f_{\mathbf{k}}^{(-)}(\mathbf{r}) | \Psi(\mathbf{r}, \tau) \rangle|^2 \tag{5.32}$$

where $f_{\mathbf{k}}^{(-)}$ is the Coulomb wave expanded in spherical harmonics as

$$f_{\mathbf{k}}^{(-)}(\mathbf{r}) = \frac{1}{\sqrt{k}} \sum_{l=0}^{N_l} \sum_{m=-l}^{l} (\mathrm{i})^l \mathrm{e}^{-\mathrm{i}\delta_l} \phi_E^l(\mathbf{r}) Y_{lm}^*(\theta_k, \phi_k) \tag{5.33}$$

where $\delta_l = \arg\Gamma(l + 1 - \mathrm{i}Z/k)$ is the Coulomb phase shift in the l^{th} partial wave and $\phi_E^l(\mathbf{r})$ is the energy normalised Coulomb function. θ_k and ϕ_k correspond to the directions of the vector $\mathbf{k}$ and Γ is the gamma function.

To initially test the program we run a calculation for a reasonably high frequency of $\omega = 0.3$ corresponding to a wavelength of 152nm and for an intensity of $I = 10^{15}$ W $\cdot$ cm^{-2}. We compare with results from a paper by Piraux and Madroñero [48] who calculate the ground state population using a Sturmian basis and using a Runge-Kutta propagator, throughout a 4 cycle pulse. We carried out the calculations in the velocity gauge and with a box of $[0, 200]$ a.u. 500 basis functions and $N_l = 10$. Figure 5.3 shows this comparison.

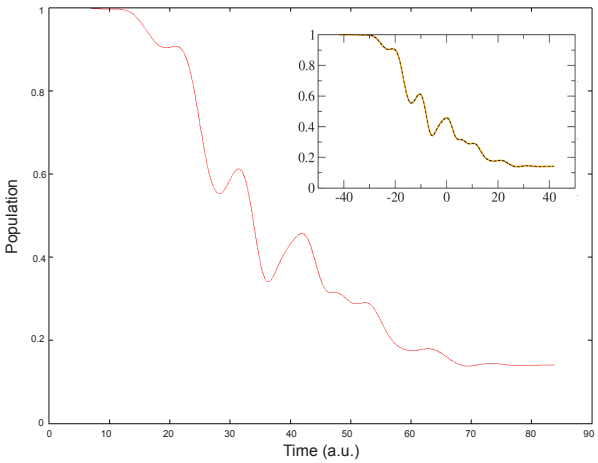

Figure 5.3: Ground state population of Hydrogen during a pulse of 4 optical cycles of frequency $\omega = 0.3$ and intensity of $I = 10^{15}$ W $\cdot$ cm^{-2} represented by the equation (5.29). For comparison, inset is the plot obtained by Piraux and Madronero [48].

5.2 Ionisation by a 620nm Wavelength Laser

We perform a more stringent test of our program by comparing with a benchmark calculation of smaller wavelength and lower intensity we now look at a case

of $\lambda = 620$nm investigated by Cormier and Lambropoulos [21, 22]. Even though the wavelength corresponding to this frequency is shorter than previously used wavelengths, the calculations are more computationally intensive due to the extension to three dimensions and the considerably longer pulse lengths. This wavelength corresponds to a frequency of $\omega = 2\text{eV} = 0.0735$ a.u. and an intensity of $I = 3.6 \times 10^{13}$ W $\cdot$ cm^{-2}. At this frequency we have a ponderomotive energy of $U_p = 1.13$ eV and a Keldysh parameter of $\gamma = 2.45$ putting us in the multiphoton regime.

In figure 5.4 we show the ATI spectrum against energy E on a logarithmic scale for the above parameters with a pulse length of 12 optical cycles. By increasing the pulse length from previous examples we allow more time for ionisation and hence rescattering which can have a significant effect on the ATI spectrum. We can see from the spectrum that we get clear peaks separated by the photon energy that we expect in the multiphoton ionisation regime.

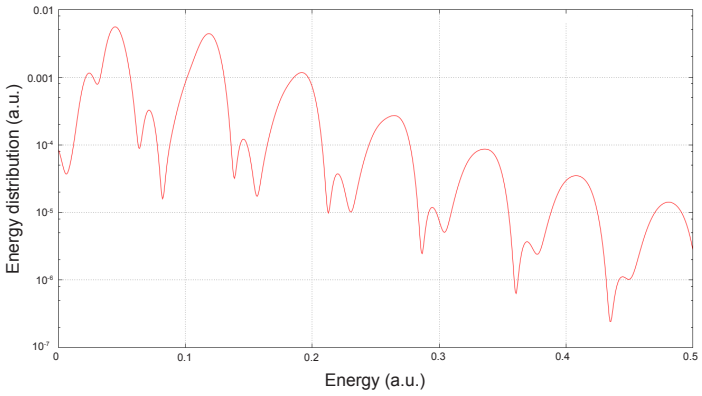

Figure 5.4: The angle integrated photoelectron energy spectrum against electron energy at the end of a pulse of 12 optical cycles of frequency $\omega = 0.0735$ a.u. and intensity $I = 3.6 \times 10^{13}$ W $\cdot$ cm^{-2} represented by the vector potential (5.29).

In figure 5.5 we show the ATI spectrum against E for the same parameters as above except for this time we have extended the pulse length further to 24 cycles. We can see that whilst we still observe peaks in the same positions as the 12 cycle case, they are now narrower and in addition see the emergence of substructures on the right

hand side of the low energy peaks. These are similar structures to what we saw in one dimension for a wavelength of $\lambda = 492$nm. The same reasoning can be used here to explain the appearance of these substructures. We saw in equation (4.19) how the pulse length is linked strongly with the appearance and shape of these substructures and this is shown here for the calculations with $n_c = 12$ and $n_c = 24$. If the number of cycles is too low then the bracketed term in equation (4.19) becomes smaller and the sub-peaks diminish in amplitude and fewer in number, or non existent as we see in figure 5.4. Physically, the lower number of optical cycles allows for less interference between wave packets emitted at different times and travelling with slightly different velocities (and thus different energies) meaning the ATI peaks become smoother. In figure 5.6 we show the comparison between the two pulse lengths more clearly by plotting both ATI spectra on the same axis. For these calculations we used a box size of $[0, 1200]$ a.u., 1200 B-spline functions for the 12 cycle case with $N_l = 16$ with a running time of about 4 hours, whereas for the 24 cycle case we use a box size of $[0, 1600]$ a.u., 1600 B-spline functions and $N_l = 16$ with a run time of 12 hours.

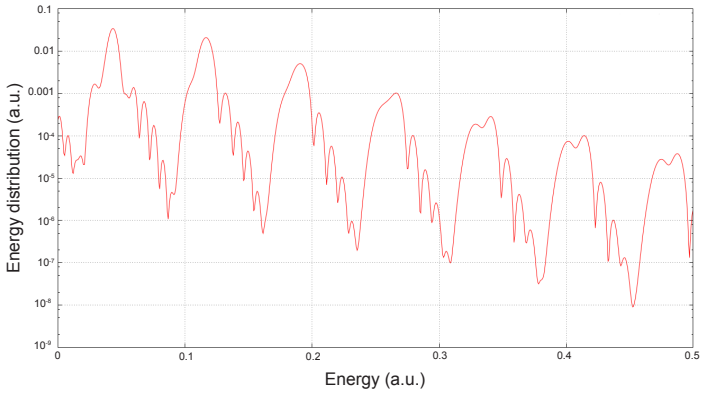

Figure 5.5: The angle integrated photoelectron energy spectrum against electron energy at the end of a pulse of 24 optical cycles of frequency $\omega = 0.0735$ a.u. and intensity $I = 3.6 \times 10^{13}$ W $\cdot$ cm^{-2} represented by the vector potential (5.29).

The angle specific spectrum for the case of a 24 cycle pulse is now investigated for the above parameters. In figure 5.7 we show a comparison of the angle integrated spectrum (red line) and the $\theta = 0$ spectrum (green line) against energy E for the

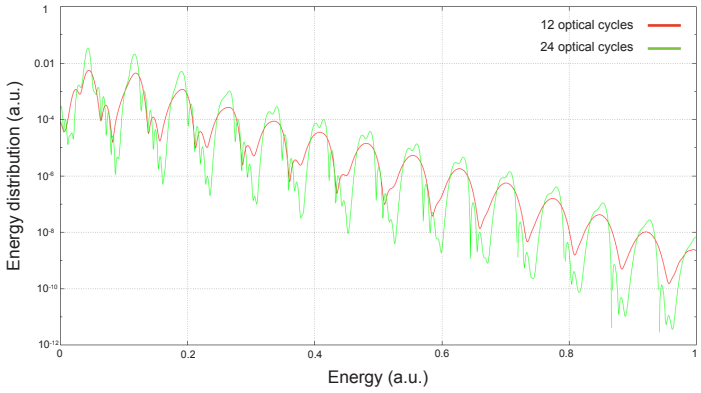

Figure 5.6: A comparison of the angle integrated photoelectron energy spectrum against electron energy at the end of a pulse of frequency $\omega = 0.0735$ a.u. and intensity $I = 3.6 \times 10^{13}$ W $\cdot$ cm^{-2} for a 12 optical cycle (red) and a 24 optical cycle pulse (green) represented by the vector potential (5.29).

above parameters. We can see that the peaks of the spectra agree up to $E = 5U_p = 0.2$ a.u. before the $\theta = 0$ spectrum dips in amplitude. This dip and change in amplitude from the angle integrated spectrum can be explained by pronounced peaks in the angular distribution in other directions which can be seen in figure 5.8. This shows the angular distribution for the energies corresponding to the peaks in the ATI distribution $s = 1$ to $s = 8$ where s is the excess number of photons absorbed past the necessary number needed for ionisation. We bare in mind here that the $s = 1$ peak is the first peak shown in the ATI spectrum due to the fact that the $s = 0$ peak has been shifted below the threshold due to Stark shifting causing an effect known as channel closing. We see that the $s = 6$ peak, where the amplitudes between the two spectra start to differ, shows pronounced peaks in the angular distribution at $\theta = 0.5$ and 2.64 rad. As s increases these two peaks begin to move towards $\theta = 0$ and $\theta = \pi$ radians respectively causing the width of the maximal peaks to widen. Therefore we can attribute the dip in the $\theta = 0$ spectrum to emission in other directions close to the $\theta = 0$ direction due to the rescattering and interference attributed to the substructures seen in section 4.4. These peaks in the angular distribution, like the substructures, become more pronounced with increasing pulse length.

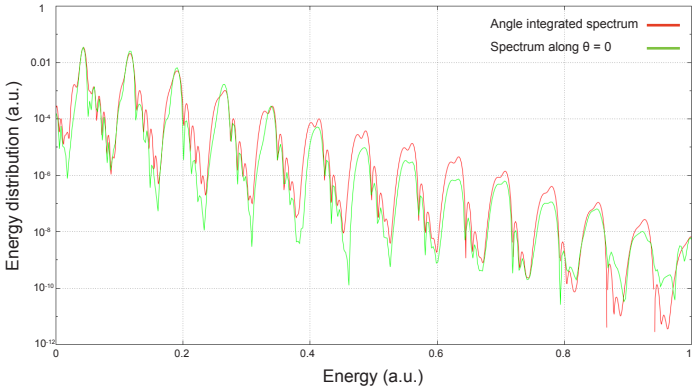

Figure 5.7: The angle integrated photoelectron energy spectrum (red) and the $\theta = 0$ spectrum (green) against electron energy at the end of a pulse of 24 optical cycles of frequency $\omega = 0.0735$ a.u. and intensity $I = 3.6 \times 10^{13}$ W $\cdot$ cm^{-2} represented by the vector potential (5.29).

Finally, we look at the angle integrated, l specific, spectra for these parameters. We calculate the l dependent partial wave spectra as

$$\frac{\partial P_l}{\partial E}(E) = |\langle \phi_E^l(\mathbf{r})|\Psi(\mathbf{r},\tau)\rangle|^2. \tag{5.34}$$

The 12 cycle pulse and the $l = 0$ (red line) and $l = 1$ (green line) spectra can be seen in figure 5.9. Here we carried out the calculation using a Coulomb Sturmian basis of 1000 Sturmian functions. We used a dilation parameter of $\kappa = 0.3$ to allow convergence of the angle integrated spectrum up to $E = 0.5$ a.u. and checked all results against the B-spline basis. We can see that we get peaks in the same positions as with the angle integrated spectrum, separated by the photon energy but shifted towards $E = 0$ by the combined ponderomotive and ionisation potential. The first peak we see in the $l = 0$ spectrum is the 8 photon peak and only even photon number peaks have significant amplitude here. For the $l = 1$ spectrum we see the opposite with the first significant peak being the 9 photon peak and then just odd peaks. This alternating peak structure is due to a manifestation of the dipole selection rule [76] and we can see in figure 5.10 that the pattern continues for higher values of l with even l values giving just even photon number peaks and odd l values giving just odd photon number peaks.

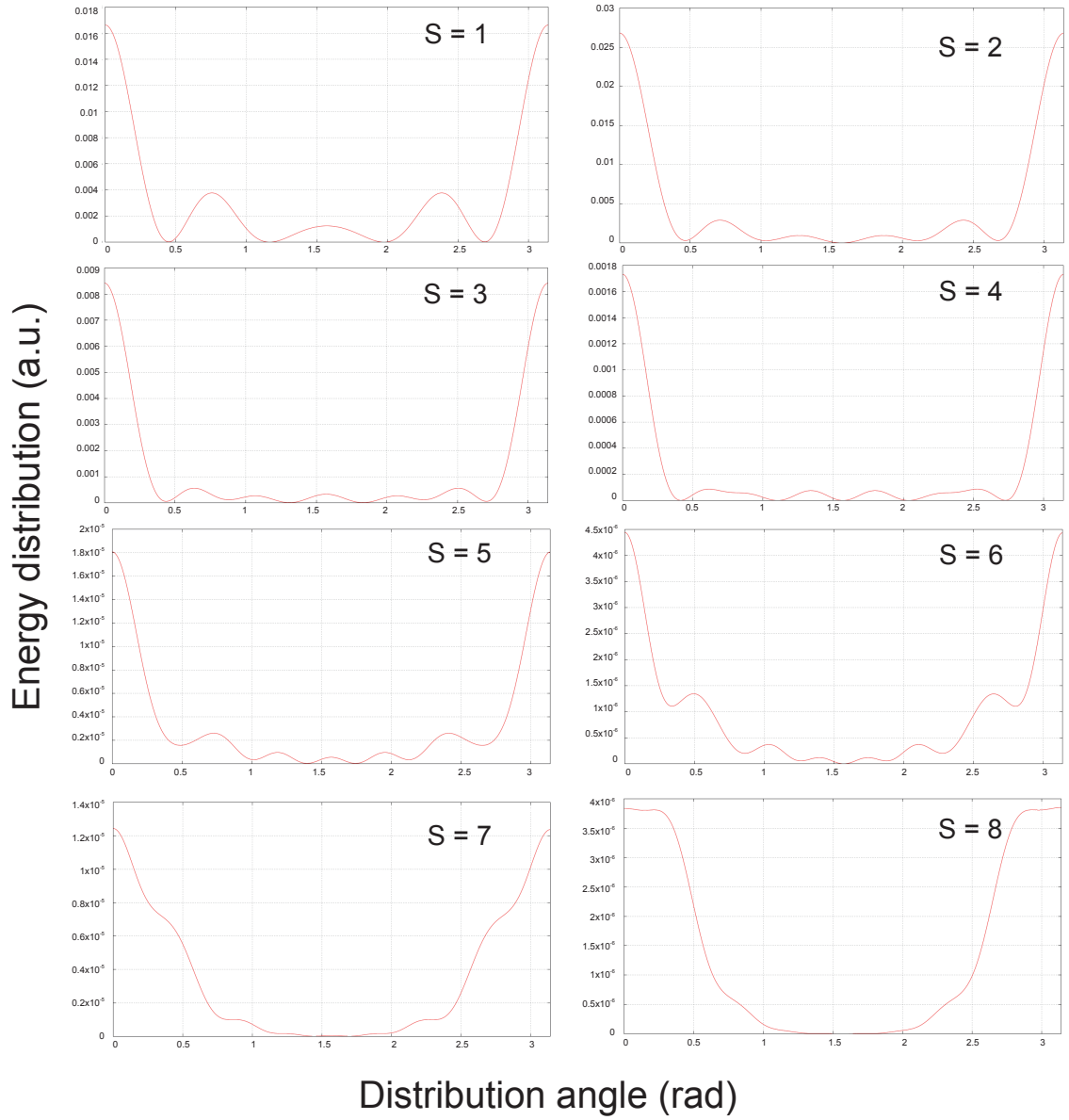

Figure 5.8: The angular distribution against angle θ for the ATI peaks $s = 1$ to $s = 8$ at the end of a pulse of 24 optical cycles of frequency $\omega = 0.0735$ a.u. and intensity $I = 3.6 \times 10^{13}$ W $\cdot$ cm^{-2} represented by the vector potential (5.29).

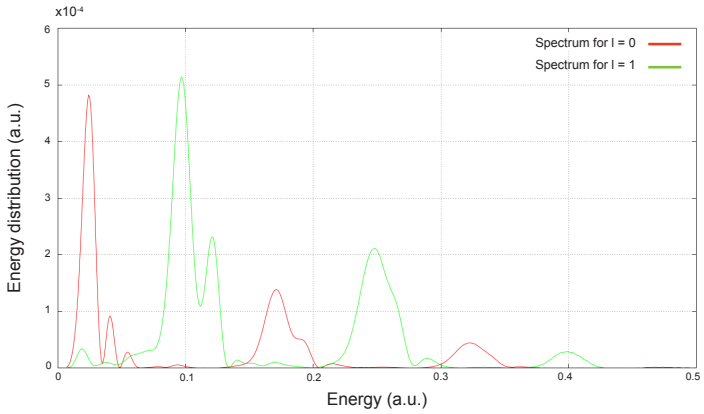

Figure 5.9: The angle integrated photoelectron energy spectrum contribution from the $l = 0$ partial wave (red) and $l = 1$ partial wave (green) against electron energy at the end of a pulse of 12 optical cycles of frequency $\omega = 0.0735$ a.u. and intensity $I = 3.6 \times 10^{13}$ W $\cdot$ cm^{-2} represented by the vector potential (5.29).

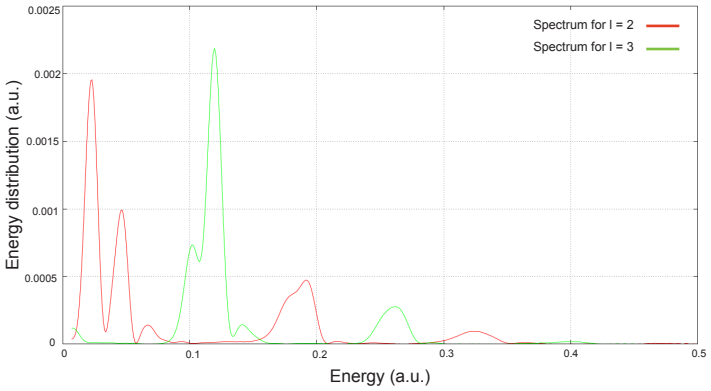

Figure 5.10: The angle integrated photoelectron energy spectrum contribution from the $l = 2$ partial wave (red) and $l = 3$ partial wave (green) against electron energy at the end of a pulse of 12 optical cycles of frequency $\omega = 0.0735$ a.u. and intensity $I = 3.6 \times 10^{13}$ W $\cdot$ cm^{-2} represented by the vector potential (5.29).

The same calculations were carried out by us for the case of 24 cycles and the same pattern was observed, showing that this is not dependent on the pulse length.

5.3 Interference Patterns in the Angular Distribution

To understand the interference patterns seen in our angular distributions for few cycle pulses at low frequency we examine the case of a half cycle and full cycle pulse as done by Arbo et al. [5].

We take a frequency of $\omega = 0.05$ a.u which corresponds to a wavelength of $\lambda = 910$nm and intensity of $I = 2 \times 10^{14}$ W $\cdot$ cm^{-2}. In this case the Keldysh parameter has a value of $\gamma = 0.66$ and the quiver radius takes a higher value of $\alpha = 30$ a.u. showing the challenging nature of the calculation. Here we use a different form of the electric field, given by

$$E(t) = \begin{cases} -E_0 f(t)\sin(\omega t) & \text{if } \ 0 \leq t \leq \tau \\ 0 & \text{otherwise} \end{cases} \tag{5.35}$$

where $f(t)$ here is the pulse envelope. This choice of electric field was to allow for easy comparison with the single cycle wave of constant pulse envelope as seen below [5]. By comparing the case of a sinusoidal envelope with a constant envelope we can more clearly see the effect of interference between ejected wave packets on the spectra. We take $E_0 = 0.075$ a.u. which gives a peak intensity of $I = 2 \times 10^{14}$ W $\cdot$ cm^{-2} and take $\tau = 251$ a.u. corresponding to two optical cycles. In figure 5.11 we show the electric field (red line) and the corresponding vector potential (green line) against time t, for the case of pulse envelope

$$f(t) = \sin^2(\frac{\pi t}{\tau}). \tag{5.36}$$

The vector potential has been divided by 33 in order to show it on the same scale. We compute this in the length gauge with a box of $[0, 800]$ a.u. and 1200 B-Spline functions with $N_l = 38$. As expected this is considerably more B-spline functions, as well as a higher density of functions, than we needed in the VG for a similar set of

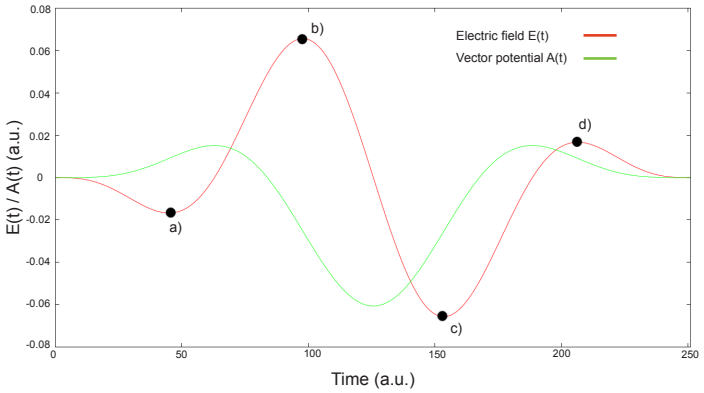

Figure 5.11: The electric field (red) and the corresponding vector potential (green) (divided by 33) for the laser pulse of frequency $\omega = 0.05$ a.u. and intensity $I = 2 \times 10^{14}$ W $\cdot$ cm^{-2} given by the equation (5.35) with $f(t) = \sin^2(\frac{\pi t}{\tau})$ for a 2 cycle pulse. The black dots correspond to the times of the potential barriers shown in figure 5.16.

parameters. The reason for the density of B-splines being higher than usual is due to the fact that the solution in the LG has more rapid oscillations and therefore is more difficult to represent. The calculation took around 9 hours to complete, over double the time that a calculation with the same laser parameters would take in the VG to achieve convergent results. The angle integrated spectrum against energy E can be seen in figure 5.12 on a logarithmic scale. We can see that the peaks are not equally spaced and that the gap between sequential peaks grows as we move to higher energy. This increase in the spacing can be attributed to the interference mentioned in the chapter 4.

We next look at a different pulse type, that of a pulse with a constant envelope function, $f(t) = 1$. In this case the electric field reaches peak values much quicker and therefore the electron experiences more ionisation and can reach higher momentum in a faster time. As such even just a single cycle in the length gauge at this frequency can require a large box and number of basis functions. Figure 5.13 shows the electric field and corresponding vector potentials, again divided by 33, against time t for the 1 and 1/2 cycle pulses. We also note that the shape and amplitude of the 1 cycle pulse is similar to the 2 cycle pulse that we saw in figure 5.11 since the small

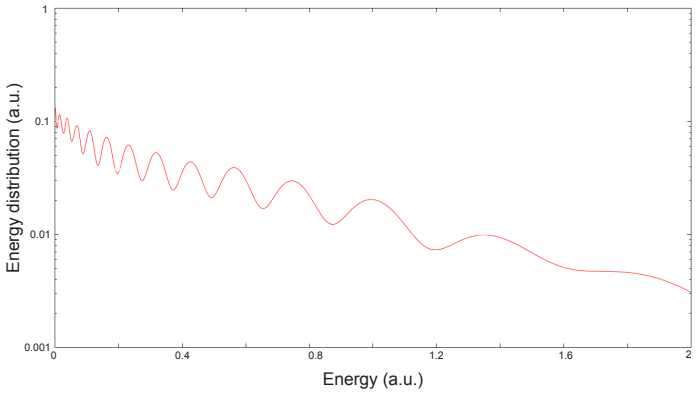

Figure 5.12: The angle integrated photoelectron energy spectrum against electron energy at the end of a pulse of 2 optical cycles of frequency $\omega = 0.05$ a.u. and intensity $I = 2 \times 10^{14}$ W $\cdot$ cm^{-2} given by the equation (5.35) with $f(t) = \sin^2(\frac{\pi t}{\tau})$.

maximum and minimums at the turning points at the beginning and end of the pulse are quite weak. Since the pulse shapes are similar then we expect the spectrum and angular distributions to be as well. This allows for similar calculations to be made but using only half the number of time steps, reducing computation times greatly. It is important to notice that for the case of half an optical cycle the vector potential at the end of the calculation is non zero. As such the calculations with just a half cycle are only to illustrate the effects we expect.

We analyse the ATI spectra for both of these cases. Figure 5.14 shows the spectrum for the case of half an optical cycle. Here we used the LG with a box of $[0, 600]$ a.u. 800 basis functions and $N_l = 14$. These are much larger parameters than would be needed if we were using a non constant envelope function for such a short pulse length of just $\tau = 61.75$ a.u.

Figure 5.15 shows the ATI spectrum against energy E for the case of a single cycle in the velocity gauge in comparison with the spectrum shown in figure 5.12 for 2 cycles with a $\sin^2$ envelope function. For this calculation we used a box of $[0, 600]$ a.u. with 800 B-splines and a large value of $N_l = 54$ was needed due to the form of the pulse. We can see that the spectrum for half a cycle is very flat with no oscillations and the amplitude is very low as would be expected for just half an optical cycle at this

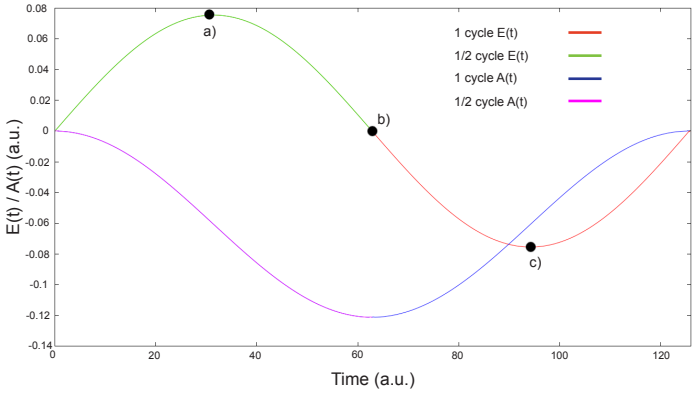

Figure 5.13: The electric field for a 1 cycle pulse (red) and for half a cycle (green) and the corresponding vector potentials for 1 cycle (blue) and half a cycle (pink) (divided by 33), for the laser pulse of frequency $\omega = 0.05$ a.u. and intensity $I = 2 \times 10^{14}$ W $\cdot$ cm^{-2} given by the equation (5.35) with $f(t) = 1$. The black dots correspond to the times of the potential barriers shown in figure 5.17.

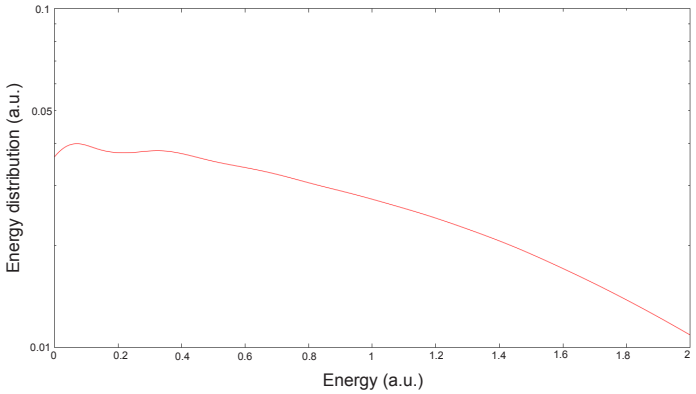

Figure 5.14: The angle integrated photoelectron energy spectrum against electron energy at the end of a pulse of half an optical cycle of frequency $\omega = 0.05$ a.u. and intensity $I = 2 \times 10^{14}$ W $\cdot$ cm^{-2} given by the equation (5.35) with $f(t) = 1$.

frequency. However, when the pulse increases to a full cycle we see the emergence of many oscillations as in the previous 2 cycle case. We again see the behaviour of the increasing spacing between peaks as the energy rises and the amplitude is larger for high energies than the 2 cycle pulse with the $\sin^2$ envelope function. The explanation as to why these oscillations appear in the 1 cycle pulse and not for half a cycle is due to the interference between the ionisation occurring in the first half cycle and the second half cycle. The wave packet is ionised and moving in the $-z$ direction during the first half cycle of the pulse (see figure 5.17 a)), and then reversed in direction as the electric field changes direction (see figure 5.17 c)). As this wave packet is moving into the positive z direction, another wave packet is created at the trough at time c) in figure 5.13. These two wave packets then interfere causing the oscillations in the ATI spectrum that we see. Arbo et al. [5] show that these interference processes can be reproduced with a simple semi-classical model and the process can be understood as the interference of two semi-classical trajectories escaping from the nucleus, one at each half cycle near the extremes of the electric field.

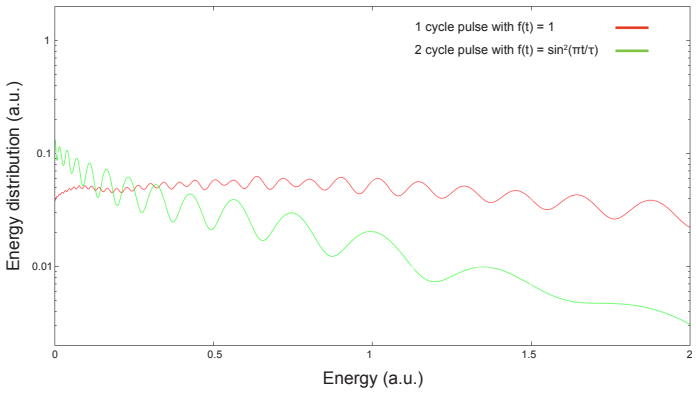

Figure 5.15: The angle integrated photoelectron energy spectrum against electron energy at the end of a pulse of frequency $\omega = 0.05$ a.u. and intensity $I = 2 \times 10^{14}$ W $\cdot$ cm^{-2} given by the equation (5.35) with $f(t) = 1$ for a 1 optical cycle pulse (red) in comparison with the spectrum obtained in figure 5.12 for 2 optical cycles with a $\sin^2$ envelope function.

The changing shape of the potential barrier created by the combination of the Coulomb potential and the electric field for the 2 cycle pulse with a $\sin^2$ enve-

lope function can be seen in figure 5.16 against position z for the times $t \approx 44$, 98, 153 and 205 a.u. corresponding to the peaks and troughs of the electric field which are shown by the circles on figure 5.11. We can see that the direction and size of the barrier changes with the changing sign and amplitude of the electric field. Figure 5.17 shows the same pattern for the case of the 1 cycle pulse with a constant envelope function for the times $t \approx 32$, 63 and 94 a.u. again corresponding to the times of the electric field which are shown by the circles on figure 5.13. All three pictures represent the maximum, middle point and minimum for the case of the 1 cycle pulse whilst the first two pictures show the maximum of the one peak and the end of the pulse for the case of half a cycle. We can see that for the half cycle case the combined potential begins flat before the field creates the barrier which the electron can tunnel through into the negative z direction. As the field amplitude decreases the barrier then disappears again. The fact that the barrier never appears in the opposite side of the potential allowing the electron to tunnel into the positive z direction is the reason that we get no interference structures. For both the 1 and 2 cycle cases we do see this change of direction of the potential barrier allowing for interference.

Finally we look at the angular distributions of these laser pulses to see if they agree with the above theory of interference. For the case of a half cycle pulse with the constant envelope we see that due to the positive amplitude of the electric field, the combination of the Coulomb potential and electric field means the barrier formed is in the negative z direction. Hence we expect to see the ionisation occur in this direction, or $\theta = \pi$ (green line). Figure 5.18 shows that this is indeed the case. Almost all of the ionisation is in this direction and since the field is positive throughout the entire half cycle then the contribution in the $\theta = 0$ (red line) direction is almost zero.

Increasing the pulse length to a full cycle, as shown in figure 5.19, we see the wave packet born in the first half cycle in the negative z direction reverses direction and combines with the newly created wave packet moving in the positive z direction so

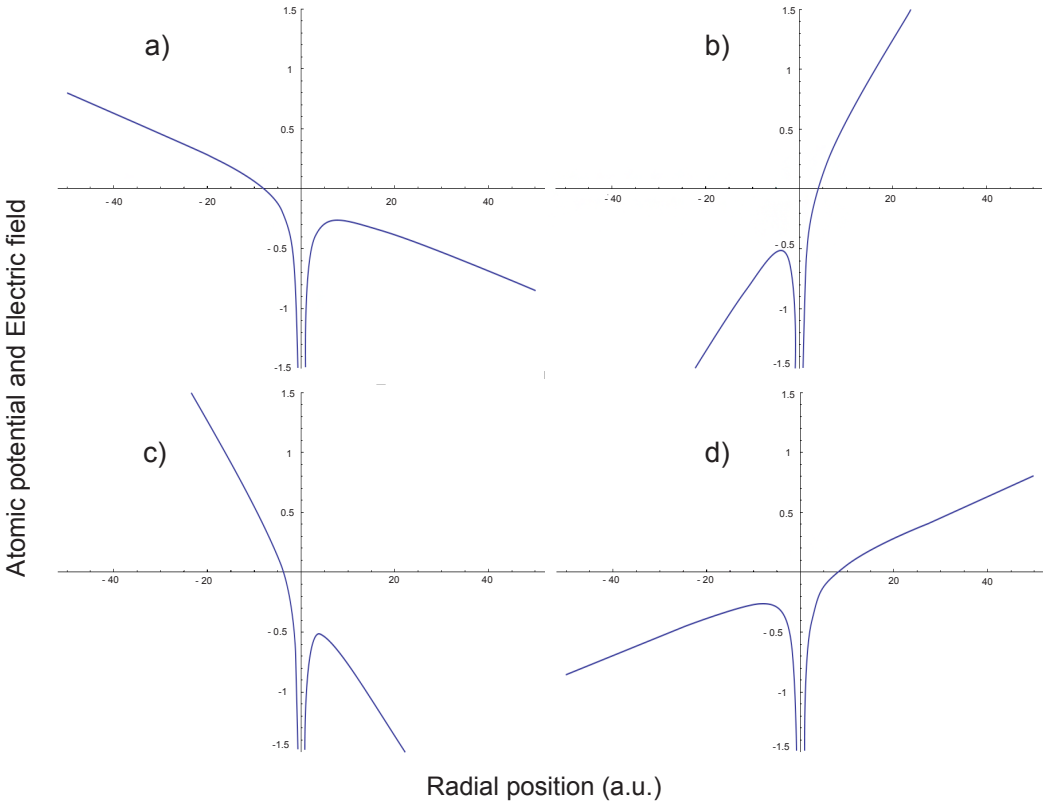

Figure 5.16: The potential barrier created by the superposition of the Coulomb potential and the electric field at times corresponding to the peaks of the field given by the circles on figure 5.11 for a field of frequency $\omega = 0.05$ a.u. and intensity $I = 2 \times 10^{14}$ W $\cdot$ cm^{-2} given by the equation (5.35) for 2 cycles with a sin^2 envelope function.

that now the majority of the distribution is in the $\theta = 0$ direction (red line). In addition we can see that the distributions in both directions now exhibit the same oscillatory pattern as the ATI spectrum, with quick small oscillations at low energy and the spacing between peaks with increasing energy become wider. This is due to the intra cycle interference.

For the case of 2 cycles with the sin^2 envelope we predict that the angular distribution should be similar to that of figure 5.19 due to the similar shape of the pulse, neglecting the small peak and trough at a) and d) respectively in figure 5.11. Indeed in figure 5.20 we can see that this is the case. Again the $\theta = 0$ direction (red line) has the highest probability and the same pattern of oscillations due to interference.

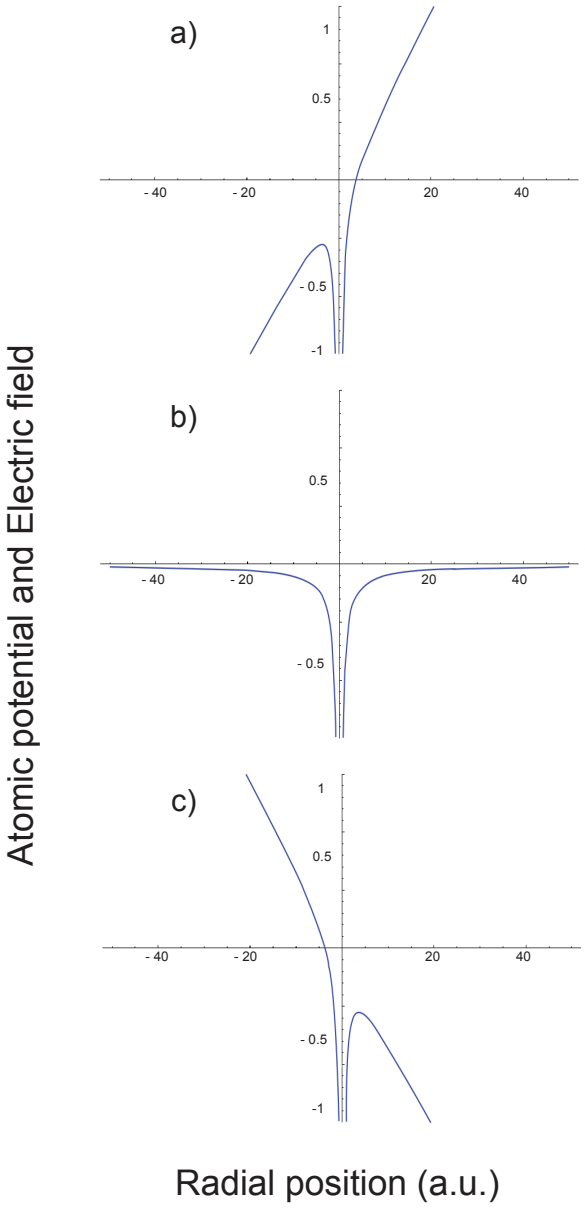

Figure 5.17: The potential barrier created by the superposition of the Coulomb potential and the electric field at times corresponding to the peaks of the field given by the circles on figure 5.13 for a field of frequency $\omega = 0.05$ a.u. and intensity $I = 2 \times 10^{14}$ W $\cdot$ cm^{-2} given by the equation (5.35) for 1 cycle (all 3 pictures) and half a cycle (first 2 pictures) with a constant envelope function.

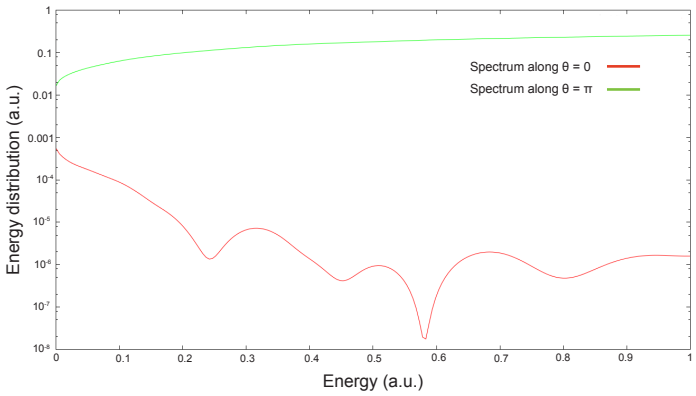

Figure 5.18: The photoelectron energy spectrum along $\theta = 0$ (red) and $\theta = \pi$ (green) against electron energy at the end of a pulse of half an optical cycle of frequency $\omega = 0.05$ a.u. and intensity $I = 2 \times 10^{14}$ W $\cdot$ cm^{-2} given by the equation (5.35) with $f(t) = 1$.

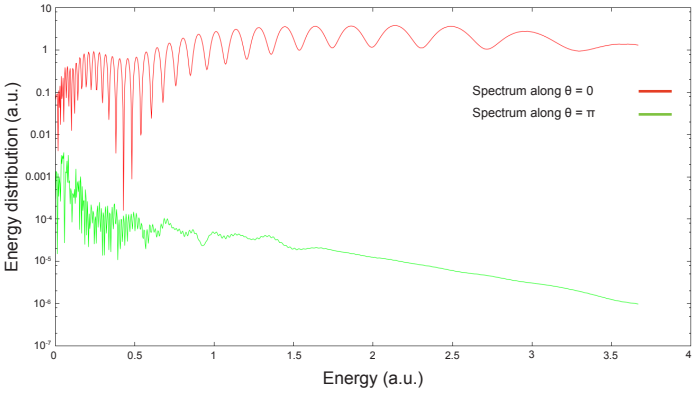

Figure 5.19: The photoelectron energy spectrum along $\theta = 0$ (red) and $\theta = \pi$ (green) against electron energy at the end of a pulse of 1 optical cycles of frequency $\omega = 0.05$ a.u. and intensity $I = 2 \times 10^{14}$ W $\cdot$ cm^{-2} given by the equation (5.35) with $f(t) = 1$.

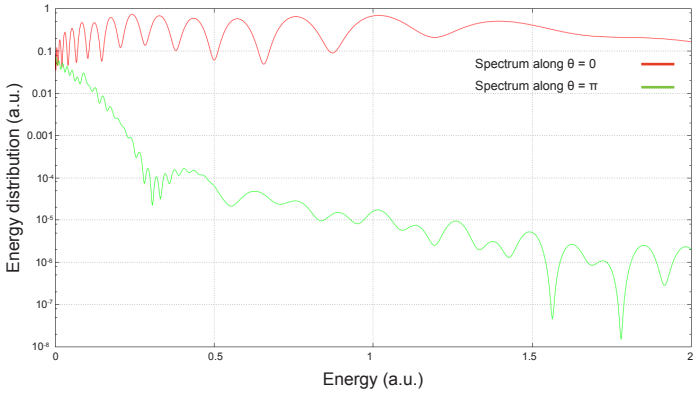

Figure 5.20: The photoelectron energy spectrum along $\theta = 0$ (red) and $\theta = \pi$ (green) against electron energy at the end of a pulse of 2 optical cycles of frequency $\omega = 0.05$ a.u. and intensity $I = 2 \times 10^{14}$ W $\cdot$ cm^{-2} given by the equation (5.35) with $f(t) = \sin^2(\frac{\pi t}{\tau})$.

5.4 Ionisation by an 800nm Wavelength Laser

As our aim is to extend the TDSE calculations to the lower frequencies required we now return to the frequency of $\omega = 0.0569$ a.u. corresponding to a wavelength of $\lambda = 800$nm. We begin by looking at the radial part of the wave function calculated in the atomic basis which is given by

$$R_l(r,t) = \sum_{i=1}^{N} a_{i,l}(t)\varphi_{i,l}(r). \tag{5.37}$$

We look at the angular momentum specific probability densities, i.e. for a specific value of l, for a laser intensity of $I = 10^{14}$ W $\cdot$ cm^{-2}. We take the pulse length to be 2 optical cycles and for these calculations we use a box of $[0, 400]$ a.u. with 400 B-spline functions to obtain the results with $N_l = 30$ partial waves. In addition we use a step size of $\delta t = 0.2$ a.u. and a Krylov space size of 60 in order to achieve convergence in time. This calculation in the velocity gauge takes around 34 minutes to run using 4 processors on the virtual machine. In writing the code we implemented openMP parallelisation throughout meaning that on a 4 processor machine a large number of calculations could be carried out simultaneously. In turn this reduced the length of the calculations approximately by a factor of the number of processors.

We checked convergence of results against the same calculation made in the length gauge.

Since the majority of the density remains in the ground state, the $l = 0$ probability density is dominated by the ground state. As such we begin in figure 5.21 by looking at the radial electron density for the next highest partial wave, that of $l = 1$ against position r. Due to the large ionisation potential in comparison to the photon frequency, the moderate intensity and the short pulse, the majority of the density remains in $l = 0$ and as such we can see that, as expected, the probability density for $l = 1$ is very low due to the low levels of ionisation and excitation.

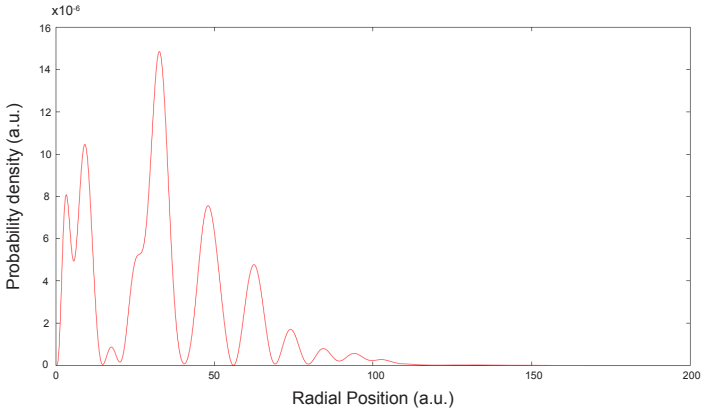

Figure 5.21: The electron radial probability density for $l = 1$ on a linear scale at the end of a pulse of 2 optical cycles of frequency $\omega = 0.0569$ a.u. and intensity $I = 10^{14}$ W $\cdot$ cm^{-2} represented by the vector potential (5.29).

Due to this low level of ionisation and the majority of the density remaining in the $1s$ initial state we need to look again at the continuum electron density in order to analyse the ionised electrons without the interference of the bound state populations. Figure 5.22 shows the continuum electron probability density for $l = 0$ (red line) and $l = 1$ (green line) partial waves. The dynamics of the electrons are now shown more clearly and we can see the movement of small amounts of density away from the bound states and into the continuum.

We now calculate a range of different spectra including the angle integrated ATI spectrum, angular specific spectra, l specific spectra and finally the angular distribution

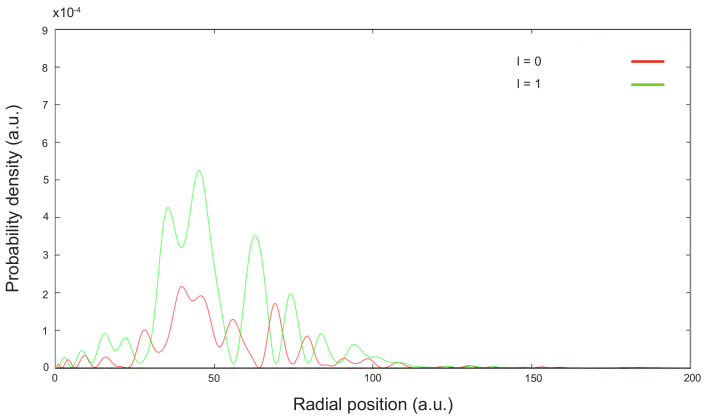

Figure 5.22: The electron continuum radial probability density for $l = 0$ (red) and $l = 1$ (green) at the end of a pulse of 2 optical cycles of frequency $\omega = 0.0569$ a.u. and intensity $I = 10^{14}$ W $\cdot$ cm^{-2}represented by the vector potential (5.29).

in order to further investigate the energy dynamics of the ejected electrons. We look how the laser parameters such as intensity, frequency, pulse length and phase affects these spectra. By investigating these spectra we can see how the Coulomb potential affects the low energy electrons which escape from the Hydrogen atom. In addition, the $\theta = 0$ spectrum is a useful case to calculate since most experimental results are very often obtained in this angular region due to the difficulties in obtaining results for other angles.

In figure 5.23 we see the angle integrated spectrum (red line), as well as the angle specific spectra for $\theta_k = 0$ (green line) and $\theta_k = \pi$ (blue) against energy E for a 2 cycle pulse of intensity $I = 10^{14}$ W $\cdot$ cm^{-2} and for carrier phase $\varphi = 0$. We see in figure 5.2 that neglecting the small fields at the beginning and end of the pulse, the field is like a 1 and a 1/2 cycle pulse with a peak-trough-peak formation. As such, from the analysis in section 5.3 we expect an interference pattern and the $\theta = \pi$ direction to dominate the angular distribution. This is indeed the case as seen in figure 5.23 as we can see that the distribution at the end of the pulse is dominated by electrons in the $\theta = \pi$ direction.

We can also investigate the angular distribution of the electrons for a specific energy. By fixing the energy we look at the distribution of low energy electrons, for instance

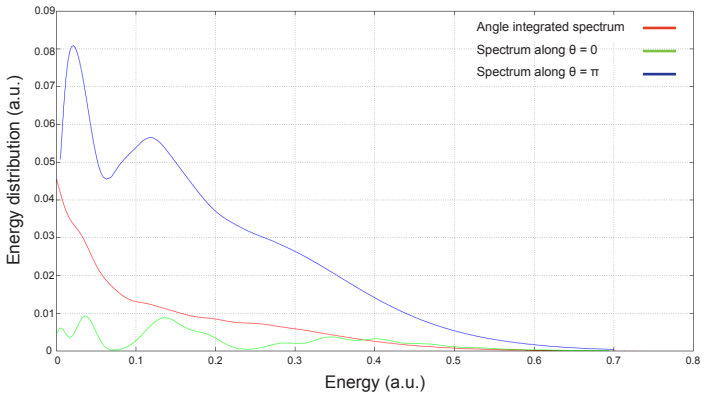

Figure 5.23: The angle integrated photoelectron energy spectrum (red), the $\theta = 0$ spectrum (green) and the $\theta = \pi$ spectrum (blue) as a function of electron energy at the end of a pulse 2 optical cycles of frequency $\omega = 0.0569$ a.u. and intensity $I = 10^{14}$ W $\cdot$ cm^{-2} represented by the vector potential (5.29) with $\varphi = 0$.

at the energy that the low energy structure is observed, and see how the electrons are distributed in this case. Figure 5.24 shows this angular distribution for the energy $E = 0.1$ a.u. for the angle range $-\pi \leq \theta \leq \pi$. We can see that for this energy the distribution reaches a maximum at $\theta = \pm\pi$ rad, whilst we can see other smaller sub-peaks at $\theta \approx \pm 2.65$ rad and $\theta = 0$ rad. The distribution is almost zero for $\theta = \pm\pi/2$. The maximums have already been explained in figure 5.23 as due to the direction of the electric field whilst the lack of distribution at $\theta = \pm\pi/2$ can be explained by the fact that these directions are orthogonal to the direction of the laser polarisation and therefore the barrier never allows for tunnel ionisation in these directions. We look at $E = 0.1$ a.u. as this is the level of energy that we expect to see the LES in the direction of the laser polarisation. We can see that the sharp rise of energy in the $\theta = \pm\pi$ is indicative of a low energy structure in the direction we expect.

With the aim of analysing the dynamics of the interaction further, we now investigate the affect of the carrier phase on the spectra. We carry out the same calculations as in figure 5.23 but this time take $\varphi = \pi/2$. For this phase we can again understand this from figure 5.2 by neglecting the smaller peak fields at the beginning and end of the pulse. So we essentially have a single cycle pulse with a trough-peak structure

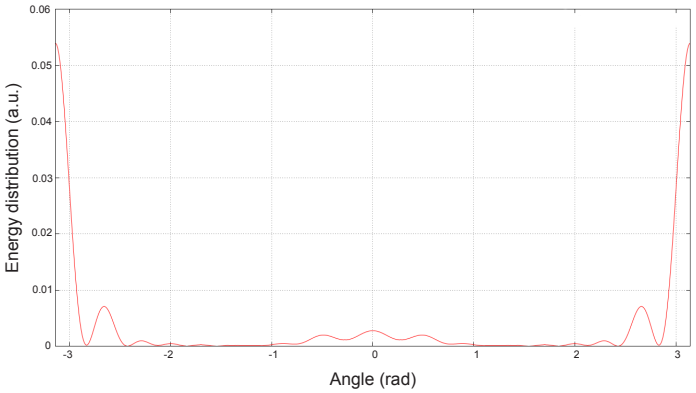

Figure 5.24: The angular distribution against angle θ for energy $E = 0.1$ a.u. at the end of a pulse of 2 optical cycles of frequency $\omega = 0.0569$ a.u. and intensity $I = 10^{14}$ W $\cdot$ cm^{-2} represented by the vector potential (5.29) with $\varphi = 0$.

sending the wave packet predominantly in the $-z$ direction.

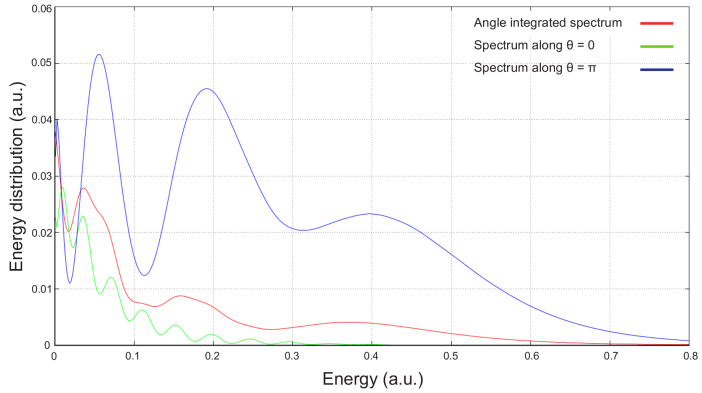

Figure 5.25: The angle integrated photoelectron energy spectrum (red), the $\theta = 0$ spectrum (green) and the $\theta = \pi$ spectrum (blue) against electron energy at the end of a pulse of 2 optical cycles of frequency $\omega = 0.0569$ a.u. and intensity $I = 10^{14}$ W $\cdot$ cm^{-2} represented by the vector potential (5.29) with $\varphi = \pi/2$.

To see how the pulse length affects calculations we now increase the length of the pulse to 4 optical cycles allowing more time for rescattering. Doubling the length of the pulse to 4 cycles has a considerable impact on the computational difficulties of the calculation. Although the Keldysh parameter and quiver radius stay constant with pulse length we now see an increase in the size of the required box, the number of basis functions and the number of Krylov vectors needed in the Arnoldi time

propagation routine. As such, converged results are obtained with a box of size $[0, 800]$ a.u. 800 B-spline functions and $N_l = 32$. We use a Krylov vector space size of 70 and a time step of $\delta t = 0.2$ a.u. Calculations take about 2.5 hours to run at these parameters using 4 processors. In figure 5.26 we show the comparison between the electron density against position r for the $l = 1$ partial wave between the 2 cycle pulse (red lines) and 4 cycle pulse (green lines). We can clearly see that by doubling the pulse length then we see some difference in the density distribution and although the amplitude of the probability remains almost constant we can see that the electrons have travelled further in the time of the pulse out to larger distances, as expected.

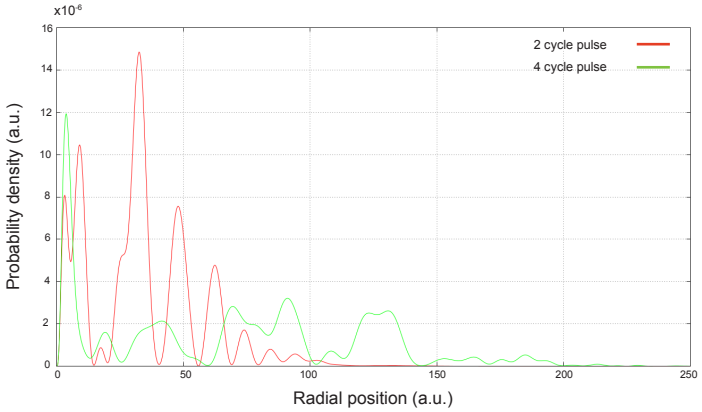

Figure 5.26: The electron radial probability density for $l = 1$ at the end of a pulse of frequency $\omega = 0.0569$ a.u. and intensity $I = 10^{14}$ W $\cdot$ cm^{-2} for a 2 optical cycle (red) and a 4 optical cycle pulse (green) represented by the vector potential (5.29).

Figure 5.27 shows the angle integrated spectrum (red line) as well as the $\theta = 0$ (green line) and $\theta = \pi$ (blue line) spectra for the 4 cycle pulse. The 4 cycle pulse follows the same structure with the majority of the ionisation occurring in the $\theta = \pi$ direction as in the 2 cycle case with $\varphi = 0$. However, with 4 cycles we see more oscillations in the field and more interference as the wave packets ionised at different times.

We now look at increasing the intensity of the laser pulse and once again look at the intensities previously examined of $I = 3 \times 10^{14}$ W $\cdot$ cm^{-2} and $I = 5 \times 10^{14}$ W $\cdot$ cm^{-2}.

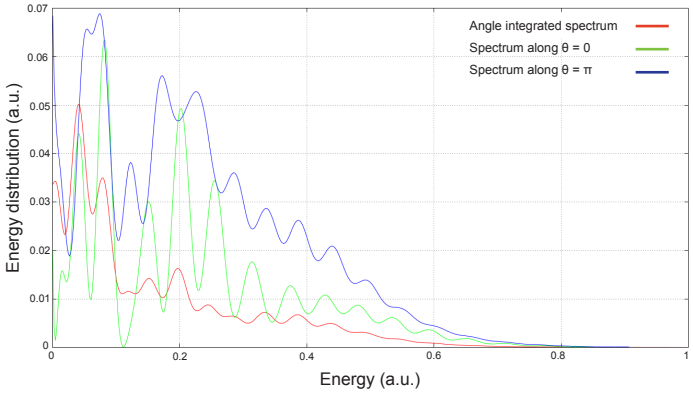

Figure 5.27: The angle integrated photoelectron energy spectrum (red), the $\theta = 0$ spectrum (green) and the $\theta = \pi$ spectrum (blue) against electron energy at the end of a pulse of 4 optical cycles of frequency $\omega = 0.0569$ a.u. and intensity $I = 10^{14}$ W $\cdot$ cm^{-2} represented by the vector potential (5.29) with $\varphi = 0$.

A converged calculation needed the use of a box of $[0, 900]$ a.u., 900 B-spline functions and $N_l = 34$ with a running time of about 2 hours using four processors for $I = 3 \times 10^{14}$ W $\cdot$ cm^{-2}. In the case of $I = 5 \times 10^{14}$ W $\cdot$ cm^{-2} we needed to use a box of $[0, 1100]$ a.u., 1100 B-spline functions and $N_l = 41$ with a running time of about 4 hours. We begin by analysing the electron probability density changes with intensity. In figure 5.28 we show the electron probability density against the radial position r for $I = 10^{14}$ W $\cdot$ cm^{-2} (red), $I = 3 \times 10^{14}$ W $\cdot$ cm^{-2} (green) and $I = 5 \times 10^{14}$ W $\cdot$ cm^{-2} (blue) for a 2 cycle pulse. We can see that the increase in intensity causes the probability of the electron finishing in the $l = 0$ partial wave to drop considerably as the intensity increases and more ionisation occurs, unlike when the pulse length is increased.

Figure 5.29 shows the probability density of the electrons left in the $l = 1$ partial wave for the same three intensities. We observe more pronounced peaks where the amplitude increases with significantly more oscillations as the increase in ionisation results in faster electrons being ejected. We also see an increase in the distance travelled by the electron as the intensity increases.

We also look at the ATI spectra and angular distributions to see how increasing the intensity affects these features. Figure 5.30 shows the angle integrated (red line) the

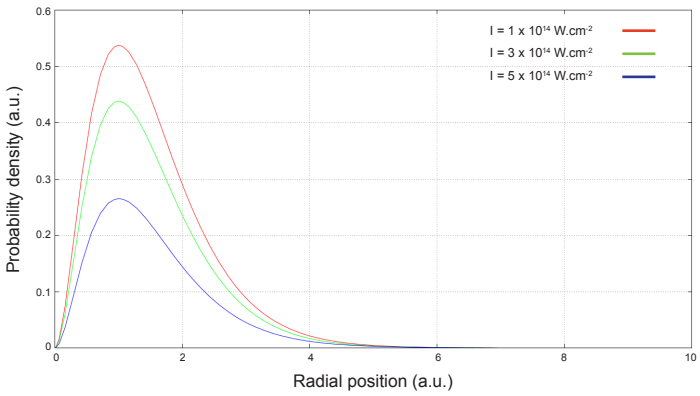

Figure 5.28: The electron radial probability density for $l = 0$ at the end of a pulse of 2 optical cycles of frequency $\omega = 0.0569$ a.u. and intensity $I = 10^{14}$ W $\cdot$ cm^{-2} (red), $I = 3 \times 10^{14}$ W $\cdot$ cm^{-2} (green) and $I = 5 \times 10^{14}$ W $\cdot$ cm^{-2} (blue) represented by the vector potential (5.29).

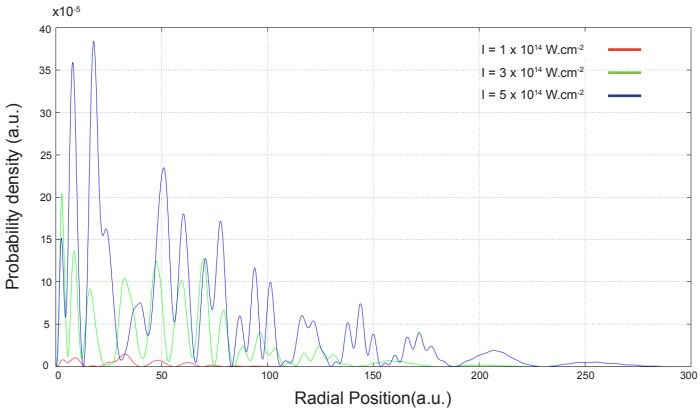

Figure 5.29: The electron radial probability density for $l = 1$ at the end of a pulse of 2 optical cycles of frequency $\omega = 0.0569$ a.u. and intensity $I = 10^{14}$ W $\cdot$ cm^{-2} (red), $I = 3 \times 10^{14}$ W $\cdot$ cm^{-2} (green) and $I = 5 \times 10^{14}$ W $\cdot$ cm^{-2} (blue) represented by the vector potential (5.29).

$\theta = 0$ spectrum (green line) and the $\theta = \pi$ spectrum (blue line) against energy E for the intensity of $I = 3 \times 10^{14}$ W $\cdot$ cm^{-2} whilst figure 5.31 shows the same picture for $I = 5 \times 10^{14}$ W $\cdot$ cm^{-2}. We can see that due to the pulse shape remaining unchanged with the increased intensity, the $\theta = \pi$ distribution still dominates in each case.

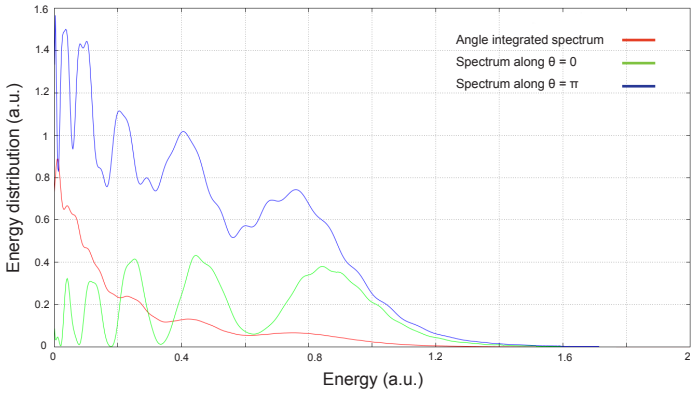

Figure 5.30: The angle integrated photoelectron energy spectrum (red), the $\theta = 0$ spectrum (green) and the $\theta = \pi$ spectrum (blue) against electron energy at the end of a pulse of 2 optical cycles of frequency $\omega = 0.0569$ a.u. and intensity $I = 3 \times 10^{14}$ W $\cdot$ cm^{-2} represented by the vector potential (5.29) with $\varphi = 0$.

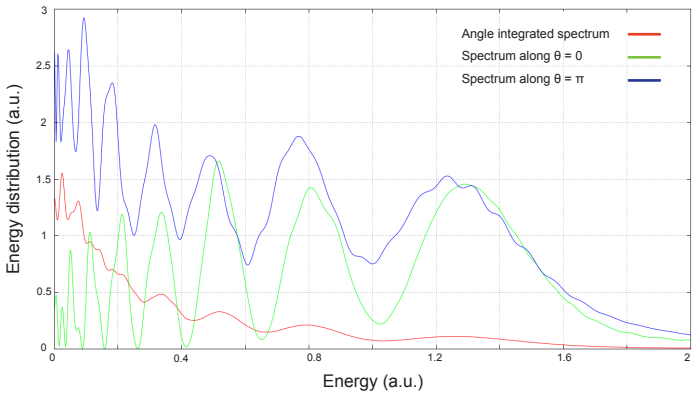

Figure 5.31: The angle integrated photoelectron energy spectrum (red), the $\theta = 0$ spectrum (green) and the $\theta = \pi$ spectrum (blue) against electron energy at the end of a pulse of 2 optical cycles of frequency $\omega = 0.0569$ a.u. and intensity $I = 5 \times 10^{14}$ W $\cdot$ cm^{-2} represented by the vector potential (5.29) with $\varphi = 0$.

5.5 Ionisation by a 2000nm Wavelength Laser

We return now to the very low frequency of $\omega = 0.0228$ a.u. corresponding to a wavelength of $\lambda = 2000$nm. At this frequency looking at the full three dimensional calculation is even more difficult since the solution becomes very oscillatory and the long pulse length means the electrons can travel very far in just 2 optical cycles. The high energy of the electrons means that a much larger number of partial wave states are needed in addition to a larger box size and basis size. All calculations here were checked for accuracy with comparison to calculations carried out in the Sturmian basis. Figure 5.32 shows the ATI spectrum and angular distribution at an intensity of $I = 10^{14}$ W $\cdot$ cm^{-2} for a 2 cycle pulse for an electric field described by the vector potential (5.29) with $\varphi = 0$. The calculation needed a box of size $[0, 1700]$ a.u. with 1700 B-spline functions and we took $n_l = 70$. For the time propagation we took the number of Krylov vectors to be 160 and a used smaller time step of $\delta t = 0.1$ a.u. meaning the calculation took around 72 hours. For these parameters the Keldysh parameter has a value of $\gamma = 0.427$ and the quiver radius is $\alpha \simeq 102$ a.u. We see that the ATI spectrum shows a maximum and a dominant structure at very low energy ($E \simeq 0.017$ a.u.) akin to the LES followed by a sharp decline to high energies. For the angle specific spectra we see there is a predominance of the distribution in the backwards direction, $\theta = \pi$. This is understood in the same way as for $\lambda = 800$nm, however now the interference pattern is much more pronounced. Figure 5.33 shows the same picture but now with a carrier phase of $\varphi = \pi/2$. For these calculations we used a relatively small box of $[0, 800]$ a.u. with 800 B-spline functions, we took $N_l = 80$ in order to achieve complete convergence although as we will see in figure 5.34 the partial waves with values between $l = 60$ and 80 do not contribute much to the final result at the end of the pulse. We again used a large number of Krylov vectors, 160 and a small time step of $\delta t = 0.1$ a.u. meaning the calculation took around 20 hours. The ATI spectrum follows a similar shape as that of $\varphi = 0$ with a maximum and a dominant structure at very low energy followed by a sharp decline. At low energies, the difference between the peaks ($E \simeq 0.0228$ a.u.) is

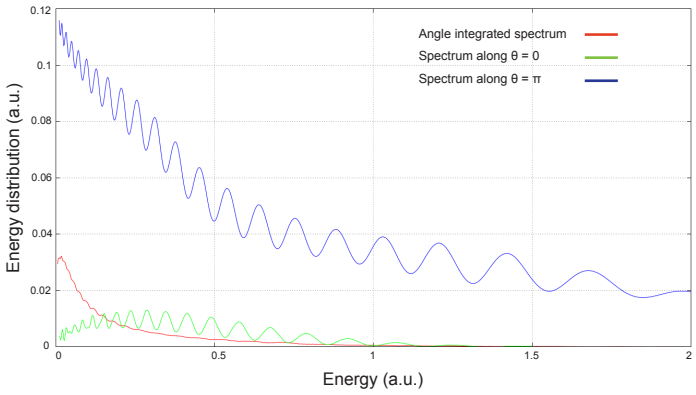

Figure 5.32: The angle integrated photoelectron energy spectrum (red), the $\theta = 0$ spectrum (green) and the $\theta = \pi$ spectrum (blue) against electron energy at the end of a pulse of 2 optical cycles of frequency $\omega = 0.0228$ a.u. and intensity $I = 10^{14}$ W $\cdot$ cm^{-2} represented by the vector potential (5.29) with $\varphi = 0$.

of the order of the field frequency and we see many more oscillations with this carrier phase due to interference between different wave packets. For the angle specific spectra the electrons are emitted both forward and in the backwards direction with a dominant contribution to the rear as in figure 5.32. In the case of both $\varphi = 0$ and $\varphi = \pi/2$ we also see that the distributions show peaks whose separation distance increases with energy as we saw for the case of $\lambda = 910$nm. As in the previous case the peaks have been interpreted by Arbo et al. [5] as a diffraction image resulting from the superposition of wave packets emitted by tunnel ionisation during a half-wave of the electric field when the field is at a maximum and then change direction following the change of the sign field (forward scattering), and direct electrons from tunnelling during the next half-cycle of the field.

Hamido [32] examined in figure 5.34 the contribution of each angular momentum partial wave towards the total ionisation probability for a) $\varphi = 0$ and b) $\varphi = \pi/2$. For $\varphi = 0$ we see a maximum in the contribution from $l = 23$ whilst for $\varphi = \pi/2$ the maximum is lower at $l = 19$. The distribution is more spread in the case of $\varphi = 0$ and we see a larger contribution for higher values of l up to a value of $l = 75$ whereas for $\varphi = \pi/2$ the maximum value of l which gives a significant contribution is $l \approx 60$. In both cases, the dominant contributions is found around the value corresponding

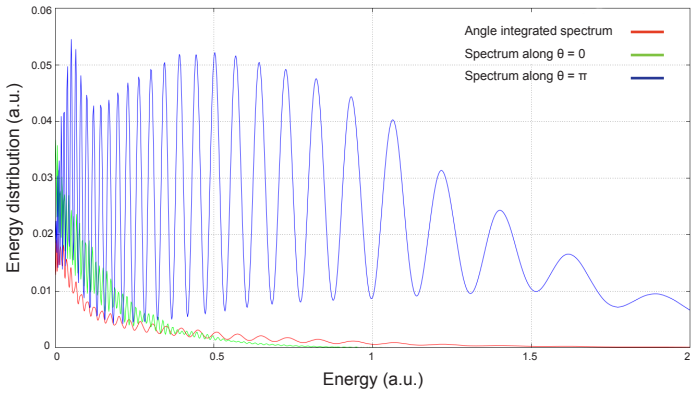

Figure 5.33: The angle integrated photoelectron energy spectrum (red), the $\theta = 0$ spectrum (green) and the $\theta = \pi$ spectrum (blue) against electron energy at the end of a pulse of 2 optical cycles of frequency $\omega = 0.0228$ a.u. and intensity $I = 10^{14}$ W $\cdot$ cm^{-2} represented by the vector potential (5.29) with $\varphi = \pi/2$.

to the number of photons that the electron must absorb to reach the continuum ($n = 22$). This could suggest that multiphoton ionisation plays an important role, but the broad distribution may rather indicate a strong polarisation of the wave packet.

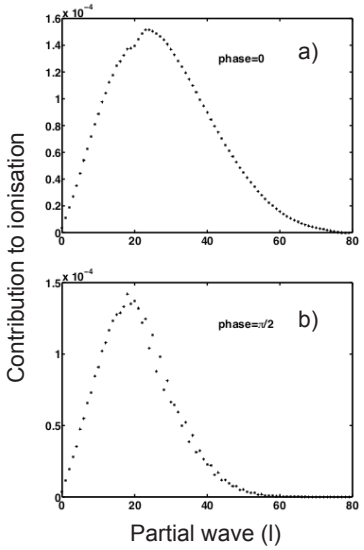

Figure 5.34: The contribution towards the total ionisation for each partial wave at the end of a pulse of 2 optical cycles of frequency $\omega = 0.0228$ a.u. and intensity $I = 10^{14}$ W $\cdot$ cm^{-2} represented by the vector potential (5.29) with a) $\varphi = 0$ and b) $\varphi = \pi/2$. [32].

5.5.1 Intensity Averaged Cross Section

As we carried out in one dimension we now consider the intensity averaging method used to more accurately model experimental laser equipment by taking into account the spatial profile of the field on the ATI spectrum. In figure 5.35 we show a) the original non-averaged ATI spectrum for a 2 cycle pulse of intensity $I = 10^{14}$ W $\cdot$ cm^{-2} described by the vector potential (4.3) and b) the intensity averaged ATI spectrum for a peak intensity of $I = 10^{14}$ W $\cdot$ cm^{-2} for the same case of 2 cycle pulse. The intensity averaged spectrum was calculated using four different intensities of $I = 5 \times 10^{13}$ W $\cdot$ cm^{-2}, $I = 8 \times 10^{13}$ W $\cdot$ cm^{-2}, $I = 9 \times 10^{13}$ W $\cdot$ cm^{-2} and $I = 3 \times 10^{14}$ W $\cdot$ cm^{-2}. We see good agreement between the two spectra in terms of structure and it appears that, as in one dimension, the inclusion of the spatial profile of the field has a smoothing effect on the spectrum. The spectrum again has a strong peak near $E = 0$.

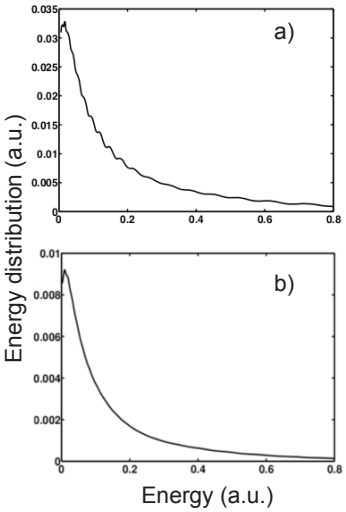

Figure 5.35: a) The original photoelectron energy spectrum at the end of a pulse of 2 optical cycles of frequency $\omega = 0.0228$ a.u. and peak intensity $I = 10^{14}$ W $\cdot$ cm^{-2} described by the vector potential (4.3) and b) the intensity averaged photoelectron energy spectrum for the same pulse.

5.5.2 Ionisation Yield

The ionisation yield investigated here gives information as to how the change from one dimension to three dimension affects the ionisation probability and about the unexpected behaviour that occurred in one dimension where the ionisation yield fell with increasing intensity. Again we show results for the ionisation probability at intensities from 10^{11} to 3×10^{14} W $\cdot$ cm^{-2}. Figure 5.36 shows this yield at the lower frequency of $\omega = 0.0228$ a.u. for a 2 cycle pulse as given in equation (5.29). The calculations were carried out by A. Hamido [32] using the Sturmian basis and Arnoldi time propagation with $N_l = 80$ for 1800 Sturmians and 80 Krylov vectors (blue line), 1500 Sturmians and 80 Krylov vectors (red circles) and 1800 Sturmians and 90 Krylov vectors (green stars). All three calculations match showing exact convergence. We can see that very similarly to the one dimensional case, the same behaviour appears with slight drops in the ionisation probability potentially due to trapping in Rydberg states indicative of excitation. In 3D we note that the effect now occurs after just 2 optical cycles, whereas this wasn't a long enough pulse in 1D.

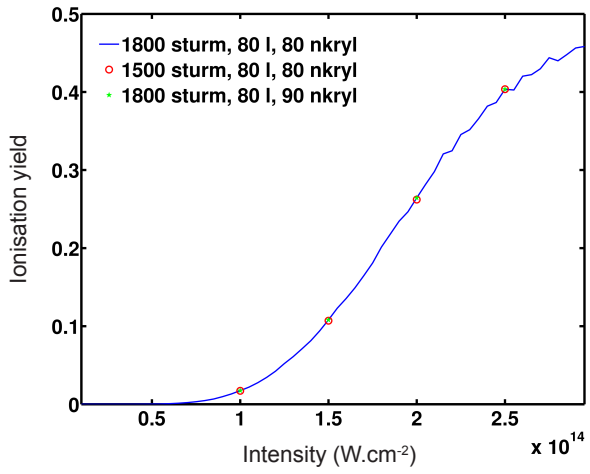

Figure 5.36: The ionisation yield as a function of intensity I, at the end of a 2 cycle pulse of frequency $\omega = 0.0228$ a.u. given by equation (5.29). (A. Hamido, private communication.)

5.5.3 Probability Current

We return now to the probability current to see how the change from one dimension to three dimensions affects the probability flux. Figure 5.37 shows the probability current against time t for an intensity of $I = 10^{14}$ W $\cdot$ cm^{-2} for 2 cycles. In cylindrical polar coordinates we measure the flux at positions $z = 40$ a.u. and $\theta = 0$ rad (blue line), $\theta \approx 7$ rad (red line) and $\theta \approx 14$ rad (green line) where θ is the angular coordinate. The dashed lines show the same pictures for $z = -40$ a.u. for the same angles and colours respectively. We can see that the picture follows a very similar structure to the one dimensional case for the same frequency. For $\theta = 0$ at $z = 40$ a.u. we see a highly oscillating large peak of positive amplitude at the beginning of the second cycle due to the large negative peak in the first optical cycle. Entering the second cycle the field changes direction again and the current reduces in amplitude before finally changing to negative total value as the electron momentum changes to a negative value as well. As we increase the angle θ and move away from the direction of the polarisation we can see the current drops and tends towards a zero current perpendicular to the laser polarisation axis. This suggests that the majority of the ionisation occurs from tunnelling in the direction of the tunnel created by the Coulomb potential and electric field superposition which oscillates from $z = 40$, $\theta = 0$ to $z = -40$ a.u. $\theta = 0$ as the electric field changes direction. In the negative direction the majority of the current is now of negative amplitude as in the one dimensional case. The similarity between 1D and 3D calculations suggest that the motion of the electron is confined to the laser polarisation axis since the 1D calculation confines the motion to this axis.

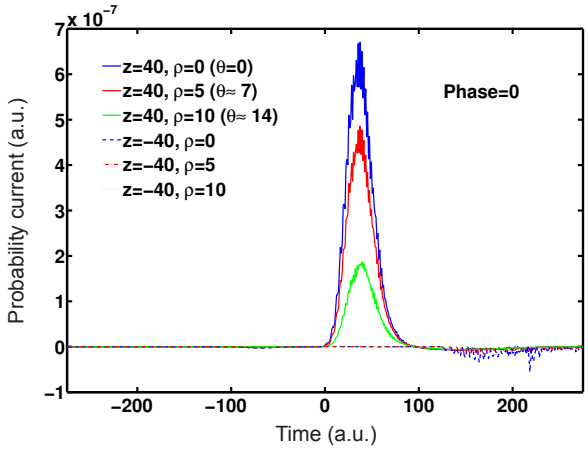

Figure 5.37: The probability current as a function of time t at positions $z = 40$ a.u. and $\theta = 0$ rad (blue), $\theta \approx 7$ rad (red) and $\theta \approx 14$ rad (green) in cylindrical polar coordinates, throughout a 2 cycle pulse of frequency $\omega = 0.0228$ a.u. and intensity $I = 10^{14}$ W $\cdot$ cm^{-2} described by (5.29) with $\varphi = 0$. (A. Hamido, private communication.)

5.6 Adiabatic Approximation

We further investigated the low frequency limit by examining the limit $\omega \to 0$ to see how we can make contact with the adiabatic approximation. If the frequency of the laser field is low enough that the field varies slowly then we can assume the *adiabatic approximation* or the *static field limit* and take the solution of the TDSE to be

$$\Psi_{\mathrm{AD}}(\mathbf{r}, t) \equiv \exp\left(-\mathrm{i}\int_0^t E_{\mathrm{DC}}[\mathbf{E}(t')]\mathrm{d}t'\right)\psi_{\mathrm{DC}}[\mathbf{E}(t); \mathbf{r}], \tag{5.38}$$

where $E_{\mathrm{DC}}[\mathbf{E}]$ are complex energies in a static field $\mathbf{E}$ given by

$$E_{\mathrm{DC}}[\mathbf{E}] = E_0 + \Delta_{\mathrm{DC}}(\mathbf{E}) - \frac{\mathrm{i}}{2}\Gamma_{\mathrm{DC}}(\mathbf{E}), \tag{5.39}$$

where $\Delta_{\mathrm{DC}}(\mathbf{E})$ is the DC Stark shift of the initial ground state and $\Gamma_{\mathrm{DC}}(\mathbf{E})$ is the ionisation width of the Stark state which in atomic units is also the ionisation rate of the atom in the static field. In equation (5.38) ψ_{DC} is the solution of the TISE given by

$$(H_0 + \mathbf{E}\cdot\mathbf{r})\psi_{\rm DC}[\mathbf{E};\mathbf{r}] = E_{\rm DC}\psi_{\rm DC}[\mathbf{E};\mathbf{r}]. \tag{5.40}$$

We solved this equation using complex scaling for a wide range of field strengths $\mathbf{E}$ which then allowed us to calculate $\Gamma_{\rm DC}(\mathbf{E})$ for Hydrogen. At the end of the pulse the wave function is equal to

$$\Psi_{\rm AD}(\mathbf{r},\tau) = \exp\left(-\frac{1}{2}\int_0^\tau \Gamma_{\rm DC}(\mathbf{E}(t'))\mathrm{d}t'\right)\psi_0 \tag{5.41}$$

where ψ_0 is the ground state. In this approximation we expect the electron to follow the field and then return back to the ground state at the end of the pulse but with a reduced amplitude. Equation (5.41) shows that some of the probability is lost during the pulse due to the tunnel ionisation caused by the complex factor in equation (5.39). Therefore the probability of ionisation can be calculated at the end of the pulse from equation (5.41) as one minus the probability of staying in the ground state,

$$P^{ion}(\tau) = 1 - \exp\left(-\int_0^\tau \Gamma_{\rm DC}(\mathbf{E}(t'))\mathrm{d}t'\right). \tag{5.42}$$

Making a substitution, $y = \omega t'$, we can then express the ionisation probability as

$$P^{ion}(\tau) = 1 - \exp\left(-\frac{1}{\omega}\int_0^{2\pi n_c} \Gamma_{\rm DC}(y)\mathrm{d}y\right). \tag{5.43}$$

Since in the calculations carried out the integrand above is small in comparison to ω we can expand this as a series of the formation

$$P^{ion}(\tau) = 1 - \left(1 - \frac{1}{\omega}\int_0^{2\pi n_c} \Gamma_{\rm DC}(y)\mathrm{d}y + \cdots\right) \simeq \frac{1}{\omega}\int_0^{2\pi n_c} \Gamma_{\rm DC}(y)\mathrm{d}y. \tag{5.44}$$

Hence the ionisation probability $P^{ion} \propto 1/\omega$.

For atomic Hydrogen in the case of a 2 cycle pulse of intensity $I = 10^{14}$ W $\cdot$ cm^{-2}, described by the vector potential (5.29), we used our calculated $\Gamma_{\rm DC}(\mathbf{E})$ to obtain P^{ion} in equation (5.44). The ionisation rate as well as the excitation rate was calculated by solving the TDSE and compared against the adiabatic limit for varying

frequency of laser. The ab initio calculations using the TDSE for low frequencies were carried out using a Sturmian basis with a radial basis of size 6000 and 160 angular momenta (B. Piraux, private communication). The results indicate that an adiabatic theory may be a correct starting point to understand, qualitatively and quantitatively, the LES and low frequency behaviour in general [77].

This comparison can be found in figure 5.38 where we show the probability of ionisation as given by the adiabatic limit (dashed line) showing the $1/\omega$ dependence and the total ionisation (blue line) and excitation (red line) probability calculated by solution of the TDSE against frequency ω. Whilst for very low frequency the ionisation probability agrees exactly with the adiabatic limit we see a clear deviation from the approximation at $\omega = 0.01$ a.u. when ionisation and excitation begins and all higher frequencies where the ionisation rate rises dramatically and away from the static field limit curve.

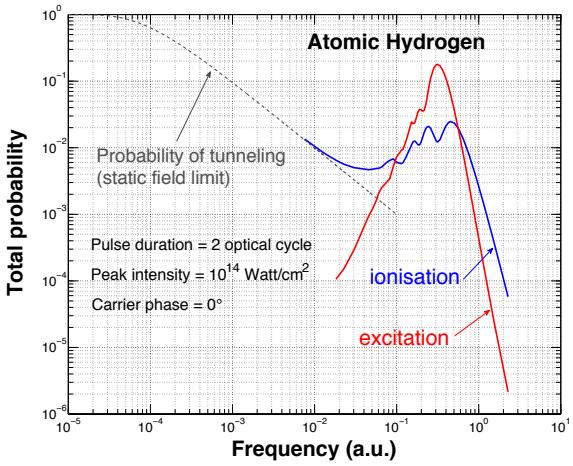

Figure 5.38: Breakdown of the adiabatic limit: Shown is the probability of ionisation as given by the adiabatic limit (dashed line) and the total ionisation (blue) and excitation (red) probability calculated by solution of the TDSE.

5.7 Exterior Complex Scaling

We describe here how we can extend the 1D exterior complex scaling (ECS) method, described in chapter 2, to 3D as an alternative method to solve the TDSE for

hydrogen. In order to gain convergence in these cases a very dense mesh within the unscaled area must be used and as we decrease the frequency of the laser it becomes necessary to use a very small scaling angle. This in turn slows the damping of the wave function and dictates the use of a larger box size and density of basis functions than in equivalent calculations in one dimension. However, since the size of the unscaled calculations grow significantly with the extension to 3D, the ECS still results in significant improvement on memory usage and run time of calculations. As in the one dimension case, the scaling radius R_0 must lie outside of the bound states and although it can be within the quiver radius this will result in the need for an increase in the density of B-splines within the unscaled area due to the increase in the flux oscillating about R_0. We begin at a wavelength of 800nm and intensity of $I = 10^{14}$ W $\cdot$ cm^{-2} and use a pulse of 2 optical cycles. We first calculate the electron density and obtain converged results using scaling parameters of $R_0 = 70$ a.u. and $\theta = 0.2$ rad for a box split into 2 sections, $[0, 75]$ a.u. to represent the unscaled part of the mesh and the transition point, between the scaled and unscaled regions, in which we used 150 B-spline basis functions and $[75, 150]$ a.u. to represent the scaled part of the mesh where we used 40 B-spline functions. We use a value of $N_l = 30$ across the whole box and for the time propagation we use a time step of $\delta t = 0.2$ a.u. and just 12 Krylov functions. The calculation took around 3 minutes, considerably less than the full unscaled calculation on a laptop with an INTEL core 2 duo processor of 2.4 GHz which took 34 minutes and hence using this method the computation time was only 10% of the time taken for the full calculation and the box under half the size. Figure 5.39 shows electron probability density against radial position r for the unscaled (red line) and scaled (blue line) calculation for the $l = 0$ electron density for the above parameters. We can see that the density in the unscaled region, including the large peak of the bound states is accurately represented in the scaled calculation and agreement is perfect until the scaling takes over and the wave packet is quickly damped. In addition the smaller unscaled box and basis size meant that we could use just 12 Krylov vectors in comparison to the

40 needed for the unscaled calculation.

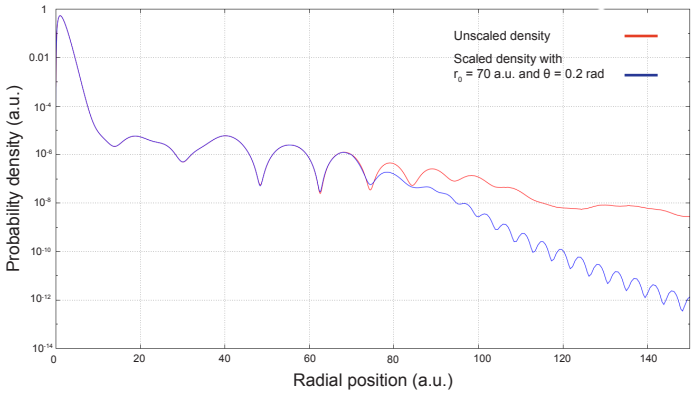

Figure 5.39: The electron probability density for $l = 0$ at the end of a 2 cycle pulse of frequency $\omega = 0.0569$ a.u. and intensity $I = 10^{14}$ W $\cdot$ cm^{-2} described by (5.29). Shown is the full unscaled density (red) and the scaled density carried out using ECS with scaling points $R_0 = 70$ a.u. for a scaling angle of $\theta = 0.2$ rad (blue).

Figure 5.40 shows the electron density with $l = 1$ for the same parameters. Here we see there is no peak due to the density remaining in the bound states and we get a series of oscillations which are also accurately represented by the scaled program. Increasing the scaling angle resulted in convergence not being achieved with the current time step and number of B-spline functions.

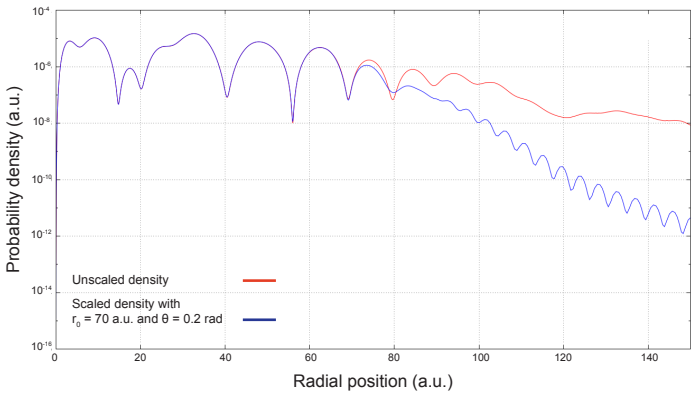

Figure 5.40: The electron probability density for $l = 1$ for a 2 cycle pulse of frequency $\omega = 0.0569$ a.u. and intensity $I = 10^{14}$ W $\cdot$ cm^{-2} described by (5.29). Shown is the full unscaled density (red) and the scaled density carried out using ECS with scaling points $R_0 = 70$ a.u. for a scaling angle of $\theta = 0.2$ rad (blue).

We now look again at $\omega = 0.0228$ a.u. corresponding to a wavelength of 2μm. We use a single cycle pulse and an intensity of $I = 10^{14}$ W $\cdot$ cm^{-2}. For the unscaled calculation we use a box of $[0, 800]$ a.u. with 1000 B-splines in order to achieve exact results to computational accuracy for large angular momentum and energy and take $N_L = 60$. We use a time step of $\delta t = 0.1$ a.u. and 100 Krylov vectors. For the scaled calculation we take a scaling radius of $R_0 = 200$ a.u. and have to reduce the scaling angle to $\theta = 0.1$ rad in order for the results to be converged. We again use a split box of $[0, 205]$ a.u. to represent the unscaled part of the mesh with 400 B-splines and $[205, 350]$ for the scaled region of the mesh with 50 basis functions. Here the box representing the scaled part is larger than in the case of higher frequency due to the higher quiver radius and the fact that the electrons travel with higher velocities as well as the scaling angle being taken smaller. This causes the damping of the wave function to occur over a larger distance and hence a larger value of $x_{\max}$ is needed to avoid reflections of the damped wave function. In spite of the larger outer box we still only need 50 B-splines to represent it, which gives a function density of one B-spline per 2.9 a.u. of mesh. This is a much lower density than the one used over the unscaled part of the box which has one B-spline per 0.5125 a.u. of mesh. For a time step of $\delta t = 0.1$ a.u. we can now use a smaller Krylov basis with just 20 functions. This is due to the reduced basis size meaning that we have a smaller maximum eigenvalue thus reducing the stiffness of the equation. In figure 5.41 we show the $l = 0$ probability density against radial position r for the above parameters. Similar to the case of 800nm, the agreement between scaled and unscaled is very good with the wave function damping immediately at the scaling radius. In figure 5.42 we show the electron probability density against radial position r for $l = 1$ for the same parameters, again achieving very good agreement within the unscaled area.

In both cases of 800nm and 2μm the majority of the density remains in the bound states due to the low frequency of the laser pulse. Therefore, as before, we now look at the continuum electron density in order to test the accuracy of the scaling more

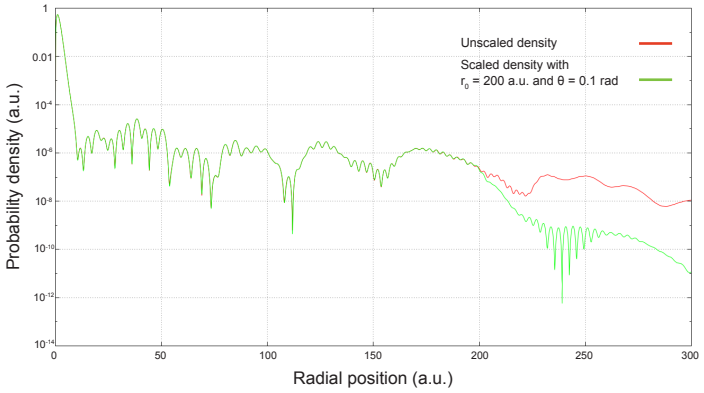

Figure 5.41: The electron probability density for $l = 0$ for a 1 cycle pulse of frequency $\omega = 0.0228$ a.u. and intensity $I = 10^{14}$ W $\cdot$ cm^{-2} described by (5.29). Shown is the full unscaled density (red) and the scaled density carried out using ECS with scaling point $R_0 = 200$ a.u. and for a scaling angle of $\theta = 0.1$ rad (green).

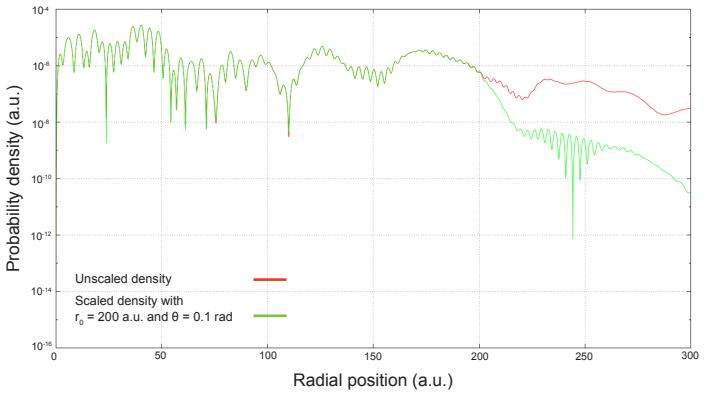

Figure 5.42: The electron probability density for $l = 1$ for a 1 cycle pulse of frequency $\omega = 0.0228$ a.u. and intensity $I = 10^{14}$ W $\cdot$ cm^{-2} described by (5.29). Shown is the full unscaled density (red) and the scaled density carried out using ECS with scaling point $R_0 = 200$ a.u. and for a scaling angle of $\theta = 0.1$ rad (green).

stringently. Since the ionisation probability in this case is low, achieving accuracy here requires the use of a dense basis within the unscaled region in order to represent the many small oscillations in probability. Figure 5.43 shows the continuum probability density for $l = 0$ for the above parameters at $\lambda = 2\mu$m. Now the large peak close to the origin containing the majority of the density is gone and just the ionised electrons in the $l = 0$ partial wave remain. Again we see very good agreement within the unscaled radius. Figure 5.44 shows the continuum probability density for $l = 1$ for the same parameters. Again we get an excellent agreement within the unscaled area.

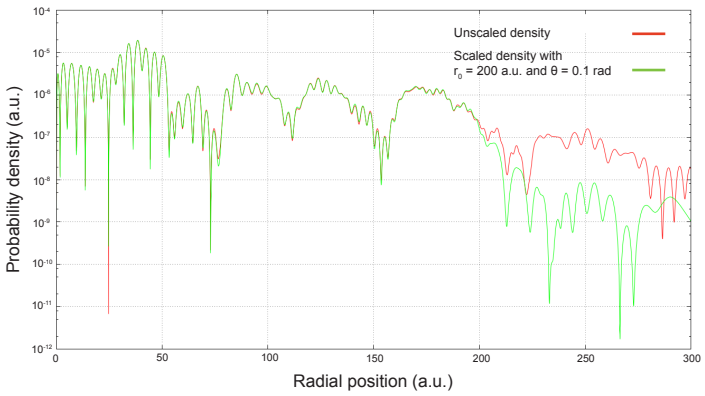

Figure 5.43: The continuum electron probability density for $l = 0$ for a 1 cycle pulse of frequency $\omega = 0.0228$ a.u. and intensity $I = 10^{14}$ W $\cdot$ cm^{-2} described by (5.29). Shown is the full unscaled density (red) and the scaled density carried out using ECS with scaling point $R_0 = 200$ a.u. and for a scaling angle of $\theta = 0.1$ rad (green).

If we are only interested in a small region of space surrounding the atom we may wish to use an even smaller box, allowing us to use less basis functions and reduce the computation time further. We now lower the scaling radius to $R_0 = 50$ a.u. and continue using a scaling angle of $\theta = 0.1$ rad allowing us to use a box now of size $[0, 55]$ a.u. for the unscaled mesh and $[55, 200]$ a.u. for the scaled part. We use 150 and 50 basis functions here allowing us to reduce the computation time by over 50% in comparison with the previous scaled calculation. Figures 5.45 and 5.46 show the comparison between the continuum electron density against radial position r for the

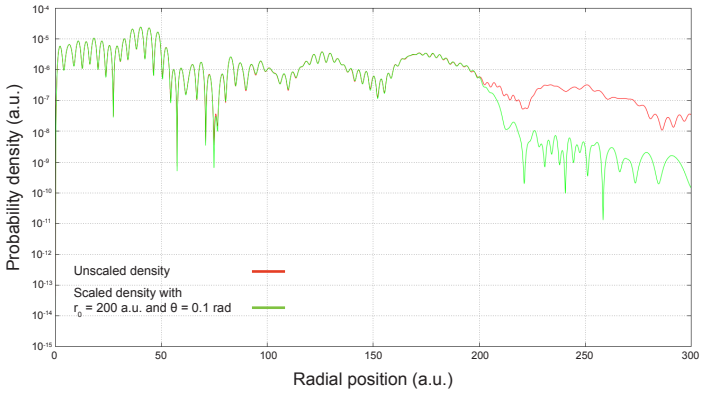

Figure 5.44: The continuum electron probability density for $l = 1$ for a 1 cycle pulse of frequency $\omega = 0.0228$ a.u. and intensity $I = 10^{14}$ W $\cdot$ cm^{-2} described by (5.29). Shown is the full unscaled density (red) and the scaled density carried out using ECS with scaling point $R_0 = 200$ a.u. and for a scaling angle of $\theta = 0.1$ rad (green).

unscaled (red lines) and scaled (green lines) calculations of the continuum electron density for the $l = 0$ and $l = 1$ partial waves respectively for these parameters. Again we see that we get perfect agreement within the unscaled areas.

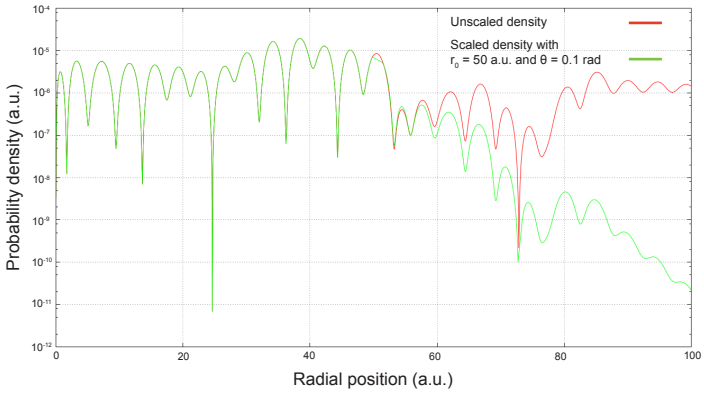

Figure 5.45: The continuum electron probability density for $l = 0$ for a 1 cycle pulse of frequency $\omega = 0.0228$ a.u. and intensity $I = 10^{14}$ W $\cdot$ cm^{-2} described by (5.29). Shown is the full unscaled density (red) and the scaled density carried out using ECS with scaling point $R_0 = 50$ a.u. and for a scaling angle of $\theta = 0.1$ rad (green).

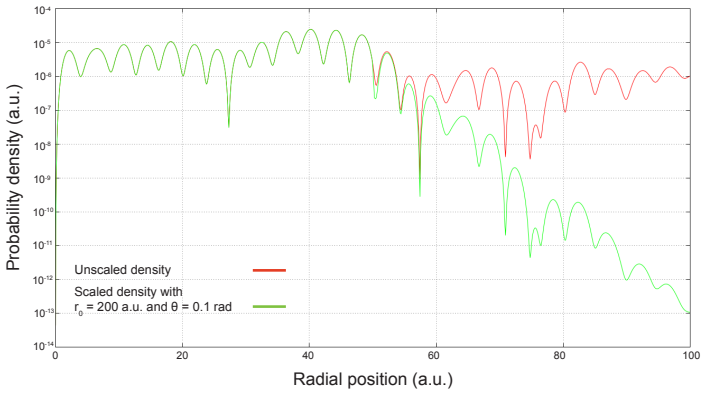

Figure 5.46: The continuum electron probability density for $l = 1$ for a 1 cycle pulse of frequency $\omega = 0.0228$ a.u. and intensity $I = 10^{14}$ W $\cdot$ cm^{-2} described by (5.29). Shown is the full unscaled density (red) and the scaled density carried out using ECS with scaling point $R_0 = 50$ a.u. and for a scaling angle of $\theta = 0.1$ rad (green).

5.8 Negatively Charged Hydrogen and Argon

We now look briefly at two other systems in order to see how the electron dynamics differ when using a different atomic potential and to see if the formation of the LES is reliant on the long range tail of the Coulomb potential as has been suggested [46, 75]. To begin we look at negatively charged Hydrogen before briefly investigating Argon.

5.8.1 Negatively Charged Hydrogen

We first look at the photodetachment of the H^- ion by an intense linearly polarised laser pulse at low frequency. We again perform a direct integration of the TDSE using the same method as for Hydrogen and approximate the negative ion using a model potential. We investigate the angle integrated photoelectron detachment spectrum obtained and compare this with results using the strong field approximation. We can then investigate the presence or otherwise of the low energy structure (LES) seen for neutral Hydrogen in similar conditions. A reason for looking at negatively charged Hydrogen is to see how rescattering after ionisation in the presence of a long range Coulomb tail, which has been suggested as a primary contribution to the formation of the LES, affects the ATI spectrum. The scattering off of the

positively charged parent ion seen in the case of Hydrogen is absent in calculations for H^- due to the presence of another electron which remains after ionisation leaving a neutrally charged Hydrogen atom. As such we do not expect to see the LES to form due to the lack of a long range Coulomb field. We treat the H^- ion as an effective one electron system in which the detached electron moves in the field of a perturbed hydrogen atom and the detachment reaction we look at is

$$H^- + h\nu \rightarrow H + e^-. \tag{5.45}$$

We conduct all calculations in the velocity gauge and begin by testing our program by comparing results of the above threshold detachment (ATD) spectrum with results obtained by O. Tolstikhin [76]. As such we use a form of the electric field given by

$$E(t) = \begin{cases} E_0 \cos^2\left(\frac{\pi t}{\tau}\right) \sin(\omega t + \varphi) & \text{if } \ 0 \leq t \leq \tau \\ 0 \ \ \text{otherwise,} \end{cases} \tag{5.46}$$

for a frequency of $\omega = \pi/10$ and use a range of four intensities for $I = 3.5 \times 10^{14}$ to $I = 1.7 \times 10^{16}$ W $\cdot$ cm^{-2}. These intensities correspond to electric field amplitudes from $E_0 = 0.1$ to 0.5 a.u. and Keldysh parameter values of $\gamma = 0.74$ to 0.11. For each intensity we use a long pulse of 25 optical cycles.

We take the initial condition as the ground state, which has a binding energy of $E = 0.755$ eV $= 0.02775$ a.u. The spherically symmetric atomic potential is chosen to be of the form

$$V(r) = -V_0 \mathrm{e}^{-r^2/r_0^2} \tag{5.47}$$

with $V_0 = 0.3831087$ and $r_0 = 2.5026$ a.u. so that one bound state is obtained at the above energy and the s-wave scattering length equal to 5.965, in full agreement with accurate variational results for H^-. We obtain perfect agreement for the full ATD spectrum and we show the first peaks of the spectrum for each intensity in figure 5.47 along with the same picture from [76] for comparison. The dependence of the intensity of the field on the shape of the peak can be clearly seen in this picture.

For low intensity the quiver amplitude ($\alpha = E_0/\omega^2$) is low and the detachment rate reaches its maximum only once, at the maximum of the pulse, giving a single peak structure with no significant substructure. As the intensity and quiver amplitude grows the detachment rate then has two maxima, one just before the maximum of the field and one just after the maximum. Now a wave packet is formed at each of these maxima of the detachment rate and interfere causing a small substructure to appear on the peak. As the quiver amplitude increases the substructures on the peak become more pronounced. From the calculations we can see that the critical value of the quiver amplitude that causes multiple maxima of the detachment rate is $\alpha \simeq 3$.

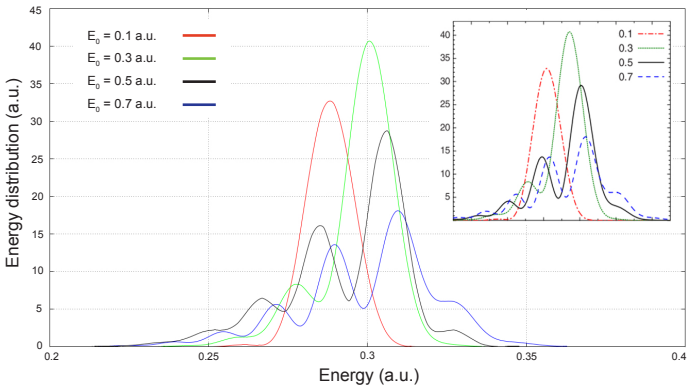

Figure 5.47: The first peak of the ATD spectrum at the end of a pulse of 25 optical cycles of frequency $\omega = \pi/10$ a.u. given by the electric field (5.46) for electric field amplitudes of $E_0 = 0.1$ (red), 0.3 (green), 0.5 (blue) and 0.7 a.u. (pink). Inset is the same peak of the ATD spectra calculated by [76] using the Siegert-state expansion method.

The full ATD spectrum for the electric field amplitude of $E_0 = 0.5$ a.u. corresponding to an intensity of $I = 1.6 \times 10^{16}$ W $\cdot$ cm^{-2} is given in figure 5.48. Here we can see that the spectrum has a clear peak structure similar to that of ATI. We see that the sequence of peaks fall near multiphoton absorption energies and the heights of the peaks fall with increasing energy as expected. There is no significant LES feature in the spectra.

The previous potential used is of a simple form and neglects to take the angular

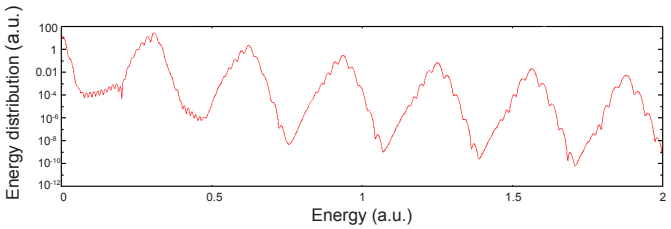

Figure 5.48: The ATD spectrum at the end of a pulse of 25 optical cycles of frequency $\omega = \pi/10$ a.u. and intensity $I = 1.6\times10^{16}$ W $\cdot$ cm^{-2} given by the electric field (5.46).

momentum into account. In order to more accurately approximate the H^- ion we now choose a spherically symmetric atomic potential which is dependent on the angular momentum. We now take the potential to be [81]

$$V_l(r) = -\left(1+\frac{1}{r}\right)\mathrm{e}^{-2r} - \frac{\alpha_d}{2r^4}\left(1-\mathrm{e}^{-(r/r_c)^6)}\right) + v_l(r) \tag{5.48}$$

where the second term is a cutoff term with $\alpha_d = 4.5$ a.u., the static polarisability of hydrogen, and $r_c = 4$ a.u. the effective hydrogen-atom radius. The last term is an angular momentum dependent short range correction given by

$$v_l(r) = (c_0 + c_1 r + c_2 r^2)\mathrm{e}^{-\beta r} \tag{5.49}$$

where β and the l dependent coefficients c_0, c_1, c_2 are chosen to approximate accurately the binding energy (0.754 eV) of H^-. It is sufficient to use 2 different functions v_0 and v_l for $l > 0$ and necessary to use more than one function since a common potential cannot sufficiently represent the phase shifts. Figure 5.49 shows this model potential against radial position r where we have split the potential into the V_0 (red line) and V_l with $l > 0$ (blue line) contributions.

We now revert back to an electric field corresponding to the vector potential given by (5.29) and take both $\varphi = 0$ and $\varphi = \pi/2$ for the phase in order to investigate the effect of the carrier envelope phase on the energy spectrum. In order to do this we now use a laser pulse with a much lower frequency of $\omega = 0.0043$ a.u., which models detachment in a 10600nm CO_2 laser pulse, for 5 optical cycles. We perform

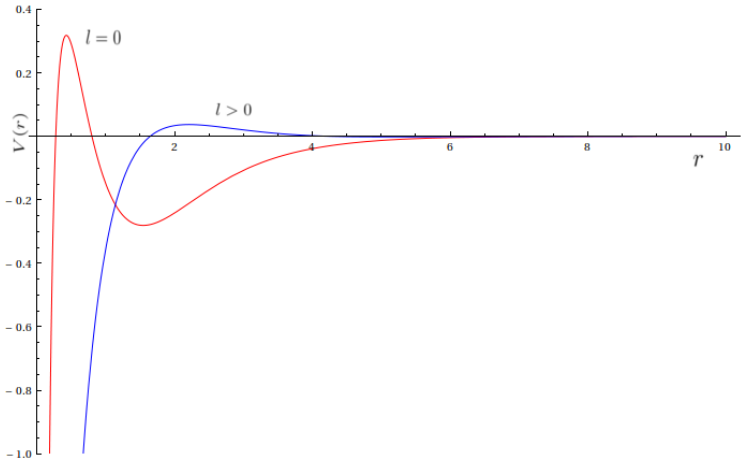

Figure 5.49: The angular dependent model potential for negatively charged Hydrogen showing $V_0(r)$ (red) and $V_l(r)$ for $l > 0$ (blue).

calculations for three different peak intensities $I = 10^{10}$ W $\cdot$ cm^{-2}, $5\times$ 10^{10} W $\cdot$ cm^{-2} and 10^{11} W $\cdot$ cm^{-2} corresponding to Keldysh parameter values $\gamma = 1.90$, 0.85 and 0.60 respectively meaning that when we reach the higher intensities we are within the tunnelling regime. We use a low intensity model laser in order to limit detachment which can occur quite easily due to the low effective ionisation potential. For the case of the highest intensity $I = 10^{11}$ W $\cdot$ cm^{-2} the ponderomotive potential of 1.05eV means that just 16 photons of $E = \hbar\omega = 0.117$ eV are required to detach the electron. In all cases we compare our results calculated using the TDSE with the results of the SFA calculated by Zhou at al. [81]. It is worth noting that these calculations are particularly intensive due to the very low frequency and large number of cycles. Using a time step of $\delta t = 0.2$ a.u. these parameters require the use of over 36000 steps, considerably more than the previous calculations at a wavelength of $\lambda = 2\mu$m. As such a very large box is needed to hold the ejected wave packets especially at the highest intensity.

Figure 5.50 shows the ATD spectrum against energy E for phases $\varphi = 0$ (red line) and $\varphi = \pi/2$ (green line) at an intensity of $I = 10^{10}$ W $\cdot$ cm^{-2}. We can see that for this lower intensity, which is in the multiphoton regime, the carrier envelope phase makes little difference to the final ATD spectrum in both numerical solution of the TDSE and the SFA. We can see that the TDSE results agree very well with the

SFA with two large peaks dominating the spectrum separated by the photon energy. This shows again that the LES is not present here as the SFA calculation only takes into account direct ionisation and no rescattering.

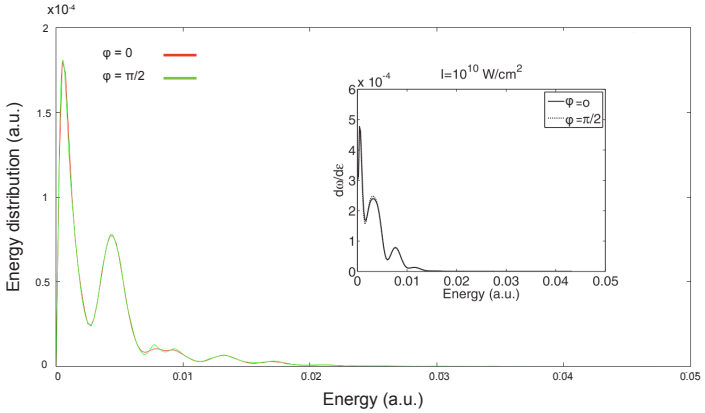

Figure 5.50: The ATD spectrum at the end of a pulse of 5 optical cycles of frequency $\omega = 0.0043$ a.u. and intensity of $I = 10^{10}$ W $\cdot$ cm^{-2} defined by (5.29) calculated from direct numerical solution of the TDSE for phases $\varphi = 0$ and $\varphi = \pi/2$. Inset is the same parameters calculated using the SFA [67].

We now increase the intensity to $I = 5 \times 10^{10}$ W $\cdot$ cm^{-2} in figure 5.51. We see that the spectra are much more complicated. For both phases we get good agreement with the SFA in the lower energy regime whereas the results differ more as the energy increases. For $\varphi = 0$ we see that the low energy peaks tend to become distorted and double peaks form as the peak splits at the top. This can be seen using both methods for the first ATD peak. For $\varphi = \pi/2$ we see a more standard peak structure, separated by photon energy, which is of higher amplitude than $\varphi = 0$ in both methods. The difference as we move to higher energy can be attributed to the fact that the full numerical calculation we undertake includes all orders of rescattering of the electron during the 5 cycle pulse whereas the SFA neglects higher levels of rescattering meaning that the emergence of high energy electrons are less likely in this approximation.

Finally we look at the highest intensity of $I = 10^{11}$ W $\cdot$ cm^{-2} in figure 5.52. We still see peaks positioned at the predicted energies and see separation distances of the photon energy although now the amplitudes are more irregular with higher

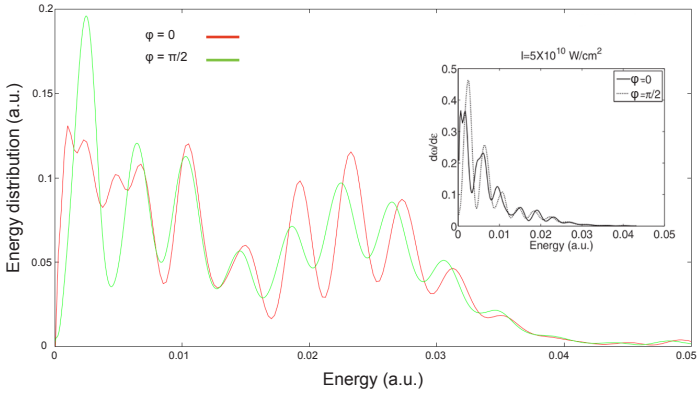

Figure 5.51: The ATD spectrum at the end of a pulse of 5 optical cycles of frequency $\omega = 0.0043$ a.u. and intensity of $I = 5 \times 10^{10}$ W $\cdot$ cm^{-2} defined by (5.29) calculated from direct numerical solution of the TDSE for phases $\varphi = 0$ and $\varphi = \pi/2$. Inset is the same parameters calculated using the SFA [67].

energy peaks having larger amplitude. We see similar behaviour with the spectrum calculated using the SFA in the suppression of the lowest energy peaks but there is not much similarity between the two methods for higher energy. The solution of the TDSE does agree with the spacing of the peaks, with the $\varphi = \pi/2$ solutions shifted to lower energy nearer the threshold in relation to the $\varphi = 0$ solution before the position of the peaks coinciding towards higher energy.

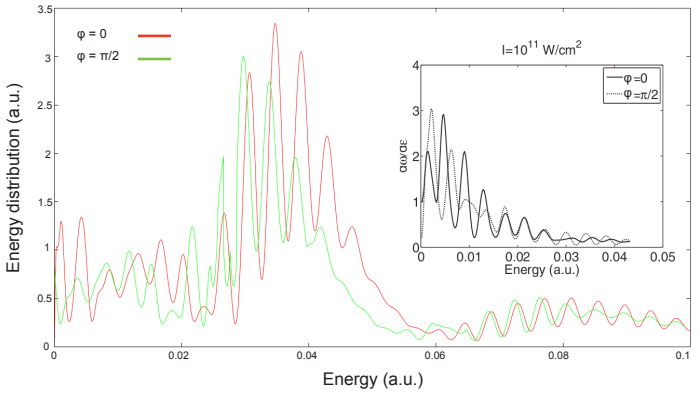

Figure 5.52: The ATD spectrum at the end of a pulse of 5 optical cycles of frequency $\omega = 0.0043$ a.u. and intensity of $I = 10^{11}$ W $\cdot$ cm^{-2} defined by (5.29) calculated from direct numerical solution of the TDSE for phases $\varphi = 0$ and $\varphi = \pi/2$. Inset is the same parameters calculated using the SFA [67].

We show the three spectra for $\varphi = 0$ now together on a logarithmic scale for comparison of structure and amplitude in figure 5.53.

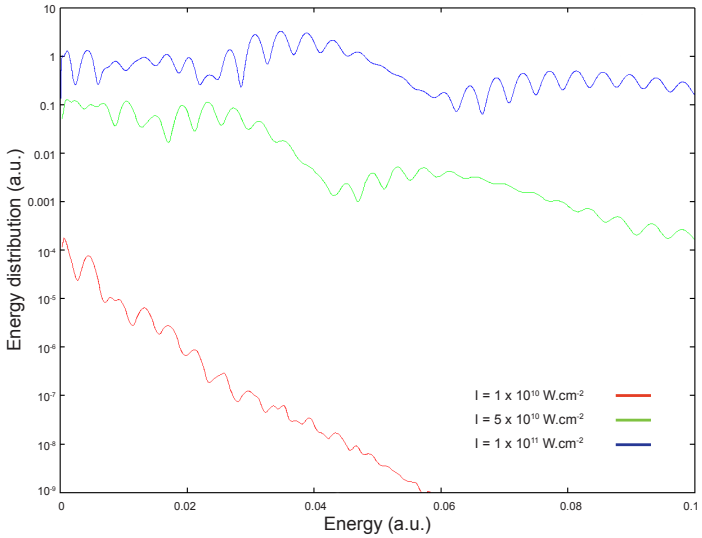

Figure 5.53: The ATD spectra at the end of a pulse of 5 optical cycles of frequency $\omega = 0.0043$ a.u. and intensities $I = 10^{10}$ (red), 5×10^{10} (green) and 10^{11} W $\cdot$ cm^{-2} (blue) defined by (5.29) for phase $\varphi = 0$.

These initial calculations show there is no indication of the low energy structure being present for any of the above intensities or phases. This suggests that the rescattering after ionisation due to the Coulomb field, absent in the case of the negative hydrogen ion, as seen in figures 5.50 to 5.52, plays an important role in the formation of the LES. We have shown here that it is possible to investigate negative ion systems using our methods in a similar way in the case of neutral atoms.

5.8.2 Argon

For completeness we report on applying the numerical methods to Argon on which most of the experiments are performed. In order to model the Argon atom we use the single active electron approximation and write the TDSE in the velocity gauge, in the form

$$\mathrm{i}\frac{\partial}{\partial t}\Psi(\mathrm{r},t) = \left[-\frac{1}{2}p^2 + V(r) + W(r) + \mathbf{p}\cdot\mathbf{A}(t)\right], \tag{5.50}$$

where the model potential is given by [54, 7]

$$V(r) = -\frac{1}{r}\left[1 + A\mathrm{e}^{-Br} + (17 - A)\mathrm{e}^{-Cr}\right]. \tag{5.51}$$

The constants A, B and C take values of $A = 5.4$, $B = 1$ and $C = 3.682$ respectively which ensures the eigenenergies of the singly excited states of Argon are obtained correctly. Furthermore, the K-shell, L-shell, and $3s$ ionisation potentials are reproduced accurately and the asymptotic behaviour of the model potential behaves as the true potential [54]. However, despite these points, equation (5.51) does not give accurate results close to the origin and hence to obtain a potential we can use in the solution of the TDSE we introduce a further soft repulsive core potential,

$$W(r) = F\left([(R_x - R)/G]^5 - [(R_x - R)/G]^4\right), \tag{5.52}$$

with $R_x = 3$, $F = 2.5$ and $G = 2.01785$. The potential is confined to the range $R < r < R_x$ where we take $R = 0.5$ a.u. Outside R_x all eigenfunctions in the well $V(r) + W(r)$ are identical to those in $V(r)$. Müller shows that imposing a hardcore boundary condition such as (5.52) on the wave function at a specific position induces only a minor distortion whilst eliminating the K and L shells [54]. Using the sum of these two potential functions gives accurate results at all positions.

We carry out calculations for a wavelength of $\lambda = 800$nm and an intensity of $I = 10^{14}$ W $\cdot$ cm^{-2} for a 2 cycle pulse. We use a B-spline basis with a box defined as $[0.5, 750]$ a.u. and 750 B-splines and take $N_l = 28$. For the time propagation we use the Arnoldi integrator with $\delta t = 0.2$ a.u. and 40 Krylov vectors. For the initial state we start in the $3s$ ground state for all calculations, with an ionisation potential of $E = 0.582148$ a.u. In figure 5.54 we show the above threshold ionisation spectrum against energy E. We can see that unlike for the negatively charged Hydrogen we do get a large peak for very low energy akin to the LES.

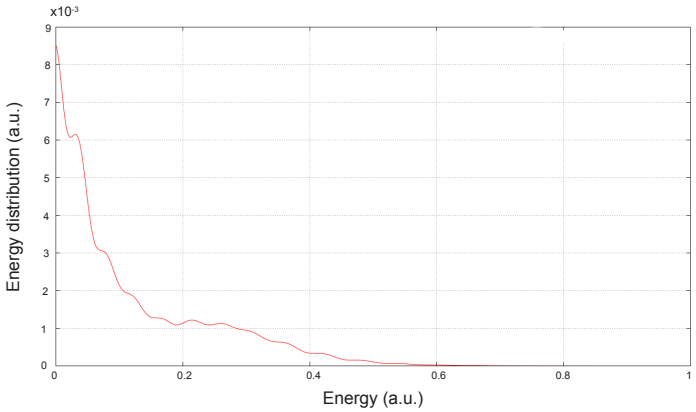

Figure 5.54: The photoelectron energy spectrum against electron energy for Argon at the end of a 2 cycle pulse of frequency $\omega = 0.0569$ a.u. and intensity $I = 10^{14}$ W $\cdot$ cm^{-2} calculated from direct numerical solution of the TDSE for phase $\varphi = 0$.

Chapter 6

Conclusion and Outlook

In this work we have focused on developing new approaches to the numerical solution of the time dependent Schrödinger equation (TDSE) using a spectral method, which in turn was used to study the interaction of atoms with an intense, low frequency laser field. The spectral method we implemented was used primarily with B-spline basis functions and we carried out the time integration using the explicit Arnoldi Krylov subspace method.

This model allowed the extraction of physical information (without projection on the eigenfunctions of the continuum) for the study of complex systems whose solutions are generally not analytically known. We were then able, using the wave function $\Psi(\mathbf{r}, t)$, to investigate the features of the system such as the probability density, the state populations, the ATI spectrum and angular distributions of the ejected electrons in detail by projecting on Coulomb functions. We analysed the influence of laser parameters such as the intensity I, frequency ω, phase φ and total pulse length τ. We also devised an interesting and intuitive way of viewing the evolution of the electron position and momentum density in three dimensional plots where in the case of the momentum we can clearly see the times of ionisation displayed as straight lines.

We carried this out first in one dimension using a model soft Coulomb potential as well as a Gaussian potential and the success of the numerical methods allowed us then to study the interaction of hydrogen as well as other three dimensional model atoms in the low frequency regime which theorists have taken a recent interest in because of the discovery of a low energy structure (LES) in the photoionisation spectra of atoms and molecules. The SFA, the most widely used method of solution

for systems in the tunnelling regime, does not reproduce this structure.

We looked at the theory and application of the two most commonly used gauges, the length gauge and the velocity gauge and investigated the effect of the choice of gauge on a number of different observables and in particular noting its effect on the observed momentum of the electron. We also made use of the Keldysh parameter γ which distinguished two regimes of ionisation, multiphoton ionisation $\gamma \gg 1$ and tunnelling ionisation $\gamma \ll 1$ which is dominant in the strong field regime. We also noted a number of situations where we lie in the region where $\gamma \simeq 1$ where we have interplay between the two regimes.

In writing our programs we paid special attention to the computation constraints that make a full numerical solution of the TDSE so difficult at low frequencies, high intensity and when the pulse length becomes long. The memory usage and run time in particular were difficult hurdles that had to be overcome in order to run our programs on the computers we had available. In order to be able to run a wider range of laser parameters and also significantly speed up other calculations we implemented exterior complex scaling (ECS) where the spatial coordinates are rotated into the complex plane with the effect of the wave packet becoming damped beyond a certain radius. This in turn allowed us to use a smaller working box and size of basis whilst the unscaled area remained unchanged from the full unscaled calculation. Thus we were able to calculate a number of the same observables including the ATI spectrum using the time dependent surface flux method (tSURFF) in much short times.

Our results at $\lambda = 800$nm and 2000nm are very similar in many respects - interference effects in angular distributions etc. However a pronounced peak is seen to develop at low frequency and becomes enhanced for more cycles and as $\omega \to 0$. So it seems the LES develops smoothly from higher frequencies. Various explanations have been put forward for the LES, both classical and semi-classical but what is clear is that a wave packet develops which has its momentum distribution peaked about $\mathbf{p} = 0$ and it remains a major challenge to understand this from a quantum perspective.

We analysed the angular distributions for a range of frequencies and showed how the dominant features could be understood via intra and inter cycle interferences. Our analysis of the limit $\omega \to 0$ shows that a promising approach to the LES may be to start from an adiabatic theory for the dynamics of the wave packet.

For future work we have already extended our program to allow the study of the interaction of atoms with circularly polarised lasers and indeed radiation of arbitrary polarisation. This extension means we now have to include the azimuthal angle ϕ as we are no longer symmetric in this angle as well as an extra quantum number m, the quantum magnetic number. This extension increases the memory usage of our program considerably with each m value running from $-l$ to l and in general more B-spline functions are needed to represent the wave function due to the more complex nature of the laser pulse and its effect on the wave function. In addition we can then use this circular polarisation in order to further the investigation into the LES, which is not present for circular polarisation [75].

Bibliography

[1] Agostini, P., Fabre, F., Mainfray, G., and Petite, G. Free-Free Transitions Following Six-Photon Ionization of Xenon Atoms. *Phys. Rev. Lett. 42*, 1127 (1979). 25

[2] Ammosov, M. V., Delone, N. B., and Krainov, V. P. Tunnel ionization of complex atoms and of atomic ions in an alternating electromagnetic field. *Sov. Phys. JETP 64*, 1191 (1986). 2, 29, 38

[3] Antoine, P., LHuillier, A., and Lewenstein, M. Attosecond Pulse Trains Using HighOrder Harmonics. *Phys. Rev. Lett. 77*, 7 (1996). 2, 38

[4] Antoine, P., Milosevic, D. B., LHuillier, A., Gaarde, M. B., Salieres, P., and Lewenstein, M. Generation of attosecond pulses in macroscopic media. *Phys. Rev. A 56*, 4960 (1997). 2

[5] Arbo, D. G., Persson, E., and Burgdorfer, J. Time Double-Slit Interference in Tunneling Ionization. *Phys. Rev. A 78*, 063407 (2008). 148, 188, 192, 207

[6] Arnoldi, W. E. The principle of minimized iteration in the solution of the matrix eigenvalue problem. *Quart. Appl. Math. 9*, 17 (1951). 69

[7] Awasthi, M., Vanne, Y. V., and Saenz, A. Single-active-electron approximation for describing molecules in ultrashort laser pulses and its application to molecular hydrogen. *Phys. Rev. A 77*, 063403 (2008). 46, 229

[8] Bachau, H., Cormier, E., Decleva, P., Hansen, J. E., and Martin, F. Applications of B-splines in atomic and molecular physics. *Rep. Prog. Phys. 64*, 1815 (2001). 53, 55, 133

[9] Baltuska, A., Udem, T., Uiberacker, M., Hentschel, M., Gouliel-makis, E., Gohle, C., Holzwarth, R., Yakovlev, V. S., Scrinzi, A., Hansch, T. W., and Krausz, F. Attosecond control of electronic processes by intense light fields. *Nature 521*, 611 (2003). 1

[10] Bardsley, J. N., Szoke, A., and Comella, M. J. Multiphoton ionisation from a short-range potential by short-pulse lasers. *J. Phys. B. 21*, 3899 (1988). 123

[11] Basile, S., Ferrante, G., and Trombetta, F. Multiphoton multichannel ionisation of hydrogen with elliptically polarised light. *J. Phys. B. At. Mol. Phys. 21*, L377 (1988). 42

[12] Bauer, D. Emergence of Classical Orbits in Few-Cycle Above-Threshold Ionization. *Phys. Rev. Lett. 94*, 113001 (2005). 115, 125, 127

[13] Bauer, D. *Theory of Intense Laser Matter Interaction.* Max-Planck-Institut fur Kernphysik, Heidelberg, Germany, 2006. 40

[14] Becker, W., Grasbon, F., Kopold, R., Milosevic, D. B., Paulus, G. G., and Walther, H. Above threshold ionization: from classical features to quantum effects. *Advances in Atomic, Molecular and Optical Physics 48* (2002). 21

[15] Becker, W., Schlicher, R. R., and Scully, M. O. Final-state effects in above-threshold ionisation. *J. Phys. B. At. Mol. Phys. 19*, L785 (1986). 42

[16] Bethe, H., and Salpeter, E. *Quantum Mechanics of One and Two Electron Atoms.* Springer, 1957. 176

[17] Blaga, C., Catoire, F., Colosimo, P., Paulus, G., Muller, H., Agostini, P., and DiMauro, L. Strong-field photoionization revisited. *Nature Phys. 5*, 335 (2009). 3, 42, 43

[18] Bucksbaum, P. H., Bashkansky, M., Freeman, R. R., McIlrath, T. J., and DiMauro, L. F. Suppression of Multiphoton Ionization with Circularly Polarized Coherent Light. *Phys. Rev. Lett. 56*, 2590 (1986). 21

[19] Corkum, P. Plasma perspective on strong field multiphoton ionization. *Phys. Rev. Lett. 71*, 1994 (1993). 35

[20] Cormier, E., Bachau, H., and Zhang, J. Discretization techniques applied to the study of multiphoton excitation of resonances in helium. *J. Phys. B 26*, 4449 (1993). 1

[21] Cormier, E., and Lambropoulos, P. Optimal gauge and gauge invariance in non-perturbative time-dependent calculation of above- threshold ionization. *J. Phys. B. At. Mol. Phys. 29*, 1667 (1996). 179, 182

[22] Cormier, E., and Lambropoulos, P. Above-threshold ionization spectrum of hydrogen using B-spline functions. *J. Phys. B. At. Mol. Phys. 30*, 77 (1997). 25, 26, 182

[23] Eden, J. G. High-order harmonic generation and other intense optical field-matter interactions: review of recent experimental and theoretical advances. *Progress in Quantum Electronics 28*, 2 (2004). 2

[24] Eiglsperger, J., Schonwetter, M., Piraux, B., and Madronero, J. *Atomic Data and Nuclear Data Tables 98*, 120 (2012). 54

[25] Faisal, F. *Theory of Multiphoton Processes*. Springer, 1987. 10

[26] Faisal, F. H. M. Multiple absorption of laser photons by atoms. *J. Phys. B. At. Mol. Phys. 6*, L89 (1973). 2, 38

[27] Fatunla, S. O. An Implicit Two-Point Numerical Integration Formula for Linear and Nonlinear Stiff Systems of Ordinary Differential Equations. *Math. Comput. 32*, 1 (1978). 64

[28] Fatunla, S. O. Numerical Integrators for Stiff and Highly Oscillatory Differential Equations. *Math. Comput. 34*, 373 (1980). 64, 65

[29] Frapiccini, A. L., Hamido, A., Schroter, S., Pyke, D., Mota-Furtado, F., OMahony, P. F., Madronero, J., Eiglsperger, J., and Piraux, B. Explicit schemes for time propagating many-body wavefunctions. *Phys. Rev. A 89*, 023418 (2014). 1, 66, 67, 69, 72, 77, 78, 79, 80, 82, 83, 84

[30] Giraud, S. *Dynamique de l'ionisation de l'atome d'hydrogene par une impulsion laser*. Ph.D. thesis, Universite Catholique De Louvain, Belgium, 2005. 35

[31] Grafe, S., Doose, J., and Burgdorfer, J. Quantum phase-space analysis of electronic rescattering dynamics in intense few-cycle laser fields. *J. Phys. B 45*, 055002 (2012). 102, 105, 106

[32] Hamido, A. *Interaction laser-atome : nouvelles approches thoriques dpendantes du temps*. Ph.D. thesis, Universite Catholique De Louvain, Belgium, 2015. 75, 207, 208, 210

[33] Hamido, A., Eiglsperger, J., Madronero, J., Mota-Furtado, F., OMahony, P., Frapiccini, A. L., and Piraux, B. Time scaling with efficient time-propagation techniques for atoms and molecules in pulsed radiation fields. *Phys. Rev. A 84*, 13422 (2011). 1, 51, 76, 96, 174

[34] Hammerling, R., Koch, O., Simon, C., and Weinmuller, E. Numerical Solution of Singular Eigenvalue Problems for ODEs with a Focus on Problems Posed on Semi-Infinite Intervals. 52

[35] Hansch, P., Walker, M. A., and Woerkom, L. D. V. Spatially dependent multiphoton multiple ionization. *Phys. Rev. A 54*, R2559 (1996). 1

[36] Hernandez-Garcia, C., Perez-Hernandez, J. A., Popmintchev, T., Murnane, M. M., Kapteyn, H. C., Jaron-Becker, A., Becker, A., and Plaja, L. Zeptosecond High Harmonic keV X-Ray Waveforms Driven by Midinfrared Laser Pulses. *Phys. Rev. Lett. 111*, 03002 (2013). 38

[37] Hochbruck, M., and Lubich, C. On Krylov subspace approximations to the matrix exponential operator. *SIAM J. Numer. Anal. 34*, 5 (1997). 72

[38] Huens, E., Piraux, B., Bugacov, A., and Gajda, M. Numerical studies of the dynamics of multiphoton processes with arbitrary field polarization: Methodological considerations. *Phys. Rev. A 55*, 2132 (1997). 1

[39] Jackson, J. D. *Classical Electrodynamics 3rd Edn.* Wiley and Sons, 1998. 19

[40] Joachain, C., Kylstra, N., and Potvliege, R. *Atoms in Intense Laser Fields*. Cambridge University Press, 2013. Available from: `http://dx.doi.org/10.1017/CBO9780511993459`. 1, 21, 28, 29, 30, 32, 36, 39

[41] Keldysh, L. V. Ionization in the field of a strong electromagnetic wave. *Sov.Phys.-JETP 20*, 1307 (1965). 2, 31

[42] Kulander, K. C., Schafer, K. J., and Krause, J. L. Dynamics of short-pulse excitation, ionization and harmonic conversion. In *Super-Intense Laser-Atom Physics*, A. L'Huillier, B. Piraux, and K. Rzazewski, Eds. Springer, 1993. 35

[43] Lambert, J. D. The initial value problem. In *Numerical Methods for Ordinary Differential Equations*, J. C. Butcher, Ed. Wiley, 1991. 61

[44] Leitner, T. *High Order Harmonic Generation as a possible Seed Source for the BESSY Free Electron Laser*. Ph.D. thesis, Humboldt-Universit at zu Berlin-Institut fur Physik, Berlin, Germany, San Diego, CA, USA, 2007. Available from: `https://www.helmholtz-berlin.de/media/media/grossgeraete/beschleunigerphysik/fel/rhyno/torsten_leitner_diplomarbeit.pdf`. 32

[45] Lemmel, C., Dimitriou, K., Tong, X., Nagele, S., Kartashov, D., Burgdorfer, J., and Grafe, S. Low-energy peak structure in strong-field ionization by mid-infrared laser-pulses. *Phys. Rev. A 45*, 011403 (1991). 43, 132

[46] Liu, C., and Hatsagortsyan, K. Origin of Unexpected Low Energy Structure in Photoelectron Spectra Induced by Mid-Infrared Strong Laser Fields. *Phys. Rev. Lett. 105*, 113003 (2010). 3, 43, 221

[47] Ludwig, A., Maurer, J., Mayer, B. W., Phillips, C. R., Gallmann, L., and Keller, U. Breakdown of the dipole approximation in strong-field ionization. *Phys. Rev. Lett. 113*, 243001 (2014). 13, 14

[48] Madronero, J., and Piraux, B. Explicit time-propagation method to treat the dynamics of driven complex systems. *Phys. Rev. A 80*, 033409 (2009). 67, 181

[49] McCurdy, C. W., and Martin, F. Implementation of exterior complex scaling in B-splines to solve atomic and molecular collision problems. *J. Phys. B. 37*, 917 (2004). 86

[50] Milonni, P. W., and Ackerhalt, J. R. Keldysh approximation, A2 and strong-field ionization. *Phys. Rev. A 39*, 1139 (1989). 42

[51] Milosevic, D. B., Paulus, G. G., Bauer, D., and Becker, W. Above-threshold ionization by few-cycle pulses. *J. Phys. B 39*, R203 (2006). 1

[52] Mohideen, U., Sher, M. H., Tom, H. W. K., Aumiller, G. D., Wood, O. R., Freeman, R. R., Boker, J., and Bucksbaum, P. H. High intensity above-threshold ionization of He. *Phys. Rev. Lett. 71*, 509 (1993). 21

[53] Morishita, T., Chen, Z., Watanabe, S., and Lin, C. D. Two-dimensional electron momentum spectra of argon ionized by short intense lasers: Comparison of theory with experiment. *Phys. Rev. A 75*, 023407 (2007). 140

[54] MULLER, H. G. Numerical simulation of high-order above-threshold-ionization enhancement in argon. *Phys. Rev. A 60*, 1341 (1999). 229

[55] NGANSO, T. *Ionization dynamics of a model atom exposed to a strong laser pulse and relativistic calculation of matrix elements for two-photon transitions in hydrogen-like ions.* Ph.D. thesis, Depot Institutionnel de l'Academie Louvain, Belgium, 2010. Available from: `http://hdl.handle.net/2078.1/73870`. 23, 31

[56] PARK, T. J., AND LIGHT, J. C. Unitary quantum time evolution by iterative Lanczos reduction. *J. Chem. Phys. 85*, 5870 (1986). 71

[57] PENG, L., AND GONG, Q. An accurate Fortran code for computing hydrogenic continuum wave functions at a wide range of parameters. *Comp. Phys. Comm. 181*, 12 (2010). 180

[58] PRESS, W. H., TEUKOLSKY, S. A., VETTERLING, W. T., AND FLANNERY, B. P. *Numerical Recipes in Fortran 77.* Cambridge University Press, 1986. 62, 63

[59] RANDERSON, P. J. *Fundamental dynamics in high intensity laser ionization.* Ph.D. thesis, Ohio State University, United States of America, 2005. Available from: `http://rave.ohiolink.edu/etdc/view?acc_num=osu1110219813`. 27

[60] REISS, H. R. Effect of an intense electromagnetic field on a weakly bound system. *Phys. Rev. A 22*, 5 (1980). 2, 38

[61] SAAD, Y. Analysis of some Krylov subspace approximations to the matrix exponential operator. *SIAM J. Numer. Anal. 29*, 209 (1992). 72

[62] SAAD, Y. *Iterative methods for sparse linear systems.* SIAM, 2003. 69

[63] SCHAFER, K., AND KULANDER, K. Energy analysis of time-dependent wave functions: Application to above-threshold ionization. *Phys. Rev. A 42*, 5794 (1990). 115

[64] Scrinzi, A. Infinite range exterior complex scaling as a perfect absorber in time-dependent problems. *Phys. Rev. A 81*, 053845 (2010). 86

[65] Shakeshaft, R. Multiphoton ionization of an atom; the choice of gauge. *Z. Phys. D 8*, 47 (1988). 19

[66] Shchatsinin, I. *Free Clusters and Free Molecules in Strong, Shaped Laser Fields*. Ph.D. thesis, Max-Born-Institut fur Nichtlineare Optik und Kurzzeit-spektroskopie, Berlin, Germany, 2009. 32

[67] Shearer, S., Smyth, M., and Gribakin, G. Electron detachment from negative ions in a short laser pulse. *Phys. Rev. A 84*, 033409 (2011). 226, 227

[68] Shore, B., and Knight, P. Enhancement of high optical harmonics by excess-photon ionisation. *J. Phys. B. At. Mol. Phys. 20*, 413 (1987). 37

[69] Siegman, A. E. *Lasers*. Mill Valley CA., 1986. 37

[70] Smirnova, O., Spanner, M., and Ivanov, M. Coulomb and polarization effects in laser-assisted XUV ionization. *J. Phys. B. At. Mol. Phys. 39*, S323 (2006). 41

[71] Smirnova, O., Spanner, M., and Ivanov, M. Analytical solutions for strong field-driven atomic and molecular one- and two-electron continua and applications to strong-field problems. *Phys. Rev. A 77*, 033407 (2008). 41

[72] Smyth, E. S., Parker, J. S., and Taylor, K. Numerical integration of the time-dependent Schrodinger equation for laser-driven helium. *Comp. Phys. Comm 114*, 1 (2012). 69

[73] Tao, L., and Scrinzi, A. Photo-electron momentum spectra from minimal volumes: the time-dependent surface flux method. *New Jour. Phys. 12*, 013021 (2012). 150, 152, 153

[74] Thomson, R., Leburn, C., and Reid, D. *Ultrafast Nonlinear Optics*. Springer, 2013. 33

[75] Titi, A. S., and Drake, G. W. F. Origin of the Low Energy Structure in Above Threshold Ionization. *ArXiv*, 1506.03034 (2015). 3, 221, 233

[76] Tolstikhin, O. Siegert-state expansion for nonstationary systems. IV. Three-dimensional case. *Phys. Rev. A 77*, 032712 (2008). 185, 222, 223

[77] Tolstikhin, O. I., and Morishita, T. Adiabatic theory of ionization by intense laser pulses: Finite-range potentials. *Phys. Rev. A 86*, 043417 (2012). 214

[78] Uzdin, R. Calculation of high-order harmonic generation spectrum and Floquet resonance states using the dynamical symmetry. *Phys. Rev. A 81*, 063429 (2010). 1, 37

[79] Wolter, B., Lemell, C., Baudisch, M., Pullen, M., Tong, X., Hemmer, M., Senftleben, A., Schroter, C. D., Ullrich, J., Moshammer, R., Biegert, J., and Burgdorfer, J. Formation of very-low-energy states crossing the ionization threshold of argon atoms in strong mid-infrared fields. *Phys. Rev. A 90*, 063424 (2014). 3, 44

[80] Yan, T., Popruzhenko, S. V., Vrakking, M., and Bauer, D. Low-Energy Structures in Strong Field Ionization Revealed by Quantum Orbits. *Phys. Rev. Lett. 105*, 253002 (2010). 43

[81] Zhou, X., Chen, Z., Morishita, T., Le, A., and Lin, C. D. Retrieval of electron-atom scattering cross sections from laser-induced electron rescattering of atomic negative ions in intense laser fields. *Phys. Rev. A 77*, 053410 (2008). 224, 225

[82] Zhou, X., and Lin, C. D. Linear-least-squares fitting method for the solution of the time-dependent Schrodinger equation: Applications to atoms in intense laser fields. *Phys. Rev. A 61*, 053411 (2000). 115